DISSERTATION

MODELING OF LASER-CREATED PLASMAS AND SOFT X-RAY LASERS

Submitted by

Mark Allen Berrill

Electrical and Computer Engineering Department

In partial fulfillment of the requirements

For the Degree of Doctor of Philosophy

Colorado State University

Fort Collins, Colorado

Summer 2010

COLORADO STATE UNIVERSITY

July 1, 2010

WE HEREBY RECOMMEND THAT THE DISSERTATION PREPARED UNDER OUR SUPERVISION BY MARK ALLEN BERRILL ENTITLED MODELING OF LASER-CREATED PLASMAS AND SOFT X-RAY LASERS BE ACCEPTED AS FULFILLING IN PART REQUIREMENTS FOR THE DEGREE OF DOCTOR OF PHILOSOPHY.

Committee on Graduate Work

Mario C. Marconi

Carmen S. Menoni

Siu Au Lee

Advisor: Jorge J. Rocca

Department Head: Anthony A. Maciejewski

ABSTRACT OF DISSERTATION

MODELING OF LASER-CREATED PLASMAS AND SOFT X-RAY LASERS

This dissertation describes the development of computer models to simulate laser created plasmas used to generate soft x-ray lasers. These compact short wavelength lasers have substantial average powers and very high peak brightness, that make them of significant interest for many applications. A better understanding of the plasmas is necessary to advance the development of these lasers into more compact, efficient, and higher power sources of coherent soft x-ray light.

The plasma phenomena involved are complex, and require a detailed computer model of the coupled magneto-hydrodynamic and atomic physics processes to simulate their behavior. The computer models developed as part of this work consist of hydrodynamic equations, coupled with an atomic model, radiation transport, and a ray propagation equation. The models solve the equations in a 1.5D or 2D approximation, and predict the spatio-temporal plasma variation of the parameters, including the electron density and temperature, and the ion populations, which are then used to compute the population inversion and the resulting laser gain. A 3D post processor ray trace code was developed to simulate the amplification of stimulated emission along the plasma column length including saturation effects. This allows for the direct calculation of the soft x-ray laser output and its characteristics.

Simulation results were compared with experiments conducted at Colorado State University. The general behavior of the plasma and the soft x-ray laser are well described by the model. A specific comparison of the model results with experimental measurements is presented for the case of a collisionally excited 13.2 nm wavelength Ni-like cadmium laser. The model predicts that an optical laser pulse of 1 J energy and 8 ps duration impinging at 23 degrees grazing incidence into a pre-created laser plasma can rapidly heat it to temperatures above 600 eV at a density of 2 x 10^{20} electrons/cm^3. This results in a computed peak small signal gain coefficient of 150 cm^{-1} in the 4d $^1S_0$ to 4p $^1P_1$ transition of Ni-like Cd at 13.2 nm. The model indicates that the amplified beam reaches the gain-saturated regime after 2.5 mm of propagation in the plasma, in agreement with the experimental observation of saturated behavior for propagation lengths of 2.5-3.0 mm. The computed soft x-ray laser pulse width of 5-9 ps moderately exceeds the experimental value of 5 ps and is the result of a stronger saturation broadening in the simulation. The simulated laser output energy of the order of 1 μJ is also in agreement with experiments. Simulations of injection-seeded Ne-like Ti and Ni-like Ag amplifiers that show very good agreement with the experimental results are presented. A direct comparison of the pulsewidth and the near and far-field beam profiles is made.

Finally, the results of a simulation of a plasma created by irradiation of solid targets with a 46.9 nm soft x-ray laser, in which single photon photoionization is the dominant energy absorption mechanism are presented. Low absorption (silicon, Z=14) and high absorption (chromium, Z=24) targets were heated by ~1 ns duration soft x-ray laser pulses. The experimental spectra agree with 1 ½ D simulations in showing that the

Si plasmas are significantly colder and less ionized than the Cr plasma, confirming that in contrast to plasmas created by visible wavelength lasers the plasma properties are largely determined by the absorption coefficient of the target material.

Mark Allen Berrill
Electrical & Computer Engineering Department
Colorado State University
Fort Collins, CO 80523
Summer 2010

TABLE OF CONTENTS

CHAPTER I) INTRODUCTION

There is a great deal of interest in short wavelength lasers for applications. One area of particular interest is soft x-ray lasers with wavelengths down to 10 nm. These very short wavelength lasers take place in plasmas, where a better understanding of the plasma behavior is needed. These plasmas are extremely complicated, operating across large variations of density and temperature, making it difficult to determine the behavior of a plasma as it evolves. To overcome these problems, magneto-hydrodynamic (MHD) codes, coupled with an advanced atomic model have been developed. MHD codes treat the plasma as a fluid and follow its evolution. When coupled to an atomic model, all of the plasma properties can be modeled numerically allowing simulations to predict the behavior of the plasma at a detailed level. The computed population densities on the species of interest can be used to calculate the laser gain and laser beam characteristics.

I.A) MHD codes:

Hydrodynamic simulations are used extensively to solve fluid problems. These problems may include water in a stream, ocean currents, etc. In addition they are used extensively for fluid-like problems such as air flow around an object, atmospheric simulations, stellar flows, and many more. All hydro codes start with the treatment of the material as a fluid and solve a system of fluid equations for the movement of the "fluid"

subjected to various forces and boundary conditions. The three fundamental fluid equations are the continuity equation, the conservation of momentum, and the conservation of energy. These equations create a complete set of coupled differential equations capable of describing the fluid. In addition to the fluid equation, additional properties are needed to describe the fluid, such as the thermal conductivity, the viscosity, etc. These properties enter into the fluid equations and can affect its evolution.

In the special case of a plasma, the "fluid" consists of charged particles. As a result it will behave differently under applied electric and magnetic fields. As a result Maxwell's equations are necessary to describe the interactions with electric and magnetic fields. These codes are commonly referred to as Magneto-Hydrodynamic (MHD) codes. They have been used extensively since Hannes Olof Gösta Alfvén received the Nobel Prize in 1970 for "fundamental work and discoveries in magneto-hydrodynamics with fruitful applications in different parts of plasma physics".[1]

While MHD codes are extensively used in plasma physics, there are few tools available for direct use. The code complexity and geometry can significantly affect their application. Very simple 0D codes can give very basic estimations for a simple geometry, while 3D codes are extremely complex requiring vast computation resources to run. Intermediate 1D, 1.5D, and 2D codes depend on simplifications that are based on the geometry and experimental conditions. Additionally the plasma properties can change rapidly over different conditions. This makes it very difficult to develop a code that would be valid over a large range of possible conditions. Finally, plasma properties are not fully developed for all conditions and are still under investigation. For all these reasons plasma

[1] http://nobelprize.org/physics/laureates/1970/

physics codes are usually developed to suit the application. There are already a number of MHD codes developed to handle problems of interest here. Some of the more sophisticated codes are Lasnex[2], Ehybrid[3], HYDRA[4,5], Radex[6], and CHIVAS[7].

This dissertation discusses codes developed for simulating the plasma conditions present in the soft x-ray laser experiments conducted here at Colorado State University. The first model developed uses a 1D planar geometry in which some lateral effects are taken into account using simple approximations. This type of geometry is commonly referred to as 1.5D. The second code is a full 2D code. The electrons and ions often have different temperatures and need to be treated independently. The simulated "fluid" is a plasma, however Maxwell's equations are not directly solved as there are no applied electric and magnetic fields. An additional approximation is that there are no self generated fields. This assumption is valid if there is no net current flow within the plasma and charge neutrality exists. Charge neutrality states that on average the net charge of a volume element is zero. If this were not true, internal electric fields would set up inside the plasma to redistribute the charge. An important consequence of charge neutrality is the coupling of the momentum equations. Charge neutrality ensures that the electrons and ions move together and only the net forces acting on the volume element need to be considered.

---

[2] G. B. Zimmerman et al., Comments Plasma Phys. Controlled Fusion, Vol. 2, p. 51, 1975.

[3] G. J. Pert, "*The hybrid model and its application for studying free expansion*", J. Fluid Mech., Vol. 131, p. 401, 1983.

[4] M. M. Marinak, S. W. Haan, T. R. Dittrich, R. E. Tipton, and G. B. Zimmerman, Phys. Plasmas 5, 1125 1998.

[5] M. M. Marinak, G. D. Kerbel, N. A. Gentile, O. Jones, D. Munro, S. Pollaine, T. R. Dittrich, and S. W. Haan, Phys. Plasmas 8, 2275 2001 .

[6] V. N. Shlyaptsev, A. V. Gerusov, A. V. Vinogradov, J. J. Rocca, O. D. Cortazar, F. Tomasel, and B. Szapiro, in Ultrashort Wavelength Lasers II, edited by S. Suckewer, SPIE Proc. Vol. 2012, pp. 99–110, 1993.

[7] S. Jacquemot, A. Decoster, "*Z scaling of collisional Ne-like X-ray lasers using exploding foils: refraction effects*", Laser and Particle Beams, Vol. 9, No. 2, pp. 517-526, 1991.

As a result the models discussed are two-temperature, single fluid magneto-hydrodynamic / atomic models.

I.B) Soft x-ray lasers:

Since the demonstration of the first lasers in 1960[8,9] there has been an interest in soft x-ray lasers for their applications in high resolution metrology, biological imaging, studies of atomic physics, photophysics, photochemistry, and diagnostics of high density plasmas. Most soft x-ray lasers, including those at Colorado State University, are based on a collisional electron excitation mechanism inspired in part by earlier work in visible and ultraviolet lasers[10,11]. Specifically these systems use electron impact excitation to excite the laser upper level in a charged ion. This differs from a recombination laser where the laser upper level is populated through a recombination process from an upper ion as first suggested by Gudzenko and Shelepin[12], or a photoionization scheme as proposed by Duguay and Rentzepis[13]. The first demonstration of substantial amplification at soft x-ray wavelengths occurred in 1985 when Matthews[14,15] and Suckewer[16,17] observed gain in

---

[8] T. H. Maiman, Nature, Vol. 187, p. 493, 1960.

[9] A. Javan, W. R. Bennett, Jr., D. R. Herriot, Physical Review, Vol. 6, p. 106, 1961.

[10] W. B. Bridges, "*Ionized gas lasers*", Handbook of Laser Science and Technol. Sec. 2, Vol. II, edited by M.J. Weber, 1982.

[11] M. A. Dunn, J. N. Ross, Prog. Quantum Electron, Vol. 4, p. 233, 1976.

[12] G. A. Gudzenko, L. A. Shelepin, Soviet Physics Journal, Vol. 18, 9. 998, 1964.

[13] M. A. Duguay, P. M. Rentzepis, Appl. Phys. Lett., Vol. 10, p. 350, 1967.

[14] D. L. Matthews *et al.*, Phys. Rev. Lett., Vol. 54, p. 110, 1985.

plasmas using collisional electron impact excitation and collisional electron-ion recombination respectively.

Early collisional lasers focused on the Ne-like series due to its stable electron configuration and well suited energy level structure. By ionizing atoms to the Ne-like state there were 10 electrons which completely filled the 1s, 2s, and 2p orbitals. Ne-like ions also have the ability to produce a steady state population inversion between the $2p^5 3p^1\ ^1S_0$ and $2p^5 3s^1\ ^1P_1$ levels. Subsequent experiments focused on the Ni-like series which is better suited to short wavelengths. This difference is due to a different atomic structure that involves a larger energy gap for the same degree of ionization and a high quantum efficiency. Lasing using the Ni-like series was demonstrated in 1987 by MacGowan[18]. Since that time a number of different collisional systems have been demonstrated using both the neon and nickel like ions, with the shortest wavelengths from the Ni-like series. A major advance in the laser created plasmas came with the use of a two pulse sequence[19]. By using two pulses the plasma conditions could be better controlled. The first pulse ablates the target and creates a large plasma volume. As the plasma expands the density gradients are reduced, minimizing the effects of refraction. However, the plasma will also undergo substantial cooling during the expansion reducing the temperature and the degree

---

[15] M. D. Rosen, P. L. Hagelstein, D. L. Matthews, E. M. Campbell, A. U. Hazi, B. L. Whitten, B. MacGowan, R. E. Turner, R. W. Lee, Phys. Rev. Lett., Vol. 57, p. 1004, 1986.

[16] S. Suckewer, C. H. Skinner, H. Milchberg, C. Keane, D. Voorhees, Phys. Rev. Lett., Vol. 55, p. 1753, 1985.

[17] S. Suckewer, C. H. Skinner, D. Kim, E. Valeo, D. Voorhees, A. Wouters, Phys. Rev. Lett., Vol. 57, p. 1004, 1986.

[18] B. J. MacGowan, S. Maxon, P. L. Hagelstein, C. J. Keane, R. A. London, D. L. Matthews, M. D. Rosen, J. H. Scofield, D. A. Whelan, "*Demonstration of Soft-X-Ray Amplification in Nickel-like Ions*", Physical Review Letters, Vol. 59, No. 19, pp. 2157-2160, 1987.

[19] Joseph Nilsen, Brian J. MacGowan, Luiz B. Da Silva, Juan C. Moreno, "*Prepulse technique for producing low-Z Ne-like x-ray lasers*", Physical Review A, Vol. 48, No. 6, pp. 4682-4685, 1993.

of ionization. As a result, a second pulse heats and ionizes the plasma creating the correct degree of ionization and the temperatures necessary to create a population inversion. By using this approach the energy required to produce a laser decreased dramatically. Additionally, the two-pulse scheme reduces refraction of the x-ray laser pulse, allowing it to travel long distances through the gain media.

The next major advance came with the use of short pump pulses[20,21]. By using a short pump pulse ~10 ps, the intensity required to achieve the temperatures needed to lase can be reached at much lower pulse energies. This allowed for significantly higher transient gain coefficients allowing the x-ray lasers to reach saturation with only 5-10 J of pump laser energy[22]. Note that because the gain is now transient the short lifetime created a new problem in the traveling wave mismatch. This occurs because the pump pulse illuminates the entire target simultaneously, while the x-ray laser requires time to traverse the plasma. For a 1 cm plasma the velocity mismatch is 33 ps. For a pulse duration of only a few tens of ps, the gain will end before the x-ray pulse can finish its amplification. To overcome this problem a traveling wave geometry must be used. This can be accomplished by delaying part of the beam with a stepped mirror[23], shifting the pulse front with

---

[20] P. V. Nickles, V. N. Shlyaptsev, M. Kalachnikov, M. Schnürer, Will, W. Sandner, "*Short Pulse X-Ray Laser at 32.6 nm Based on Transient Gain in Ne-like Titanium*", Physical Review Letters, Vol. 78, No. 14, pp. 2748-2751, 1997.

[21] J. Dunn, A. L. Osterheld, W. E. White, V. N. Shlyaptsev, R. E. Stewart, "*Demonstration of X-Ray Amplification in Transient Gain Nickel-like Palladium Scheme*", Physical Review Letters, Vol. 80, No. 13, pp. 2825-2828, 1998.

[22] J. Dunn, Y. Li, A. L. Osterheld, J. Nilsen, J. R. Hunter, V. N. Shlyaptsev, "*Gain Saturation Regime for Laser-Driven Tabletop, Transient Ni-Like Ion X-Ray Lasers*", Physical Review Letters, Vol. 84, No. 21, pp. 4834-4837, 2000.

[23] José R. Crespo López-Urrutia, Ernst E. Fill, "*Traveling-wave excitation of an X-ray laser medium*", SPIE Vol. 2012 Ultrashort Wavelength Lasers II, pp. 258-264, 1993.

diffraction gratings[24,25], or the use of a longitudinal pumping scheme[26,27]. These methods can minimize the difference between the pump pulse and the x-ray laser pulse, allowing for the continued amplification in very short duration gain media.

A final important advance is the use of the Grazing Incidence Pump (GRIP) scheme[28,29]. In this setup a pre-pulse is focused on the target at normal incidence creating the plasma, then a pump pulse is sent in at grazing incidence angle, as shown in figure 1.1,

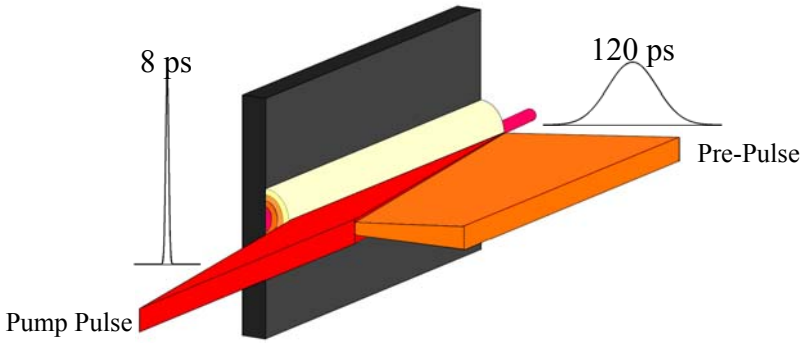

Figure 1.1: Slab target is illuminated by a 120 ps pre-pulse followed by a 8 ps pump pulse. Both pulses are line focused. The soft x-ray laser pulse is emitted along the line.

---

[24] H. J. Polland, T. Elasesser, A. Sellmeier, W. Kaiser, M. Kussler, N. J. Marx, B. Sens, K. H. Drexhage, "*Picosecond dye laser emission in the infrared between 1.4 and 1.8 μm*", Applied Physics B, Vol. 32, pp. 53-57, 1983.

[25] Zs. Bor, S. Szatmári, A. Müller, "*Picosecond pulse shortening by traveling wave amplified spontaneous emission*", Applied Physics B, Vol. 32, pp. 101-104, 1983.

[26] N. H. Burnett, G. D. Enright, "*Population inversion in the recombination of optically-ionized plasmas*", IEEE Journal of Quantum Electronics, Vol. 26, No. 10, pp. 1797-1808, 1990.

[27] D. C. Eder, P. Amendt, S. C. Wilks, "*Optical-field-ionized plasma X-ray lasers*", Physical Review A, Vol. 49, No. 9, pp. 6761-6776, 1992.

[28] V. N. Shlyaptsev, J. Dunn, S. Moon, R. Smith, R. Keenan, J. Nilsen, K. B. Fournier, J. Kuba, A. L. Osterheld, J. J. Rocca, B. Luther, Y. Wang, and M. Marconi, "*Numerical studies of transient and capillary x-ray lasers and their applications*", in Soft X-Ray Lasers and Applications V, E. E. Fill, S. Suckewer, eds., Proc. of SPIE, Vol. 5197, pp. 221-228, 2003.

[29] R. Keenan, J. Dunn, V. N. Shlyaptsev, R. Smith, P. K. Patel, D. F. Price, "*Efficient pumping schemes for high average brightness collisional x-ray lasers*", in Soft X-Ray Lasers and Applications V, E. E. Fill, S. Suckewer, eds., Proc. of SPIE, Vol. 5197, pp. 213-220, 2003.

heating the plasma to the required temperature. The use of grazing incidence pumping can significantly decrease the pumping energy by more efficiently depositing the energy into the optimum density. As the pump pulse travels through the plasma it is refracted by the plasma gradient, allowing it to travel a long distance through the density where total internal reflection occurs. The index of refraction of a plasma is given by $n = \sqrt{1 - n_e / n_c}$ where n_e is the electron density (#/cm^3), and n_c is the critical density $n_c = 1.11 \cdot 10^{21} / \lambda^2$ (λ in μm, n_c in #/cm^3). Using Snell's law, the density at which total internal reflection will occur is $n_e = n_c \sin^2 \theta$, where θ is the grazing incidence angle. At this density a large fraction of the laser energy will be coupled into the plasma. By adjusting the incident angle, the energy can be coupled to the region with the density for optimum gain. Note that this geometry is also inherently traveling wave. Its setup is similar to the longitudinal pumping scheme, except for the grazing angle. This difference will create a small temporal mismatch between the gains at the two ends of the plasma. This mismatch can be expressed by $\Delta t = (1 - \cos\theta) L / c$.

For experiments conducted at CSU[30,31,32,33,34], the pump laser consisted of a 5 Hz, 800 nm Ti:sapphire laser with three amplification stages. It produced a 350 mJ, 120 ps pre-pulse and a 1J, 1-20 ps pump pulse. These pulses were then focused onto a slab target to form a 4 mm x 30 μm line. Figure 1.2 shows the target chamber with the geometry to focus the two laser pulses on the target. This geometry was used to produce soft x-ray lasers with wavelengths ranging from 18.9 nm – 10.9 nm in Ni-like Molybdenum to Tellurium (Fig. 1.3).

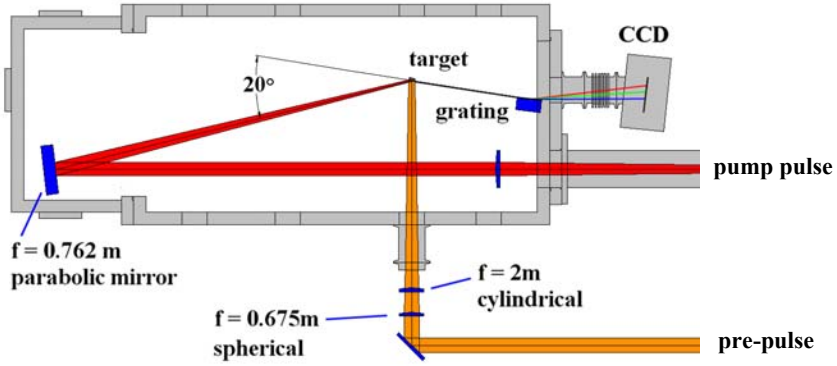

Figure 1.2: Target chamber design used to focus the two beams onto the target, Luther, et. al, Ref [28].

---

[30] B. M. Luther, Y. Wang, M. A. Larotonda, D. Alessi, M. Berrill, M. C. Marconi, J. J. Rocca, and V. N. Shlyaptsev, "*Saturated high-repetition-rate 18.9-nm tabletop laser in nickellike molybdenum*", Optics Letters, Vol. 30, 2005, pp. 165-167.

[31] J. J. Rocca, Y. Wang, M. A. Larotonda, B. M. Luther, D. Alessi, M. Berrill, A. Weith, M. C. Marconi, and C. S. Menoni, V. N. Shlyaptsev, "*Demonstration of saturated high repetition rate tabletop soft x-ray lasers at wavelengths down to 13.2 nm*", Proceedings of SPIE, Vol. 5919, Soft X-Ray Lasers and Applications VI, Ernst E. Fill, Editor, 591901, 2005.

[32] J. J. Rocca, Y. Wang, M. A. Larotonda, B. M. Luther, M. Berrill, and D. Alessi, "*Saturated 13.2 nm high-repetition-rate laser in nickellike cadmium*", Optics Letters, Vol. 30, 2005, pp. 2581-2583.

[33] Y. Wang, M. A. Larotonda, B. M. Luther, D. Alessi, M. Berrill, V. N. Shlyaptesev, J. J. Rocca, "*Demonstration of high-repetition-rate tabletop soft-x-ray lasers with saturated output at wavelengths down to 13.9 nm and gain down to 10.9 nm*", Physical Review A, Vol. 72, 053807, 2005.

[34] B. M. Luther, Y. Wang, M. A. Larotonda, D. Alessi, M. Berrill, J. J. Rocca, J. Dunn, R. Keenan, V.N. Shlyaptsev, "*High repetition rate collisional soft x-ray lasers based on grazing incidence pumping*", IEEE Journal of Quantum Electronics, in press.

As an example, Figure 1.3 shows sample spectra for each of the laser lines obtained from the first diffracted order off a variable spaced grating shown in figure 1.2. The 18.9 nm Mo (not shown) – 11.9 nm Sn are all saturated, the 11.4 nm Sb laser dominates the spectra, while the 10.9 nm laser clearly indicates gain but does not dominate the spectra. Figure 1.4 shows the output laser intensity with varying plasma length for Ni-like silver. The small signal gain and gain-length product were obtained by fitting the formula from Tallents[35] that accounts for a line integrated, saturated ASE laser. The small signal gain coefficient was 67.5 cm^{-1} and the gain-length product was 16.8.

[35] G. J. Tallents, Y. Abou-Ali, M. Edwards, R. E. King, G. J. Pert, S. J. Pestehe, F. Strati, R. Keenan, C. L. S. Lewis, S. Topping, O. Guilbaud, A. Klisnick, D. Ros, R. Clarke, D. Neely, and M. Notley, "*Saturated and Short Pulse Duration X-Ray Lasers*", X-Ray Lasers 2002: 8th International Conference on X-ray Lasers, J. J. Rocca, J. Dunn, and S. Suckewer, eds., AIP Conference Proceedings Vol. C641 (AIP, 2002), pp. 291-298.

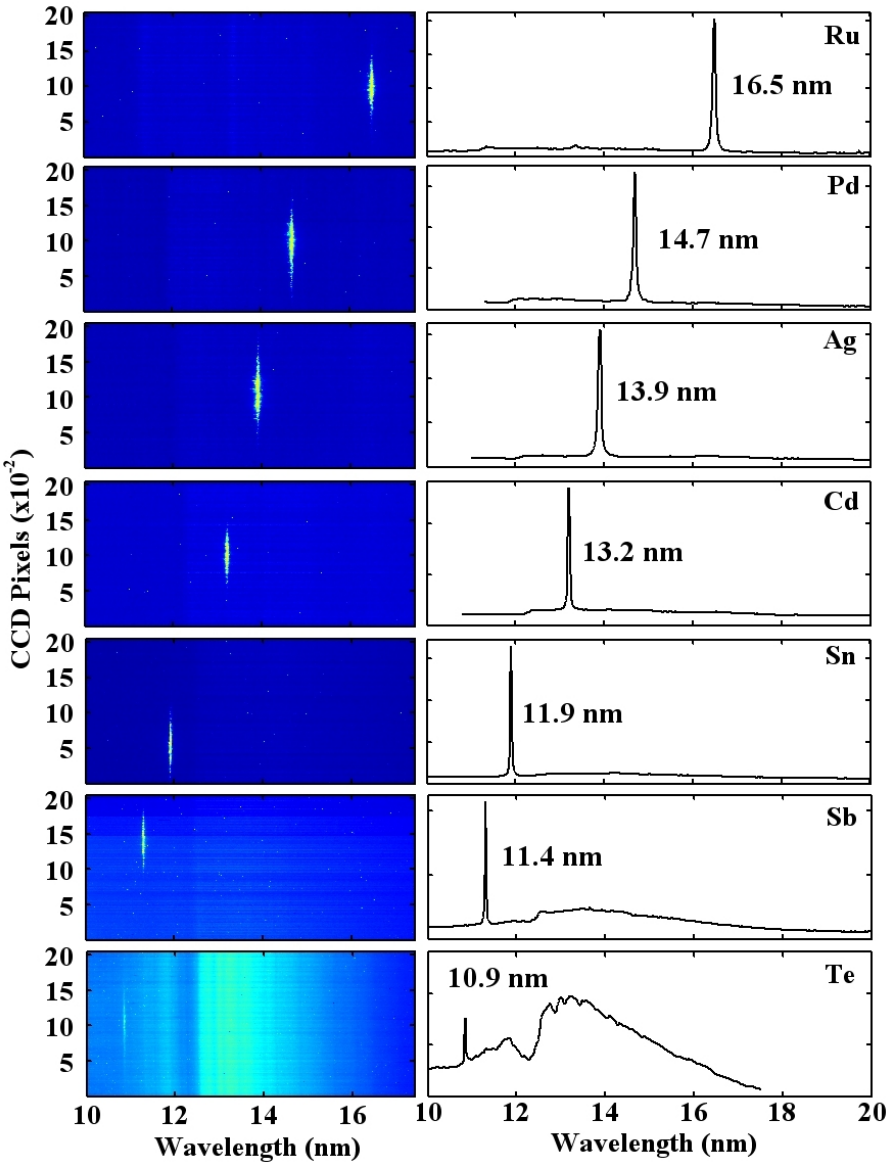

Figure 1.3: Sample of on-axis spectra obtained for each Ni-like element. Yong, et. al., Ref [33].

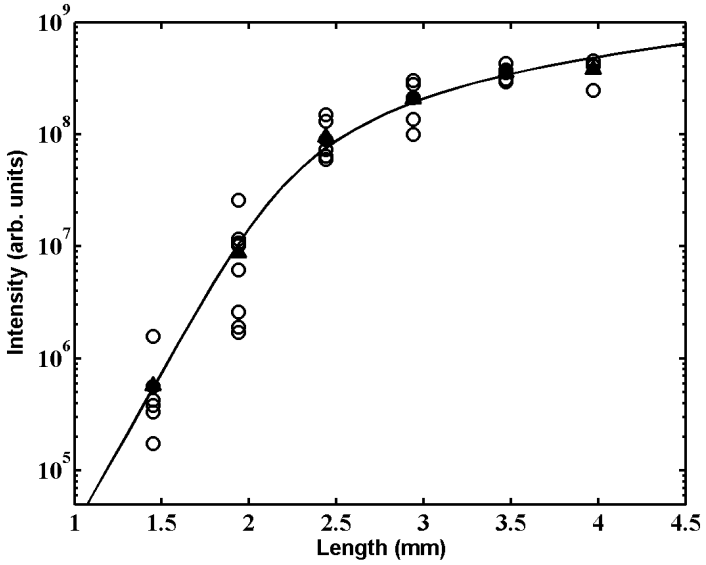

Figure 1.4: Intensity vs. length for Ni-like silver at 20 degrees, 300 ps delay. The small signal gain coefficient is 68 cm^{-1} with a total gain-length product of 16.8. Yong, et. al., Ref [33].

Figure 1.5a shows the intensity vs. grazing incidence angle θ for the Ni-like silver laser. Each angle measurement was taken at the optimum delay for that angle. Figure 1.5b shows the intensity vs. delay between the pre-pulse and pump pulsed taken at 20 degrees. The optimum pumping conditions were 20 degrees with a delay of 300 ps. At a repetition rate of 5 Hz the average power of the laser is greater than 2 μW.

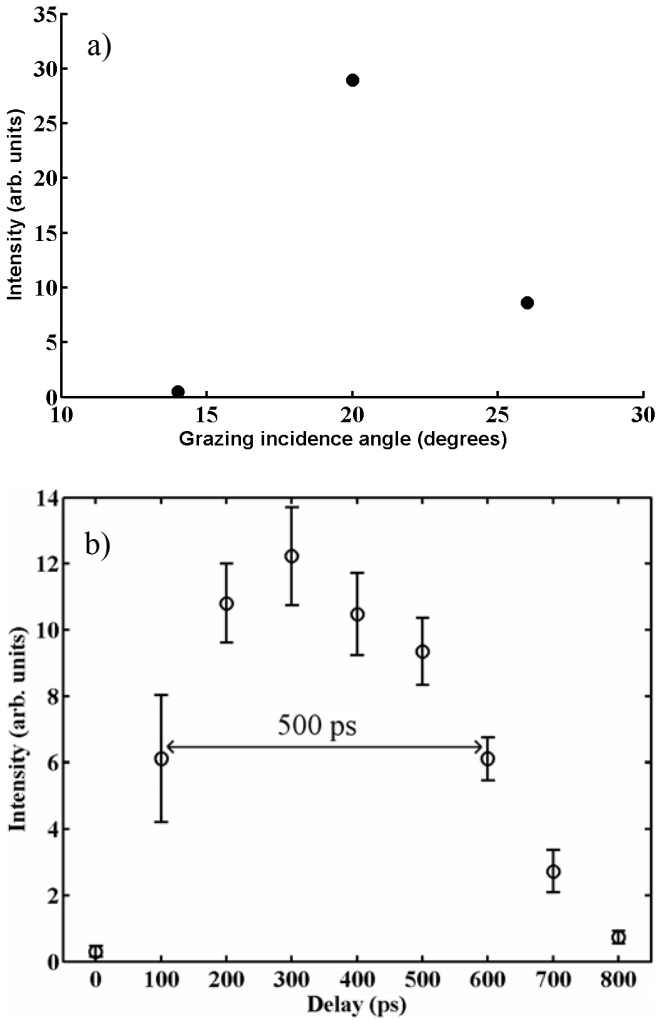

Figure 1.5: a) Intensity vs. angle for silver, b) Intensity vs. delay. Yong, et. al., Ref [33].

One of the major problems with the ASE lasers is that they have limited spatitial coherence (Fig. 1.6), and there is little control of the beam profiles. One possible improvement is by seeding the soft x-ray laser amplifier[36,37,38,39]. By seeding the amplifier with an initial pulse, the coherence of the initial seed can be preserved (Fig. 1.6).

[36] Ph. Zeitoun, et. al., "*A high-intensity highly coherent soft X-ray femtosecond laser seeded by a high harmonic beam*", Nature, 431, p. 426 (2004).

[37] Y. Wang, E. Granados, M.A. Larotonda, M. Berrill, B. M. Luther, D. Patel, C. S. Menoni, J. J. Rocca, "*High-Brightness Injection-Seeded Soft-X-Ray-Laser Amplifier Using a Solid Target*", Physical Review Letters, 97, 123901 (2006).

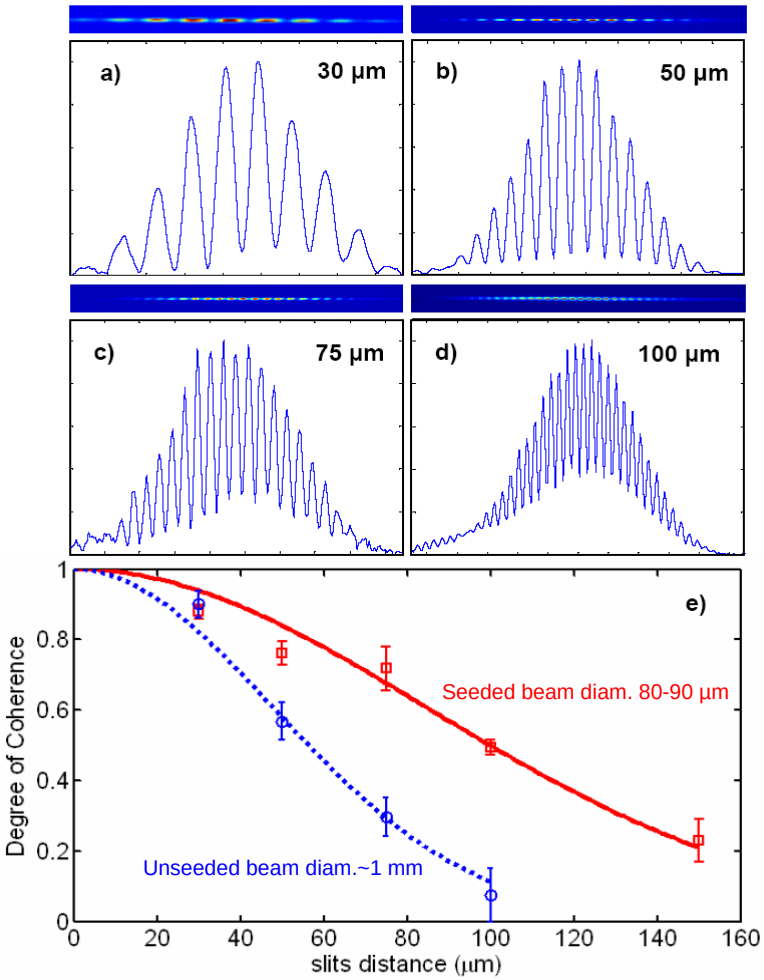

Figure 1.6: Plots of the fringe visibility for different slit widths (a-d) and the degree of coherence for a seeded and unseeded soft x-ray laser

The experimental setup for seeding a soft x-ray laser is illustrated in figure 1.7. The plasma amplifier is created by the same prepulse and short pulse as previously described. A small portion of the Ti:sapphire laser is split and focused into a Ne gas cell to generate high harmonic pulses (HHG). These are then focused using a toroidal mirror into the

[38] Y. Wang, E. Granados, F. Pedaci, D. Alessi, B. M. Luther, M. Berrill, J. J. Rocca, "Phase-*coherent, injection-seeded, table-top soft-X-ray lasers at 18.9 nm and 13.9 nm*" Nature Photonics 2, pp. 94-98 (2008)

[39] F. Pedaci, Y. Wang, M. Berrill, B. Luther, E. Granados, J. J. Rocca, "*Highly coherent injection-seeded 13.2 nm tabletop soft x-ray laser*", Optics Letters, 33, 491 (2008).

plasma amplifier. The center bandwidth of the Ti:sapphire laser can be tuned so that the high harmonic pulse is aligned with the wavelength of the amplifier.

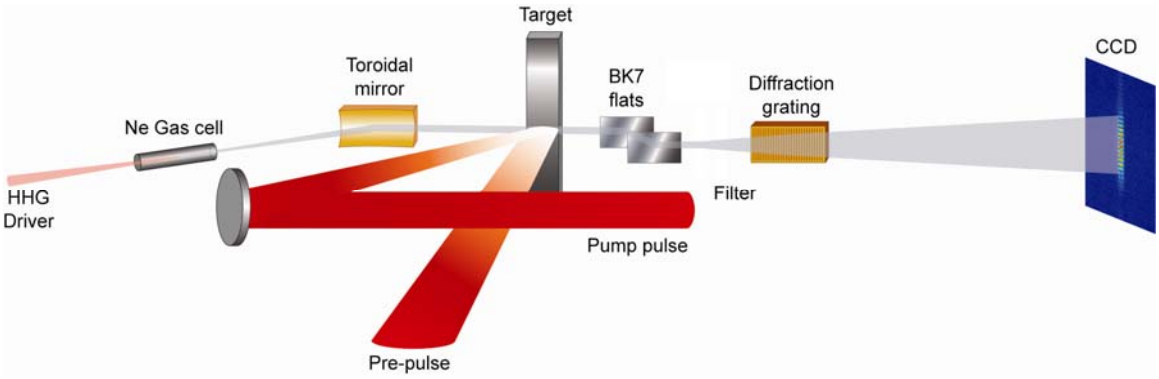

Figure 1.7: Experimental setup for the seeded soft x-ray lasers

In addition to improving the spatial coherence, the divergence of the amplified pulse can also be improved. Figure 1.8 shows the far-field beam patterns for a seeded and unseeded soft x-ray laser. By seeding the laser, a ~10x reduction in the divergence is observed. Section VII.D includes simulation and experimental results of the near and far-field beam profiles for the seeded and unseeded soft x-ray lasers. Finally, the duration of the seeded laser is significantly reduced to ~ 1 ps[40].

[40] Y. Wang, M. Berrill, F. Pedaci, M. M. Shakya, S. Gilbertson, Z. Chang, E. Granados, B. M. Luther, M. A. Larotonda, J. J. Rocca, "Measurement of 1-ps soft-x-ray laser pulses from an injection-seeded plasma amplifier", Physical Review A, 79, 023810 (2009)

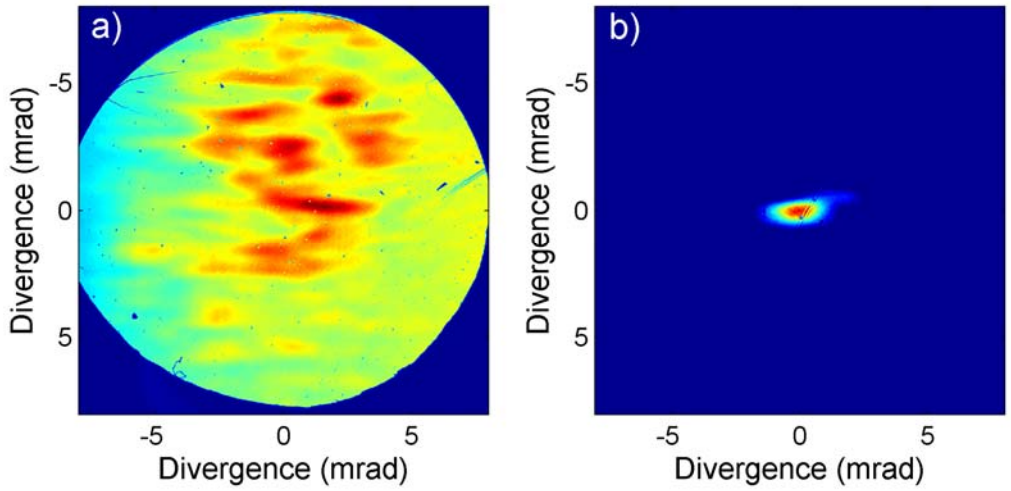

Figure 1.8: Far-field beam pattern for an unseeded (a) and seeded (b) soft x-ray laser

CHAPTER II.) MAGNETO-HYDRODYNAMIC (MHD) EQUATIONS:

The time evolution of the plasma dynamics can be described by a charged fluid. This allows for the use of a set of Magneto-Hydrodynamic (MHD) equations. The equations are similar to the standard hydrodynamic equations except that they include the charged particle nature of the plasma. One of the major differences between a MHD model of the type described here and a single fluid, single temperature hydrodynamic model is the need to take into account the different temperatures of the electrons and ions. The plasma consists of both free electrons and ions, but because there are different physical processes involved the electrons and ions need to be treated separately in many cases. The models described are a single fluid, 2-temperature code with temperatures for both the electrons and ions.

The plasma can be characterized by several parameters. The key parameters are the electron and ion temperatures T_e and T_i, the electron and ion densities N_e and N_i, the distribution among the possible ionization states, and the mean degree of ionization Zm (average number of free electrons per ion). In addition there are typical characterizations of a fluid such as the velocity $\vec{v}$ and the mass density ρ. To determine these parameters a complete set of equations are used: the continuity equation, the conservation of momentum, and the conservation of energy[41]. In addition, the equation of state (EOS) and thermodynamic properties are needed, as well as an atomic model. A full atomic code is used to calculate the ion populations and the resulting electron density (see chapter V).

---

[41] Victor L. Streeter, *Handbook of Fluid Dynamics*, McGraw-Hill Book Company, New York, 1961.

The absorption of the laser pulse can then be calculated (see chapter VI). With the knowledge of the energy losses and gains, the conservation of energy equation, conservation of momentum, and the continuity equation can be solved.

II.A) Lagrangian scheme, convective derivative:

To write the equations, we use either a Lagrangian or Eulerian formulation. In the case of a Eulerian formulation we write all of the derivatives with respect to a fixed point in space. By contrast, the idea behind a Lagrangian method is to replace the derivatives with respect to space with a derivative with respect to a fixed variable. As a result, instead of creating a spatial grid to evaluate the plasma properties, the grid can be with respect to any variable, in this work we use mass. We then create a fixed grid in mass, not in space. As the plasma evolves, the grid will follow the same amount of mass regardless of its spatial location. This presents a clear advantage in the case of an expanding plasma, where the spatial extent can be large and where the locations of interest may be small and move. For a similar level of detail, a smaller mass based grid may be used in place of a large or complex spatial grid. This can drastically reduce the required number of calculations. Note that because the Lagrangian scheme uses a fixed frame, all temporal derivatives must be written with total derivatives instead of partial derivatives. If we consider G(x,t) to be a property of a fluid, the change of G with respect to time in a moving frame with the fluid is the sum of the change of G at a fixed point in space and the change of G as the observer moves with the fluid

$$\frac{dG(x,t)}{dt} = \frac{\partial G}{\partial t} + \frac{\partial G}{\partial x}\frac{dx}{dt} = \frac{\partial G}{\partial t} + v_x \frac{\partial G}{\partial x} \qquad \text{(Eq. 2.1)}$$

If we generalize to three dimensions we obtain the convective derivative

$$\frac{d}{dt} = \frac{\partial}{\partial t} + \vec{v} \cdot \nabla \qquad \text{(Eq. 2.2)}$$

To complete the conversion to our Lagrangian scheme, we need to relate the spatial derivatives to derivatives with respect to mass. If we consider the width of a zone Δz and the mass density ρ, the mass per unit area within the zone ΔM is $\Delta M = \rho \Delta z$. In 1D, the derivatives are then related by

$$\frac{\partial}{\partial z} = \rho \frac{\partial}{\partial M} \qquad \text{(1D)} \qquad \text{(Eq. 2.3)}$$

We can approximate 2D effects by dividing by a factor $\frac{W}{2R}$ to account for the expansion in the transverse direction (see section III.A.4), where R is the half width of the expansion and W is the full width of the laser beam. Then, the relationship between the derivative in space and the derivative in mass is

$$\frac{\partial}{\partial z} = \rho \frac{2R}{W} \frac{\partial}{\partial M} \qquad \text{(1.5D)} \qquad \text{(Eq. 2.4)}$$

With these equations we will be able to covert the fluid equations to our Lagrangian scheme.

II.B) Continuity Equation:

The Continuity Equation describes the rate at which the mass density of a species s (ρ_s) changes. It is related to the expansion and the creation rate of the number density of species s ($\dot{n}_s$), the velocity of species s ($\vec{v}_s$), and the mass of species s (m_s).

We start with the change in the mass contained within a material volume[42]

$$\frac{D}{Dt}\int_V \rho_s dV = \int_V m_s \dot{n}_s dV \qquad \text{(Eq. 2.5)}$$

Apply Reynolds theorem

$$\int_V \left[\frac{d\rho_s}{dt} + \rho_s \left(\nabla \cdot \vec{v}_s \right) \right] dV = \int_V m_s \dot{n}_s dV \qquad \text{(Eq. 2.6)}$$

Since the control volume is arbitrary, we can let the volume tend toward zero

$$\frac{d\rho_s}{dt} + \rho_s \left(\nabla \cdot \vec{v}_s \right) = m_s \dot{n}_s \qquad \text{(Eq. 2.7)}$$

If there are no sources (no particles being created) we arrive at the familiar equation

$$\frac{d\rho_s}{dt} + \rho_s \left(\nabla \cdot \vec{v}_s \right) = 0 \qquad \text{(Eq. 2.8)}$$

While traditionally one would expect this to always hold true, it does not hold true for the electrons. As the plasma changes conditions, the atoms and ions will ionize and recombine, resulting in free electrons being created and destroyed. However, the total number of atoms and ions must remain constant, resulting in a global conservation of the mass.

$$\frac{d\rho}{dt} + \rho \left(\nabla \cdot \vec{v} \right) = 0 \qquad \text{(Eq. 2.9)}$$

Note that for the global continuity equation to hold all the species must have the same velocity. This is referred to as a single fluid model.

We can use the convective derivative (Eq. 2.2) to rewrite the equation in spatial coordinates

[42] Dimitri Mihalas and Barbra Weibel-Mihalas, *Foundations of Radiation Hydrodynamics*, Dover Publications, INC, 1999. pp. 60-61

$$\frac{\partial \rho}{\partial t} + \nabla \cdot (\rho \vec{v}) = 0 \qquad \text{(Eq. 2.10)}$$

Integrating over a volume element, we obtain

$$\frac{\partial}{\partial t}\int_V \rho d^3x + \oint_S \rho \vec{v} \cdot \hat{n} da = 0 \qquad \text{(Eq. 2.11)}$$

Using the cell average value of ρ over the differential volume V we get the final result

$$\frac{\partial \rho_V}{\partial t} = -\frac{1}{V}\oint_S \rho \vec{v} \cdot \hat{n} da \qquad \text{(Eq. 2.12)}$$

II.C) Conservation of Momentum:

Again, starting with a material volume, Newton's 2nd Law states that the time rate of change of the momentum associated with material element equals the force[43]

$$\frac{d}{dt}\int_V \rho_s \vec{v}_s dV = \int_V \vec{f}_s dV + \int_S \vec{t} dS \qquad \text{(Eq. 2.13)}$$

$t_j = T_{ij} n^i$ t is the surface force

Assuming single fluid model

$$\frac{d}{dt}\int_V \rho \vec{v} dV = \int_V \vec{f} dV + \int_S \vec{t} dS \qquad \text{(Eq. 2.14)}$$

Using global conservation of mass

$$\int_V \rho \frac{dv^i}{dt} dV = \int_V f^i dV + \int_S t^i dS \qquad \text{(Eq. 2.15)}$$

Using the divergence theorem

[43] Mihalas, pp. 70-71

$$\int_V \rho \frac{dv^i}{dt} dV = \int_V f^i dV + \int_S T^{ji} n_j dS = \int_V \left(f^i + T^{ji}_{,j} \right) dV \qquad \text{(Eq. 2.16)}$$

Again, the volume is arbitrary

$$\rho \frac{d\vec{v}}{dt} = \vec{f} + \nabla \cdot \vec{T} \qquad \text{(Eq. 2.17)}$$

Note: T_{ij} is the stress tensor[44]

$$T_{ij} = -p\delta_{ij} + \sigma_{ij} + Q_{ij} \qquad \text{(Eq. 2.18)}$$

where σ_{ij} is the viscous stress tensor and Q_{ij} is the artificial viscosity tensor

The viscous stress tensor is defined as:

$$\sigma_{ij} = \mu\left(\partial_i v_j + \partial_j v_i\right) + \lambda \partial_k v_k \delta_{ij} \qquad \text{(Eq. 2.19)}$$

μ is the coefficient of shear viscosity (or the coefficient of dynamical viscosity) and λ is the dilation coefficient of viscosity (or the second coefficient of viscosity).

If the media is isotropic (violated if there is a magnetic field)[45]:

$$\sigma_{ij} = \mu\left(\partial_i v_j + \partial_j v_i - \tfrac{2}{3} \nabla \cdot \vec{v} \delta_{ij}\right) + \varsigma \nabla \cdot \vec{v} \delta_{ij} \qquad \text{(Eq. 2.20)}$$

ς is the coefficient of bulk viscosity and is zero for a monatomic gas[46].

The artificial viscosity tensor is defined as:[47]

$$Q_{ij} = \mu_Q \left(\partial_i v_j + \partial_j v_i - \tfrac{2}{3} \nabla \cdot \vec{v} \delta_{ij}\right) \qquad \text{(Eq. 2.21)}$$

$$\mu_Q = \begin{cases} -\rho l^2 \nabla \cdot \vec{v} = l^2 \left(d\rho / dt\right) & \nabla \cdot \vec{v} < 0 \\ 0 & otherwise \end{cases} \qquad \text{(Eq. 2.22)}$$

l has units of length and is usually chosen to be some small multiple of the grid spacing

---

[44] Mihalas, pp. 82-83
[45] *Review of Plasma Physics*, S.I. Braginskii, "*Transport Processes in a Plasma*", pp 205-311.
[46] Schaum's Outiline on Fluid Dynamics, Second Edition, pp.54.
[47] Mihalas, p. 283

Note: This is the same form as the viscous stress tensor with $\varsigma = 0$, so there is no need to repeat the analysis in the following equations, simply incorporate it into the viscous stress.

If we have a monatomic gas and perform some simplifications (See APPENDIX D for the divergence of the stress tensor):

$$\rho \frac{d\vec{v}}{dt} = -\nabla p + \nabla \cdot \vec{\tau}_{vis} + \vec{f}_{ext} \qquad \text{(Eq. 2.23)}$$

$$\nabla \cdot \vec{\tau}_{vis} = \mu \nabla^2 \vec{v} + \tfrac{1}{3} \mu \nabla \left(\nabla \cdot \vec{v} \right) \qquad \text{(Eq. 2.24)}$$

Form 1 (Face-Centered Velocity):

One natural form for the momentum equation is to calculate the face-centered velocities. This is compatible with many finite volume techniques since we need the velocity at cell faces to calculate the flux of the different variables. Starting with equation 2.23, applying the convective derivative (Eq. 2.2) and simplifying we get

$$\frac{\partial \vec{v}}{\partial t} = -\left(\vec{v} \cdot \nabla \right) \vec{v} + \frac{1}{\rho} \left(-\nabla p + \nabla \cdot \vec{\tau}_{vis} \right) + \frac{1}{\rho} \vec{f}_{ext} \qquad \text{(Eq. 2.25)}$$

The i^{th} component is

$$\frac{\partial v_i}{\partial t} = -\left(\vec{v} \cdot \nabla \right) v_i + \frac{1}{\rho} \left(-\nabla p + \nabla \cdot \vec{\tau}_{vis} \right)_i + \frac{1}{\rho} f_{ext,i} \qquad \text{(Eq. 2.26)}$$

Form 2 (Cell-centered Momentum):

While it is natural to write the face-centered velocity, this does not enforce conservation of momentum. If we would like to guarantee conservation of momentum we need a cell-centered momentum equation. Starting with

$$\frac{\partial \rho \vec{v}}{\partial t} = \rho \frac{\partial \vec{v}}{\partial t} + \vec{v} \frac{\partial \rho}{\partial t}$$

Using equations 2.25 and 2.10 and looking at the ith component of the momentum

$$\frac{\partial \rho v_i}{\partial t} = -\nabla \cdot \left(\rho v_i \vec{v}\right) + \left(-\nabla p + \nabla \cdot \vec{\tau}_{vis}\right)_i + f_{ext,i} \qquad \text{(Eq. 2.27)}$$

Integrating over a volume element

$$\frac{\partial}{\partial t}\int_V \rho v_i d^3x + \oint_S \left(\rho v_i \vec{v} + p\hat{i}\right) \cdot \hat{n} da = \int_V \left(\nabla \cdot \vec{\tau}_{vis}\right)_i d^3x + \int_V \left(\vec{f}_{ext}\right)_i d^3x \qquad \text{(Eq. 2.28)}$$

Using the cell average value of ρv over the differential volume V we get

$$\frac{\partial \left(\rho v_i\right)_V}{\partial t} = -\frac{1}{V}\oint_S \left(\rho v_i\right)\left(\vec{v} \cdot \hat{n}\right) da - \frac{1}{V}\oint_S p\left(\hat{i} \cdot \hat{n}\right) da + \frac{1}{V}\int_V \left(\nabla \cdot \vec{\tau}_{vis}\right)_i d^3x + \frac{1}{V}\int_V \left(\vec{f}_{ext}\right)_i d^3x$$

(Eq. 2.29)

Alternatively, using a flux-based viscosity and pressure:

$$\frac{\partial \left(\rho v_i\right)_V}{\partial t} = -\frac{1}{V}\oint_S \left(\rho v_i\right)\left(\vec{v} \cdot \hat{n}\right) da + \frac{1}{V}\oint_S T_{ij}\left(\hat{j} \cdot \hat{n}\right) da + \frac{1}{V}\int_V \left(\vec{f}_{ext}\right)_i d^3x \qquad \text{(Eq. 2.30)}$$

Note: we are evaluating the momentum directly, not the velocity (see section III.B.4). This has two advantages. First, it ensures conservation of momentum across refinement levels. Second, the mass conservation equation uses the momentum, not the velocity. The disadvantage is that it does not handle discontinuities in density well. As mass travels between cells, the momentum may be conserved, but the velocity changes suddenly resulting in an unstable form. Special care is needed if viscosity is used.

II.D) Conservation of Energy:

The final hydrodynamic equation is conservation of energy. As stated earlier, the electrons and ions can have different temperatures and must have independent equations governing the conservation of energy. Proper treatment of energy conservation is vital for an accurate description of the plasma, as every property is strongly dependent on the temperature. Also, the plasma temperature is usually not uniform, leading to pressure gradients and other effects.

We can write the energy conservation equation for a material volume[48]

$$\frac{d}{dt}\int_V \varepsilon_s dV = \int_V \vec{f}_{ext}\cdot\vec{v}dV + \int_S \vec{t}\cdot\vec{v}dS - \int_S \vec{q}\cdot d\vec{S} + \int_V \dot{q}dV \qquad \text{(Eq. 2.31)}$$

where ε is the gas dynamic energy (the sum of the internal and kinetic energy), $\vec{f}_{ext}$ are the external forces doing work, $\vec{t}$ are the surface forces arising from stresses, $\vec{q}$ is the rate of energy flow out of the volume surface, and $\dot{q}$ is a heat source/sink.

Applying Reynolds theorem

$$\int_V \left[\frac{d\varepsilon_s}{dt} + \varepsilon_s\left(\nabla\cdot\vec{v}\right)\right]dV = \int_V \vec{f}_{ext}\cdot\vec{v}dV + \int_S \vec{t}\cdot\vec{v}dS - \int_S \vec{q}\cdot d\vec{S} + \int_V \dot{q}dV \qquad \text{(Eq. 2.32)}$$

Using the divergence theorem

$$\int_V \left[\frac{d\varepsilon_s}{dt} + \varepsilon_s\left(\nabla\cdot\vec{v}\right) + \vec{f}_{ext}\cdot\vec{v} - \nabla\cdot\left(\vec{t}\cdot\vec{v}\right) + \nabla\cdot\vec{q} + \dot{q}\right]dV = 0 \qquad \text{(Eq. 2.33)}$$

Since the volume is arbitrary

$$\frac{d\varepsilon_s}{dt} + \varepsilon_s\left(\nabla\cdot\vec{v}\right) + \vec{f}_{ext}\cdot\vec{v} - \nabla\cdot\left(\vec{t}\cdot\vec{v}\right) + \nabla\cdot\vec{q} + \dot{q} = 0 \qquad \text{(Eq. 2.34)}$$

Note that (see APPENDIX D):

[48] Mihalas, pp. 88-89

$$\vec{\vec{t}} \cdot \vec{v} = -p\vec{v} + \vec{\vec{\sigma}} \cdot \vec{v}$$

$$\frac{d\varepsilon_s}{dt} + \varepsilon_s\left(\nabla \cdot \vec{v}\right) + \nabla \cdot \left(p_s \vec{v}\right) = \nabla \cdot \left(\vec{\vec{\sigma}} \cdot \vec{v}\right) + \nabla \cdot \vec{q} + \dot{q} \qquad \text{(Eq. 2.35)}$$

For species s the gas dynamic energy becomes

$$\varepsilon_s = \frac{p_s}{\gamma - 1} + \frac{1}{2}\rho_s \vec{v}_s \cdot \vec{v}_s \qquad \text{(Eq. 2.36)}$$

Note: γ is the ratio of specific heats

$$\gamma = \frac{c_p}{c_v} = 1 + \frac{p\Delta V}{\Delta U} \qquad \text{(Eq. 2.37)}$$

Note: U is the internal energy of the plasma

$$\varepsilon_s = \frac{\Delta U}{\Delta V} + \frac{1}{2}\rho_s \vec{v}_s \cdot \vec{v}_s \qquad \text{(Eq. 2.38)}$$

If we split the gas dynamic energy into the internal and kinetic energy

$$\frac{d}{dt}\left(\frac{\Delta U_s}{\Delta V}\right) + \frac{1}{2}\frac{d}{dt}\left(\frac{1}{2}\rho_s \vec{v}_s \cdot \vec{v}_s\right) + \left(\frac{\Delta U_s}{\Delta V} + \frac{1}{2}\rho_s \vec{v}_s \cdot \vec{v}_s\right)\left(\nabla \cdot \vec{v}\right) + \nabla \cdot \left(p_s \vec{v}\right) = \nabla \cdot \left(\vec{\vec{\sigma}} \cdot \vec{v}\right) - \nabla \cdot \vec{q} + \dot{q}$$

(Eq. 2.39)

Using the conservation of mass and the conservation of momentum, noting that all species have the same velocity (single fluid model) and assuming there are no external forces:

$$\frac{d}{dt}\left(\frac{\Delta U_s}{\Delta V}\right) + \left(\frac{\Delta U_s}{\Delta V}\right)\left(\nabla \cdot \vec{v}\right) + p_s \nabla \cdot \vec{v} = \nabla \cdot \left(\vec{\vec{\sigma}} \cdot \vec{v}\right) - \vec{v} \cdot \nabla \cdot \vec{\vec{\sigma}} - \nabla \cdot \vec{q} + \dot{q} \qquad \text{(Eq. 2.40)}$$

Let Φ be the dissipation function (see APPENDIX D):

$$\frac{d}{dt}\left(\frac{\Delta U_s}{\Delta V}\right) + \left(\frac{\Delta U_s}{\Delta V}\right)\left(\nabla \cdot \vec{v}\right) + p_s \nabla \cdot \vec{v} = \Phi - \nabla \cdot \vec{q} + \dot{q} \qquad \text{(Eq. 2.41)}$$

Form 1 (Lagrangian Temperature Equation):

For an ideal plasma or gas

$$\gamma = 5/3, \quad p_s = n_s T_s, \quad \frac{\Delta U_s}{\Delta V_s} = 3/2\, n_s T_s \tag{Eq. 2.42}$$

$$\frac{3}{2}\frac{d(n_s T_s)}{dt} + \frac{3}{2} n_s T_s (\nabla \cdot \vec{v}) + p_s \nabla \cdot \vec{v} = \Phi - \nabla \cdot \vec{q} + \dot{q} \tag{Eq. 2.43}$$

By applying the continuity equation:

$$\frac{dn_s}{dt} + n_s (\nabla \cdot \vec{v}_s) = \dot{n}_s \tag{Eq. 2.44}$$

$$\frac{d(n_s T_s)}{dt} = n_s \frac{dT_s}{dt} + T_s (-n_s (\nabla \cdot \vec{v}_s) + \dot{n}_s) \tag{Eq. 2.45}$$

We can apply the previous relationship to the conservation of energy resulting in

$$\frac{3}{2} n_s \frac{dT_s}{dt} + p_s \nabla \cdot \vec{v} + \frac{3}{2} T_s \dot{n}_s = \Phi - \nabla \cdot \vec{q} + \dot{q} \tag{Eq. 2.46}$$

Form 2 (Cell-Centered Energy Equation):

If we apply the convective derivative to equation 2.41

$$\frac{\partial}{\partial t}\left(\frac{\Delta U}{\Delta V}\right) + \nabla \cdot \left(\frac{\Delta U}{\Delta V}\vec{v}\right) = -p_s \nabla \cdot \vec{v} + \Phi - \nabla \cdot \vec{q} - \dot{q} \tag{Eq. 2.47}$$

Integrating over a volume element

$$\frac{\partial}{\partial t}\left(\frac{\Delta U}{\Delta V}\right)_V = -\frac{1}{V}\oint_S \frac{\Delta U}{\Delta V}\vec{v} \cdot \hat{n} da - \frac{1}{V}\oint_S p\vec{v} \cdot \hat{n} da + \frac{1}{V}\oint_S v_i \sigma_{ij} dA_j - \frac{1}{V}\oint_S \vec{q} \cdot \hat{n} da - \frac{1}{V}\int_V \dot{q} d^3 x$$

(Eq. 2.48)

Note on the heat sources:

In this model we need to include all atomic processes as well as absorption of the incident laser beam and electron-ion collisions. The atomic losses are split into two terms, the stored potential energy and the radiated energy.

The atomic stored energy is the energy required to obtain the current population distribution. It includes the ionization energies and the energy needed to create the excited states weighted by their relative population densities. It is included directly within the internal energy and must be subtracted to obtain the current temperature.

The radiation is an energy loss term that is treated as an energy sink. Once the radiation rate is obtained it is included in $\dot{q}$.

The absorption is an energy source that is included in $\dot{q}$.

The energy transferred from electrons to ions is

$$\dot{q}_{ei} = \frac{3}{2}\frac{n_e}{\tau_{eq}}\left(T_e - T_i\right) \qquad \text{(Eq. 2.49)}$$

where τ_{eq} is the electron-ion equilibrium time and is discussed in chapter IV.

The thermal flux is simply thermal conduction and is given by the standard conduction equation. The thermal conductivity at cell faces between two cells is given by a flux average (see Appendix D).

$$\vec{q} = -\kappa_s \nabla T_s \qquad \text{(Eq. 2.50)}$$

II.E) Magnetic equation and validity of single fluid:

The use of the single fluid approximation stated previously is due to the electro-magnetic and electrostatic forces in the plasma. In general each species will be subject to different forces due to the different pressures of the species, the mass of the species, and the diffusion rates. As an example, the electrons typically have a higher temperature and therefore a larger pressure. Combined with their lighter mass, they tend to accelerate very quickly creating a charge imbalance between the electrons and ions. This will lead to an electrostatic force between the electrons and ions that will quickly exceed the other force terms causing the electrons and ions to redistribute to create a quasi-neutral plasma that behaves as a single fluid.

Despite the single fluid nature of the plasma, it still consists of charged particles and can therefore respond to electric and magnetic fields. To determine the magnetic fields within a plasma we would need to solve Maxwell's equations (ESU units).

$$\nabla \cdot \mathbf{D} = 4\pi\rho \qquad \text{(Eq. 2.51)}$$

$$\nabla \times \mathbf{H} = 4\pi\mathbf{J} + \frac{\partial \mathbf{D}}{\partial t} \qquad \text{(Eq. 2.52)}$$

$$\nabla \times \mathbf{E} = -\frac{\partial \mathbf{B}}{\partial t} \qquad \text{(Eq. 2.53)}$$

$$\nabla \cdot \mathbf{B} = 0 \qquad \text{(Eq. 2.54)}$$

Using Ohm's law:

$$\mathbf{E} = -\vec{v} \times \mathbf{B} + \eta 4\pi\mathbf{J} \qquad \text{(Eq. 2.55)}$$

$$\frac{\partial \mathbf{B}}{\partial t} = \nabla \times \left(\vec{v} \times \mathbf{B}\right) - \nabla \times \left(\eta 4\pi\mathbf{J}\right) \qquad \text{(Eq. 2.56)}$$

Assuming a quasi-static case

$$\frac{\partial \mathbf{B}}{\partial t} = \nabla \times \left(\vec{v} \times \mathbf{B}\right) - \nabla \times \left(\eta \nabla \times \mathbf{B}\right) \qquad \text{(Eq. 2.57)}$$

$$\frac{\partial \mathbf{B}}{\partial t} = \nabla \times \left(v \times \mathbf{B}\right) + \eta \nabla^2 \mathbf{B} \qquad \text{Induction equation} \qquad \text{(Eq. 2.58)}$$

Additionally, the Lorentz force will affect the momentum equation:

$$\vec{f} = \mathbf{J} \times \mathbf{B} \qquad \text{(Eq. 2.59)}$$

For the remainder of this work, we will be assuming a laser created plasma with no external magnetic fields. As a result there is no net current flow through the plasma and no resulting magnetic fields. It is still possible for the plasma to generate magnetic fields internally through cross temperature and density gradients. In the case of a 1D plasma this can not occur. In addition, the plasmas studied as part of this work have relatively limited cross gradients ensuring that the self-generated magnetic fields are weak. As a result, the current model does not need to explicitly solve the magnetic equation simplifying the model. The resulting model that is described only solves the hydrodynamic equations with a two-temperature energy equation.

CHAPTER III.) MAGNETO-HYDRODYNAMIC (MHD) MODELS:

In chapter II we discussed the hydrodynamic equations that are the foundation of any hydrodynamic model. At this point it is useful to begin to describe the two hydrodynamic models created as part of this work. The plasma parameters used are obtained from the conductivity model (see chapter IV) and the atomic properties are obtained from the atomic model (see chapter V). The two models used are a 1.5D and a 2D plasma model, both of which solve the full set of hydrodynamic equations using a two-temperature, single fluid approximation.

III.A.) 1D Magneto-Hydrodynamic (MHD) Model

The first model created is a 1.5D hydrodynamic model. This model solves the hydrodynamic equations in a 1D approximation using Lagrangian coordinates. This provides a very efficient and relatively simple scheme. Each equation is written in a 1D formulation utilizing the total derivative and solved independently of the other equations. By separating the equations we will be able to write efficient numerical forms (see section III.A.3). Each equation can then be solved using an implicit solver, and looping over all of the equations using an explicit time integrator. 2D effects on the plasma expansion can be approximated through the use of a self-similar solution of the equations (see section III.A.4).

III.A.1.) Flow Diagram

The basic flow of the 1.5D model is outlined in figure 3.1. The model starts with a desired time step (see section III.A.5). It will then calculate the atomic properties of the plasma using the atomic model described in chapter 5. Next we will calculate the plasma properties such as the electron and ion thermal conductivities, the electron-ion equilibration time, and the complex index of refraction using the conductivity model in chapter IV. We can then calculate the laser intensity and the resulting laser absorption using the absorption model in chapter VI. At this point we sequentially solve each of the equations, the electron and ion temperatures, the equation of motion, and the continuity equation. Finally we can calculate the self-similar width to approximate the second dimension and repeat until we reach the final time.

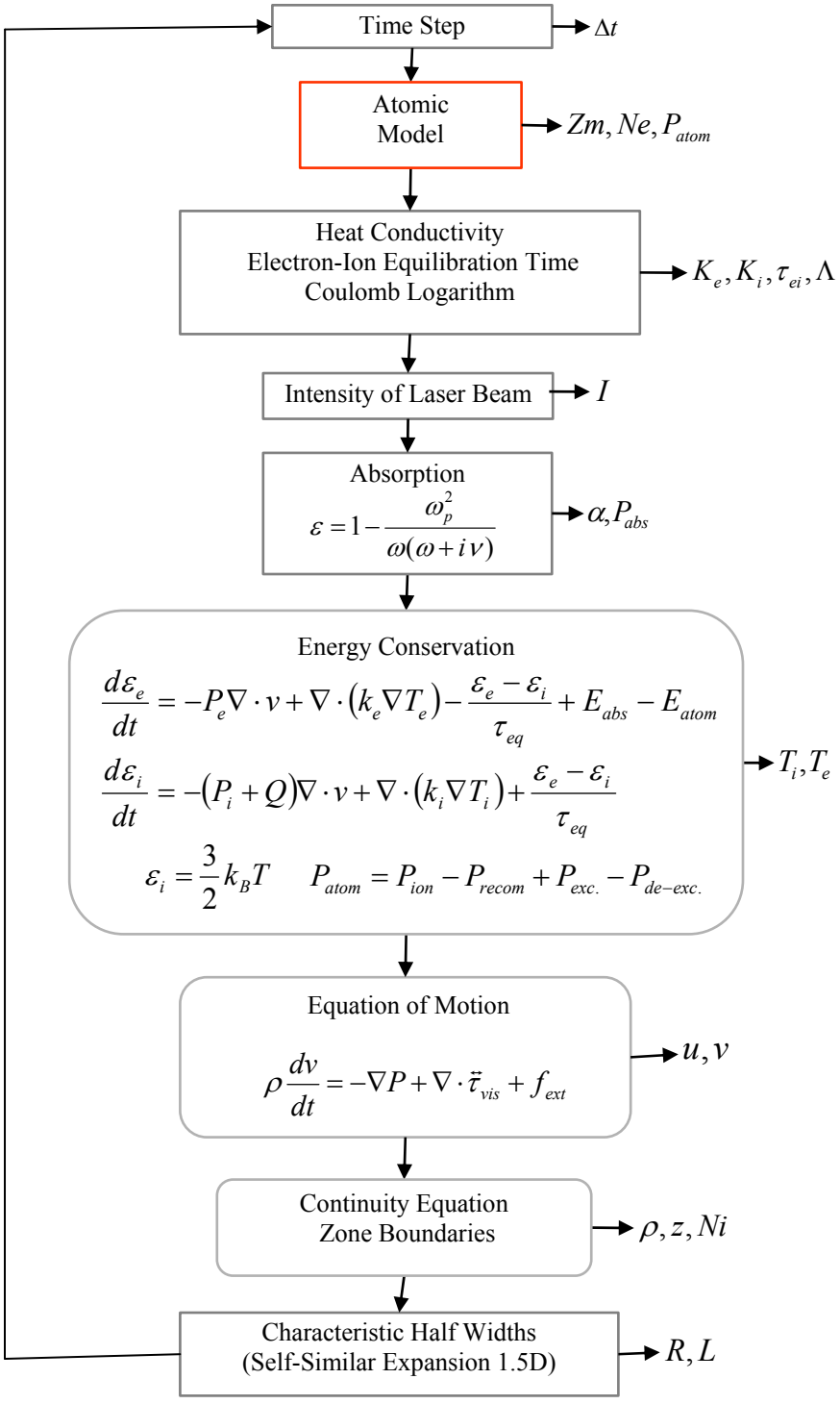

Figure 3.1: Flow chart for the model.

III.A.2.) Summary of MHD Equations

In chapter II we derived the different Magneto-Hydrodynamic (MHD) equations starting with the total derivative. For each hydrodynamic equation we had the equation written in terms of the total derivative which is used for the Lagrangian coordinates in the 1.5D model. The primary equations are summarized below.

$$\frac{d\rho}{dt} + \rho\left(\nabla \cdot \vec{v}\right) = 0 \qquad \text{(Eq. 3.1)}$$

$$\rho \frac{d\vec{v}}{dt} = -\nabla p + \nabla \cdot \vec{\tau}_{vis} + \vec{f}_{ext} \qquad \text{(Eq. 3.2)}$$

$$\frac{3}{2} n_s \frac{dT_s}{dt} + p_s \nabla \cdot \vec{v} + \frac{3}{2} T_s \dot{n}_s = \Phi - \nabla \cdot \vec{q} + \dot{q} \qquad \text{(Eq. 3.3)}$$

We can rewrite these equations in one dimension assuming the quantities of interest vary only in the z-direction

$$\frac{d\rho}{dt} = -\rho \frac{\partial v_z}{\partial z} \qquad \text{(Eq. 3.4)}$$

$$\rho \frac{dv_z}{dt} = -\frac{\partial p}{\partial z} + \frac{\partial}{\partial z}\left(\frac{4}{3}\mu \frac{\partial v_z}{\partial z}\right) + f_{ext,z} \qquad \text{(Eq. 3.5)}$$

$$\frac{dT_s}{dt} = -\frac{2}{3} T_s \frac{\partial v_z}{\partial z} + \frac{8}{9 n_s} \mu_s \left(\frac{\partial v_z}{\partial z}\right)^2 + \frac{2}{3 n_s} \frac{\partial}{\partial z}\left(\kappa_s \frac{\partial T_s}{\partial z}\right) + \frac{2}{3 n_s} \dot{q}_s \qquad \text{(Eq. 3.6)}$$

Converting to Lagrangian coordinates (using mass) and assuming no external forces we arrive at the final form of the hydrodynamic equations in 1D

$$\frac{d\rho}{dt} = -\rho^2 \frac{\partial v_z}{\partial M} \qquad \text{(Eq. 3.7)}$$

$$\frac{dv_z}{dt} = -\frac{\partial p}{\partial M} + \frac{4}{3} \frac{\partial}{\partial M}\left(\rho \mu \frac{\partial v_z}{\partial M}\right) \qquad \text{(Eq. 3.8)}$$

$$\frac{dT_i}{dt} = \left\{ \begin{array}{l} -\frac{2}{3}\rho\frac{2R}{W}\frac{\partial u}{\partial M}T_i + \frac{8}{9n_i}\eta_i\left(\rho\frac{2R}{W}\frac{\partial v_z}{\partial M}\right)^2 \\ +\frac{2}{3n_i}\rho\frac{2R}{W}\frac{\partial}{\partial M}\left(\kappa_i\rho\frac{2R}{W}\frac{\partial T_i}{\partial M}\right) \\ -\frac{2}{3}T_i\frac{\partial v_y}{\partial y} + \frac{2}{3n_i}\frac{\partial}{\partial y}\left(\kappa_i\frac{\partial T_i}{\partial y}\right) \\ +\frac{Z}{\tau_{eq}}\left(T_e - T_i\right) \end{array} \right\} \qquad \text{(Eq. 3.9)}$$

$$\frac{dT_e}{dt} = \left\{ \begin{array}{l} -\frac{2}{3}\rho\frac{2R}{W}\frac{\partial v_z}{\partial M}T_e + \frac{8}{9n_e}\eta_e\left(\rho\frac{2R}{W}\frac{\partial v_z}{\partial M}\right)^2 \\ +\frac{2}{3n_e}\rho\frac{2R}{W}\frac{\partial}{\partial M}\left(\kappa_e\rho\frac{2R}{W}\frac{\partial T_e}{\partial M}\right) \\ -\frac{2}{3}\frac{\partial v_y}{\partial z}T_e + \frac{2}{3n_e}\frac{\partial}{\partial y}\left(\kappa_e\frac{\partial T_e}{\partial y}\right) \\ -\frac{T_e - T_i}{\tau_{eq}} + \frac{2}{3n_e}\left(E_{abs} - E_{atom}\right) + \left(\frac{m_e v_z^2}{3} - T_e\right)\frac{1}{Z}\frac{dZ}{dt} \end{array} \right\} \qquad \text{(Eq. 3.10)}$$

III.A.3.) Numerical Form

The continuity equation is the easiest equation to put in numerical form. By using the lagrangian coordinates, we can use the fact that mass is not allowed to cross cell boundaries due to mass conservation. Then, instead of solving equation 3.7 we can use equations 2.3 or 2.4 to get the mass density directly.

To solve the velocity equation 3.8, we want to know the velocities at the boundaries between zones and will use the Crank-Nicholson scheme (see APPENDIX C). Knowledge of the velocity at the boundaries gives the expansion / compression for each zone. Because we know the temperature, density, and the resulting pressure at the midpoints, this works very well. See figure 3.2 for a sample drawing of points where the velocity and pressure are known.

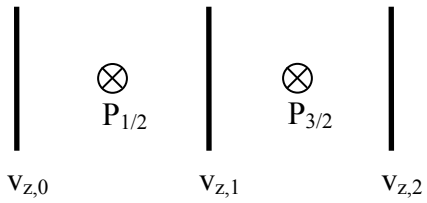

Figure 3.2: Sample zoning diagram showing the velocity u at the zone boundaries and the pressure P at the zone midpoints.

The temporal derivative may be written as

$$\left.\frac{dv_z}{dt}\right|_j^{n+1/2} = \frac{v_{zj}^{\,n+1} - v_{zj}^{\,n}}{\Delta t^{n+1/2}}$$

The pressure term can be written as

$$-\frac{2}{W}\left.\frac{\partial(RP)}{\partial M}\right|_j^{n+1/2} = -\frac{2}{W}\frac{R_{j+1/2}^{n+1/2}P_{j+1/2}^{n+1/2} - R_{j-1/2}^{n+1/2}P_{j-1/2}^{n+1/2}}{\Delta M_j}$$

$$\text{Let } \gamma_j^{n+1/2} = -\frac{2\Delta t^{n+1/2}}{W}\frac{R_{j+1/2}^{n+1/2}P_{j+1/2}^{n+1/2} - R_{j-1/2}^{n+1/2}P_{j-1/2}^{n+1/2}}{\Delta M_j}$$

Finally, the viscosity term is written as

$$\frac{16R}{3W^2}\frac{\partial}{\partial M}\left.\left(R\rho\eta\frac{\partial v_z}{\partial M}\right)\right|_j^{n+1/2} = \frac{16R}{3W^2}\frac{\left.\left(R\rho\eta\frac{\partial v_z}{\partial M}\right)\right|_{j+1/2}^{n+1/2} - \left.\left(R\rho\eta\frac{\partial v_z}{\partial M}\right)\right|_{j-1/2}^{n+1/2}}{\Delta M_j}$$

$$= \frac{16R_{j+1}^{n+1/2}}{3W^2\Delta M_j}\left[\begin{array}{l} R_{j+1/2}^{n+1/2}\rho_{j+1/2}^{n+1/2}\eta_{j+1/2}^{n+1/2}\dfrac{v_{zj+1}^{\,n+1/2} - v_{zj}^{\,n+1/2}}{\Delta M_{j+1/2}} \\ -R_{j-1/2}^{n+1/2}\rho_{j-1/2}^{n+1/2}\eta_{j-1/2}^{n+1/2}\dfrac{v_{zj}^{\,n+1/2} - v_{zj-1}^{\,n+1/2}}{\Delta M_{j-1/2}} \end{array}\right]$$

$$\text{Let } \alpha_j^{n+1/2} = \frac{8\Delta t^{n+1/2}}{3W^2}\frac{R_{j+1}^{n+1/2}R_{j+1/2}^{n+1/2}\rho_{j+1/2}^{n+1/2}\eta_{j+1/2}^{n+1/2}}{\Delta M_j\Delta M_{j+1/2}}$$

$$\beta_j^{n+1/2} = \frac{8\Delta t^{n+1/2}}{3W^2}\frac{R_{j-1}^{n+1/2}R_{j-1/2}^{n+1/2}\rho_{j-1/2}^{n+1/2}\eta_{j-1/2}^{n+1/2}}{\Delta M_j\Delta M_{j-1/2}}$$

Equating both sides of the differential equation yields

$$v_{z\,j}^{\,n+1} - v_{z\,j}^{\,n} = \gamma_j^{n+1/2} + \alpha_j^{n+1/2}\left(v_{z\,j+1}^{\,n+1} - v_{z\,j}^{\,n+1} + v_{z\,j+1}^{\,n} - v_{z\,j}^{\,n}\right) - \beta_j^{n+1/2}\left(v_{z\,j}^{\,n+1} - v_{z\,j-1}^{\,n+1} + v_{z\,j}^{\,n} - v_{z\,j-1}^{\,n}\right)$$

Simplifying we have

$$\left\{\begin{array}{l} -\alpha_j^{n+1/2} v_{z\,j+1}^{\,n+1} \\ +\left(1+\alpha_j^{n+1/2}+\beta_j^{n+1/2}\right) v_{z\,j}^{\,n+1} \\ -\beta_j^{n+1/2} v_{z\,j-1}^{\,n+1} \end{array}\right\} = \alpha_j^{n+1/2} v_{z\,j+1}^{\,n} + \left(1-\alpha_j^{n+1/2}-\beta_j^{n+1/2}\right) v_{z\,j}^{\,n} + \beta_j^{n+1/2} v_{z\,j-1}^{\,n} + \gamma_j^{n+1/2}$$

Let: $D_j = \left(1+\alpha_j^{n+1/2}+\beta_j^{n+1/2}\right)$

$$Y_j = \alpha_j^{n+1/2} v_{z\,j+1}^{\,n} + \left(1-\alpha_j^{n+1/2}-\beta_j^{n+1/2}\right) v_{z\,j}^{\,n} + \beta_j^{n+1/2} v_{z\,j-1}^{\,n} + \gamma_j^{n+1/2}$$

We can now write the equation in a tridiagonal form

$$-\beta_j^{n+1/2} v_{z\,j-1}^{\,n+1} + D_j v_{z\,j}^{\,n+1} - \alpha_j^{n+1/2} v_{z\,j+1}^{\,n+1} = Y_j$$

Rewriting in matrix form, we see that it is in fact tridiagonal.

$$\begin{bmatrix} D_1 & -\alpha_1 & 0 & 0 \\ -\beta_2 & D_2 & -\alpha_2 & 0 \\ 0 & -\beta_3 & D_3 & -\alpha_3 \\ 0 & 0 & -\beta_4 & D_4 \end{bmatrix} \begin{bmatrix} v_{z,1} \\ v_{z,2} \\ v_{z,3} \\ v_{z,4} \end{bmatrix} = \begin{bmatrix} Y_1 \\ Y_2 \\ Y_3 \\ Y_4 \end{bmatrix}$$

The boundary conditions are important to solve the system of equations correctly. The first boundary condition occurs at the plasma-wall interface. At the surface of the wall, the velocity is zero. At the second boundary, the plasma-vacuum interface, the pressure of the vacuum is zero. We also assume that the viscosity is unimportant at the interface, so α is zero. Note that the unknowns in this system of equations are the velocities of the zone

boundaries at the next iteration in time. They are all solved for simultaneously, using the conditions at the previous iteration in time.

Ion Temperature

The ion temperature equation was derived in section II.A.4

$$\frac{dT_i}{dt} = \left\{ \begin{array}{l} -\frac{2}{3}\rho\frac{2R}{W}\frac{\partial v_z}{\partial M}T_i + \frac{8}{9n_i}\eta_i\left(\rho\frac{2R}{W}\frac{\partial v_z}{\partial M}\right)^2 \\ +\frac{2}{3n_i}\rho\frac{2R}{W}\frac{\partial}{\partial M}\left(\kappa_i\rho\frac{2R}{W}\frac{\partial T_i}{\partial M}\right) \\ -\frac{2}{3}T_i\frac{\partial v_y}{\partial y} + \frac{2}{3n_i}\frac{\partial}{\partial y}\left(\kappa_i\frac{\partial T_i}{\partial y}\right) \\ +\frac{Z}{\tau_{eq}}\left(T_e - T_i\right) \end{array} \right\}$$

We will evaluate the equation using the implicit form at y=0 (on axis) at the zone midpoints.

The first term is the temporal derivative

$$\left.\frac{dT_i}{dt}\right|_{j+1/2}^{n+1/2} = \frac{T_{i\,j+1/2}^{n+1} - T_{i\,j+1/2}^{n}}{\Delta t^{n+1/2}}$$

Next we have the compression term

$$\left.-\frac{2}{3}\rho\frac{2R}{W}\frac{\partial v_z}{\partial M}T_i\right|_{j+1/2}^{n+1/2} = -\frac{2}{3}T_{i\,j+1/2}^{n+1/2}\rho_{j+1/2}^{n+1/2}\frac{2R_{j+1/2}^{n+1/2}}{W}\frac{v_{z\,j+1}^{\;n+1/2} - v_{z\,j}^{\;n+1/2}}{\Delta M_{j+1/2}}$$

Let $\chi_{j+1/2}^{n} = -\frac{1}{3}\Delta t^{n+1/2}\rho_{j+1/2}^{n}\frac{2R_{j+1/2}^{n}}{W}\frac{v_{z\,j+1}^{\;n} - v_{z\,j}^{\;n}}{\Delta M_{j+1/2}}$

$$-\frac{2}{3}T_i\rho\frac{2R}{W}\frac{\partial v_z}{\partial M}\bigg|_{j+1/2}^{n+1/2}=\frac{1}{\Delta t^{n+1/2}}\left(\chi_{j+1/2}^{n}T_{i\,j+1/2}^{n}+\chi_{j+1/2}^{n+1}T_{i\,j+1/2}^{n+1}\right)$$

We have the associated viscosity term

$$\frac{8}{9N_i}\eta_0\left(\rho\frac{2R}{W}\frac{\partial v_z}{\partial M}\right)^2\bigg|_{j+1/2}^{n+1/2}=0.853T_i\tau_i\left(\rho\frac{2R}{W}\frac{\partial v_z}{\partial M}\right)^2\bigg|_{j+1/2}^{n+1/2}$$

Let $q_{j+1/2}^{n}=0.427\Delta t^{n+1/2}\tau_{i\,j+1/2}^{\;\;n}\left(\rho_{j+1/2}^{n}\frac{2R_{j+1/2}^{n}}{W}\frac{v_{z\,j+1}^{\;\;n}-v_{z\,j}^{\;\;n}}{\Delta M_{j+1/2}}\right)^2$

$$\frac{8}{9N_i}\eta_0\left(\rho\frac{2R}{W}\frac{\partial v_z}{\partial M}\right)^2\bigg|_{j+1/2}^{n+1/2}=\frac{1}{\Delta t^{n+1/2}}\left(q_{j+1/2}^{n}T_{i\,j+1/2}^{n}+q_{j+1/2}^{n+1}T_{i\,j+1/2}^{n+1}\right)$$

The thermal conduction is next

$$\frac{2}{3N_i}\rho\frac{2R}{W}\frac{\partial}{\partial M}\left(k_i\rho\frac{2R}{W}\frac{\partial T_i}{\partial M}\right)\bigg|_{j+1/2}^{n+1/2}=\frac{4R_{j+1/2}^{n+1/2}\rho_{j+1/2}^{n+1/2}}{3WN_{i\,j+1/2}^{\;\;n+1/2}}\frac{\left(k_i\rho\frac{2R}{W}\frac{\partial T_i}{\partial M}\right)_{j+1}^{n+1/2}-\left(k_i\rho\frac{2R}{W}\frac{\partial T_i}{\partial M}\right)_{j}^{n+1/2}}{\Delta M_{j+1/2}}$$

$$=\frac{4R_{j+1/2}^{n+1/2}}{3WN_{i\,j+1/2}^{\;\;n+1/2}}\frac{\rho_{j+1/2}^{n+1/2}}{\Delta M_{j+1/2}}\begin{pmatrix}k_{i\,j+1}^{\;\;n+1/2}\rho_{j+1}^{n+1/2}\frac{2R_{j+1}^{n+1/2}}{W}\frac{T_{i\,j+3/2}^{n+1/2}-T_{i\,j+1/2}^{n+1/2}}{\Delta M_{j+1}}\\-k_{i\,j}^{\;\;n+1/2}\rho_{j}^{n+1/2}\frac{2R_{j}^{n+1/2}}{W}\frac{T_{i\,j+1/2}^{n+1/2}-T_{i\,j-1/2}^{n+1/2}}{\Delta M_{j}}\end{pmatrix}$$

Let $\alpha_{j+1/2}^{n+1/2}=\frac{\Delta t^{n+1/2}}{3N_{e\,j+1/2}^{\;\;n+1/2}}\frac{2R_{j+1/2}^{n+1/2}\rho_{j+1/2}^{n+1/2}}{W\Delta M_{j+1/2}}\frac{2R_{j+1}^{n+1/2}\rho_{j+1}^{n+1/2}}{W\Delta M_{j+1}}k_{i\,j+1}^{\;\;n+1/2}$

$$\beta_{j+1/2}^{n+1/2}=\frac{\Delta t^{n+1/2}}{3N_{e\,j+1/2}^{\;\;n+1/2}}\frac{2R_{j+1/2}^{n+1/2}\rho_{j+1/2}^{n+1/2}}{W\Delta M_{j+1/2}}\frac{2R_{j}^{n+1/2}\rho_{j}^{n+1/2}}{W\Delta M_{j}}k_{i\,j}^{\;\;n+1/2}$$

$$\frac{4R\rho}{3WN_i}\frac{\partial}{\partial M}\left(k_i\rho\frac{2R}{W}\frac{\partial T_i}{\partial M}\right)\Bigg|_{j+1/2}^{n+1/2}=\frac{1}{\Delta t^{n+1/2}}\begin{bmatrix}\alpha_{j+1/2}^{n+1}\left(T_{i\,j+3/2}^{n+1}-T_{i\,j+1/2}^{n+1}\right)\\+\alpha_{j+1/2}^{n}\left(T_{i\,j+3/2}^{n}-T_{i\,j+1/2}^{n}\right)\\-\beta_{j+1/2}^{n+1}\left(T_{i\,j+1/2}^{n+1}-T_{i\,j-1/2}^{n+1}\right)\\-\beta_{j+1/2}^{n}\left(T_{i\,j+1/2}^{n}-T_{i\,j-1/2}^{n}\right)\end{bmatrix}$$

We can write the numerical form for the 1.5D effects

$$-\frac{2}{3}T_i\frac{\partial v_y}{\partial y}-\frac{2}{3N_ik_B}\frac{4k_iT_i}{5L\sqrt{L^2+\left(\Delta z-\Delta z_0\right)^2}}\Bigg|_{j+1/2}^{n+1/2}=\left\{\begin{array}{l}-\frac{2}{3}T_{i\,j+1/2}^{n+1/2}\left|\frac{v_{y\,j+1/2}^{n+1/2}}{R_{j+1/2}^{n+1/2}}\right|\\-\frac{2T_{i\,j+1/2}^{n+1/2}}{3N_{i\,j+1/2}^{n+1/2}}\frac{4}{5L_{j+1/2}^{n+1/2}\sqrt{L_{j+1/2}^{n+1/2\,2}+\left(\Delta z_{j+1/2}^{n+1/2}-\Delta z_0\right)^2}}\end{array}\right\}$$

Let $\delta_{j+1/2}^{n+1/2}=-\frac{\Delta t^{n+1/2}}{3}\frac{\partial v_y}{\partial y}\Big|_{j+1/2}^{n+1/2}-\frac{1}{3k_B}\frac{\Delta t^{n+1/2}}{N_{i\,j+1/2}^{n+1/2}}\frac{4}{5}\frac{k_{i\,j+1/2}^{n+1/2}}{L_{j+1/2}^{n+1/2}\sqrt{L_{j+1/2}^{n+1/2\,2}+\left(x_{j+1/2}^{n+1/2}-x_0\right)^2}}$

$$-\frac{2}{3}T_i\frac{\partial v_y}{\partial y}-\frac{2}{3N_{i\,B}}\frac{4k_iT_i}{5L\sqrt{L^2+\left(x-x_0\right)^2}}\Bigg|_{j+1/2}^{n+1/2}=\frac{1}{\Delta t^{n+1/2}}\left(\delta_{j+1/2}^{n+1}T_{i\,j+1/2}^{n+1}+\delta_{j+1/2}^{n}T_{i\,j+1/2}^{n}\right)$$

Finally we have the electron-ion heat transfer

$$\frac{T_e-T_i}{\tau_{eq}}\Bigg|_{j+1/2}^{n+1/2}=\frac{T_{e\,j+1/2}^{n+1/2}-T_{i\,j+1/2}^{n+1/2}}{\tau_{eq\,j+1/2}^{n+1/2}}\approx\frac{T_{e\,j+1/2}^{n+1}+T_{e\,j+1/2}^{n}-T_{i\,j+1/2}^{n+1}-T_{i\,j+1/2}^{n}}{2\tau_{eq\,j+1/2}^{n}}$$

We can equate both sides:

$$T_{i\,j+1/2}^{n+1} - T_{i\,j+1/2}^{n} = \left\{ \begin{array}{l} \chi_{j+1/2}^{n} T_{i\,j+1/2}^{n} + \chi_{j+1/2}^{n+1} T_{i\,j+1/2}^{n+1} + q_{j+1/2}^{n} T_{i\,j+1/2}^{n} + q_{j+1/2}^{n+1} T_{i\,j+1/2}^{n+1} \\ + \alpha_{j+1/2}^{n+1} \left(T_{i\,j+3/2}^{n+1} - T_{i\,j+1/2}^{n+1} \right) + \alpha_{j+1/2}^{n} \left(T_{i\,j+3/2}^{n} - T_{i\,j+1/2}^{n} \right) \\ - \beta_{j+1/2}^{n+1} \left(T_{i\,j+1/2}^{n+1} - T_{i\,j-1/2}^{n+1} \right) - \beta_{j+1/2}^{n} \left(T_{i\,j+1/2}^{n} - T_{i\,j-1/2}^{n} \right) \\ + \dfrac{\Delta t^{n+1/2}}{2\tau_{eq}{}_{j+1/2}^{n}} \left(T_{e\,j+1/2}^{n+1} + T_{e\,j+1/2}^{n} - T_{i\,j+1/2}^{n+1} - T_{i\,j+1/2}^{n} \right) \\ + \delta_{j+1/2}^{n+1} T_{i\,j+1/2}^{n+1} + \delta_{j+1/2}^{n} T_{i\,j+1/2}^{n} \end{array} \right\}$$

We can simplify be moving all terms that depend on t_{n+1} to the left side, and all terms that depend on t_{n+1} to the right size of the equation.

$$\left\{ \begin{array}{l} -\beta_{j+1/2}^{n+1} T_{i\,j-1/2}^{n+1} \\ + \left(\begin{array}{l} 1 - \chi_{j+1/2}^{n+1} - q_{j+1/2}^{n+1} + \alpha_{j+1/2}^{n+1} \\ + \beta_{j+1/2}^{n+1} + Z \dfrac{\Delta t^{n+1/2}}{2\tau_{eq}{}_{j+1/2}^{n}} - \delta_{j+1/2}^{n+1} \end{array} \right) T_{i\,j+1/2}^{n+1} \\ -\alpha_{j+1/2}^{n+1} T_{i\,j+3/2}^{n+1} \end{array} \right\} = \left\{ \begin{array}{l} \beta_{j+1/2}^{n} T_{i\,j-1/2}^{n} + \\ \left(\begin{array}{l} 1 + \chi_{j+1/2}^{n} + q_{j+1/2}^{n} - \alpha_{j+1/2}^{n} \\ - \beta_{j+1/2}^{n} - \dfrac{\Delta t^{n+1/2}}{2\tau_{eq}{}_{j+1/2}^{n}} + \delta_{j+1/2}^{n} \end{array} \right) T_{i\,j+1/2}^{n} \\ + \alpha_{j+1/2}^{n} T_{i\,j+3/2}^{n} \\ + Z \dfrac{\Delta t^{n+1/2}}{\tau_{eq}{}_{j+1/2}^{n}} T_{e\,j+1/2}^{n+1/2} + q_{j+1/2}^{n} \end{array} \right\}$$

Let $L_j = -\beta_{j+1/2}^{n+1}$

$$D_j = 1 - \chi_{j+1/2}^{n+1} - q_{j+1/2}^{n+1} + \alpha_{j+1/2}^{n+1} + \beta_{j+1/2}^{n+1} + Z \frac{\Delta t^{n+1/2}}{2\tau_{eq}{}_{j+1/2}^{n}} - \delta_{j+1/2}^{n+1}$$

$$U_j = -\alpha_{j+1/2}^{n+1}$$

$$Y_j = \left\{ \begin{array}{l} \beta^n_{j+1/2} T^n_{i\,j-1/2} \\ + \left(1 + \chi^n_{j+1/2} + q^n_{j+1/2} - \alpha^n_{j+1/2} - \beta^n_{j+1/2} - \dfrac{\Delta t^{n+1/2}}{2\tau_{eq}{}^n_{j+1/2}} + \delta^n_{j+1/2} \right) T^n_{i\,j+1/2} \\ + \alpha^n_{j+1/2} T^n_{i\,j+3/2} \\ + Z \dfrac{\Delta t^{n+1/2}}{\tau_{eq}{}^n_{j+1/2}} T_e{}^{n+1/2}_{j+1/2} + q^n_{j+1/2} \end{array} \right\}$$

Again we have a tridiagonal form:

$$L_j T^{n+1}_{i\,j-1/2} + D_j T^{n+1}_{i\,j+1/2} + U_j T^{n+1}_{i\,j+3/2} = Y_j$$

Electron Temperature

The electron temperature equation is very similar to the ion temperature:

$$\frac{dT_e}{dt} = \left(\begin{array}{l} -\dfrac{2}{3}\rho \dfrac{2R}{W} \dfrac{\partial v_z}{\partial M} T_e + \dfrac{8}{9n_e} \eta_e \left(\rho \dfrac{2R}{W} \dfrac{\partial v_z}{\partial M} \right)^2 \\ + \dfrac{2}{3n_e} \rho \dfrac{2R}{W} \dfrac{\partial}{\partial M} \left(\kappa_e \rho \dfrac{2R}{W} \dfrac{\partial T_e}{\partial M} \right) \\ - \dfrac{2}{3} \dfrac{\partial v_y}{\partial z} T_e + \dfrac{2}{3n_e} \dfrac{\partial}{\partial y} \left(\kappa_e \dfrac{\partial T_e}{\partial y} \right) \\ - \dfrac{T_e - T_i}{\tau_{eq}} + \dfrac{2}{3n_e} \left(E_{abs} - E_{atom} \right) + \left(\dfrac{m_e v_z^2}{3} - T_e \right) \dfrac{1}{Z} \dfrac{dZ}{dt} \end{array} \right)$$

We will evaluate the implicit form in the same manner as the ion temperature.

The temporal term

$$\left. \frac{dT_e}{dt} \right|^{n+1/2}_{j+1/2} = \frac{T_e{}^{n+1}_{j+1/2} - T_e{}^n_{j+1/2}}{\Delta t^{n+1/2}}$$

The compression term

$$-\frac{2}{3}T_e\rho\frac{2R}{W}\frac{\partial v_z}{\partial M}\bigg|_{j+1/2}^{n+1/2}=-\frac{2}{3}T_{e\,j+1/2}^{\;n+1/2}\rho_{j+1/2}^{n+1/2}\frac{2R_{j+1/2}^{n+1/2}}{W}\frac{v_{z\,j+1}^{\;n+1/2}-v_{z\,j}^{\;n+1/2}}{\Delta M_{j+1/2}}$$

Let $\chi_{j+1/2}^{n}=-\Delta t^{n+1/2}\frac{2}{3}\frac{\rho_{j+1/2}^{n}R_{j+1/2}^{n+1/2}}{W}\frac{v_{z\,j+1}^{\;n}-v_{z\,j}^{\;n}}{\Delta M_{j+1/2}}$

$$-\frac{2}{3}T_e\rho\frac{2R}{W}\frac{\partial v_z}{\partial M}\bigg|_{j+1/2}^{n+1/2}=\frac{1}{\Delta t^{n+1/2}}\left(\chi_{j+1/2}^{n}T_{e\,j+1/2}^{\;n}+\chi_{j+1/2}^{n+1}T_{e\,j+1/2}^{\;n+1}\right)$$

The viscosity term

$$\frac{8}{9N_e}\eta_e\left(\rho\frac{2R}{W}\frac{\partial v_z}{\partial M}\right)^2\bigg|_{j+1/2}^{n+1/2}=0.652T_e\tau_e\left(\rho\frac{2R}{W}\frac{\partial v_z}{\partial m}\right)^2\bigg|_{j+1/2}^{n+1/2}$$

Let $q_{j+1/2}^{n}=0.326\Delta t^{n+1/2}\tau_{e\,j+1/2}^{\;n}\left(\rho_{j+1/2}^{n}\frac{2R_{j+1/2}^{n}}{W}\frac{u_{j+1}^{n}-u_{j}^{n}}{\Delta M_{j+1/2}}\right)^2$

$$\frac{8}{9N_e}\eta_e\left(\rho\frac{2R}{W}\frac{\partial v_z}{\partial M}\right)^2\bigg|_{j+1/2}^{n+1/2}=\frac{1}{\Delta t^{n+1/2}}\left(q_{j+1/2}^{n}T_{e\,j+1/2}^{\;n}+q_{j+1/2}^{n+1}T_{e\,j+1/2}^{\;n+1}\right)$$

Thermal conduction

$$\frac{2}{3N_e}\rho\frac{2R}{W}\frac{\partial}{\partial M}\left(k_e\rho\frac{2R}{W}\frac{\partial T_e}{\partial M}\right)\bigg|_{j+1/2}^{n+1/2}=\frac{4\rho_{j+1/2}^{n+1/2}R_{j+1/2}^{n+1/2}}{3N_{e\,j+1/2}^{\;n+1/2}W}\frac{\left(k_e\rho\frac{2R}{W}\frac{\partial T_e}{\partial M}\right)_{j+1}^{n+1/2}-\left(k_e\rho\frac{2R}{W}\frac{\partial T_e}{\partial M}\right)_{j}^{n+1/2}}{\Delta M_{j+1/2}}$$

$$=\frac{2}{3N_{e\,j+1/2}^{\;n+1/2}}\frac{\rho_{j+1/2}^{n+1/2}2R_{j+1/2}^{n+1/2}}{W}\frac{1}{\Delta M_{j+1/2}}\left(\begin{array}{l}k_{i\,j+1}^{\;n+1/2}\dfrac{\rho_{j+1}^{n+1/2}2R_{j+1}^{n+1/2}}{W}\dfrac{T_{e\,j+3/2}^{\;n+1/2}-T_{e\,j+1/2}^{\;n+1/2}}{\Delta M_{j+1}}\\ -k_{i\,j}^{\;n+1/2}\dfrac{\rho_{j}^{n+1/2}2R_{j}^{n+1/2}}{W}\dfrac{T_{e\,j+1/2}^{\;n+1/2}-T_{e\,j-1/2}^{\;n+1/2}}{\Delta M_{j}}\end{array}\right)$$

$$\text{Let } \alpha_{j+1/2}^{n+1/2} = \frac{\Delta t^{n+1/2}}{3N_{e\,j+1/2}^{\;n+1/2}} \frac{2R_{j+1/2}^{n+1/2}\rho_{j+1/2}^{n+1/2}}{W\Delta M_{j+1/2}} \frac{2R_{j+1}^{n+1/2}\rho_{j+1}^{n+1/2}}{W\Delta M_{j+1}} k_{e\,j+1}^{\;n+1/2}$$

$$\beta_{j+1/2}^{n+1/2} = \frac{\Delta t^{n+1/2}}{3N_{e\,j+1/2}^{\;n+1/2}} \frac{2R_{j+1/2}^{n+1/2}\rho_{j+1/2}^{n+1/2}}{W\Delta M_{j+1/2}} \frac{2R_{j}^{n+1/2}\rho_{j}^{n+1/2}}{W\Delta M_{j}} k_{e\,j}^{\;n+1/2}$$

$$\frac{2}{3N_e}\rho\frac{2R}{W}\frac{\partial}{\partial m}\left(k_e\rho\frac{2R}{W}\frac{\partial T_e}{\partial m}\right)\Bigg|_{j+1/2}^{n+1/2} = \frac{1}{\Delta t^{n+1/2}}\begin{bmatrix}\alpha_{j+1/2}^{n+1}\left(T_{e\,j+3/2}^{\;n+1} - T_{e\,j+1/2}^{\;n+1}\right)\\ +\alpha_{j+1/2}^{n}\left(T_{e\,j+3/2}^{\;n} - T_{e\,j+1/2}^{\;n}\right)\\ -\beta_{j+1/2}^{n+1}\left(T_{e\,j+1/2}^{\;n+1} - T_{e\,j-1/2}^{\;n+1}\right)\\ -\beta_{j+1/2}^{n}\left(T_{e\,j+1/2}^{\;n} - T_{e\,j-1/2}^{\;n}\right)\end{bmatrix}$$

We can write the numerical form for the 1.5D effects

$$-\frac{2}{3}T_e\frac{v_y}{R} - \frac{2}{3N_e k_B}\frac{4k_e T_e}{5L\sqrt{L^2+\left(\Delta z-\Delta z_0\right)^2}}\Bigg|_{j+1/2}^{n+1/2} = \begin{pmatrix} -\frac{2}{3}T_{e\,j+1/2}^{\;n+1/2}\frac{v_{y\,j+1/2}^{\;n+1/2}}{R_{j+1/2}^{n+1/2}} \\ -\frac{2T_{e\,j+1/2}^{\;n+1/2}}{3N_{e\,j+1/2}^{\;n+1/2}}\frac{4k_e}{5L_{j+1/2}^{n+1/2}\sqrt{L^2{}_{j+1/2}^{n+1/2}+\left(\Delta z_{j+1/2}^{n+1/2}-\Delta z_0\right)^2}}\end{pmatrix}$$

$$\text{Let } \delta_{j+1/2}^{n+1/2} = -\frac{1}{3}\frac{v_{y\,j+1/2}^{\;n+1/2}\Delta t^{n+1/2}}{R_{j+1/2}^{n+1/2}} - \frac{4\Delta t^{n+1/2}}{15k_B N_{e\,j+1/2}^{\;n+1/2}}\frac{k_{e\,j+1/2}^{\;n+1/2}}{L_{j+1/2}^{n+1/2}\sqrt{L_{j+1/2}^{n+1/2\,2}+\left(x_{j+1/2}^{n+1/2}-x_0\right)^2}}$$

$$\delta_{j+1/2}^{n+1/2} = -\frac{\Delta t^{n+1/2}}{3}\left(\frac{v_{y\,j+1/2}^{\;n+1/2}}{R_{j+1/2}^{n+1/2}} + \frac{4}{5k_B N_{e\,j+1/2}^{\;n+1/2}}\frac{k_{e\,j+1/2}^{\;n+1/2}}{L_{j+1/2}^{n+1/2}\sqrt{L_{j+1/2}^{n+1/2\,2}+\left(x_{j+1/2}^{n+1/2}-x_0\right)^2}}\right)$$

$$-\frac{2}{3}T_e\frac{\partial v_y}{\partial y} - \frac{2}{3N_e k_B}\frac{4k_e T_e}{5L\sqrt{L^2+\left(x-x_0\right)^2}}\Bigg|_{j+1/2}^{n+1/2} = \frac{1}{\Delta t^{n+1/2}}\left(\delta_{j+1/2}^{n+1}T_{e\,j+1/2}^{\;n+1} + \delta_{j+1/2}^{n}T_{e\,j+1/2}^{\;n}\right)$$

The terms that correspond to the creation / destruction (ionization / recombination) of electrons:

$$\left(\frac{m_e u^2}{3} - T_e\right)\frac{1}{Z}\frac{dZ}{dt}\bigg|_{j+1/2}^{n+1/2} = -\left(\frac{T_{e\,j+1/2}^{\,n} + T_{e\,j+1/2}^{\,n+1}}{2} + \frac{m_e u^{2\,n+1/2}_{j+1/2}}{3}\right)\frac{1}{Z}\frac{dZ}{dt}\bigg|_{j+1/2}^{n+1/2}$$

Let $ZT_{j+1/2}^{n+1/2} = \dfrac{\Delta t^{n+1/2}}{2}\left(\dfrac{1}{Z}\dfrac{dZ}{dt}\right)\bigg|_{j+1/2}^{n+1/2}$

$$Zv_{j+1/2}^{n+1/2} = \frac{m_e \vec{v}^{\,2\,n+1/2}_{j+1/2}\Delta t^{n+1/2}}{3}\left(\frac{1}{Z}\frac{dZ}{dt}\right)\bigg|_{j+1/2}^{n+1/2}$$

Finally, the electron-ion heat transfer:

$$\frac{T_e - T_i}{\tau_{eq}}\bigg|_{j+1/2}^{n+1/2} = \frac{T_{e\,j+1/2}^{\,n+1/2} - T_{i\,j+1/2}^{\,n+1/2}}{\tau_{eq}{}_{j+1/2}^{\,n+1/2}} \approx \frac{T_{e\,j+1/2}^{\,n+1} + T_{e\,j+1/2}^{\,n} - T_{i\,j+1/2}^{\,n+1} - T_{i\,j+1/2}^{\,n}}{2\tau_{eq}{}_{j+1/2}^{\,n}}$$

Equating both sides:

$$T_{e\,j+1/2}^{\,n+1} - T_{e\,j+1/2}^{\,n} = \left\{\begin{array}{l} \chi_{j+1/2}^{n} T_{e\,j+1/2}^{\,n} + \chi_{j+1/2}^{n+1} T_{e\,j+1/2}^{\,n+1} + q_{j+1/2}^{n} T_{e\,j+1/2}^{\,n} + q_{j+1/2}^{n+1} T_{e\,j+1/2}^{\,n+1} \\ + \alpha_{j+1/2}^{n+1}\left(T_{e\,j+3/2}^{\,n+1} - T_{e\,j+1/2}^{\,n+1}\right) + \alpha_{j+1/2}^{n}\left(T_{e\,j+3/2}^{\,n} - T_{e\,j+1/2}^{\,n}\right) \\ - \beta_{j+1/2}^{n+1}\left(T_{e\,j+1/2}^{\,n+1} - T_{e\,j-1/2}^{\,n+1}\right) - \beta_{j+1/2}^{n}\left(T_{e\,j+1/2}^{\,n} - T_{e\,j-1/2}^{\,n}\right) \\ - \dfrac{\Delta t^{n+1/2}}{2\tau_{eq}{}_{j+1/2}^{\,n}}\left(T_{e\,j+1/2}^{\,n+1} + T_{e\,j+1/2}^{\,n} - T_{i\,j+1/2}^{\,n+1} - T_{i\,j+1/2}^{\,n}\right) \\ + \delta_{j+1/2}^{n+1} T_{e\,j+1/2}^{\,n+1} + \delta_{j+1/2}^{n} T_{e\,j+1/2}^{\,n} \\ + \dfrac{2\Delta t^{n+1/2}}{3N_e}\left(E_{abs} - E_{atom}\right) \\ - ZT_{j+1/2}^{n+1} T_{e\,j+1/2}^{\,n+1} - ZT_{j+1/2}^{n+1} T_{e\,j+1/2}^{\,n+1} - Zv_{j+1/2}^{n+1/2} \end{array}\right\}$$

Simplifying:

$$\left\{\begin{array}{l} -\beta_{j+1/2}^{n+1} T_{e\,j-1/2}^{\;n+1} \\ +\left(\begin{array}{l} 1-\chi_{j+1/2}^{n+1}-q_{j+1/2}^{n+1} \\ +\alpha_{j+1/2}^{n+1}+\beta_{j+1/2}^{n+1} \\ +\dfrac{\Delta t^{n+1/2}}{2\tau_{eq}{}_{j+1/2}^{\;n}}-\delta_{j+1/2}^{n+1} \\ +ZT_{j+1/2}^{n+1} \end{array}\right) T_{e\,j+1/2}^{\;n+1} \\ -\alpha_{j+1/2}^{n+1} T_{e\,j+3/2}^{\;n+1} \end{array}\right\} = \left\{\begin{array}{l} \beta_{j+1/2}^{n} T_{e\,j-1/2}^{\;n} + \\ \left(\begin{array}{l} 1+\chi_{j+1/2}^{n}+q_{j+1/2}^{n} \\ -\alpha_{j+1/2}^{n}-\beta_{j+1/2}^{n} \\ -\dfrac{\Delta t^{n+1/2}}{2\tau_{eq}{}_{j+1/2}^{\;n}}+\delta_{j+1/2}^{n} \\ -ZT_{j+1/2}^{n+1} \end{array}\right) T_{e\,j+1/2}^{\;n} \\ +\alpha_{j+1/2}^{n} T_{e\,j+3/2}^{\;n} \\ +\dfrac{T_{i\,j+1/2}^{n+1/2}}{\tau_{eq}{}_{j+1/2}^{\;n}}+\dfrac{2\Delta t^{n+1/2}}{3N_e k_B}\left(E_{abs}-E_{atom}\right)-Zv_{j+1/2}^{n+1} \end{array}\right\}$$

Let $L_j = -\beta_{j+1/2}^{n+1}$

$$D_j = 1-\chi_{j+1/2}^{n+1}-q_{j+1/2}^{n+1}+\alpha_{j+1/2}^{n+1}+\beta_{j+1/2}^{n+1}+\frac{\Delta t^{n+1/2}}{2\tau_{eq}{}_{j+1/2}^{\;n}}-\delta_{j+1/2}^{n+1}+ZT_{j+1/2}^{n+1}$$

$$U_j = -\alpha_{j+1/2}^{n+1}$$

$$Y_j = \left\{\begin{array}{l} \beta_{j+1/2}^{n} T_{i\,j-1/2}^{\;n} \\ +\left(1+\chi_{j+1/2}^{n}+q_{j+1/2}^{n}-\alpha_{j+1/2}^{n}-\beta_{j+1/2}^{n}-\dfrac{\Delta t^{n+1/2}}{2\tau_{eq}{}_{j+1/2}^{\;n}}+\delta_{j+1/2}^{n}-ZT_{j+1/2}^{n+1}\right) T_{i\,j+1/2}^{\;n} \\ +\alpha_{j+1/2}^{n} T_{i\,j+3/2}^{\;n} \\ +\dfrac{T_{e\,j+1/2}^{\;n+1/2}}{\tau_{eq}{}_{j+1/2}^{\;n}} \\ +\dfrac{2\Delta t^{n+1/2}}{3N_e k_B}\left(E_{abs}-E_{atom}\right) \\ -Zv_{j+1/2}^{n+1/2} \end{array}\right\}$$

Again we arrive at a tridiagonal form:

$$L_j T_{e\,j-1/2}^{\;n+1} + D_j T_{e\,j+1/2}^{\;n+1} + U_j T_{e\,j+3/2}^{\;n+1} = Y_j$$

III.A.4.) 1D vs. 1.5D

A simple 1D approximation is often used to reduce the number of calculations. This approximation assumes the plasma is infinite in extent transverse to the direction of expansion. While this easily holds for the direction parallel to a line focus, it does not necessarily hold for the direction perpendicular to the line. On the other hand, a more complete 2D model requires extensive computational resources. To overcome these limitations, we can implement approximations for the dominant processes in the transverse direction, resulting in a so called 1.5 D code. Under this approximation, the direction parallel to the line is taken as infinite, while the perpendicular direction is taken as finite with expansion. We account for the expansion by using the self-similar solution for the expansion of a gas in a vacuum. Under this approximation, we only need to evaluate the properties on the axis. Following Jacquemot[49], the mass density transverse to the beam is given by:

$$\rho(y,t) = \frac{m}{2R(t)} \exp\left(-\frac{\pi y^2}{4R^2(t)} \right)$$

where $R(t)$ is the half width. The rate of change $\frac{dR}{dt} = v_y$. Note v_y is the velocity in the transverse direction parallel to the target (y-direction). The expansion of this self-similar solution into a vacuum was analytically derived by Pert[50]

$$R\frac{dv_y}{dt} = \frac{\pi}{2}\frac{p}{\rho}$$

---

[49] S. Jacquemot, L. Bonnet, L.B. Da Silva, A. Decoster, D. Desenne, J.P. Le Brenton, M. Louis-Jacquemot, B.J. MacGowan, D.L. Matthews, "*Effects of Line Focus Width Narrowing on Amplification in Ne-like Se X-Ray Laser Experiments*", SPIE Vol. 2012, 1993, pp. 180-189.

[50] G.J. Pert, "*The Hybrid Model and its Application for Studying Free Expansion*", Journal of Fluid Mechanics, Vol. 131, 1983, pp. 401-426.

If we use the relation between ∂z and ∂M from II.A.1 we obtain the final relation for the expansion of the half width

$$\frac{dv_y}{dt} = \frac{\pi p}{2R\rho} = \frac{\pi p}{W}\frac{\partial z}{\partial M}$$

Similarly, the expression for the self-similar solution of the temperature is given as

$$T_e(y,t) = T_m(t)\left(1 - \frac{y^2}{L^2(t)}\right)^{2/5}$$

Here $L(t)$ is the half width of the temperature and $T_m(t)$ is the temperature on the axis. With this profile, we can obtain the expression for the heat flux through the transverse direction. The heat flux is given by

$$q = \frac{2}{3n_e}\frac{\partial}{\partial y}\left(\kappa_e \frac{\partial T_e}{\partial y}\right)$$

If we assume the conductivity does not depend on y we get

$$q = \frac{2\kappa_e}{3n_e}\frac{\partial^2}{\partial y^2}\left(T_m(t)\left(1 - \frac{y^2}{L^2(t)}\right)^{2/5}\right)$$

Now we will calculate the heat flux on axis (y=0):

$$q = -\frac{8}{15}\frac{\kappa_e}{n_e}\frac{T_m(t)}{L^2(t)}$$

Finally to limit the conduction in the outward moving corona, we multiply q by a factor equal to

$$\frac{L}{\sqrt{L^2 - (\Delta z - \Delta z_0)^2}}$$

This will account for the fact that heat flows on a path from (x,y=0) to (x_0,y=L) in the unmoved part of the target. The heat flux then becomes

$$q = -\frac{8}{15}\frac{\kappa_e}{n_e}\frac{T_m(t)}{L^2(t)}\frac{L}{\sqrt{L^2 - (\Delta z - \Delta z_0)^2}}$$

One word of caution, the heat flux limit must be applied to ensure that the heat flux does not become unphysical (see chapter II.B.4). This will be applied at the point $y = \frac{\sqrt{5}}{3}L$.

With these effects transverse effects, the model is capable of including the most important 2D effects while solving all the equations in a 1D approximation. This forms the basis of the 1.5D approximation.

III.A.5.) Time Step Considerations

Once the numerical equations are written, an important question deals with the issue of the time step. Trying to choose the proper time step between iterations has several important implications. First, it determines the total number of iterations. Since the average time per iteration is almost independent of the time step, the smaller the time step, the larger the time required to complete the simulation. For example, if one iteration takes 20 ms, but 1 million iterations are required then the total simulation time is 6 hours. Unfortunately, the time step cannot be arbitrarily large. Increasing the time step increases the error of the numerical formulation. This error often has large O(t) and O(t^2) terms. In addition to an increasing error, feedback between the different equations can occur which may result in unstable and erroneous solutions. For example, a change in the electron temperature can affect the degree of ionization and the atomic losses, which can affect the

electron temperature. The net result is that if the time step is too large, then the solution may be invalid.

In order to obtain the most efficient calculations, the largest possible time step should be used at each iteration. This is significantly more efficient than choosing one single time step. Unfortunately, since the different spatial zones are coupled the smallest time step for each zone must be used $\Delta t^n = \min\left\{\Delta t^n_{j+1/2}\right\}$. The time step for each zone is calculated by checking a number of conditions based on both numerical and physical considerations. Also, we ensure that the time step does not increase suddenly, as this would cause problems in a marginally stable system.

The first constraint on the time step should be a fraction of the FWHM of the heating beam. Note that this does not apply if there is no applied laser, for example the time between pre-pulse and pump pulse. This condition ensures that the conditions do not change rapidly because of a rapid change in the intensity of the beam.

A second constraint should be observed if there is a phase change. If we reduce the time step during phase changes, we can prevent problems where the material may make several phase changes in a single iteration.

A very important consideration is based upon the adiabatic speed of sound. A shock wave should not be allowed to cross a zone in less than a single iteration. Since these shock waves propagate at the adiabatic speed of sound c_s, this puts a limit on the time step. In a plasma the adiabatic speed of sound is

$$c_s = \sqrt{\gamma \frac{P}{\rho}} = \sqrt{\gamma \frac{N_e T_e + N_i T_i}{m_i N_i}}$$

The time step is then

$$\Delta t_j^n = \frac{\Delta x_{j+1/2}^n}{c_{s,j+1/2}^n} = \Delta x_{j+1/2}^n \sqrt{\frac{m_i / \gamma}{Z_{j+1/2}^n T_{e\,j+1/2}^n + T_{i\,j+1/2}^n}}$$

In a two temperature model, the time step should be less than the electron-ion equilibration time. If this is not the case, a single temperature model should be used. Since this time is often on the order of hundreds of picoseconds we will always need to use a two temperature model.

Other time step constraints can be derived by setting various limiting conditions. Frequently the most important time step is found by requiring that no more than a 10% change in the electron temperature can take place in any zone. Because there are a number of processes that can rapidly heat or cool the electrons, this is often the most difficult and most rigorous time step consideration. To see how this works we can write the electron temperature in the following form (ignoring heat conduction)

$$T_{j+1/2}^{n+1} = T_{j+1/2}^n \frac{1 - \Delta t X_{j+1/2}}{1 + \Delta t X_{j+1/2}} + \Delta t Y_{j+1/2}$$

Imposing the limitation that the temperature cannot change by more than 10% we can separate the equation into two restrictions

$$0.9 < \frac{1 - \Delta t X_{j+1/2}}{1 + \Delta t X_{j+1/2}} < 1.1$$

$$\left| \Delta t Y_{j+1/2} \right| < 0.1 * T_{j+1/2}^n$$

Simplifying we get the constraints $\Delta t^n < \frac{0.1}{2\left|X_{j+1/2}\right|}$ and $\Delta t^n < 0.1\frac{T^n_{j+1/2}}{\left|Y_{j+1/2}\right|}$.

If we perform the same analysis on the ion temperature, velocity equation, etc., we will arrive at similar expressions. For each iteration the maximum time step is the smallest of the various limits imposed. Additionally, a sudden increase in the time step can yield an unstable result. To prevent this a further limit is imposed that restricts the time step to increase by no more than 5% over its previous value. Note that a sudden decrease does not have the same effect and is allowed. In fact a sudden decrease in the time step may be required to recover from a stability problem. One additional improvement was made to enhance stability by allowing the model to recover from a serious stability problem. In the event that a sudden and dramatic change is detected, the model will back up several iterations and restart the calculations with a significantly smaller time step. This prevents the problem from occurring and reduces the total time required for the model.

III.B.) 2D Magneto-Hydrodynamic (MHD) Model

The 2D hydrodynamic model is similar to the 1.5D model in that it solves the same equations and utilizes the same conductivity and atomic models. However it differs in several key aspects. These differences arise out of the increased difficulty in solving the hydro equations in 2D instead of 1D.

The first difference is due to the complexity of a Lagrangian formulation. In 1D a Lagrangian formulation has a very direct change from the partial derivative in space to the

mass (see equation 2.3). In 2D this simple transform does not exist. It is still possible to construct a numerical mesh that moves with the mass and does not allow the cells to lose or gain mass. However, these formulations typically suffer from mesh entanglement in which the cells of the mesh will move sufficiently that their shape will distort and eventually may intersect other cells. At this point a remapping technique must be employed during which conservation must be ensured as well as ensuring that the remapping does not alter the simulation. By contrast a much simpler Eulerian mesh is desireable due to the ease of writing the derivatives in space and the lack of a complete remeshing. Utilizing a simple Eulerian mesh has traditionally been computationally prohibitive due to the very large numbers of cells necessary to achieve the desired resolution and domain. To overcome this difficulty our 2D model utilizes Adaptive Mesh Refinement (AMR) to achieve these goals without the need for a more complex formulation (see section III.B.4).

The choice of a Eulerian grid necessitates the solution of the partial form of the hydrodynamic equation (see section III.B.2). In addition, the solution of the atomic rate equation relies on the material derivative. Re-writing to account for convection would link the cells substantially increasing the computational complexity. To prevent this, the 2D code utilizes only the steady-state atomic model. Finally, the absorption model is very different as the techniques in 1D cannot be extrapolated to 2D (see Chapter VI).

III.B.1.) Model Flow

Unlike the 1.5D model, the individual equations cannot be re-written into a tridiagonal form. Instead of solving the equations independently (necessary to preserve the

tridiagonal form in 1D), it is desirable to solve them simultaneously. This has the advantage of ensuring that coupling between the equations will not create an instability. We can write the time rate of change of the variables as:

$$\frac{\partial}{\partial t}\begin{bmatrix}\rho\\ \rho\vec{v}\\ Ue\\ Ui\end{bmatrix} = f(\rho,\rho\vec{v},Ue,Ui,t) \qquad \text{(Eq. 3.11)}$$

We can then solve for the variables as a function of time using any time integration method. Currently, we use the simple Forward Euler method.

III.B.2.) Summary of MHD Equations

In chapter II we derived the different Magneto-Hydrodynamic (MHD) equations starting with the total derivative. The primary equations are summarized below written in a conservative form.

$$\frac{\partial}{\partial t}\int_V \rho d^3x + \oint_S \rho\vec{v}\cdot\hat{n}da = 0 \qquad \text{(Eq. 3.12)}$$

$$\frac{\partial v_i}{\partial t} = -(\vec{v}\cdot\nabla)v_i + \frac{1}{\rho}\left(-\nabla p + \nabla\cdot\vec{\tau}_{vis}\right)_i + \frac{1}{\rho}f_{ext,i} \quad \text{(Form 1)} \qquad \text{(Eq. 3.13)}$$

$$\frac{\partial(\rho v_i)_V}{\partial t} = -\frac{1}{V}\oint_S(\rho v_i)(\vec{v}\cdot\hat{n})da + + \frac{1}{V}\oint_S T_{ij}(\hat{j}\cdot\hat{n})da + \frac{1}{V}\int_V\left(\vec{f}_{ext}\right)_i d^3x \quad \text{(Form 2)}$$

(Eq. 3.14)

$$\frac{\partial}{\partial t}\left(\frac{\Delta U}{\Delta V}\right)_V = -\frac{1}{V}\oint_S\frac{\Delta U}{\Delta V}\vec{v}\cdot\hat{n}da - \frac{1}{V}\oint_S p\vec{v}\cdot\hat{n}da + \frac{1}{V}\oint_S v_i\sigma_{ij}dA_j - \frac{1}{V}\oint_S\vec{q}\cdot\hat{n}da - \frac{1}{V}\int_V\dot{q}d^3x$$

(Eq. 3.15)

III.B.3.) Numerical Form

To write the numerical form we will use the fact that on any given level the grid contains a uniform spacing in time. Additionally, we do not need to perform any discretization in time. The first thing to note is that we will need to know the value of various points at cell faces for cell-centered variables. To do this we can use a variety of interpolation methods as discussed in appendix C.3. For stability reasons the choice of an upwind or SMART interpolation will usually provide the best option because they are total variation diminishing (TVD).

III.B.4.) AMR

Adaptive Mesh Refinement (AMR) provides an efficient method of obtaining both high resolution and a large spatial domain. Adaptive Mesh refinement is a relatively new mathematical technique and has already been used to solve several problems[51]. In addition there have been several mathematical packages to help users develop AMR-based models, one of which is a package called SAMRAI[52] (Structured Adaptive Mesh Refinement Application Infrastructure). The basic idea is to divide the domain into different computational regions (patches). Within each region we can then provide a localized refinement that contains a new grid at a higher resolution (levels). By changing which cells

[51] *Adaptive Mesh Refinement - Theory and Applications*, Series: Lecture Notes in Computational Science and Engineering, vol. 41, eds. T. Plewa, T. Linde, and G. Weirs (Berlin: Springer).
[52] https://computation.llnl.gov/casc/SAMRAI/

are refined to higher resolution dynamically, it is possible to simultaneously have a high resolution where needed and a coarser resolution where it is not. While this technique can be applied to any structured mesh (Eulerian, Lagrangian, ALE, etc.) I will be assuming a fixed Eulerian domain.

Figure 3.3 shows a sample mesh that illustrates how different levels of refinement can be used to obtain high spatial resolution over a limited spatial region. In this example, the entire domain is covered by a single coarse region. Next is the yellow level of resolution that doubles the resolution. Finally, there is the blue level which further doubles the resolution to achieve the final desired resolution. At each level, the cells can be grouped into rectangular regions called patches. In this example, the coarsest level can be covered by 1 or more patches, the yellow level by 3 or more patches, and the blue level by 3 or more patches. These patches are processed separately and can be divided between different processors to achieve a high level of parallelism.

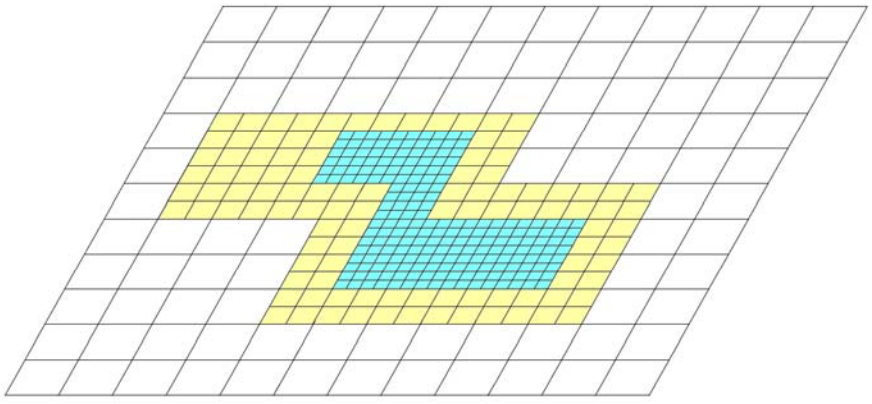

Figure 3.3: Sample mesh showing AMR grid

Figure 3.4 shows an AMR grid used to simulate the plasma created by a curved target. The grid shown is the initial gird at the start of the simulation. Plotted is the mass density. It is necessary to achieve high resolution at the target surface where the target will

be ablated by an incoming laser beam. The different colored boxes indicate the different patches for the different levels of resolution. Achieving the desired resolution with a simple fixed Eulerian grid would require in excess of 2.3 million cells to achieve the desired resolution. The actual number of cells needed was 94,525 cells, a 36x improvement. Additionally the different patches were distributed among different processors for parallel efficiency using 16 processors for this particular resolution.

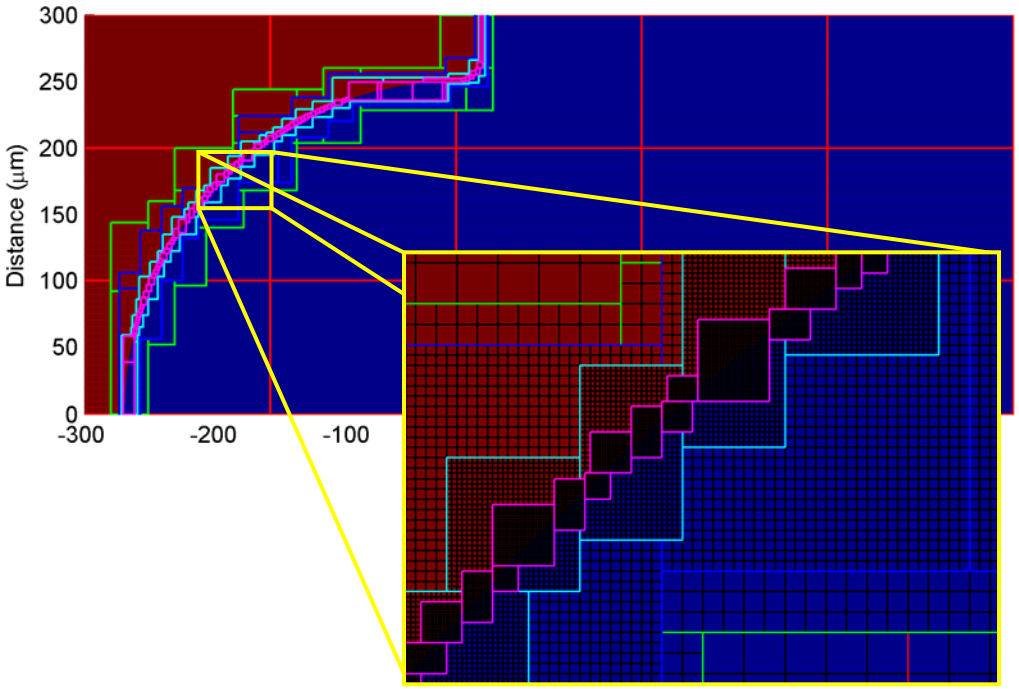

Figure 3.4: AMR grid use to simulate a curved target surface

III.B.5.) Time Step Considerations

The time step requirements for the 2D model are more complex. Unlike the 1.5 D model we do not treat the equations separately, but instead we combine all the equations when we evaluate the nonlinear function. This means that there are no interactions between the equations that would limit the time step. Instead, all of the time step criteria

can be considered through the time integrator used. The most accurate time step criteria can be obtained by considering the nonlinear function and the time integrator used. A much simpler criteria is to limit the change in any of the variables.

III.C.) Comparison of 1.5D and 2D Models

The general behavior of the two hydrodynamic models is very similar. While we used different formulations for the hydrodynamic equations in a 1D approximation both models must still produce the same results. Figure 3.5 shows the electron temperature maps for the 1.5D and 2D models for sample runs used to compare the models. Detailed simulation results and discussion of the physics is included in chapter VIII. When both models are run in a 1D approximation the agreement is vey good. There are a few slight differences in the electron temperature near the peak due to the different absorption models. When run in the 1.5D and 2D approximations respectively the differences are more noticeable. In general both models are able to account for lateral effects either directly (in the 2D model) or with the self-similar approximation (in the 1.5D model). These effects cause a reduction in the peak electron temperature from ~600 eV to ~450 eV. The absorption in the 1.5D model penetrates a little deeper into the plasma due to a difference in the absorption model where absorption off line-centered is approximated using the self-similar solutions and then averaged along that direction. The 2D model by contrast uses a full 2D absorption model that is able to account for refraction and a non-uniform absorption profile parallel to the target surface (the second direction). Finally the thermal conduction away from the target surface is different between the two models and is

not able to be accounted for by the self-similar solution. The most important difference between the models is we are able to get full 2D profiles for the various properties off the line-center without relying on the self-similar solution.

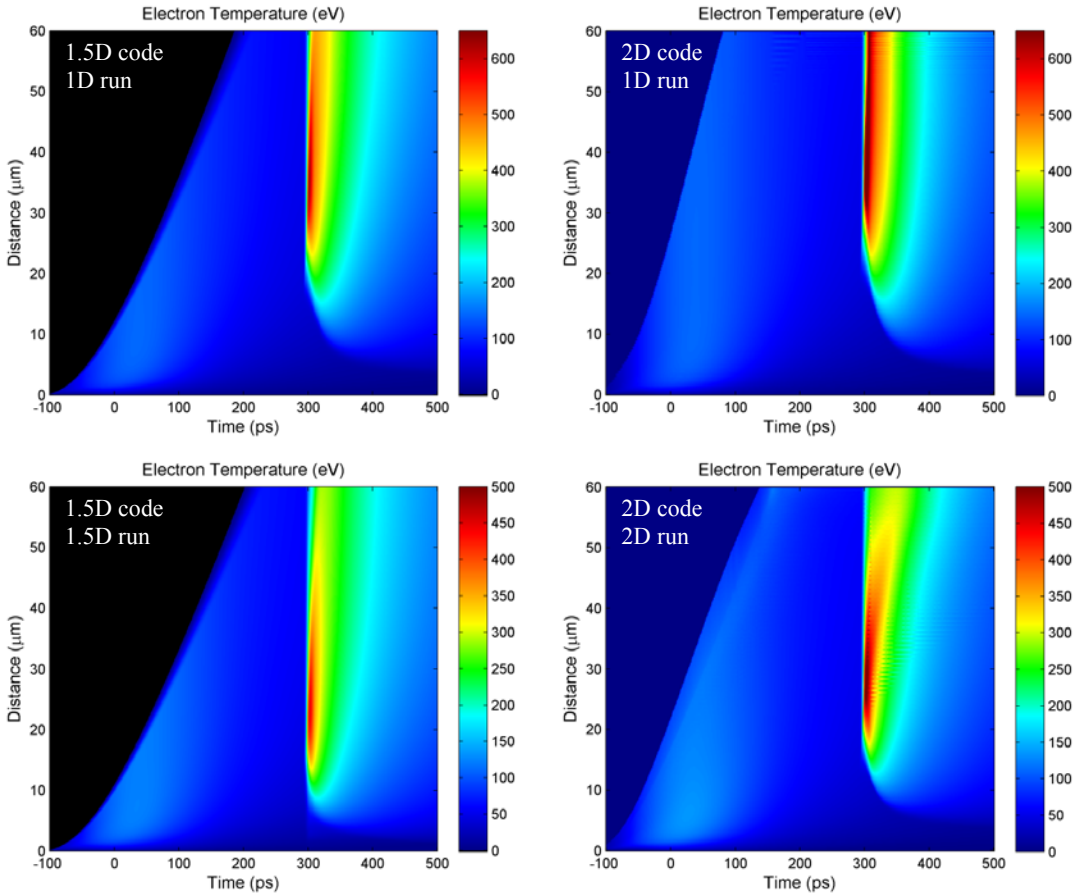

Figure 3.5: Plots of the electron temperature comparing the two hydro models in a 1D approximation and a 1.5D and 2D approximation. The plots are a function of time and distance from the target surface.

CHAPTER IV) CONDUCTIVITY MODEL:

In order to solve the MHD equations, a large number of physical properties of the plasma must be known. These include properties like the thermal conductivity, the collision frequency, the viscosity, the absorption coefficient, etc. These properties depend on the physical conditions of the plasma including the electron and ion temperatures, the electron and ion densities, and degree of ionization. The dependencies can be quite complex and are in general not linear, however most of the properties are related to a single quantity, the electron-ion collision time.

IV.A) The collision time:

The collision time is the average time between collisions in the plasma. It affects most of the plasma properties, and has different approximations for each region of validity. Unless otherwise noted, we will assume that the time scale of interest is larger than the collision time. This allows us to use an analytical velocity distribution to simplify the problem. Also, we assume that the mean free path (average distance between collisions) is smaller than the dimensions of interest. This allows us to assume that the plasma is solely determined by collisions and that all of the effects due to its confinement are negligible.

The calculation of the collision time and most properties will follow the work of Lee and More[53,54]. Their model covers the wide range of density and temperature combinations needed for the plasma evolution in our model. In general, the collision time between electrons and ions is given by

$$\tau_{ei} = 1/n_i v \sigma_{ei} \qquad \text{(Eq. 4.1)}$$

where σ_{ei} is the electron-ion cross section, v is the velocity of the collision, and n_i is the ion density. If we assume that the cross section is due to Coulomb interactions we can use the Coulomb cross section given by

$$\sigma_{ei} = 4\pi \frac{Z_i^2 e^4 \ln\Lambda}{m^2 v^4} \qquad \text{(Eq. 4.2)}$$

The Coulomb logarithm $\ln\Lambda$ is

$$\ln\Lambda = \tfrac{1}{2}\ln\left(1 + b_{\max}^2 / b_{\min}^2\right)$$

where b_{max} and b_{min} are the upper and lower cutoffs on the Coulomb impact parameter. By substituting the Coulomb cross section in the collision time for a single velocity we get

$$\tau_c(v) = \frac{m^2 v^3}{4\pi n_i Z_i^2 e^4 \ln\Lambda} \qquad \text{(Eq. 4.3)}$$

This equation represents the collision time for a mono-energetic electron beam with one particular charged species. To calculate the average collision time, this needs to be integrated over the velocity distributions and all charged states of the ion.

The first approximation is the use of the average charge Z instead of the charge of a particular ion. This can yield errors for plasmas with a very low degree of ionization. In

---

[53] Y.T. Lee and R.M. More, "*An electron conductivity model for dense plasmas*", Physics of Fluids, **27**, 1984, pp. 1273-1285.

[54] *Handbook of Plasma Physics*, Volume 3, Edited by M.N. Rosenbluth, R.Z. Sagdeev, "Atomic *Physics of Laser-Produced Plasmas*", Richard M. More, Elsevier Science publishers, 1991.

this case the average charge is usually set to a minimum value of 1. To treat the problem correctly, one needs to include the cross section of an electron-neutral collision.

The second approximation deals with the integration of the collision time over a velocity distribution. If the lifetime of the plasma is much less than the collision time, the velocity distribution can be quite complicated. However, if the lifetime of the plasma is much larger than the collision time, the plasma will reach thermodynamic equilibrium. In this case we can assume an analytical velocity distribution. In a non-degenerate ideal plasma, the velocity distribution of interest will be Maxwellian. This case was solved by Spitzer[55].

$$\tau_c = \frac{\sqrt{m}(3kT)^{3/2}}{8\times 0.714\pi n Z^4 e^4 \ln\Lambda} \qquad \text{(Self collision time)} \qquad \text{(Eq. 4.4)}$$

$$\tau_{ei} = \frac{\sqrt{m}(3kT)^{3/2}}{8\times 0.714\pi n_i Z^2 e^4 \ln\Lambda} \qquad \text{(Electron-ion collision time)} \qquad \text{(Eq. 4.5)}$$

$$\Lambda = \overline{h/p_0} = \frac{3}{2Z}\frac{(kT)^{3/2}}{\sqrt{\pi n_e}} \qquad \text{(Coulomb logarithm)} \qquad \text{(Eq. 4.6)}$$

While commonly used, these equations neglect a large number of effects including degeneracy and non-ideal effects. To properly incorporate these effects the distribution function should be a Fermi-Dirac distribution. Also special treatment of Coulomb logarithm is necessary. In this case the collision time reduces to

$$\tau_{ei} = \frac{3}{8\pi}\frac{h^3 n_e\left(1+e^{-\mu/kT}\right)}{4\pi Z^2 e^4 n_i m \ln\Lambda}$$

where μ is the chemical potential. For an ideal plasma

---

[55] L. Spitzer, *Physics of Fully Ionized Gases*, 2nd ed. Interscience Publishers, **27**, 1984.

$$\frac{\mu_0}{kT} = \ln\left[\left(\frac{n}{2}\right)\left(\frac{h^2}{2\pi mkT}\right)^{3/2}\right] \qquad \text{(Eq. 4.7)}$$

If the plasma is non-ideal, corrections to the chemical potential can be included. The model includes the corrections to μ from Mohanti[56]

$$\frac{\Delta\mu}{kT} = \left(1 + \frac{1}{\tau_{ei}\nu_p}\right)\frac{1}{3N_D} \qquad \text{(Eq. 4.8)}$$

ν_p is the plasma frequency

N_D is the Debye number

If the plasma is ideal and non-degenerate: $e^{-\mu/kT} >> 1$

$$\tau_{ei} = \frac{3}{4}\frac{\sqrt{m}}{\sqrt{2\pi}}\frac{(kT)^{3/2}}{Z^2 e^4 n_i \ln\Lambda} \qquad \text{This agrees with the Spitzer limit.} \qquad \text{(Eq. 4.9)}$$

In the completely degenerate case: $e^{-\mu/kT} << 1$ ($Z = n_e / n_i$)

$$\tau_{ei} = \frac{3\pi}{4}\frac{\hbar^3}{Ze^4 m \ln\Lambda} \qquad \text{(Eq. 4.10)}$$

This agrees with Ziman's[57] results for a metallic conductor.

To determine the collision time, Lee and More break up the conductivity model into five regions (figure 4.1):

---

[56] R.B. Mohanti and J.G. Gillgan, "*Electrical conductivity and thermodynamic functions of weakly nonideal plasma*", J. Appl. Phys., Vol. 68, 1990, pp. 5044-5051.

[57] J.M. Ziman, *Principle of Theory of Solids*, Cambridge University Press, 1969.

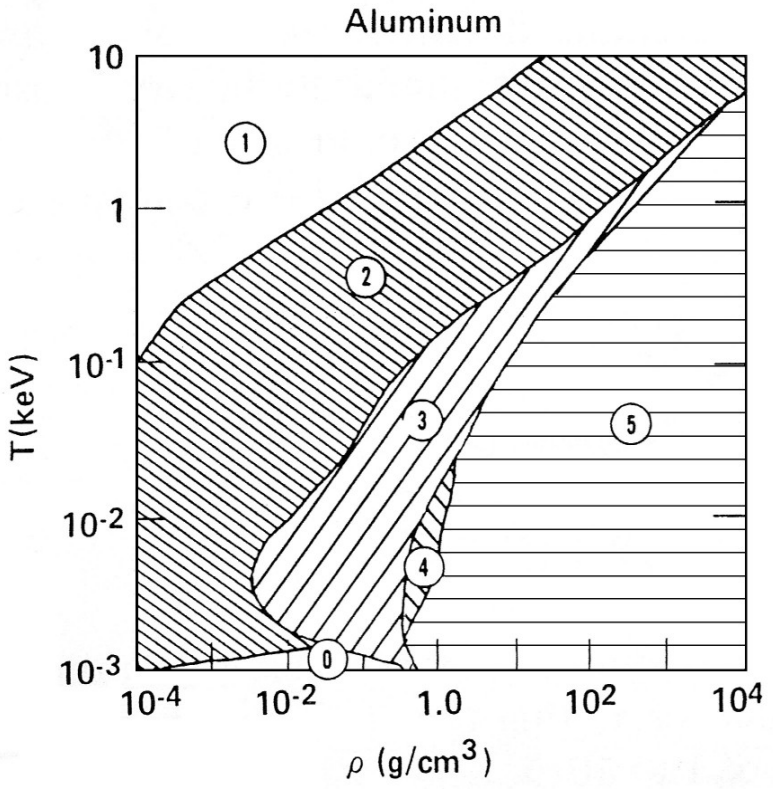

Figure 4.1: Density-temperature phase-plane for aluminum plasma.
Shows the regions of applicability for the different regions (Lee-More: Ref[54])

Region 1: The ideal plasma. In this region the impact paramenters are derived assuming an ideal plasma. The minimum impact parameter b_{min} is the maximum of the classical distance of closest approach and the uncertainty principle. The maximum impact parameter b_{max} is the Debye-Hückel screening length λ_D. To account for degeneracy, the Fermi energy is used at low temperatures.

$$\ln\Lambda = \tfrac{1}{2}\ln\left(1+\frac{b_{\max}^2}{b_{\min}^2}\right) \qquad \text{(Eq. 4.11)}$$

$$b_{\min} = \sqrt{\left(b_{\min}^{c}\right)^2 + \left(b_{\min}^{Q}\right)^2} \qquad \text{(Eq. 4.12)}$$

$$b_{\min}^{c} = Z^2 e^2 / mv^2$$

$$b_{\min}^{Q} = h/2mv$$

$$b_{\max} = \lambda_D = \left(\frac{4\pi Z^2 e^2 n_i}{kT_i} + \frac{4\pi e^2 n_e}{kT} \right)^{-1/2} \qquad \text{(Eq. 4.13)}$$

$$T = \sqrt{T_e^2 + \left(\tfrac{2}{3} T_F\right)^2}$$

In the minimum impact parameter, v and m are the velocity and mass of the electron. The degeneracy of the plasma is taken into account in the maximum impact parameter through the effective electron temperature T. The effective electron temperature contains both the actual electron temperature T_e and the Fermi temperature T_F.

Region 2: The dense or strongly coupled region. In this region, the plasma is dense so the particles do not travel very far before they collide. The maximum impact parameter b_{max} must be replaced by the interatomic distance R_0. An adjustable parameter $p_1 \approx 1$ may be used to improve the accuracy.

$$b_{\max} = p_1 R_0 \qquad \text{(Eq. 4.14)}$$

$$R_0 = \left(3/4\pi n_i\right)^{1/3}$$

Region 3: Region 3 represents a region of higher density where the analysis of the Coulomb logarithm breaks down. In this region, a minimum value of $\ln\Lambda = 2$ is used. This is a technique commonly employed by many researchers.

Region 4: Region 4 occurs between the solid/liquid phase and the traditional plasma phase. In this region the analysis of the Coulomb cross section breaks down, so the collision time is calculated by placing a constraint on the mean free path. The mean free path must not be

less than the atomic radius. With the mean velocity $\bar{v}_e$, the minimum collision time can be calculated. Another adjustable parameter $p_2 \approx 1$ may be used.

$$l_{\min} = \tau \cdot \bar{v}_e = p_2 R_0 \qquad \text{(Eq. 4.15)}$$

$$\bar{v}_e = \sqrt{\frac{2T}{m}}$$

$$\tau_{\min} = p_2 \frac{R_0}{\bar{v}_e} \qquad \text{(Eq. 4.16)}$$

Region 5: Region 5 is a region used to describe the solid and liquid phases. Region 5 uses the Bloch-Gruneison law to describe conduction. Θ_D is the Debye temperature, p_3 is another adjustable parameter, and γ is chosen for each metal to give the rise in resistivity due to melting.

$$\tau_{ei} = 50 p_3 \frac{R_0}{\bar{v}_e} \frac{T_m}{T} \qquad \Theta_D < T < T_m \qquad \text{(Eq. 4.17)}$$

$$\tau_{ei} = 50 p_3 \frac{R_0}{\bar{v}_e} \frac{T_m}{T} \frac{1}{\gamma} \qquad T > T_m \qquad \text{(Eq. 4.18)}$$

Region 0: A 6th region may be used and is governed by the electron scattering by neutral atoms. This region is characterized by a cold, low density region with a mean degree of ionization less than one. It is weakly approximated and rarely occurs within our model. For simplicity a fixed electron-neutral cross section of $\sim 10^{-14}$ cm^2 can be used.

While the conductivity model proposed by Lee and More can be considered sufficiently accurate over a broad range of conditions, additional corrections can be made to improve

its accuracy. These changes primarily affect the solid-density cold region. For example, see Desjarlais[58], which is used to adjust the factor p_2 for region 4.

IV.B) Electron-Ion Equilibration Time:

The electron-ion equilibration time is the time it will take for the electrons and ions to thermalize and establish the same temperature. This is an important quantity because it determines if a two temperature model is necessary and will determine the ion temperature. In most cases, the time required for the electrons and ions to equilibrate is longer than the timescales of interest. In this situation the electron-ion collision time determines the rate of heat transfer between the electrons and ions. The electron-ion equilibration time is simply the product of the electron-ion collision time and the ratio of the masses of the particles.

$$\tau_{eq} = \tau_{ei} \frac{m_i}{m_e} \qquad \text{(Eq. 4.19)}$$

IV.C) The thermal conductivity:

The thermal conductivity is an important property that determines how quickly heat is transported within the model. The thermal conductivity can be directly related to the collision time. Specifically, the electron thermal conduction coefficient is

$$\kappa_e = B \frac{n_e k T_e}{m_e} \tau_{ei} \qquad \text{(Eq. 4.20)}$$

---

[58] M. P. Desjarlais, "*Practical Improvements to the Lee-More Conductivity Near the Metal-Insulator Transition*", Contrib. Plasma Phys., Vol. 41, 2001, pp. 267-270.

In this equation B is a constant that depends on the degeneracy and any external magnetic field. Braginskii[59] solved the transport coefficients for a magnetized ideal plasma. When a magnetic field is present, the thermal conduction perpendicular to the field is inhibited. The magnetic field reduces the B coefficient according to the strength of the magnetic field. One measure of the strength of the magnetic field is the cyclotron frequency

$$\omega_e = \frac{e\mathbf{B}}{m_e c} \qquad \text{(Eq. 4.21)}$$

If $\tau_e \omega_e << 1$, the present analysis is accurate and correcting the B coefficient is sufficient. However if $\tau_e \omega_e > 1$, this treatment is insufficient and the characteristic property is the magnetic field, not the electron-ion collision time. Even if $\tau_e \omega_e < 1$, the B coefficient can still be reduced by as much as an order of magnitude due to the presence of a magnetic field. For an ideal unmagnitized plasma the thermal conductivity is

$$\kappa_e = 8\left(\frac{2}{\pi}\right)^{3/2} \frac{(kT_e)^{5/2}}{\sqrt{m_e} Ze^4 \ln \Lambda} \qquad \text{(Eq. 4.22)}$$

Note that the thermal conductivity scales as $T_e^{5/2}$, resulting in a strong temperature dependence.

If the plasma is not ideal, then the B coefficient is dependent on both the plasma degeneracy and the magnetic field **B**. Lee and More include fitting tables for this case. If the plasma is unmagnitized we can look at the degeneracy limits

$$B = \frac{128}{3\pi} \qquad \text{(Ideal, non-degenerate plasma)} \qquad \text{(Eq. 4.23)}$$

---

[59] *Review of Plasma Physics*, S.I. Braginskii, "*Transport Processes in a Plasma*", pp 205-311.

$$B = \frac{\pi^2}{3} \qquad \text{(Completely degenerate plasma)} \qquad \text{(Eq. 4.24)}$$

IV.D) Flux limiter:

When the temperature gradients are very large, the thermal conductivity can become unphysical. Recall the classical heat flux $q_c = -\kappa \nabla T$; as the temperature gradient approaches infinity, the heat transported approaches infinity. In classical theory[60] it is assumed that the scale length of the temperature is much larger than the electron mean free path. As the gradient becomes large this assumption does not hold and a heat flux limiter is needed. We use a harmonic heat flux limiter[61,62,63]

$$q = \left(1/q_c + 1/q_f\right)^{-1} \qquad \text{(Eq. 4.25)}$$

With this limiter the heat flux is limited to the lesser of the classical heat flux q_c or the free flow limited q_f. The free flow limit can be expressed as the product of the number of particles *n*, their thermal velocity $\bar{v}$, and the energy per particle *T*. A constant *f* is adjusted between 0.1-0.3 to control the degree of the free flow limit.

$$q_f = fnT\sqrt{T/m} \qquad \text{(Eq. 4.26)}$$

---

[60] Lyman Spitzer Jr. and Richard Harm, "*Transport Phenomena in a Completely Ionized Gas*", Physical Review, Vol. 89, No. 5, 1953, pp. 977-981.

[61] R.C. Malone, R.L. McCroy, R.L. Morse, "*Indications of Strongly Flux-Limited Electron Thermal Conduction in Laser-Targets*", Physical Review Letters, Vol. 24, 1975, pp. 721-724.

[62] P.A. Holstein, J. Delettrez, S. Skupsky, "*Modeling nonlocal heat flow in laser-produced plasma*", J. Appl. Phys., Vol. 60, 1986, pp. 2296-2300.

[63] J.H. Rogers, J.S. De Groot, Z. Abou-Assaleh, J.P. Matte, T.W. Johnston, M.D. Rosen, "*Electron heat transport in a steep temperature gradient*", Phys. Fluids B, Vol 1, 1989, pp. 741-749.

IV.E) Electrical conductivity:

Electrical conductivity is an important property. For a DC field the conductivity behaves very similar to the thermal conductivity. The DC conductivity can be written as

$$\sigma_e = A\frac{n_e e^2}{m_e}\tau_{ei} \qquad \text{(Eq. 4.27)}$$

Again, A is a constant that depends on both the degeneracy and the strength of transverse magnetic fields. In an unmagnitized plasma the limits of A are:

$$A = \frac{32}{3\pi} \qquad \text{(Ideal, non-degenerate plasma)} \qquad \text{(Eq. 4.28)}$$

$$A = 1 \qquad \text{(Completely degenerate plasma)} \qquad \text{(Eq. 4.29)}$$

For an ideal, non-degenerate unmagnitized plasma the electrical conductivity is

$$\sigma_e = 2\left(\frac{2}{\pi}\right)^{3/2}\frac{(kT_e)^{3/2}}{\sqrt{m_e}Ze^2\ln\Lambda} \qquad \text{(Eq. 4.30)}$$

The similar forms of the electrical and thermal conductivity illustrates their connection. According to the Wiedemann-Franz law, good heat conductors are also good electrical conductors. If we take the ratio of the thermal conductivity divided by the temperature times the electrical conductivity, we can get the Lorentz number

$$L = \frac{\kappa}{\sigma T} = \frac{B}{A}\left(\frac{k}{e^2}\right) \qquad \text{(Eq. 4.31)}$$

Note that L is weakly dependent on the conditions (B/A is 3.3 for the degenerate case and 4 for the ideal, non-degenerate case).

IV.F) Absorption and the complex index of refraction:

Of vital importance is the absorption of the incident laser light, it gives the energy necessary to create and heat the plasma. The absorption is due to the imaginary part of the index of refraction. As a result we need to calculate the complex index of refraction. Additionally, the real part of the index is important to calculate the effect of refraction on the grazing incidence pumping and the propagation of the EUV laser beam.

To calculate the index of refraction, we need to review some notation. I will be using the same notation as Jackson[64]. The plane wave electric and magnetic fields can be written as

$$E(x,t) = E_0 e^{ikx - i\omega t} \qquad \text{(Eq. 4.32)}$$

$$B(x,t) = B_0 e^{ikx - i\omega t} \qquad \text{(Eq. 4.33)}$$

The complex wavenumber k can be expressed as $k = \sqrt{\mu\varepsilon}\,\omega = n\omega/c$. The attenuation of the plane wave can be directly expressed through the real and imaginary parts of the wavenumber.

$$k = n\frac{\omega}{c} = \beta + i\frac{\alpha}{2} \qquad \text{(Eq. 4.34)}$$

Here α is the attenuation constant ($I = e^{-\alpha z}$). Using the Drude model,[65,66] we can express the complex index of refraction in terms of the collision time

---

[64] John David Jackson, *Classical Electrodynamics*, third edition, John Wiley & Sons Inc., New York, 1999.

[65] W. Jones and N. H. March, *Theoretical Solid State Physics*, Wiley, New York, 1973, Vol. 2.

[66] E. M. Lifshitz and L. P. Pitaevskii, *Physical Kinetics*, Pergamon, Oxford, 1981.

$$n^2 = 1 - \frac{\omega_p^2}{\omega(\omega + i\nu_{ei})} \qquad \nu_{ei} = \frac{1}{\tau_{ei}} \qquad \text{(Eq. 4.35)}$$

Note that ω_p is the plasma frequency: $\omega_p^2 = 4\pi \frac{e^2 n_e}{m_e}$ (Eq. 4.36)

Simplifying we get

$$n^2 = 1 - \frac{\omega_p^2 \tau_{ei}}{\omega(\omega\tau_{ei} + i)} \qquad \text{(Eq. 4.37)}$$

$$n^2 = 1 + i\frac{\omega_p^2}{\omega}\frac{\tau_{ei}}{1 - i\omega\tau_{ei}} \qquad \text{(Eq. 4.38)}$$

However, this is only valid for one collision time while we need the result in terms of the average collision time. When we apply thermodynamic averaging we get

$$n^2 = 1 + i\frac{\omega_p^2}{\omega}\left\langle \frac{\tau_{ei}}{1 - i\omega\tau_{ei}} \right\rangle \qquad \text{(Eq. 4.39)}$$

We can substitute for ω_p

$$n^2 = 1 + i\frac{4\pi}{\omega}\frac{e^2 n_e}{m_e}\left\langle \frac{\tau_{ei}}{1 - i\omega\tau_{ei}} \right\rangle \qquad \text{(Eq. 4.40)}$$

The conductivity can be defined as $n^2 = 1 + \frac{i4\pi}{\omega}\sigma(\omega)$, yielding the expression from Price[67]

$$\sigma(\omega) = \frac{e^2 n_e}{m_e}\left\langle \frac{\tau_{ei}}{1 - i\omega\tau_{ei}} \right\rangle \qquad \text{(Eq. 4.41)}$$

For DC conductivity $(\omega \approx 0)$

$$\sigma(0) = \frac{e^2 n_e}{m_e}\langle \tau_{ei} \rangle = \frac{e^2 n_e}{m_e}\tau_{ei} \qquad \text{(Eq. 4.42)}$$

---

[67] D.F. Price, R.M. More, R.S. Walling, G. Guethlein, R.L. Shepherd, R.E. Stewart, W.E. White, "*Absorption of Ultrashort Laser Pulses by Solid Targets Heated Rapidly to Temperatures 1-1000 eV*", Physical Review Letters, Vol. 75, No. 2, July 1995, pp. 252-255.

For frequencies much less then the collision frequency $\nu << \nu_{ei}$ we need to include Spitzer's electron-electron correction factor γ_E. This is the missing A coefficient. We now recover the DC conductivity discussed in section IV.E:

$$\sigma = A\frac{e^2 n_e}{m_e}\tau_{ei} \qquad \text{(Eq. 4.43)}$$

To get the absorption of an optical laser we start with the expression for the complex index of refraction

$$n^2 = 1 + i\frac{\omega_p^2}{\omega}\left\langle \frac{\tau_{ei}}{1 - i\omega\tau_{ei}} \right\rangle \qquad \text{(Eq. 4.44)}$$

We can simplify

$$n^2 = 1 + i\frac{\omega_p^2}{\omega}\left\langle \frac{1}{\tau_{ei}^{-1} - i\omega} \right\rangle \qquad \text{(Eq. 4.45)}$$

$$n^2 = 1 + i\frac{\omega_p^2}{\omega}\left\langle \frac{\tau_{ei}^{-1} + i\omega}{\tau_{ei}^{-2} + \omega^2} \right\rangle \qquad \text{(Eq. 4.46)}$$

In the high frequency limit $\omega >> \frac{1}{\tau_{ei}}$

$$n^2 = 1 + i\frac{\omega_p^2}{\omega}\left\langle \frac{\tau_{ei}^{-1} + i\omega}{\omega^2} \right\rangle \qquad \text{(Eq. 4.47)}$$

$$n^2 = 1 + i\frac{\omega_p^2}{\omega}\left\langle \frac{\tau_{ei}^{-1} + i\omega}{\omega^2} \right\rangle \qquad \text{(Eq. 4.48)}$$

$$n^2 = 1 - \frac{\omega_p^2}{\omega^2} + i\frac{\omega_p^2}{\omega^3}\left\langle \frac{1}{\tau_{ei}} \right\rangle \qquad \text{(Eq. 4.49)}$$

If $\mathrm{Re}(\varepsilon) >> \mathrm{Im}(\varepsilon)$ $(\varepsilon = n^2)$

$$n \approx \sqrt{\mathrm{Re}(\varepsilon)} + \frac{i}{2}\frac{\mathrm{Im}(\varepsilon)}{\sqrt{\mathrm{Re}(\varepsilon)}} \qquad \text{(Eq. 4.50)}$$

$$n \approx \sqrt{1 - \frac{\omega_p^2}{\omega^2}} + \frac{i}{2}\frac{\omega_p^2 \langle 1/\tau_{ei} \rangle}{\omega^2 \sqrt{\omega^2 - \omega_p^2}} \qquad \text{(Eq. 4.51)}$$

First we will look at the real part of the index of refraction

$$n \approx \sqrt{1 - \frac{\omega_p^2}{\omega^2}} = \sqrt{1 - 4\pi \frac{e^2 n_e}{m_e \omega^2}} \qquad \text{(Eq. 4.52)}$$

The frequency when $\omega = \omega_p$ is called the critical frequency, and the electron density that corresponds to that point is called the critical density:

$$n_c = \frac{\omega^2 m_e}{4\pi e^2} = \frac{1.11 \times 10^{21} \quad e/cm^3}{\lambda^2 (\mu m)} \qquad \text{(Eq. 4.53)}$$

The real part of the index of refraction can then be written as

$$n \approx \sqrt{1 - \frac{n_e}{n_c}} \qquad \text{(Eq. 4.54)}$$

This derivation is also carried out in Attwood[68].

Next we will derive the absorption coefficient.

$$n \approx \sqrt{1 - \frac{\omega_p^2}{\omega^2}} + \frac{i}{2}\frac{\omega_p^2 \langle 1/\tau_{ei} \rangle}{\omega^2 \sqrt{\omega^2 - \omega_p^2}} \qquad \text{(Eq. 4.55)}$$

$$k \approx \frac{1}{c}\sqrt{\omega^2 - \omega_p^2} + \frac{i}{2c}\frac{\omega_p^2}{\omega}\frac{\langle 1/\tau_{ei} \rangle}{\sqrt{\omega^2 - \omega_p^2}} \qquad \text{(Eq. 4.56)}$$

---

[68] David Attwood, *Soft X-Rays and Extreme Ultraviolet Radiation*, Cambridge University Press, 1999.

The absorption coefficient α is from the imaginary component of k $\left(k = \beta + i\frac{\alpha}{2} \right)$.

$$\alpha \approx \frac{\omega_p^2}{\omega} \frac{\langle 1/\tau_{ei} \rangle}{c\sqrt{\omega^2 - \omega_p^2}} \qquad \text{(Eq. 4.57)}$$

The group velocity is defined as $v_g = \frac{\partial \omega}{\partial k} = c\sqrt{1 - \frac{\omega_p^2}{\omega^2}}$

$$\alpha \approx \frac{\omega_p^2}{\omega^2} \frac{1}{v_g} \left\langle \frac{1}{\tau_{ei}} \right\rangle \qquad \text{(Eq. 4.58)}$$

Recall $\frac{\omega_p^2}{\omega^2} = \frac{n_e}{n_c}$ from the definition of the critical density

$$\alpha \approx \frac{n_e}{n_c v_g} \left\langle \frac{1}{\tau_{ei}} \right\rangle \qquad \text{(Eq. 4.59)}$$

If we assume $\left\langle \frac{1}{\tau_{ei}} \right\rangle = \frac{1}{\tau_{ei}} = \nu_{ei}$, we get the simplified expression for the absorption coefficient:

$$\alpha \approx \frac{n_e \nu_{ei}}{n_c v_g} \qquad \text{(Eq. 4.60)}$$

The absorption length is

$$l_{abs} \approx \frac{n_c v_g}{n_e \nu_{ei}} \qquad \text{(Eq. 4.61)}$$

For an ideal, non-degenerate plasma this agrees with the expression from Johnston and Dawson[69,70]

---

[69] T. W. Johnston and J. M. Dawson, "*Correct values for high-frequency power absorption by inverse bremsstrahlung in plasmas*", Phys. Fluids, **16**, 1973, p. 722.

$$\alpha = \frac{16\pi Z^2 n_e n_i e^6 \ln\Lambda}{3c\nu^2 (2\pi m_e kT)^{3/2}\sqrt{1-\omega_p^2/\omega^2}} \qquad \text{(Eq. 4.62)}$$

Note that at high frequencies $\omega_p << \omega$ the laser frequency should be used in place of the plasma frequency in the coulomb logarithm[71].

For low densities $(n_e << n_c)$:

$$l_{abs} \propto \frac{T_e^{3/2}}{Zn_e^2} \qquad \text{(Eq. 4.63)}$$

From the absorption length, we note that there is a strong temperature dependence. As the plasma absorbs the laser light, it will heat reducing the absorption coefficient, which will then limit further absorption and heating. As a result, the hotter a plasma is, the more difficult it is to further heat it. Because the absorption length is $\propto n_e^{-2}$, a higher density plasma will absorb more energy per electron and therefore reach a larger temperature. The simple approximations given will break down at electron densities approaching the critical density. In the absorption model (chapter VI) I use the full expression from the Drude model, so the index of refraction and absorption are valid for densities much closer to the critical density.

---

[70] J. M. Dawson, "*On the Production of Plasma by Giant Pulse Lasers*", The Physics of Fluids, **7**, 1964, pp. 981-987

[71] J. Dawson and C. Oberman, "*High Frequency Conductivity and the Emission and Absorption Coefficients of a Fully Ionized Plasma*", Phys. Fluids, **5**, 1973, pp. 517-524.

IV.G) Viscosity:

A final plasma property that is often needed are the viscosity coefficients. In a compressing plasma they can slow the compression and dramatically increase the temperature. While viscosity can slow the expansion, the effect is much less dramatic and can often be neglected. Under most conditions the ion viscosity is much larger than the electron viscosity due to the large mass of the ions. This can cause the ion temperature to exceed the electron temperature in a compressing plasma. From Braginskii, the viscosity coefficients are

$$\eta_0^e = 0.733 n_e T_e \tau_e \qquad \text{(electron viscosity coefficient)} \qquad \text{(Eq. 4.64)}$$

$$\eta_0^i = 0.96 n_i T_i \tau_i \qquad \text{(ion viscosity coefficient)} \qquad \text{(Eq. 4.65)}$$

Note that in the presence of a magnetic field the coefficients can be affected due to the cyclotronic motion of the electrons and ions. However this effect is weaker than the corrections to the thermal and electrical conductivities. In addition, viscosity tends to be small within a plasma. See Braginskii for more information.

IV.H) Numerical Implications:

The conductivity model for a given cell does not depend on adjacent cells. As a result there is not a numerical form. Additionally while most of the thermodynamic properties affect the plasma, they do not have specific considerations on the time step. For example, the thermal conductivity obviously affects the thermal transport, which affects the time step, but those effects are accounted for in the numerical formulation of the hydrodynamic equations. The one variable that has a direct impact on the equations is the

electron-ion equilibration time. If the equations are not solved simultaneously, then the time step of the model would need to be less than the electron-ion equilibration time and should be included in the time step criteria. For the plasmas studied in this work, this timescale is generally larger than many of the other timescales in the model.

CHAPTER V.) ATOMIC MODEL:

In order to understand the plasma dynamics and calculate the plasma properties, we need to know the details about the atomic properties of the plasma. These details include the mean degree of ionization (average number of free electrons per ion) and all atomic losses. The detailed level populations of the ions of interest are needed in order to calculate the gain. To obtain this information I have created an accurate atomic model. The atomic model consists of three different cases. The first case is a simple model in which the degree of ionization is calculated assuming a steady-state solution for both the ions and the excited states within the ion. This model is pre-solved with a data lookup table, and can be used at high densities where the time scale to achieve steady state is less than the time during which the plasma conditions change. The second case involves a detailed ion calculation in which the distributions of different ions are calculated using a full transient solution, but a steady-state solution is used for excited states within an ion. This approximation is used for most of the plasma evolution and for most ion species. The third and most complicated case involves a detailed transient calculation for both the ions and their excited state populations. This case must be used for short lived transients and is necessary to calculate the population inversion and gain. In all cases a large number of energy levels are needed for an accurate solution. This is especially important for transient populations, in which the upper levels play a more important role. Within the atomic model I use all of the energy levels to within 10% of the ionization potential, which typically requires $n \geq 12$ for the ions of interest. These levels are then bundled to form a

small number (20-40) of effective levels per ion. This bundling yields accurate atomic physics while keeping the number of calculations to a minimum.

V.A) Overview of the atomic structure

In a plasma, the atomic structure is both important and complicated. First, there are the different ion populations. Ions can change their charge state through various ionization and recombination processes, affecting their atomic characteristics. In addition, each ion has a number of excited states that can be excited or de-excited. Spontaneous, radiative transitions can occur between two excited states. These transitions can be partially trapped in which a photon emitted by one ion can be absorbed by another ion resulting in a reduced decay rate. This process is called radiation trapping and must be included. An important physical principle is that for every process there is an inverse process. This is known as the first principle of detailed balance. Once we are able to calculate one process, using the principle of detailed balance we can easily calculate its inverse.

Consider the energy level diagram in figure 5.1 with both ground and excited states. There are many processes at work within this example:

$I_{n,m}^{Z}$ = Electron impact ionization from the n^{th} level of the Z^{th} ionization to the m^{th} level of the $Z+1^{th}$ ionization. This process involves an energetic free electron colliding with an ion, causing it to release an electron resulting in two slower free electrons and the next ion state.

$\beta_{n,m}^{Z}$ = 3-Body recombination from the n^{th} level of the $Z+1^{st}$ ionization to the m^{th} level of the Z^{th} ionization. This is the inverse process of electron impact ionization, in

which 2 free electrons collide with an ion, one electron is captured and the other electron caries the excess energy.

$\alpha_{n,m}^{Z}$ = Radiative recombination from the n^{th} level of the $Z+1^{st}$ ionization to the m^{th} level of the Z^{th} ionization. This is the inverse process of photo-ionization (not included) and involves a free electron colliding with an ion, being captured by the ion and emitting a photon with the excess energy.

$D_{n,m}^{Z}$ = Dielectronic recombination from the n^{th} level of the $Z+1^{st}$ ionization to the m^{th} level of the Z^{th} ionization. This is the inverse process of auto-ionization (not included) and involves a free electron colliding with the ion, being captured resulting in a highly excited state and then radiativly decaying to a stable state.

$E_{n,p}^{Z}$ = Electron impact excitation from the n^{th} level to the p^{th} level in the Z^{th} ionization. This process involves a free electron colliding with an ion, imparting some of its energy to the ion resulting in an excited state within the ion.

$d_{p,n}^{Z}$ = Electron impact de-excitation from the p^{th} level to the n^{th} level in the Z^{th} ionization. This is the inverse process of electron impact excitation, involving a free electron collision and resulting in a lower excited state.

$A_{p,n}^{Z}$ = Radiative de-excitation from the p^{th} level to the n^{th} level in the Z^{th} ionization. Its inverse process is photo-excitation (not included) and represents a spontaneous decay from an excited state to a lower state, emitting a photon to account for the energy difference.

$C_{q\to p,i\to j}$ = Coupling from zone i to j. Probability that a photon emitted in the q to p transition in zone i will be absorbed in zone j, causing p to transition to q (see section V.I).

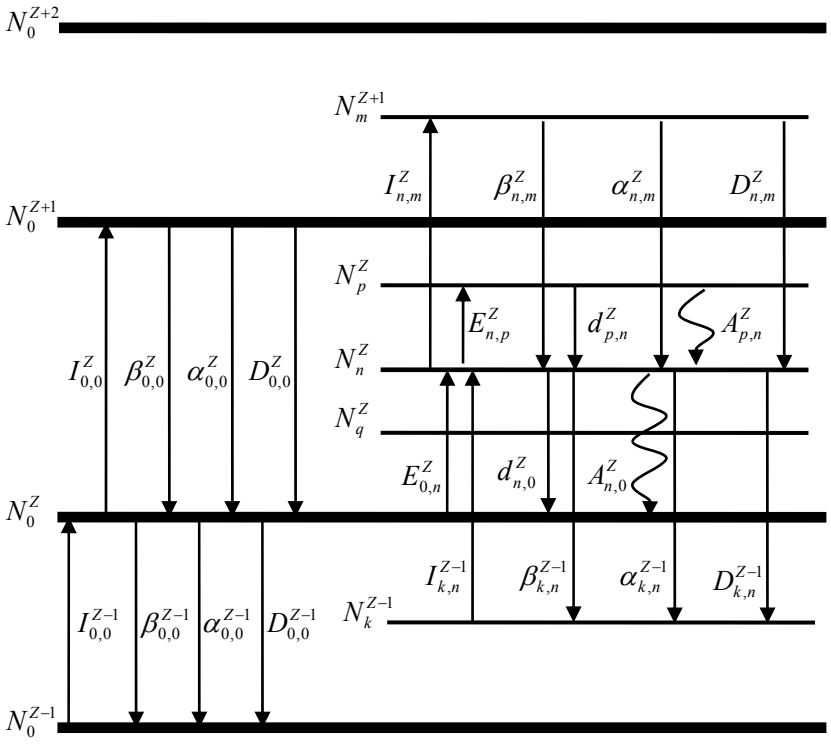

Figure 5.1: Atomic level and rate diagram

V.B) Rate Equations

All of the possible transitions either populate or de-populate a given level within an ion. As a result a rate equation can be written for the time rate of change of a level. The basic rate equation for ion Z, excited state ρ is

$$\frac{dN_\rho^Z}{dt}=\left\{\begin{array}{l}\sum_{q=0}^{M_{Z-1}}\left[n_e I_{q,\rho}^{Z-1}N_q^{Z-1}-n_e N_\rho^Z\left(\alpha_{\rho,q}^{Z-1}+D_{\rho,q}^{Z-1}+n_e\beta_{\rho,q}^{Z-1}\right)\right]\\ -\sum_{q=0}^{M_{Z+1}}\left[n_e I_{\rho,q}^{Z}N_\rho^{Z}-n_e N_q^{Z+1}\left(\alpha_{q,\rho}^{Z}+D_{\rho,q}^{Z}+n_e\beta_{\rho,q}^{Z}\right)\right]\\ +\sum_{q=0}^{\rho-1}\left[n_e E_{q,\rho}^{Z}N_q^{Z}-N_\rho^Z\left(A_{\rho,q}^{Z}+n_e d_{\rho,q}^{Z}\right)\right]\\ -\sum_{q=\rho+1}^{M_Z}\left[n_e E_{\rho,q}^{Z}N_\rho^{Z}-N_q^Z\left(A_{q,\rho}^{Z}+n_e d_{q,\rho}^{Z}\right)\right]\end{array}\right\}$$

This includes all of the important populating and de-populating processes. These are electron impact ionization, radiative recombination, dielectronic recombination, 3-body recombination, electron impact excitation, electron impact de-excitation, and radiative de-excitation.

If radiation trapping is included (often important for dense plasmas)

$$\frac{dN_{\rho,i}^Z}{dt}=\left\{\begin{array}{l}\sum_{q=0}^{M_{Z-1}}\left[n_e I_{q,\rho}^{Z-1}N_{q,i}^{Z-1}-n_e N_{\rho,i}^Z\left(\alpha_{\rho,q}^{Z-1}+D_{\rho,q}^{Z-1}+n_e\beta_{\rho,q}^{Z-1}\right)\right]\\ -\sum_{q=0}^{M_{Z+1}}\left[n_e I_{\rho,q}^{Z}N_{\rho,i}^{Z}-n_e N_{q,i}^{Z+1}\left(\alpha_{q,\rho}^{Z}+D_{q,\rho}^{Z}+n_e\beta_{q,\rho}^{Z}\right)\right]\\ +\sum_{q=0}^{\rho-1}\left[n_e E_{q,\rho}^{Z}N_{q,i}^{Z}-N_{\rho,i}^Z\left(A_{\rho,q}^{Z}+n_e d_{\rho,q}^{Z}\right)+\sum_{j=1}^{J}N_{\rho,j}^Z C_{ji}^{\rho q,Z}A_{\rho,q}^Z\right]\\ -\sum_{q=\rho+1}^{M_Z}\left[n_e E_{\rho,q}^{Z}N_{\rho,i}^{Z}-N_{q,i}^Z\left(A_{q,\rho}^{Z}+n_e d_{q,\rho}^{Z}\right)+\sum_{j=1}^{J}N_{q,j}^Z C_{ji}^{q\rho,Z}A_{q,\rho}^Z\right]\end{array}\right\}$$

In this equation we consider the different spatial regions identified by i and j. The solution of this set of rate equations constitutes a collisional-radiative model with full radiation transport.

V.C) Effective Rate Calculations

A simpler model can be obtained if a steady-state solution is assumed for all of the excited states within an ion. In this case, the level diagram is simplified (see figure 5.2). The rate equation simplifies to

$$\frac{dN^Z}{dt} = \begin{Bmatrix} n_e I_{eff}^{Z-1} N^{Z-1} - n_e N^Z \left(\alpha_{eff}^{Z-1} + D_{eff}^{Z-1} + n_e \beta_{eff}^{Z-1} \right) \\ - n_e I_{eff}^{Z} N^{Z} + n_e N^{Z+1} \left(\alpha_{eff}^{Z} + D_{eff}^{Z} + n_e \beta_{eff}^{Z} \right) \end{Bmatrix}$$

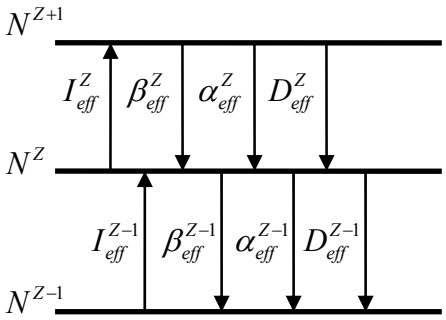

Figure 5.2: Simplified atomic level and rate diagram

The subscript *eff* refers to the effective rate for the total transition rate from one ion to the next. The effective rates can be calculated using one of three models. The first model is the radiative model. Under this assumption the excited states quickly decay radiatively to the ground state. This model is typically valid at very low densities. The next model is the collisional model, in this approximation all excited states are populated according to the Boltzmann equation. This is typically valid at very high densities. The most accurate form is solved assuming a steady-state solution with have to be solved taking both collisional excitations/de-excitation and radiative decay into account. The collisional-radiative model is valid for all densities, and is the form that I use for the effective rates.

V.C.1) Radiative Model

Under the radiative approximation, all excited states are quickly depopulated through radiative decay. As a result, the effective rates are very easy to calculate. The effective ionization rate is the sum of all rates from the ground state in the lower ion to all states in the upper ion.

$$I_{eff}^{Z} = \sum_{n} I_{0,n}^{Z}$$

The effective recombination rate is the sum of all rates from the ground state of the upper ion to the states of the lower ion.

$$\beta_{eff}^{Z} = \sum_{n} \beta_{0,n}^{Z}$$

$$\alpha_{eff}^{Z} = \sum_{n} \alpha_{0,n}^{Z}$$

$$D_{eff}^{Z} = \sum_{n} D_{0,n}^{Z}$$

The effective energy of the ion is the energy of the ground state.

$$E_{eff}^{Z} = E_{0,n}^{Z}$$

V.C.2) Collisional Model

Under the collisional approximation, all excited states are populated according to the Boltzmann equation.

$$N_{n}^{Z} = N_{0}^{Z} \frac{g_{n}}{g_{0}} e^{-\Delta E / kT}$$

Where g_n is the multiplicity of level n, and ΔE is the energy difference between states n and the ground state. As a result, the effective rates are relatively easy to calculate. The effective ionization rate is the sum of all rates from the n[th] state in the lower ion to all states in the upper ion weighted by the relative populations.

$$I_{eff}^{Z} = \frac{\sum_{n} N_n^Z \sum_{k} I_{n,k}^Z}{\sum_{n} N_n^Z}$$

The effective recombination rate is the sum of all rates from the n[th] state in the upper ion to all states of the lower ion.

$$\beta_{eff}^{Z} = \frac{\sum_{n} N_n^{Z+1} \sum_{k} \beta_{n,k}^Z}{\sum_{n} N_n^{Z+1}}$$

$$\alpha_{eff}^{Z} = \frac{\sum_{n} N_n^{Z+1} \sum_{k} \alpha_{n,k}^Z}{\sum_{n} N_n^{Z+1}}$$

$$D_{eff}^{Z} = \frac{\sum_{n} N_n^{Z+1} \sum_{k} D_{n,k}^Z}{\sum_{n} N_n^{Z+1}}$$

The effective energy of the ion is the weighted average of the excited states.

$$E_{eff}^{Z} = \frac{\sum_{n} N_n^{Z+1} E_n^Z}{\sum_{n} N_n^Z}$$

V.C.3) Collisional-Radiative Model

In the collisional-radiative model, the excited states must be solved for using the rate equation assuming a steady-state solution. Without radiation trapping, the rate equation for the n^{th} level is

$$\frac{dN_n^Z}{dt} = \left\{ \begin{array}{l} \sum_{q=0}^{\rho-1} \left[n_e E_{q,n}^Z N_q^Z - N_n^Z \left(A_{n,q}^Z + n_e d_{n,q}^Z \right) \right] \\ - \sum_{q=n+1}^{M_Z} \left[n_e E_{n,q}^Z N_n^Z - N_q^Z \left(A_{q,n}^Z + n_e d_{q,n}^Z \right) \right] \end{array} \right\}$$

With trapping this becomes

$$\frac{dN_{n,i}^Z}{dt} = \left\{ \begin{array}{l} \sum_{q=0}^{n-1} \left[n_e E_{q,n}^Z N_{n,i}^Z - N_{n,i}^Z \left(A_{n,q}^Z + n_e d_{n,q}^Z \right) \right] + \sum_{j=1}^{J} N_{n,J}^Z C_{ji}^{n0,Z} A_{n,0}^Z \\ - \sum_{q=n+1}^{M_Z} \left[n_e E_{n,q}^Z N_{n,i}^Z - N_{n,i}^Z \left(A_{q,n}^Z + n_e d_{q,n}^Z \right) \right] \end{array} \right\}$$

The solution of the system of equations is subject to the normalization condition:

$$N_{total}^Z = \sum_n N_n^Z$$

With the population of the individual levels, the calculation of the effective rates is the same as the collisional model weighted by the new level populations. Note that without trapping the populations are temperature and electron density dependent. With trapping, they are completely dependent on the plasma conditions. This complication can be very expensive and difficult to deal with, but is also the most accurate. In the high density limit of complete trapping for all lines, the collisional-radiative model approaches the collisional model.

V.D) Atomic rate calculations

The calculation of the actual atomic rates can be very difficult. There are a number of atomic codes which calculate the atomic rates for different species (ADAS[72], Cowan's[73], FAC[74,75], HULLAC[76], LANL[77], …). In addition to theoretical codes, some rates can be obtained through experiment measurements. While a complete description of the rates is not possible here, a simple description of the physics as well as any simple equations is given below. The majority of atomic data currently used in the model is from FAC. However, the model is also capable of using data from ADAS. At this time the use of other atomic data is usually restricted to checking the accuracy of the atomic data, but could be included in the future. The simple ionization rates from Lotz (described in the next section) are used in conjunction with the ADAS data sets. In most cases, only the principal cross sections (excitation, collisional ionization, photo-ionization, and auto-ionization) are calculated by the atomic code. The inverse processes are calculated through the principle of detailed balance (or microscopic reversibility).

---

[72] Atomic Data and Analysis Structure (ADAS) is an interconnected set of computer codes and data collections. See http://adas.phys.strath.ac.uk/ for more information.

[73] Code to calculate the atomic structures and spectra via the superposition-of-configuration method. Currently available at ftp://aphysics.lanl.gov/pub/cowan/readme.

[74] The Flexible Atomic Code (FAC) is an integrated software package to calculate various atomic radiative and collisional processes. Developed by M. F. Gu, currently available at http://kipac-tree.stanford.edu/fac/.

[75] M. F. Hu, "*Indirect X-Ray Line-Formation Processes in Iron L_shell Ions*", The Astophysical Journal, Vol. 582, pp. 1241-1250, 2003.

[76] Bar-Shalom, A.; Klapisch, M.; Oreg, J., "*HULLAC, an integrated computer package for atomic processes in plasmas*", JQSRT, vol. 71, p. 169-188.

[77] Los Alamos Atomic Physics Codes, See http://aphysics2.lanl.gov/tempweb/ for more information and interactive online version.

V.D.1) Collisional Ionization

Collisional ionization is the process in which a free electron collides with an ion and imparts some of its energy to the ion. This in turn releases another electron from the ion leaving it in an ionized state. A semi-empirical formula for the ionization rate coefficient was developed by Lotz[78]:

$$I = 1.42\times10^{-6} * \frac{aq}{Te^{3/2}}\left\{\frac{1}{\Delta E/Te}\int_{\Delta E/Te}^{\infty}\frac{e^{-x}}{x}dx - \frac{be^{c}}{\Delta E/Te+c}\int_{\Delta E/Te+c}^{\infty}\frac{e^{-x}}{x}dx\right\}$$

In this formula *Te* and ΔE are both in eV, *a*, *b*, and *c* are constants that depend on the specific ion. If the a, b, c coefficients are not known, default values of 4, 0, 0 are used. The variable *q* represents the equivalent number of electrons in the outer shell. The final rate coefficient (I) has units of cm^3/s. While easy to implement, Lotz is only accurate to about a factor of 2 and tends to be less accurate for highly excited states. More accurate ionization rates may be obtained using atomic codes based on one of several approximation techniques: the Born plane-wave approximation (BPWA), the distorted-wave approximation (DWA), the Coulomb-Born approximation (CB), K- and R-matrix approaches, and the close-coupling method (CC). Figure 5.3 illustrates a sample electron impact ionization cross section and rate coefficient for the Ni-like ion of silver obtained from FAC using the Coulomb-Born approximation. Note that the cross section is zero for electron energies below the ionization potential (~880 eV), while the rate coefficient drops rapidly for temperatures below ~200 eV.

---

[78] Wolfgang Lotz, "Electron-Impact Ionization Cross-Sections and Ionization Rate Coefficients for Atoms and Ions for Scandium to Zinc", Z. Physik, Vol. 220, pp 466-472, December 19, 1968.

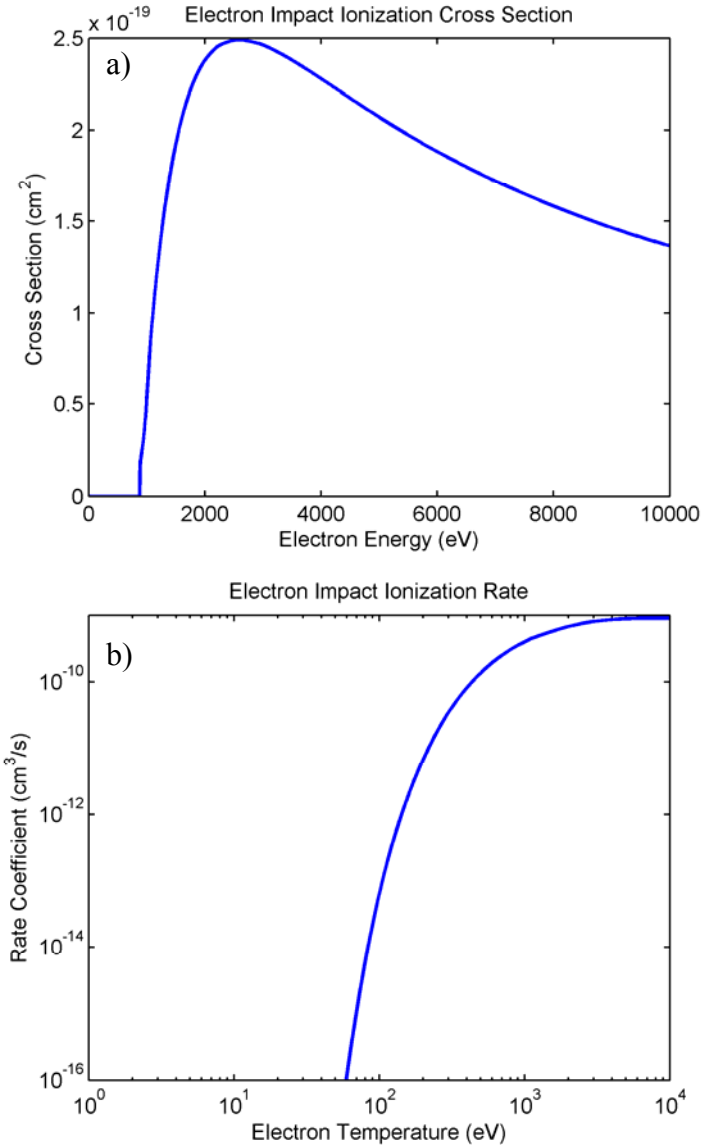

Figure 5.3: a) Plot of the total electron impact ionization cross section from the ground level ($3d^{10}\ ^1S_0$) of Ni-like silver to the Co-like silver ion. b) Plot of the total electron impact ionization rate coefficient from the ground level of Ni-like silver to the Co-like silver ion.

V.D.2) Electron Impact (3-Body) Recombination

Electron impact (3-body) recombination is the inverse process of collisional ionization. Two slow-moving electrons collide with the atom, resulting in the capture of one electron and the other electron carrying the excess energy. Because this is a 3-body

process involving two electrons the rate depends on n_e^2 instead of n_e. Regardless of how collisional ionization is calculated, 3-body recombination can be calculated using the principle of detailed balance. To apply detailed balance, the relationship between two levels in thermal equilibrium is established according to the Saha equation[79,80]

$$\frac{n_e N_q^{Z+1}}{N_n^Z} = 2\frac{g_q^{Z+1}}{g_n^Z}\left(\frac{2\pi m_e k_B T_e}{h^2}\right)^{3/2} e^{-\Delta E_{n,q}^Z / k_B T_e}$$

Next, the rate equation can be written assuming steady state

$$\frac{dN_n^Z}{dt} = -n_e I_{n,q}^Z N_n^Z + n_e^2 \beta_{q,n}^Z N_q^{Z+1} = 0$$

Solving for the recombination rate coefficient we have

$$\beta_{q,n}^Z = I_{n,q}^Z \frac{N_n^Z}{n_e N_q^{Z+1}}$$

$$\beta_{q,n}^Z = I_{n,q}^Z \frac{g_n^Z}{2g_q^{Z+1}}\left(\frac{2\pi m_e k_B T_e}{h^2}\right)^{-3/2} e^{\Delta E_{n,q}^Z / k_B T_e}$$

Note that while the inverse rate coefficient is calculated assuming steady state, its value is based on the intrinsic properties of the ion. As a result, the recombination rate coefficient is valid outside of equilibrium. The units of the rate coefficient are cm^6/s. Figure 5.4 illustrates a sample 3-body recombination rate coefficient for the Co-like ion of silver obtained from the previous ionization rate in figure 5.3. Note that unlike ionization, it increases as the electron temperature approaches zero.

---

[79] Saha, M.N., "*Ionization in the Solar Chromosphere*", Philos. Mag., Vol. 40, No. 238, 1920, pp. 472-489.

[80] Saha, M.N., "*On a Physical Theory of Stellar Spectra*", Proc. R. Soc. London, Ser. A, Vol. 99, 1921, pp. 135-153.

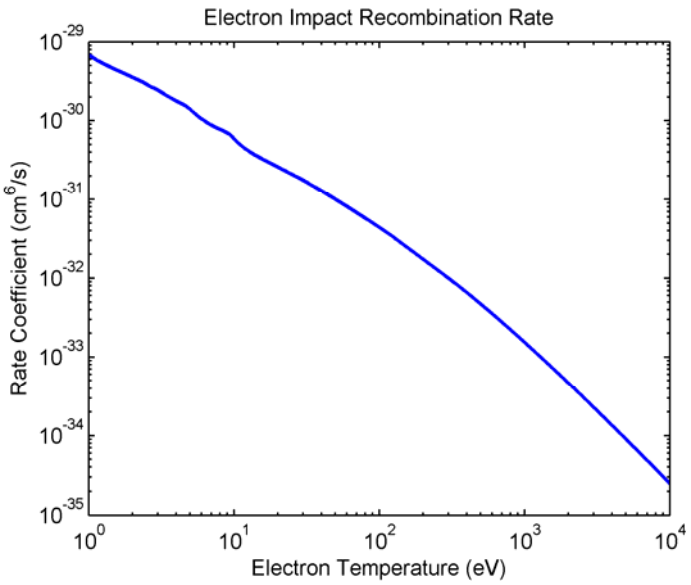

Figure 5.4: Plot of the total electron impact recombination (3-body) rate coefficient from the ground level of Co-like silver ($3d^9\ ^2D_{2.5}$) to the Ni-like silver ion.

V.D.3) Radiative Recombination

Radiative recombination is an important recombination and cooling mechanism of the plasma. It is a single step process that emits a photon. In radiative recombination, a free electron is captured by an ion, which emits a photon that conserves energy and momentum. Radiative recombination is the inverse process of photoionization. As a result, it can be calculated through the principle of detailed balance. The relationship between the radiative recombination and photoionization cross sections can be described by the Milne formula[81]

$$g_{Z+1}\sigma_{rr} = \frac{(\hbar\omega)^2}{2m_e c^2 E} g_Z \sigma_\nu$$

[81] E. A. Milne, Philos. Mag., Vol. 47, 1924, p. 209.

Figure 5.5 illustrates a sample radiative recombination cross section and rate coefficient for the Co-like ion of silver obtained from FAC using a distorted-wave approximation. Note that the radiative recombination favors lower energy due to its closer match to the resonance of the transition that occurs at zero energy.

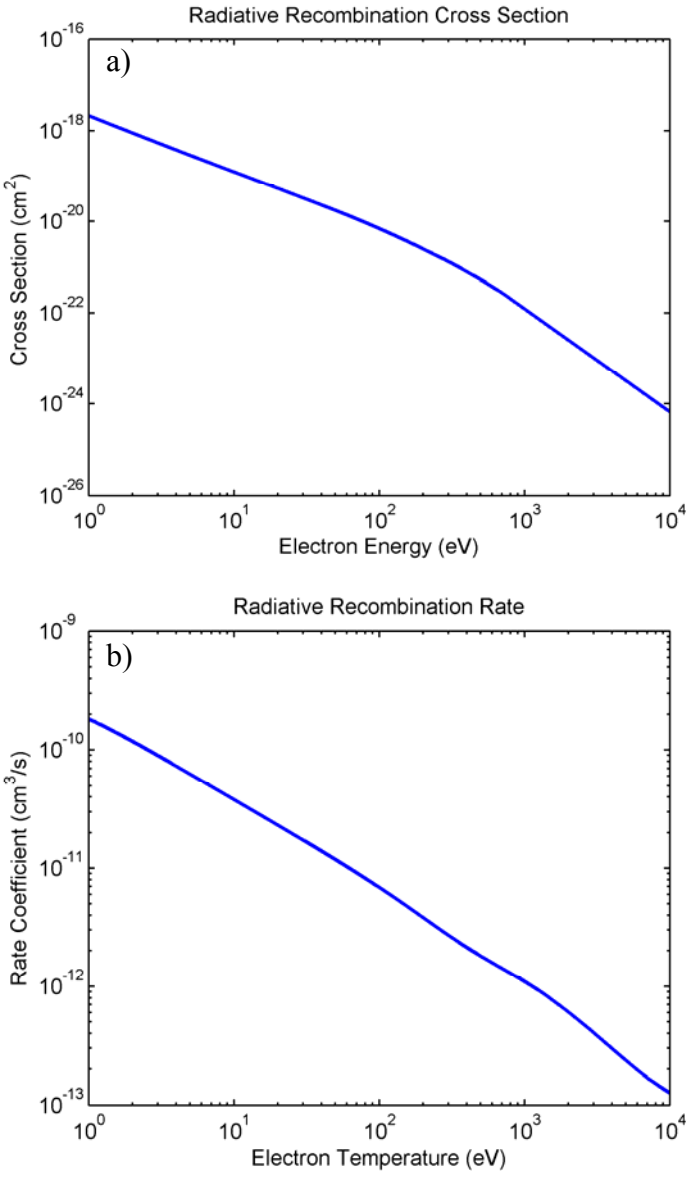

Figure 5.5: a) Plot of the total radiative recombination cross section from the ground level ($3d^9\ ^2D_{2.5}$) of Co-like silver to the Ni-like silver ion. b) Plot of the total radiative recombination rate coefficient from the ground level of Co-like silver to the Ni-like silver ion.

V.D.4) Dielectronic recombination

Dielectronic recombination can be an important recombination process for ions. It consists of a two-step process. In the first step, an ion captures an electron while exciting a second electron to an excited state. This allows the ion to both capture the free electron and conserve energy. This process is the inverse of auto-ionization. If we let A^a represent the autoionization rate and A^r represent the radiative decay rate, we can relate the first step of dielectronic recombination to the autoionization rate with the Saha equation

$$\alpha_{DR}(n \to i) = \frac{\hbar^3}{\left(2\pi m_e k_B T\right)^{3/2}} \frac{g_i}{2g_n} A^a(i \to n) e^{\left(\frac{-E_{i,n}}{k_B T}\right)}$$

where i is the index of the autoionizing state in the lower ion, and n is the index of the recombining state in the upper ion.

In the second step, the highly excited state decays radiatively into a stable state below the ionization limit. The probability of decaying to the lower, stable state is given by the radiative branching ratio B(i):

$$B(i) = \frac{\sum_k A^r(i \to k) + \sum_{k'} A^r(i \to k') B(k')}{\sum_k A^r(i \to k) + \sum_{k'} A^r(i \to k') B(k') + \sum_a A^a(i \to a)}$$

Note that in this equation *k* represents states below the ionization potential, *k'* represents state above the ionization potential, and *a* represents the autoionized states in the next ion. With the branching ratio, we can calculate the total dielectronic recombination rate from state n

$$\alpha_{DR}(n) = \frac{\hbar^3}{\left(2\pi m_e k_B T\right)^{3/2}} \sum_i \frac{g_i}{2g_n} A^a(i \to n) B(i) e^{\left(\frac{-E_{i,n}}{k_B T}\right)}$$

The total dielectronic process tends to leave the ion in an excited state near the ionization limit. Dielectronic recombination requires a bound electron to form the doubly-excited state and therefore cannot occur with a bare ion. Note that a photon is emitted to stabilize the ion, so dielectronic recombination can be a cooling mechanism for the plasma.

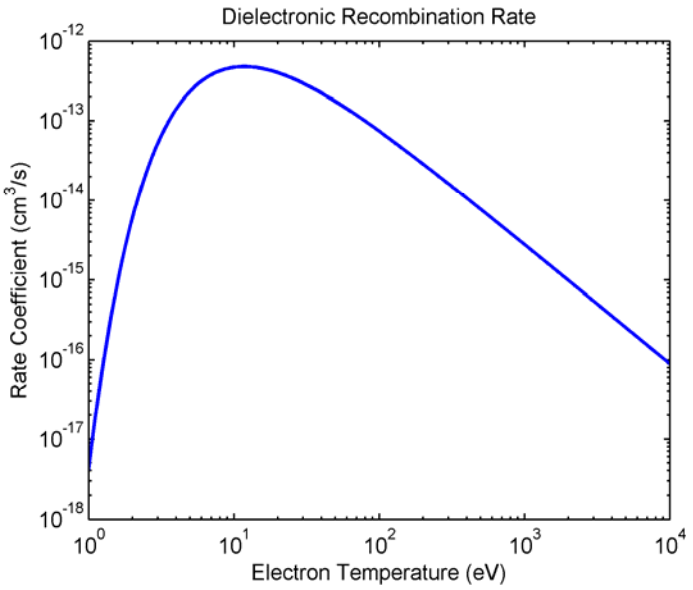

Figure 5.6: Plot of the total dielectronic recombination rate coefficient from the ground level of Co-like silver ($3d^9\ ^2D_{2.5}$) to the Ni-like silver ion.

Figure 5.6 illustrates a sample dielectronic recombination rate coefficient for the Co-like ion of silver obtained from FAC. Note that unlike the other recombination processes, the rate coefficient approaches zero as the electron temperature approaches zero. This is due to the fact that dielectronic recombination requires an excitation to the doubly excited state in the lower ion. This state lies above the ionization potential and therefore requires some kinetic energy.

V.D.5) Collisional Excitation

Collisional excitation (electron-impact excitation) is the process where a free electron collides with an ion, imparting some of its energy to the ion leaving the ion in an excited state. Collisional excitation can occur between any two states in an ion, but is most probable for monopole transitions (transitions in which the angular momentum of the ion does not change). Normally collisional excitation cross sections are calculated using a plane-wave or distorted wave calculation with an atomic code. For a dipole allowed transition in the high energy limit, the cross section can be described by the Bethe formula[82,83]

$$\sigma_{pn} = \frac{2\pi a_0^2 Ry}{E_e}\left[\frac{2Ry}{E_{pn}} f_{pn} \ln\left(\frac{E_e}{2Ry}\right) + B_{pn}\right],$$

In this formula Ry is the Rydberg energy, a_0 is the Bohr radius, E_{pn} is the transition energy, f_{pn} is the absorption oscillator strength, E_e is the electron energy, and B_{pn} is the high energy limit. Figure 5.7 illustrates a sample electron impact excitation cross section and rate coefficient for a monopoles excitation from the $3d^{10}\ {}^1S_0$ level to the $3d^9\ {}^1S_0$ level in the Ni-like ion of silver obtained from FAC. Note that the cross section is zero for electron energies below the excitation energy (~500 eV), while the rate coefficient drops rapidly for temperatures below ~100 eV.

---

[82] Mitio Inokuti, "*Ineleastic Collisions of Fast Charged Particles with Atoms and Molecules* ", Review of Modern Physics, Vol. 43, No. 3, 1971, pp 297-347.

[83] L. Vriens and A. H. M. Meets, "*Cross-section and rate formulas for electron-impact ionization, excitation, deexcitation, and total depopulation of excited atoms*", Physical Review A, Vol. 22, No. 3, 1980, pp 940-951.

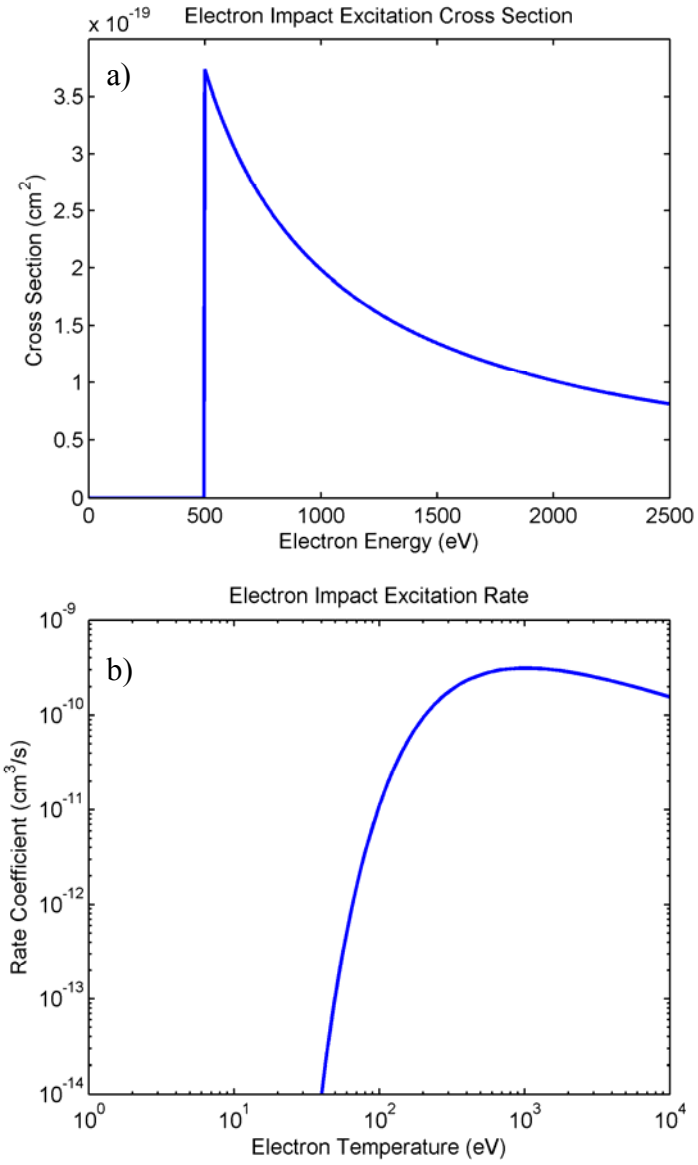

Figure 5.7: a) Plot of the total electron impact excitation cross section from the ground level ($3d^{10}\ ^1S_0$) to the laser upper level ($3d^9\ 4d\ ^1S_0$) in the Ni-like silver ion. b) Plot of the total electron impact excitation rate coefficient from the ground level to the laser upper level in the Ni-like silver ion.

V.D.6) Collisional De-Excitation

Collisional de-excitation is the inverse processes of collisional excitation. In this process, a free electron collides with an ion in an excited state, gains some of the potential energy of the ion, and leaves the ion in a lower state. The de-excitation rate can be easily

calculated using the principle of detailed balance. In the collisional limit, two states within the same ion are populated according to Boltzman's equation

$$N_n = N_q \frac{g_n}{g_q} e^{-\Delta E / kT}$$

Again, the rate equation can be written assuming steady state

$$\frac{dN_n}{dt} = -n_e d_{n,q} N_n + n_e E_{q,n} N_q = 0$$

Solving for the de-excitation rate coefficient we have

$$d_{n,q} = E_{q,n} \frac{g_q}{g_n} e^{\Delta E / kT}$$

Figure 5.8 illustrates the electron impact de-excitation rate coefficient for the same transition figure 5.7.

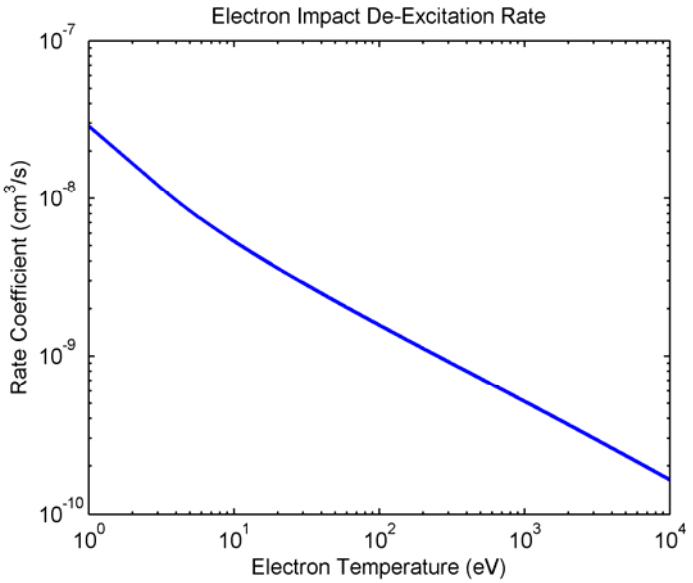

Figure 5.8: Plot of the total electron impact de-excitation rate coefficient from the laser upper level ($3d^9$ $4d$ $^1S_0$) to the ground level ($3d^{10}$ $^1S_0$) in the Ni-like silver ion.

V.D.7) Radiative Decay

Radiative decay (spontaneous emission) is an important process, accounting for all of the line radiation and is one of the most important cooling mechanisms in many plasmas. An ion in an excited state can spontaneously decay to a lower state emitting a photon with the rate given by Einstein's A coefficient. A more complete treatment of this process can be found in many quantum mechanics textbooks. Frequently many atomic codes will return the weighted oscillator strength (*gf*). In this case the radiative decay rate (*A*) is related to the weighted oscillator strength by

$$A = \frac{2\alpha^3 \omega^2 gf}{g_u}$$

where α is the fine structure constant and ω is the transition energy. If we substitute for the constants (hν in eV) we get:

$$A = 4.34 \times 10^7 (h\nu)^2 \frac{gf}{g_u} \quad (\mathrm{s}^{-1})$$

V.E) Solution of rate matrix

The numerical form for the atomic model is more complex. Unlike the previous equations it may not be tridiagonal. There are two cases of interest. The first case is the simplified rate equation with ion populations only. This form will be tridiagonal. The more general case, when both the ions and excided states are solved in the full transient form, will not be tridiagonal. The simplified rate equation for the atomic model for the ion populations from section V.A is:

$$\frac{dN^Z}{dt} = \begin{Bmatrix} n_e I_{eff}^{Z-1} N^{Z-1} - n_e N^Z \left(\alpha_{eff}^{Z-1} + D_{eff}^{Z-1} + n_e \beta_{eff}^{Z-1}\right) \\ - n_e I_{eff}^{Z} N^{Z} + n_e N^{Z+1} \left(\alpha_{eff}^{Z} + D_{eff}^{Z} + n_e \beta_{eff}^{Z}\right) \end{Bmatrix}$$

In the implicit form:

$$\frac{N_{n+1}^Z - N_n^Z}{\Delta t} = \begin{Bmatrix} \frac{1}{2} N_e I_{eff}^{Z-1} \left(N_{n+1}^{Z-1} + N_n^{Z-1}\right) \\ - \frac{1}{2} N_e \left(\alpha_{eff}^{Z-1} + D_{eff}^{Z-1} + N_e \beta_{eff}^{Z-1}\right)\left(N_{n+1}^{Z} + N_n^{Z}\right) \\ - \frac{1}{2} N_e I_{eff}^{Z} \left(N_{n+1}^{Z} + N_n^{Z}\right) \\ + \frac{1}{2} N_e \left(\alpha_{eff}^{Z} + D_{eff}^{Z} + N_e \beta_{eff}^{Z}\right)\left(N_{n+1}^{Z+1} + N_n^{Z+1}\right) \end{Bmatrix}$$

Simplifying:

$$\begin{Bmatrix} - N_e I_{eff}^{Z-1} N_{n+1}^{Z-1} \\ + \left(\frac{2}{\Delta t} + N_e \begin{pmatrix} I_{eff}^{Z} + \alpha_{eff}^{Z-1} \\ + D_{eff}^{Z-1} + N_e \beta_{eff}^{Z-1} \end{pmatrix} \right) N_{n+1}^{Z} \\ - N_e \left(\alpha_{eff}^{Z} + D_{eff}^{Z} + N_e \beta_{eff}^{Z}\right) N_{n+1}^{Z+1} \end{Bmatrix} = \begin{Bmatrix} N_e I_{eff}^{Z-1} N_{n}^{Z-1} \\ + \left(\frac{2}{\Delta t} - N_e \begin{pmatrix} I_{eff}^{Z} + \alpha_{eff}^{Z-1} \\ + D_{eff}^{Z-1} + N_e \beta_{eff}^{Z-1} \end{pmatrix} \right) N_{n}^{Z} \\ + N_e \left(\alpha_{eff}^{Z} + D_{eff}^{Z} + N_e \beta_{eff}^{Z}\right) N_{n}^{Z+1} \end{Bmatrix}$$

Let $L^Z = -N_e I_{eff}^{Z-1}$

$$D^Z = \left(\frac{2}{\Delta t} + N_e \begin{pmatrix} I_{eff}^{Z} + \alpha_{eff}^{Z-1} \\ + D_{eff}^{Z-1} + N_e \beta_{eff}^{Z-1} \end{pmatrix} \right)$$

$$U^Z = -N_e \left(\alpha_{eff}^{Z} + D_{eff}^{Z} + N_e \beta_{eff}^{Z}\right)$$

$$Y^Z = \begin{Bmatrix} N_e I_{eff}^{Z-1} N_{n}^{Z-1} \\ + \left(\frac{2}{\Delta t} - N_e \begin{pmatrix} I_{eff}^{Z} + \alpha_{eff}^{Z-1} \\ + D_{eff}^{Z-1} + N_e \beta_{eff}^{Z-1} \end{pmatrix} \right) N_{n}^{Z} \\ + N_e \left(\alpha_{eff}^{Z} + D_{eff}^{Z} + N_e \beta_{eff}^{Z}\right) N_{n}^{Z+1} \end{Bmatrix}$$

Again, we have the tridiagonal form:

$$L^Z N_{n+1}^{Z-1} + D^Z N_{n+1}^{Z} + U^Z N_{n+1}^{Z+1} = Y^Z$$

Note that in this form there is one tridiagonal system of equations for each zone. Also, any radiation coupling between the zones is neglected, as that would affect the forms. As will be shown below, the inclusion of excited states will no longer produce a tridiagonal form.

The full transient solution, in which both the ion and excited state populations are solved for, is significantly more complicated. The rate equation from section V.A is

$$\frac{dN_{\rho,i}^{Z}}{dt}=\left\{\begin{array}{l}\sum_{q=0}^{M_{Z-1}}\left[n_e I_{q,\rho}^{Z-1}N_{q,i}^{Z-1}-n_e N_{\rho,i}^{Z}\left(\alpha_{\rho,q}^{Z-1}+D_{\rho,q}^{Z-1}+n_e\beta_{\rho,q}^{Z-1}\right)\right]\\ -\sum_{q=0}^{M_{Z+1}}\left[n_e I_{\rho,q}^{Z}N_{\rho,i}^{Z}-n_e N_{q,i}^{Z+1}\left(\alpha_{q,\rho}^{Z}+D_{q,\rho}^{Z}+n_e\beta_{q,\rho}^{Z}\right)\right]\\ +\sum_{q=0}^{\rho-1}\left[n_e E_{q,\rho}^{Z}N_{q,i}^{Z}-N_{\rho,i}^{Z}\left(A_{\rho,q}^{Z}+n_e d_{\rho,q}^{Z}\right)+\sum_{j=1}^{J}N_{\rho,j}^{Z}C_{ji}^{\rho q,Z}A_{\rho,q}^{Z}\right]\\ -\sum_{q=\rho+1}^{M_Z}\left[n_e E_{\rho,q}^{Z}N_{\rho,i}^{Z}-N_{q,i}^{Z}\left(A_{q,\rho}^{Z}+n_e d_{q,\rho}^{Z}\right)+\sum_{j=1}^{J}N_{q,j}^{Z}C_{ji}^{q\rho,Z}A_{q,\rho}^{Z}\right]\end{array}\right\}$$

In implicit form:

$$\frac{N_{\rho,i}^{Z+1,n+1}-N_{\rho,i}^{Z,n}}{\Delta t}=\left\{\begin{array}{l}\sum_{q=0}^{M_{Z-1}}\left[n_e I_{q,\rho}^{Z-1}N_{q,i}^{Z-1,n+1/2}-n_e N_{\rho,i}^{Z,n+1/2}\left(\alpha_{\rho,q}^{Z-1}+D_{\rho,q}^{Z-1}+n_e\beta_{\rho,q}^{Z-1}\right)\right]\\ -\sum_{q=0}^{M_{Z+1}}\left[n_e I_{\rho,q}^{Z}N_{\rho,i}^{Z,n+1/2}-n_e N_{q,i}^{Z+1,n+1/2}\left(\alpha_{q,\rho}^{Z}+D_{q,\rho}^{Z}+n_e\beta_{q,\rho}^{Z}\right)\right]\\ +\sum_{q=0}^{\rho-1}\left[n_e E_{q,\rho}^{Z}N_{q,i}^{Z,n+1/2}-N_{\rho,i}^{Z,n+1/2}\left(A_{\rho,q}^{Z}+n_e d_{\rho,q}^{Z}\right)+\sum_{j=1}^{J}N_{\rho,j}^{Z,n+1/2}C_{ji}^{\rho q,Z}A_{\rho,q}^{Z}\right]\\ -\sum_{q=\rho+1}^{M_Z}\left[n_e E_{\rho,q}^{Z}N_{\rho,i}^{Z,n+1/2}-N_{q,i}^{Z,n+1/2}\left(A_{q,\rho}^{Z}+n_e d_{q,\rho}^{Z}\right)+\sum_{j=1}^{J}N_{q,j}^{Z,n+1/2}C_{ji}^{q\rho,Z}A_{q,\rho}^{Z}\right]\end{array}\right\}$$

Simplifying:

$$
\left\{
\begin{aligned}
&-\sum_{q=0}^{M_{Z-1}} n_e I_{q,\rho}^{Z-1} N_{q,i}^{Z-1,n+1} \\
&-\sum_{q=0}^{\rho-1}\left[n_e E_{q,\rho}^{Z} N_{q,i}^{Z,n+1}\right] \\
&+\left[\begin{aligned}
&\frac{2}{\Delta t} \\
&+\sum_{q=0}^{M_{Z-1}} n_e\left(\alpha_{\rho,q}^{Z-1}+D_{\rho,q}^{Z-1}+n_e\beta_{\rho,q}^{Z-1}\right) \\
&+\sum_{q=0}^{\rho-1}\left(A_{\rho,q}^{Z}+n_e d_{\rho,q}^{Z}\right) \\
&+\sum_{q=\rho+1}^{M_Z} n_e E_{\rho,q}^{Z} \\
&+\sum_{q=0}^{M_{Z+1}} n_e I_{\rho,q}^{Z}
\end{aligned}\right] N_{\rho,i}^{Z,n+1} \\
&-\sum_{q=\rho+1}^{M_Z}\left(A_{q,\rho}^{Z}+n_e d_{q,\rho}^{Z}\right) N_{q,i}^{Z,n+1} \\
&-\sum_{q=0}^{M_{Z+1}} n_e\left(\alpha_{q,\rho}^{Z}+D_{q,\rho}^{Z}+n_e\beta_{q,\rho}^{Z}\right) N_{q,i}^{Z+1,n+1} \\
&-\sum_{j=1}^{J}\left[\begin{aligned}
&\sum_{q=0}^{\rho-1} N_{\rho,j}^{Z,n+1} C_{ji}^{\rho q,Z} A_{\rho,q}^{Z} \\
&-\sum_{q=\rho+1}^{M_Z} N_{q,j}^{Z,n+1} C_{ji}^{q\rho,Z} A_{q,\rho}^{Z}
\end{aligned}\right]
\end{aligned}
\right\}
=
\left\{
\begin{aligned}
&\sum_{q=0}^{M_{Z-1}} n_e I_{q,\rho}^{Z-1} N_{q,i}^{Z-1,n} \\
&+\sum_{q=0}^{\rho-1} n_e E_{q,\rho}^{Z} N_{q,i}^{Z,n} \\
&+\left[\begin{aligned}
&\frac{2}{\Delta t} \\
&-\sum_{q=0}^{M_{Z-1}} n_e\left(\alpha_{\rho,q}^{Z-1}+D_{\rho,q}^{Z-1}+n_e\beta_{\rho,q}^{Z-1}\right) \\
&-\sum_{q=0}^{\rho-1}\left(A_{\rho,q}^{Z}+n_e d_{\rho,q}^{Z}\right) \\
&-\sum_{q=\rho+1}^{M_Z} n_e E_{\rho,q}^{Z} \\
&-\sum_{q=0}^{M_{Z+1}} n_e I_{\rho,q}^{Z}
\end{aligned}\right] N_{\rho,i}^{Z,n} \\
&+\sum_{q=\rho+1}^{M_Z}\left(A_{q,\rho}^{Z}+n_e d_{q,\rho}^{Z}\right) N_{q,i}^{Z,n} \\
&+\sum_{q=0}^{M_{Z+1}} n_e\left(\alpha_{q,\rho}^{Z}+D_{q,\rho}^{Z}+n_e\beta_{q,\rho}^{Z}\right) N_{q,i}^{Z+1,n} \\
&+\sum_{j=1}^{J}\left[\begin{aligned}
&\sum_{q=0}^{\rho-1} N_{\rho,j}^{Z,n} C_{ji}^{\rho q,Z} A_{\rho,q}^{Z} \\
&-\sum_{q=\rho+1}^{M_Z} N_{q,j}^{Z,n} C_{ji}^{q\rho,Z} A_{q,\rho}^{Z}
\end{aligned}\right]
\end{aligned}
\right\}
$$

Let $T_{\rho,i}^{Z}=\sum_{q=0}^{M_{Z-1}} n_e\left(\alpha_{\rho,q}^{Z-1}+D_{\rho,q}^{Z-1}+n_e\beta_{\rho,q}^{Z-1}\right)+\sum_{q=0}^{\rho-1}\left(A_{\rho,q}^{Z}+n_e d_{\rho,q}^{Z}\right)+\sum_{q=\rho+1}^{M_Z} n_e E_{\rho,q}^{Z}+\sum_{q=0}^{M_{Z+1}} n_e I_{\rho,q}^{Z}$

$$
\left\{\begin{array}{l}
-\sum_{q=0}^{M_{Z-1}} n_e I_{q,\rho}^{Z-1} N_{q,i}^{Z-1,n+1} \\
-\sum_{q=0}^{\rho-1}\left[n_e E_{q,\rho}^{Z} N_{q,i}^{Z,n+1}\right] \\
+\left[\frac{2}{\Delta t}+T_{\rho,i}^{Z}\right] N_{\rho,i}^{Z,n+1} \\
-\sum_{q=\rho+1}^{M_Z}\left(A_{q,\rho}^{Z}+n_e d_{q,\rho}^{Z}\right) N_{q,i}^{Z,n+1} \\
-\sum_{q=0}^{M_{Z+1}} n_e\left(\alpha_{q,\rho}^{Z}+D_{q,\rho}^{Z}+n_e\beta_{q,\rho}^{Z}\right) N_{q,i}^{Z+1,n+1} \\
-\sum_{j=1}^{J}\left[\begin{array}{l}\sum_{q=0}^{\rho-1} N_{\rho,j}^{Z,n+1} C_{ji}^{\rho q,Z} A_{\rho,q}^{Z} \\ -\sum_{q=\rho+1}^{M_Z} N_{q,j}^{Z,n+1} C_{ji}^{q\rho,Z} A_{q,\rho}^{Z}\end{array}\right]
\end{array}\right\}=\left\{\begin{array}{l}
\sum_{q=0}^{M_{Z-1}} n_e I_{q,\rho}^{Z-1} N_{q,i}^{Z-1,n} \\
+\sum_{q=0}^{\rho-1} n_e E_{q,\rho}^{Z} N_{q,i}^{Z,n} \\
+\left[\frac{2}{\Delta t}-T_{\rho,i}^{Z}\right] N_{\rho,i}^{Z,n} \\
+\sum_{q=\rho+1}^{M_Z}\left(A_{q,\rho}^{Z}+n_e d_{q,\rho}^{Z}\right) N_{q,i}^{Z,n} \\
+\sum_{q=0}^{M_{Z+1}} n_e\left(\alpha_{q,\rho}^{Z}+D_{q,\rho}^{Z}+n_e\beta_{q,\rho}^{Z}\right) N_{q,i}^{Z+1,n} \\
+\sum_{j=1}^{J}\left[\begin{array}{l}\sum_{q=0}^{\rho-1} N_{\rho,j}^{Z,n} C_{ji}^{\rho q,Z} A_{\rho,q}^{Z} \\ -\sum_{q=\rho+1}^{M_Z} N_{q,j}^{Z,n} C_{ji}^{q\rho,Z} A_{q,\rho}^{Z}\end{array}\right]
\end{array}\right\}
$$

Note that because of trapping all the zones are coupled. This creates a computational problem. If J is the total number of zones and M is the total number of states, one needs to solve a J*M x J*M matrix. If the zones are not coupled one only needs to solve J MxM matrices. Since the matrices are not tridiagonal, the computations required scale as $O(n^3)$ (see APPENDIX C.2), where n is the number of equations. This causes the time required to increase by a factor of $\frac{1}{3}M^2$ due to the excited states, and a factor of J^2 due to coupling. This does not include the time required to calculate the coupling coefficients. To reduce the computational problem, we assume that $N_{q,j}^{Z,n+1} \approx N_{q,j}^{Z,n}$ for the purpose of calculating the coupling between zones.

We can then let $\Omega_{\rho,i}^{\rho,Z} = 2\sum_{j=1}^{J}\left[\sum_{q=0}^{\rho-1} N_{\rho,j}^{Z,n} C_{ji}^{\rho q,Z} A_{\rho,q}^{Z} - \sum_{q=\rho+1}^{M_Z} N_{q,j}^{Z,n} C_{ji}^{q\rho,Z} A_{q,\rho}^{Z}\right]$

$$\left\{\begin{array}{l} -\sum_{q=0}^{M_{Z-1}} n_e I_{q,\rho}^{Z-1} N_{q,i}^{Z-1,n+1} \\ -\sum_{q=0}^{\rho-1}\left[n_e E_{q,\rho}^{Z} N_{q,i}^{Z,n+1}\right] \\ +\left[\frac{2}{\Delta t}+T_{\rho,i}^{Z}\right] N_{\rho,i}^{Z,n+1} \\ -\sum_{q=\rho+1}^{M_Z}\left(A_{q,\rho}^{Z}+n_e d_{q,\rho}^{Z}\right) N_{q,i}^{Z,n+1} \\ -\sum_{q=0}^{M_{Z+1}} n_e\left(\alpha_{q,\rho}^{Z}+D_{q,\rho}^{Z}+n_e\beta_{q,\rho}^{Z}\right) N_{q,i}^{Z+1,n+1} \end{array}\right\} = \left\{\begin{array}{l} \sum_{q=0}^{M_{Z-1}} n_e I_{q,\rho}^{Z-1} N_{q,i}^{Z-1,n} \\ +\sum_{q=0}^{\rho-1} n_e E_{q,\rho}^{Z} N_{q,i}^{Z,n} \\ +\left[\frac{2}{\Delta t}-T_{\rho,i}^{Z}\right] N_{\rho,i}^{Z,n} \\ +\sum_{q=\rho+1}^{M_Z}\left(A_{q,\rho}^{Z}+n_e d_{q,\rho}^{Z}\right) N_{q,i}^{Z,n} \\ +\sum_{q=0}^{M_{Z+1}} n_e\left(\alpha_{q,\rho}^{Z}+D_{q,\rho}^{Z}+n_e\beta_{q,\rho}^{Z}\right) N_{q,i}^{Z+1,n} \end{array}\right\} + \Omega_{\rho,i}^{Z}$$

Note that even in this case, the population of one level is linked to many other levels. As a result, the system of linear equations cannot be written in a tridiagonal matrix. In this case, we can use Gaussian Elimination with back substitution and partial pivoting to solve the systems of equations.

V.F) Pressure ionization

Pressure ionization is a complex but important phenomena at high densities. At high densities the ions are very close to each other, violating the usual assumption of a single ion used in the atomic codes. This effect causes the central potential of an ion to change, freeing previously bound states. As a result the ionization potential is effectively reduced, which in turn affects the rates. Specifically, it affects the collisional ionization rate and the 3-body recombination rates. From Zaghloul[84] the reduction in the ionization potential for the z^{th} ion is

[84] Mofreh R Zaghloul, "*Ionization Equilibrium and Partition Functions of High-Temperature Weakly Non-Ideal Flibe Gas*", Journal of Physics D: Applied Physics, Vol. 36, 2003, pp 2249-2254.

$$\Delta I_z = \frac{(1+z)e^2}{\lambda_D + \Lambda_B / 8}$$

Where λ_D is the Debye length, and Λ_B is the DeBroglie Wavelength.

$$\lambda_D = \sqrt{\frac{k_B T}{4\pi e^2 Ne}}$$

$$\frac{\Lambda_B}{8} = \frac{h}{8\sqrt{2\pi m_e k_B T}}$$

The effect of ionization potential lowering on the collisional ionization rate can be observed by examining the expression given by Lotz. The dominant term involving the ionization potential IP is

$$\frac{1}{IP/Te}\int_{IP/Te}^{\infty}\frac{e^{-x}}{x}dx$$

The new ionization potential can be written as $\varepsilon \equiv IP - \Delta I$.

If we let $I' = IP/Te$ and $y = \Delta I / IP$

$$\frac{1}{\varepsilon/Te}\int_{\varepsilon/Te}^{\infty}\frac{e^{-x}}{x}dx = \frac{1}{I'(1-y)}\int_{I'(1-y)}^{\infty}\frac{e^{-x}}{x}dx$$

If we divide by the uncorrected term we get the correction factor F

$$F = \frac{1}{1-y}\frac{\int_{I'(1-y)}^{\infty}\frac{e^{-x}}{x}dx}{\int_{I'}^{\infty}\frac{e^{-x}}{x}dx}$$

This factor *F* should multiply the ionization rate to account for pressure ionization

The effect of pressure ionization on the 3-body recombination rate is twofold. First, the correction factor F to the ionization rate is also present because of the relationship established using detailed balance. Second, the correction to the ionization potential affects the Saha equation, and therefore the relation between the ionization and recombination rates. The relation between the recombination rate and ionization rate scales as $\exp(IP/kT_e)$, so the correction to this relation is $\exp(-\Delta I/kT_e)$. The final result is that the 3-body recombination rate needs to be corrected by the factor

$$F * \exp(-\Delta I/kT_e)$$

Radiative and dielectronic recombination are also affected by pressure ionization, but the effect can be more difficult to determine. Because pressure ionization is only important at high densities, the primary recombination method is 3-body due to its n_e^2 dependence. As a result, the effect on radiative and dielectronic recombination can be neglected. For more information on high pressure effects see Griem[85,86].

So far, the discussion on pressure ionization has focused on a single transition. However, the effective rates are obviously affected because the individual rates from each level are affected. Additionally, states that were previously below the ionization level may now reside above the ionization level. As a result they should no longer be included in the

---

[85] Hans R. Griem, *Principles of Plasma Spectroscopy*, Cambridge University Press, United Kingdom, 1997.

[86] Hans R. Griem, "*High-Density Corrections in Plasma Spectroscopy*", Physical Review, Vol. 128, No. 3, 1962, pp. 997-1003.

effective rates. To ease the use of a data lookup table for the effective rates two approximations may be made.

Approximation 1: $F_n = F_0$

In this approximation, the correction factor F is assumed to be the same for the excited states as it is for the ground state. Its accuracy becomes questionable for high-lying states, but greatly simplifies the problem. In addition, those states are less likely to be populated and therefore contribute less to the ionization. Also, the error introduced is equal in both the ionization and recombination so the equilibrium point is nearly maintained. As a result, the time constant may be a little off but the steady-state solution is still accurate.

$$I'^{Z}_{eff} = F_0 \sum_{n=0}^{n<X^Z} N_n^Z I_n^Z / N^Z$$

$$\beta'^{Z+1}_{eff} = F_0 e^{-\Delta X / kT} \sum_{n=0}^{n<X^Z} \beta_n^{Z+1}$$

Approximation 2: Populations do not change, and previously bound states do not affect the ionization rate.

In this approximation, the removal of states above the reduced ionization potential does not affect the populations of the other states. This is likely to be true because of the reduced probability of occupation of the highly excited states. This allows us to use the collisional-radiative tables with no modifications.

$$I'^{Z}_{eff} = F_0 I^Z_{eff}$$

$$\beta'^{Z+1}_{eff} = F_0 e^{-\Delta X / kT} \beta^{Z+1}_{eff}$$

V.G) Radiation

One important cooling mechanism in most plasmas is radiation. To properly calculate the radiative losses it is necessary to have an accurate radiation model. The treatment of the radiation depends on its type. There are three types of radiation: bound-bound, free-bound, and free-free radiation, referring to the electrons initial and final states respectively. Each of these radiation types is created by a different physical mechanism and interacts with the plasma in a different manner.

Bound-bound radiation:

Bound-bound radiation consists of line radiation within the plasma. It occurs when an excited state spontaneously decays to a lower state. There are many lines emitting within a plasma, each of which has a different central frequency and line width (see section V.H). Line radiation is responsible for the distinctive spectra and is often the dominant radiation component. It is also the most difficult to treat. Because the radiation in a given line is emitted in a narrow bandwidth, its intensity can be very large. This will cause absorption and re-emission along the same line, but in a different part of the plasma. This creates an energy transport effect that can re-distribute the energy within the plasma. As a result, radiation trapping and transport effects have to be accounted for (see section V.I).

Free-bound radiation:

Compared to bound-bound radiation, free-bound radiation can be treated less carefully. This is justifiable by considering the processes involved; free-bound radiation

occurs when an ion recombines with an electron through radiative recombination. Unlike bound-bound radiation, free-bound radiation creates a continuum due to the continuum of possible free electron energies. As a result, the intensity of any single frequency is dramatically reduced, so trapping plays a less important role. However, free-bound radiation cannot be neglected as it often emits as much energy as bound-bound radiation.

Free-free radiation:

The last and least important radiation type is free-free radiation (Bremsstrahlung radiation). It occurs when an electron travels near an ion and accelerates. Like free-bound radiation its spectrum is a continuum due to the continuum nature of the free electrons. If we neglect trapping effects, the emitted power per unit volume is[87]

$$P_{brem} = \frac{32\pi}{3}\left(\frac{2\pi k_B T}{3m_e}\right)^{1/2} \frac{Z^2 e^6}{m_e c^3 h} N_i N_e$$

Note that unless the plasma is completely ionized (no bound electrons), Bremsstrahlung radiation tends to be several orders of magnitude weaker than any other type of radiation.

V.H) Line Widths

Of importance to any radiation model are the atomic line widths. Both radiation trapping and gain depend on the line width. Additionally if we want to generate a synthetic spectrum we need to know the line widths. Atomic lines can be broadened through a

[87] Ya. B. Zel'dovich and Yu. P. Raizer, *Physics of Shock Waves and High-Temperature Hydrodynamic Phenomena*, Dover Publications Inc., New York, 2002.

number of processes including natural broadening, collisional broadening, Doppler broadening, and Stark broadening to name a few.

V.H.1) Natural Broadening

Natural broadening occurs because the lifetime of the atomic level is finite. According to Heisenberg's uncertainty principle $\Delta E \Delta t \geq \hbar$. The energy of a photon is $E = h\nu$, so the broadening is

$$\Delta\nu = \frac{1}{2\pi\Delta t} = \frac{\sum_{i<j} A_{ji}}{2\pi}$$

Similarly, collisional broadening decreases the lifetime of the state and increases $\Delta\nu$. Collisional broadening is often the dominate broadening in dense plasmas. In both cases, the broadening results in a Lorentzian line shape.

$$g(\nu) = \frac{1}{2\pi} \frac{\Delta\nu}{(\nu_0 - \nu)^2 + (\Delta\nu/2)^2}$$

V.H.2) Doppler Broadening

Doppler broadening is caused by the thermal motion of the ions. This motion causes Doppler shifts in the direction of travel. Because the thermal motion is random the Doppler shifts result in a broadened line. This broadening is one of the most important broadening mechanisms in hot plasmas. The width of the line is

$$\Delta\nu_D = \nu_0 \sqrt{\frac{8kT \ln 2}{Mc^2}}$$

The resulting line profile is a Gaussian

$$g(\nu) = \frac{1}{\Delta\nu_D}\sqrt{\frac{4\ln 2}{\pi}}\exp\left[-4\ln 2\left(\frac{\nu-\nu_0}{\Delta\nu_D}\right)^2\right]$$

V.H.3) Voigt Profile

When more than one broadening mechanism is important, the different line profiles must be convoluted. When adding two profiles of the same type, the widths add. This is not true for different profiles. For example, when both Doppler broadening and natural or collisional broadening are important, you must convolute a Lorentzian and a Gaussian line shape resulting in a Voigt profile[88].

$$g(\nu) = \frac{i}{\pi}\int_{-\infty}^{\infty}\frac{\exp\left(-t^2\right)}{\sqrt{\ln 2}\left[\left(\nu-\nu_0\right)-i\Delta\nu_L\right]/\Delta\nu_D - t}\,dt$$

Here $\Delta\nu_D$ and $\Delta\nu_L$ are the Doppler and Lorentzian widths.

Often only the Voigt cross section on resonance Γ_V is needed. This can be approximated by[89]

$$\Gamma_V = \sqrt{c^2\Gamma_L^2 + \Gamma_D^2} + (1-c)\Gamma_L, \text{ where } \; c = 0.3435\,.$$

The error for estimating the stimulated emission cross section is accurate within about 0.3%.

If the full Voigt profile is needed, it can be efficiently approximated by[90]

---

[88] Z. Shippony and W.G. Read, "*A Highly Accurate Voigt Function Algorithm*", J. Quant. Spectrosc. Radiative Transfer, Vol. 50, No. 6, pp. 635-646, 1993.

[89] Peter L. Hagelstein, "*Development of the MIT tabletop soft x-ray laser*", SPIE Vol. 1551 Ultrashort-Wavelength Lasers, 1991, pp. 254-274.

[90] A.B. McLean, C.E.J. Mitchell, D.M. Swanston, "*Implementation of an efficient analytical approximation to the Voigt function for photoemission lineshape analysis*", Journal of Electron Spectroscopy and Related Phenomena, Vol. 69, pp. 125-132, 1994.

$$g(\nu) = \frac{2}{\pi}\frac{\sqrt{\pi \ln 2}}{\Delta\nu_D} \cdot \sum_{i=1}^{4} \frac{C_i(Y - A_i) + D_i(X - B_i)}{(Y - A_i)^2 + (X - B_i)^2}$$

$$X = \frac{2\sqrt{\ln 2}}{\Delta\nu_D}(\nu - \nu_0),\ Y = \frac{\Delta\nu_L}{\Delta\nu_D}\sqrt{\ln 2}$$

i	A_i	B_i	C_i	D_i
1	−1.2150	1.2359	−0.3085	0.0210
2	−1.3509	0.3786	0.5906	−1.1858
3	−1.2150	−1.2359	−0.3085	−0.0210
4	−1.3509	−0.3786	0.5906	1.1858

The error in this approximation is less than 0.6%, and the typical error is about 0.03%.

V.H.4) Stark Broadening

A final broadening mechanism that may be important for dense plasmas is Stark broadening. Stark broadening is generated by Stark shifts caused by the microfields within the plasma. Because the plasma consists of charged particles, electric fields exist between any pair of particles. If one looks at a single ion, there is a non-zero time average field caused by the motion of the surrounding particles. Statistically, there are many different possible configurations of charged particles within the plasma. Each configuration will have a different electric field, which will result in a microfield distribution for the ions. Each field can then cause a Stark shift within the ion, resulting in a range of Stark shifts. This range is the basis for Stark broadening. It can be very complex, depending on the details of the atomic structure and the approximations used. In the standard approximation, the ions are heavy and static producing a static electric field, while the electrons are light producing a time-dependent electric field. The standard approximation is valid for heavy ions or when the electron temperature is greater than or equal to the ion temperature, both

assumptions are valid in this model. Under the standard approximation the expression for a Stark broadened line shape is

$$\Phi(\omega) = \int_0^\infty \mathrm{P}(\varepsilon) \cdot J(\omega, \varepsilon) d\varepsilon \,,$$

where $\mathrm{P}(\varepsilon)$ is the microfield distribution function for a normalized field strength and $J(\omega, \varepsilon)$ is the line shape function with Stark shifts caused by an external electric field ε. The microfield distribution function can be described through statistical mechanics. Under a high-temperature, low-density limit we can make an ideal gas approximation, neglecting particle correlations due to coulomb interactions. This was first done by Holtsmark.[91]

$$\mathrm{P}(\varepsilon) = \frac{2\varepsilon}{\pi} \int l \cdot T(l) \cdot \sin(\varepsilon \cdot l) \cdot dl$$

$$T(l) = e^{-\frac{2}{5}(2\pi)^{1/2} l^{3/2}} \,,\; \varepsilon = \frac{E}{E_0} \,,\; E_0 = \frac{q}{r_0^2} \,,\; r_0^3 = \frac{3}{4\pi n}$$

Here ε is the relative field strength, E is the electric field strength, E_0 is intrinsic field strength, q is the charge of an electron, r_0 is the average inter-particle distance, and n is the density of electrons. This microfield distribution can be seen in figure 5.9. This theory was further extended through Monte Carlo simulations by Hooper[92,93].

---

[91] J. Holtsmark, "*Über die Verbreiterung von Spektrallinien*" Annalen der Physik, Vol. 58, No. 7, pp. 577-630, 1919.

[92] C. F. Hooper, Jr., "*Low-Frequency Component Electric Microfield Distributions in Plasmas*", Physical Review, Vol. 165, pp. 215-222, 1968.

[93] C. F. Hooper, Jr., "*Electric Microfield Distributions in Plasmas*", Physical Review, Vol. 149, pp. 77-91, 1968.

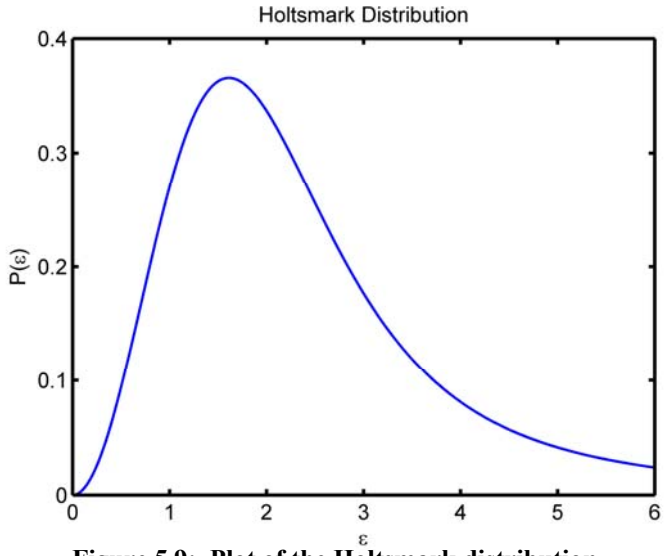

Figure 5.9: Plot of the Holtsmark distribution used to calculate the microfield distribution.

For each microfield value, we need to know the shift in the energy levels due to the Stark effect. This can be done with the use of quantum perturbation theory. The Hamiltonian under a perturbation can be written as

$$H = H_0 + V$$

$$H_{nm} = \langle n \mid H_0 \mid m \rangle + \langle n \mid V \mid m \rangle$$

The new states can be written as a linear combination of the previous states

$$|\alpha\rangle = \sum_n c_n |n\rangle$$

The perturbation potential due to an applied electric field is[94]

$$\langle n \mid V \mid m \rangle = -2E(-1)^{J-M} \begin{pmatrix} J & 1 & J' \\ -M & 0 & M' \end{pmatrix} \langle \gamma J \parallel \mathbf{P}^{(1)} \parallel \gamma' J' \rangle$$

[94] Robert D. Cowan, *The Theory of Atomic Structure and Spectra*, University of California Press, Berkeley and Los Angeles, California, 1981.

E is the static electric field, $\mathbf{P}^{(1)}$ is the electric dipole moment, and $|\gamma J\rangle$ is the state ket. Note that there is a factor of 2 to account for the fact that the electric field is measured in units of e/a_0^2, while the energies are measured in rydbergs (e/a_0^2).

Figure 5.10 shows the shift of the 4d $^1S_0$ state and the splitting and shift of the 4p $^1P_1$ state in Ni-like silver due to an applied electric field. In both cases the applied electric field causes an interaction between the different levels of the atom. Note that only like values of the magnetic level m are linked with the perturbation potential. As a result this causes the 4d $^1P_1$ m=1 and the 4d $^1P_1$ m=0 levels to interact with different levels. Because the interact with different levels they will behave differently under an applied field. This difference causes the splitting shown.

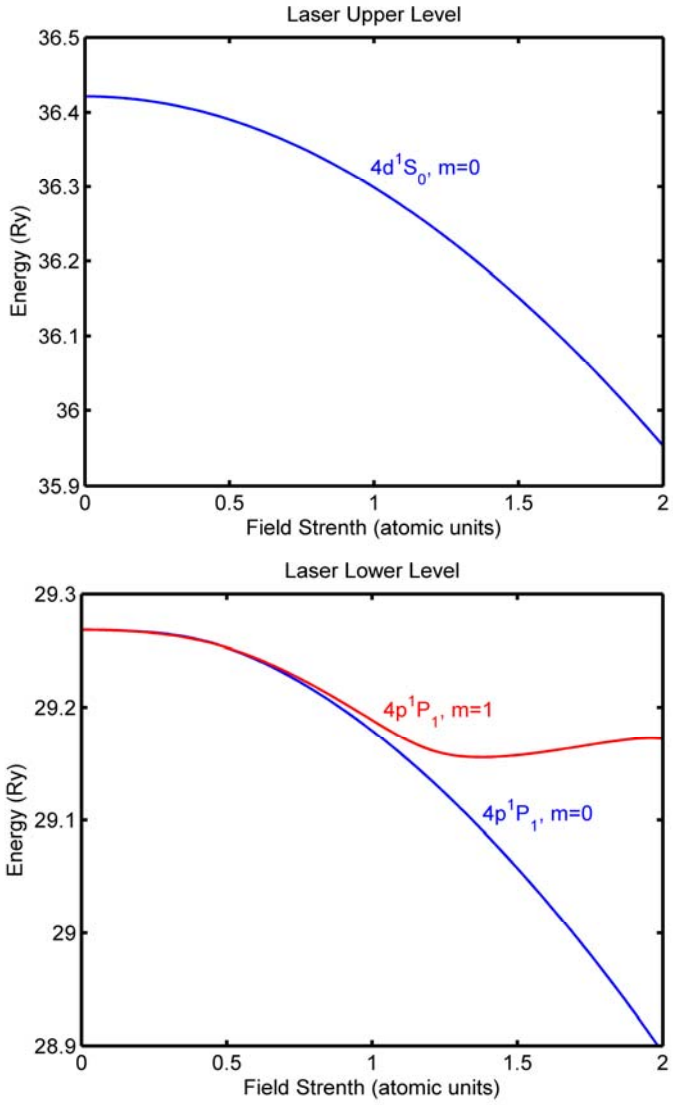

Figure 5.10: Plot of the effects of an applied electric field on the laser upper and lower levels in Ni-like silver.

With the calculation of the Stark shift, we can calculate the Stark broadening. By integrating the line shape function for each level over the microfield distribution we obtain the final line shape function. Figure 5.11 shows the line shape function for the Ni-like silver laser transition for different electron densities with Doppler and Stark broadening. From the plot it is clear that the Stark effect does not play a significant role until the electron density exceeds 10^{21} electrons/cm^3. In this calculation, collisional broadening was

not included to illustrate the Stark effect. When included, it represents the dominate broadening at electron densities above 10^{20} electrons/cm^3. As result, stark broadening is not an important broadening mechanism for the collisional soft x-ray lasers. Note that at very high densities (above $2x10^{22}$ electrons/cm^3) the stark shift is sufficient to alter the basic atomic structure of the atoms. This can alter the A coefficients and could affect the laser.

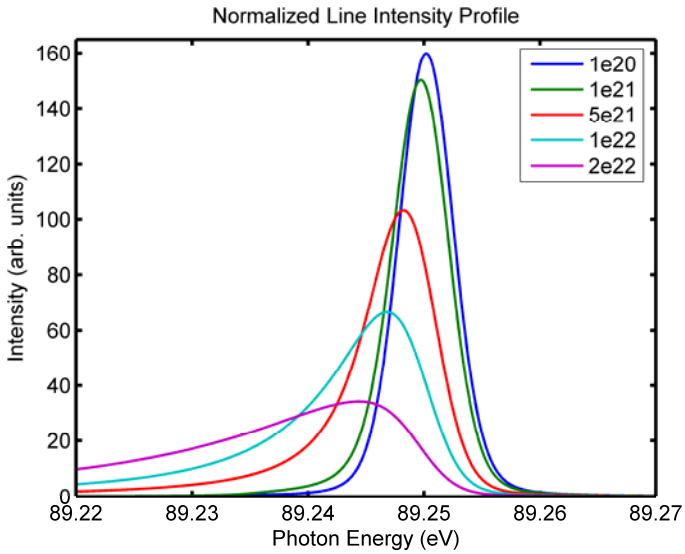

Figure 5.11: Stark broadened line shape for the Ni-like silver laser transition at different electron densities at an electron temperature of 800 eV and an ion temperature of 50 eV. Note: collisional broadening is not included.

V.I) Radiation Trapping

Radiation trapping can be a very important phenomenon in a large variety of plasmas. From a conceptual point of view it is very simple. A photon emitted on a line by one atom can be absorbed by another atom in the lower state. This will excite the absorbing atom to the higher state. As a net result, the number of atoms in the lower and upper states is unchanged. However, some of the light escapes and a large portion of the

light is transferred from one region to another. Consequently, radiation trapping reduces the net radiation loss from the plasma and is an energy transport mechanism. The different spatial regions become linked through the coupling coefficients, which are the probability that a photon emitted in one region will be absorbed in another. The notation I use is $C_{ji}^{pq,Z}$, where j is the emitting zone (or spatial region), i is the absorbing zone, p and q are the upper and lower levels of the radiative transition, and Z is the ion in which the transition takes place. Note that the number of coupling coefficients depends on the total number of zones squared times the total number of radiative transitions in each ion, summed over all the possible ions. As a result, a very large number of coupling coefficients may be needed. The solution of the populations and the calculation of the coupling coefficients can be extremely time consuming.

For the calculation of the coupling coefficients, we will be following the notation of Apruzese[95]. Here we will only consider one transition. Additionally, we will be assuming an infinite plane geometry. The plasma is assumed to be uniform and infinite in extent parallel to the target. This assumption is valid if the changes in the plasma properties parallel to the target is much less than the direction perpendicular to the target. The coupling coefficients are calculated using the optical depths of the plasma. For a general lineshape the optical depth is:

$$\tau_{(\nu)} = N_f d \frac{\lambda_c^2 A_{ul}}{2\pi} \frac{g_u}{g_l} g_{(\nu)}$$

At line center:

---

[95] J.P. Apruzese, J. Davis, D. Duston, K.G. Whitney, "Direct Solution of the Equation of Transfer Using Frequency and Angled Averaged Photon-Escape Probabilities, with Applications to a Multistage, Multilevel Aluminum Plasma", JQSRT, Vol. 23, pp. 479-487, 1980.

$$\tau_{(\nu)} = \frac{N_f d}{\Delta\nu}\frac{\lambda_c^2 A_{ul}}{2\pi}\frac{g_u}{g_l}$$

The optical depth for a Doppler-broadened spectral line matches that in Elton[96]

$$\tau = \frac{A_{ul}}{8\pi^2}\frac{g_u}{g_l}\left(\frac{m_i\pi}{2kT_i}\right)^{1/2}\lambda_c^3 N_f d$$

With the optical depth, one can calculate the escape probability following Holstein[97]

The probability of radiation traversing an optical depth τ is:

$$P_e(\tau) = \int P\big(\tau(\nu)\big)e^{-\tau(\nu)}d\nu$$

For Doppler Profile $P(x) = \frac{1}{\sqrt{\pi}}e^{-x^2}$, $x = \left[\frac{\nu-\nu_0}{\nu_0}\right]\sqrt{\frac{c^2 m_i}{2kT_i}}$

$$P_e(\tau) = \int_{-\infty}^{\infty}\frac{1}{\sqrt{\pi}}e^{-x^2}e^{\left[-\tau\cdot e^{-x^2}\right]}dx$$

Using substitution of variables: $P_e(\tau_0) = \frac{1}{\sqrt{\pi}}\int_0^1 \frac{e^{-\tau_0 y}}{\sqrt{-\ln(y)}}dy$

Up to this point, we have calculated the probability of escape for a single path. However we need to calculate the probability of escape from one zone. This requires the use of an angle-averaged escape probability. According to Apruzese this is

$$\overline{P}_e(\tau_0) = \int_0^1 P_e\left(\frac{\tau_0}{\mu}\right)d\mu = \frac{1}{\sqrt{\pi}}\int_0^1\int_0^1 \frac{e^{-\tau_0 y/\mu}}{\sqrt{-\ln(y)}}dyd\mu$$

In the planar limit, the second integral may be replaced by letting $\mu = 0.51$.

$$\overline{P}_e(\tau_0) \approx \frac{1}{\sqrt{\pi}}\int_0^1 \frac{e^{-\tau_0 y/\mu}}{\sqrt{-\ln(y)}}dy$$

---

[96] Raymond C. Elton, *X-Ray Lasers*, Academic Press Inc., 1990.

[97] T. Holstein, "*Imprisonment of Resonance Radiation in Gases*", Physical Review, Vol. 72, No. 12, pp. 1212-1233, 1947.

The problem can be further simplified by approximating $\overline{P}_e(\tau_0)$

$$\overline{P}_e(\tau_0) \approx \begin{cases} \dfrac{0.286}{\tau_0\sqrt{\ln(1.95\tau_0)}} & \tau_0 > 3 \\ \dfrac{1}{1+1.861607\tau_0+0.817393\tau_0^2} & \tau_0 \le 3 \end{cases}$$

This is accurate to within 7% for $\tau_0 < 5$, and 4% for $5 \le \tau_0 < 3\times10^4$.

Now, the coupling coefficient from zone j to zone i is:

$$C_{ji} = \frac{1}{2\Delta\tau_j}\left\{\int_{\tau_{ji}}^{\tau_{ji}+\Delta\tau_j}\overline{P}_e(\tau)d\tau - \int_{\tau_{ji}+\Delta\tau_i}^{\tau_{ji}+\Delta\tau_i+\Delta\tau_j}\overline{P}_e(\tau)d\tau\right\}$$

With the given assumptions the integral of the angle average escape probability can be solved analytically:

$$\int_L^U \overline{P}_e(\tau)d\tau = \begin{cases} \displaystyle\int_L^U \overline{P}_{e,1}(\tau)d\tau & U \le 3 \\ \displaystyle\int_L^U \overline{P}_{e,2}(\tau)d\tau & L > 3 \\ \displaystyle\int_L^3 \overline{P}_{e,1}(\tau)d\tau + \int_3^U \overline{P}_{e,2}(\tau)d\tau & otherwise \end{cases}$$

$$\int_L^U \overline{P}_{e,1}(\tau)d\tau = \frac{c}{2}\log\left(\frac{(aL+b-1)(aU+b+1)}{(aU+b-1)(aL+b+1)}\right)$$

(a=3.692523956, b= 4.204849102, c=-4.517440150)

$$\int_L^U \overline{P}_{e,2}(\tau)d\tau = 0.572 * \sqrt{\ln(1.95\tau)}\Big|_L^U$$

V.J) Velocity and Temperature Gradients

The preceding analysis of radiation trapping can be strongly affected by large temperature and velocity gradients. A temperature gradient will cause the Doppler

broadening of two regions to be different. This in turn will reduce the probability of a photon being reabsorbed. A strong velocity gradient will cause a Doppler shift in the emission and absorption widths, which will reduce the overlap and reduce the probability of re-absorption. Figure 5.12 shows the effect of temperature and velocity gradients. In the presence of a temperature gradient the Doppler broadened line profile will have different widths depending on the ion temperature. This will reduce the overlap between the two line shapes. In the presence of a velocity gradient the two line profiles will have a Doppler shift with respect to each other. This will again reduce the overlay. In both cases, the mismatch between the line shapes will reduce the opacity of the plasma. We can see the effect of the temperature and velocity gradients by looking at the line profiles. For a Doppler broadened medium[98]

$$g_{(\upsilon-\upsilon_0)} = \frac{1}{\upsilon_0}\left(\frac{Mc^2}{2\pi kT}\right)^{1/2} e^{-\frac{Mc^2}{2kT}\left(\frac{\upsilon-\upsilon_0}{\upsilon_0}\right)^2}$$

$$\Delta\upsilon_D = 2\upsilon_0\sqrt{\frac{2kT\ln 2}{Mc^2}}$$

For simplicity let $K = \upsilon_0\sqrt{\frac{2kT}{Mc^2}} = \frac{1}{2\sqrt{\ln(2)}}\Delta\upsilon_D$

[98] Orazio Svelto, Principles of Lasers, 1998 Plenum Press, New York, p49

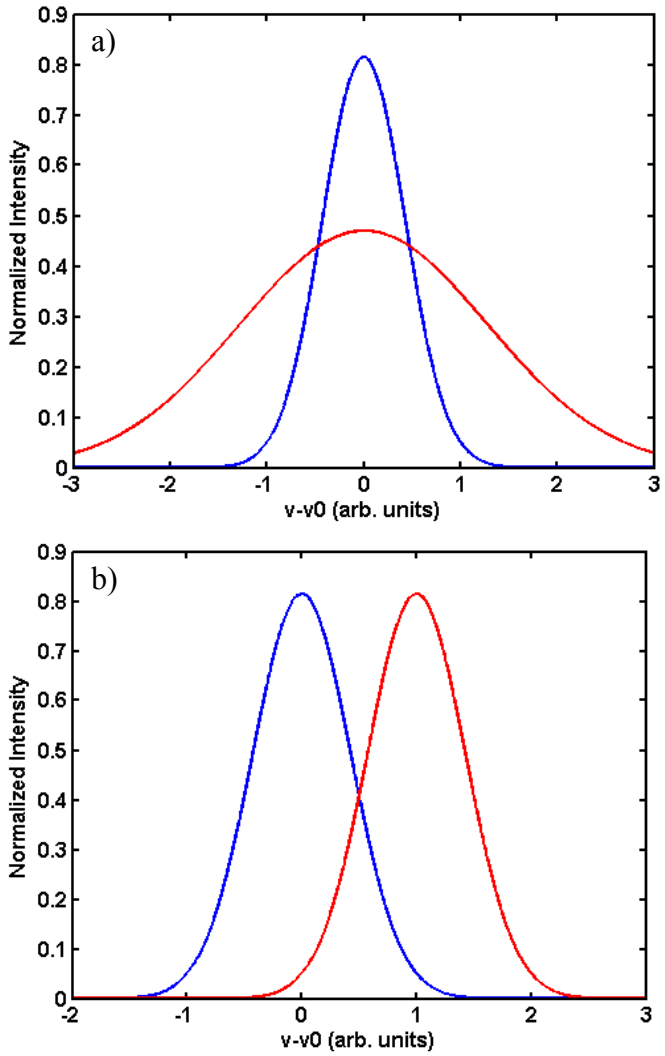

Figure 5.12: The photoemission and absorption profiles for two cases:
a) effect of a temperature gradient increasing the FWHM by a factor of 3
b) effect of a velocity gradient shifting the central peak by the FWHM

The normalized function $\left(\int_{-\infty}^{\infty} f_{(\upsilon-\upsilon_0)} f_{(\upsilon-\upsilon_0)} d\upsilon = 1 \right)$ for a Gaussian profile is

$$f_{(\upsilon-\upsilon_0)} = \sqrt{\frac{2}{K\sqrt{2\pi}}} e^{-\left(\frac{\upsilon-\upsilon_0}{K}\right)^2}$$

If the zone is moving with an average velocity of v_z, there will be a Doppler shift

$$\upsilon_0' = \frac{\upsilon_0}{1 - v_z / c}$$

If we define a de-coupling constant for the decrease in the optical path length τ due to changes in the frequency profiles from zone i to j:

$$\gamma = \int_{-\infty}^{\infty} f_{i,(\upsilon-\upsilon_0)} f_{j,(\upsilon-\upsilon_0')} d\upsilon$$

By assuming non-relativistic speeds (v_z<<c):

$$\gamma_{i,j} = \sqrt{2\frac{\sqrt{T_i T_j}}{T_i + T_j}} \exp\left[-\frac{M\Delta v_{i,j}^2}{2k(T_i + T_j)}\right]$$

$\Delta v_{i,j}$ is the velocity difference between the two zones, and T_i and T_j are the ion temperatures of the two zones. γ is the factor that represents the decrease in the coupling between the two zones. When $\gamma = 1$, the there is no change due to temperature or velocity gradients. When $\gamma = 0$, the two line profiles no longer overlap and there is no coupling between the zones. Note that if there is a temperature gradient, but no velocity gradient:

$$\gamma_{i,j} = \sqrt{2\frac{\sqrt{T_i T_j}}{T_i + T_j}}$$

Likewise, if there is a velocity gradient, but no temperature gradient:

$$\gamma_{i,j} = \exp\left[-\frac{M\Delta v_{i,j}^2}{4kT}\right]$$

In most cases, the presence of a velocity gradient limits the opacity of the plasma, and the temperature gradient has negligible effect. The presence of a velocity gradient is known as the Sobelev effect[99,100].

---

[99] V.V. Sobelev, Soviet Astronomy A, Vol. 1, 1957, p. 665.

[100] D.G. Hummer, G.B. Rybicki, "*The Sobolev Approximation for Line Formation with Partial Frequency Redistribution*", The Astrophysical Journal, Vol. 387, 1992, pp. 248-257.

V.K) Spectral Model

The atomic model described in this chapter is capable of modeling the spectra of a plasma. If we solve for the atomic level populations in a steady-state equilibrium or transient solution, we can use the resulting populations, the A coefficients, and the trapping calculations to compute the radiation emitted from the plasma. This radiation can then be integrated over time and space for a direct comparison with experimental results. For most experiments, the spectrometer will introduce additional instrumental broadening to the measurement. The actual spectra can be de-convolved from the measurement, or added to the simulation. When the instrumental broadening represents the dominate broadening mechanism, it is easiest to include it in the simulation and allows us to neglect all other broadening mechanisms and calculate the line-centered profiles. This was used to study a plasma generated by a soft x-ray laser, and the results are presented in section VIII.E.

CHAPTER VI.) ABSORPTION MODEL:

Since the plasmas simulated are laser-created plasmas, the absorption model is very important. We need to calculate the absorption as a function of position and time in the plasma. The incident laser light will be reflected, refracted, transmitted, and absorbed throughout the plasma. As a result, all these processes must be included. A complete simulation could solve Maxwell's equations directly at all points in the simulation. As an example we could use a finite-difference finite-time domain method[101,102] to simulate the absorption. Unfortunately, this type of model is both computationally expensive and places large restrictions on the spatial grid size. Depending on the geometry we can make some simplifications to the equations allowing us to simulate the absorption accurately with a substantial reduction in the computations. In the 1D model, we can use the planar geometry to implement a simple matrix method that will solve Maxwell's equations directly. In the 2D model we can use a ray-based method in which we include all relevant physical processes. In both cases we use the complex index of refraction computed with the Drude model (See section IV.F).

---

[101] Kane Yee (1966). "*Numerical solution of initial boundary value problems involving Maxwell's equations in isotropic media*". IEEE Transactions on Antennas and Propagation 14: 302–307.

[102] J. Berenger (1994). "*A perfectly matched layer for the absorption of electromagnetic waves*". Journal of Computational Physics 114:

VI.A.) 1D Absorption Model:

In the 1D plasma model we can take advantage of the geometry to solve the electromagnetic equations in a computationally efficient way. In a 1D planar geometry the discretization reduces the problem to a multilayer stack. Then we can use the same techniques used to solve a complex multilayer stack for the plasma absorption. To do this, consider the sequence shown in figure 6.1. The incident laser field encounters alternating layers of surfaces and bulk propagation. At each layer we wish to write a relation between the complex electric fields entering and exiting the layers. Then we can multiply the resulting interaction matrices to get a relationship between the fields entering and exiting the stack.

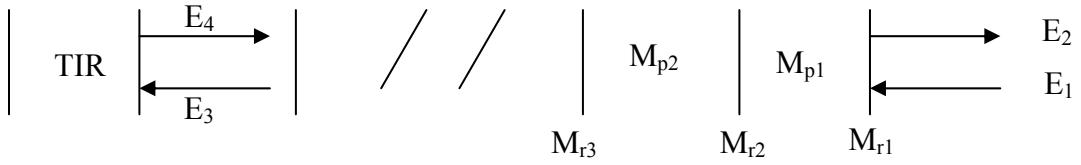

Figure 6.1: Flow chart for the model.

If we let M_r represent the matrix for reflection (see section VI.A.2), M_p represents the matrix for propagation (see section VI.A.1). E_1 is the input beam, E_2 is the net reflected beam. We can write the relationship between the fields:

$$\begin{bmatrix} E_1 \\ E_2 \end{bmatrix} = M_{r1}M_{p1}M_{r2}M_{p2}\cdots M_{rn}M_{pn}\begin{bmatrix} E_3 \\ E_4 \end{bmatrix} = M\begin{bmatrix} E_3 \\ E_4 \end{bmatrix}$$

If there is not TIR (total internal reflection):

$E_4 = 0$

$$E_3 = E_1 / M_{11}$$

If TIR occurs:

$$E_4 = E_3 e^{i\phi}$$

$$E_3 = \frac{E_1}{M_{11} + M_{12} e^{i\phi}}$$

$$\tan^2\left(\frac{\phi_\perp}{2}\right) = \frac{\sin^2\theta - (n'/n)^2}{\cos^2\theta}, \quad \tan\left(\frac{\phi_\parallel}{2}\right) = \left(\frac{n'}{n}\right)^2 \tan\left(\frac{\phi_\perp}{2}\right)$$

Note θ is the angle with respect to normal

VI.A.1) Propagation Matrix M_p

We would like to derive the interaction matrix for propagation of the electromagnetic wave. Consider the following diagram:

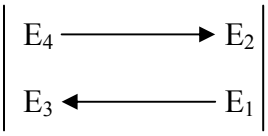

We need to relate E_1 and E_2 to E_3 and E_4. This is relatively simple:

$$\begin{bmatrix} E_1 \\ E_2 \end{bmatrix} = \begin{bmatrix} e^{-iknd} & 0 \\ 0 & e^{iknd} \end{bmatrix} \begin{bmatrix} E_3 \\ E_4 \end{bmatrix}$$

k is the wavevector $k = 2\pi / \lambda$

n is the complex index of refraction

The distance d is the propagation length in the layer, which is simply the layer thickness Δz divided by the cosine of the angle with respect to normal θ.

$$d = \Delta z / \cos\theta$$

To get the angle in every zone we can successively apply Snell's Law at each surface

$$n_1 \sin\theta_1 = n_2 \sin\theta_2$$

VI.A.2) Interface Matrix M_r

Deriving the interaction matrix for a surface is slightly more complicated. Consider the following diagram:

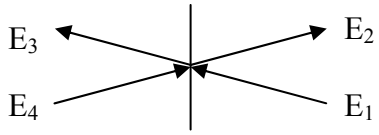

We can then write the expression for a propagating wave at a dielectric interface.

$$E_2 = E_1\Gamma_{12} + E_4\tau_{42}$$

$$E_1\tau_{13} = E_3 - E_4\Gamma_{43}$$

where Γ_{12} is the reflection coefficient from 1 to 2, and τ_{13} is the transmission coefficient from 1 to 3 (see section VI.A.3).

The interaction matrix can then be writted as:

$$\begin{bmatrix} E_1 \\ E_2 \end{bmatrix} = \frac{1}{\tau_{13}} \begin{bmatrix} 1 & -\Gamma_{43} \\ \Gamma_{12} & \left(\tau_{42}\tau_{13} - \Gamma_{12}\Gamma_{43}\right) \end{bmatrix} \begin{bmatrix} E_3 \\ E_4 \end{bmatrix}$$

Note: $\Gamma_{43} = -\Gamma_{12}$ and $\left(\tau_{42}\tau_{13} - \Gamma_{12}\Gamma_{43}\right) = 1$ (see section VI.A.3)

$$\begin{bmatrix} E_1 \\ E_2 \end{bmatrix} = \frac{1}{\tau_{13}} \begin{bmatrix} 1 & \Gamma_{12} \\ \Gamma_{12} & 1 \end{bmatrix} \begin{bmatrix} E_3 \\ E_4 \end{bmatrix}$$

The subscript $\perp$ refers to the perpendicular polarization of the input field with respect to the plane of incidence. and || is the parallel component.

Note that p polarization refers to in the plane of incidence which is ||, s polarization refers to perpendicular to plane of incidence which is then $\perp$. η is the impedance of the dielectric

$\eta_1 = \sqrt{\mu/\varepsilon}$, $n_1 = \sqrt{\mu\varepsilon/\mu_0\varepsilon_0}$

VI.A.3) Reflection and Transmission Coefficients

The reflection and transmission coefficients are obtained from the Fresnel reflection and transmission coefficients[103]

$$\Gamma_{\perp} = \frac{E_r}{E_i} = \frac{\eta_1 \cos\theta_2 - \eta_2 \cos\theta_1}{\eta_2 \cos\theta_1 + \eta_1 \cos\theta_2} \qquad \tau_{\perp} = \frac{E_t}{E_i} = \frac{2\eta_2 \cos\theta_1}{\eta_2 \cos\theta_1 + \eta_1 \cos\theta_2}$$

$$\Gamma_{\parallel} = \frac{E_r}{E_i} = \frac{\eta_1 \cos\theta_1 - \eta_2 \cos\theta_2}{\eta_1 \cos\theta_1 + \eta_2 \cos\theta_2} \qquad \tau_{\parallel} = \frac{E_t}{E_i} = \frac{2\eta_2 \cos\theta_1}{\eta_1 \cos\theta_1 + \eta_2 \cos\theta_2}$$

If we assume $\mu = \mu_0 \Rightarrow \eta_1 = 1/n_1$

$$\Gamma_{\perp} = \frac{n_2 \cos\theta_2 - n_1 \cos\theta_1}{n_1 \cos\theta_1 + n_2 \cos\theta_2} \qquad \tau_{\perp} = \frac{2n_1 \cos\theta_1}{n_1 \cos\theta_1 + n_2 \cos\theta_2}$$

$$\Gamma_{\parallel} = \frac{n_2 \cos\theta_1 - n_1 \cos\theta_2}{n_2 \cos\theta_1 + n_1 \cos\theta_2} \qquad \tau_{\parallel} = \frac{2n_1 \cos\theta_1}{n_2 \cos\theta_1 + n_1 \cos\theta_2}$$

The reflectance R is defined at the ratio of the reflect power to the incident power:

$$R \equiv \frac{I_r A \cos\theta_r}{I_i A \cos\theta_i} = \frac{I_r}{I_i} = \left(\frac{E_{0r}}{E_{0i}}\right)^2 = r^2$$

$$T \equiv \frac{I_r \cos\theta_r}{I_i \cos\theta_i} = \frac{n_2 \cos\theta_2}{n_1 \cos\theta_1}\left(\frac{E_{0r}}{E_{0i}}\right)^2 = \left(\frac{n_2 \cos\theta_2}{n_1 \cos\theta_1}\right) t^2$$

Conservation of Energy:

$$I_i \cos\theta_i = I_r \cos\theta_r + I_t \cos\theta_t$$

We can derive relationships between some of the coefficients

$$\Gamma_{\perp(1,2)} = \frac{n_2 \cos\theta_2 - n_1 \cos\theta_1}{n_1 \cos\theta_1 + n_2 \cos\theta_2} = -\frac{n_1 \cos\theta_1 - n_2 \cos\theta_2}{n_2 \cos\theta_2 + n_1 \cos\theta_1} = -\Gamma_{\perp(4,3)}$$

$$\Gamma_{\parallel(1,2)} = \frac{n_2 \cos\theta_1 - n_1 \cos\theta_2}{n_2 \cos\theta_1 + n_1 \cos\theta_2} = -\frac{n_1 \cos\theta_2 - n_2 \cos\theta_1}{n_1 \cos\theta_2 + n_2 \cos\theta_1} = -\Gamma_{\parallel(4,3)}$$

[103] John David Jackson, *Classical* Electrodynamics, John Wiley & Sons, Inc., 1999. pp. 305-306

$$\Gamma_{\|(4,3)} = -\Gamma_{\|(1,2)}$$

$$\tau_{42}\tau_{13} - \Gamma_{12}\Gamma_{43} = \tau_{42}\tau_{13} + \Gamma_{12}^2 = 1$$

VI.B.) 2D Absorption Model:

For a 2D or 3D plasma, solving for the electromagnetic fields is more complicated. As a result, the techniques developed in the previous section do not work. Instead, we will be using a ray-based absorption model. Some advantages of a ray based model are the fact that it does not put limitations on the spatial grid, it is an efficient method, and can be written in a parallel form. The main disadvantages include the fact that it does not solve for the fields and cannot include diffraction effects. Care must also be taken when including both transmission and reflection from surfaces and gradients. For the plasmas studied by this model, the feature size is significantly larger than the wavelength so we can neglect diffraction. This allows us to use a ray-based absorption model. We will include refraction, reflection, transmission, and absorption throughout the plasma and from all surfaces and gradients. To do this we first break the laser beam into a series of rays. We then follow each ray path using the ray equation (see section VI.B.1). If a discrete surface is encountered the ray can be transmitted or reflected according to the reflection and transmission coefficients (see section VI.A.3). The new path of the transmitted wave can be calculated according to Snell's law. Finally the ray will be absorbed as $e^{-\alpha d}$ where α is the absorption coefficient and d is the propagation distance of the ray in each cell.

VI.B.1) Ray Equation

The path of the rays is governed by the ray equation. To derive it we will start with Maxwell's equations (Gaussian Units):

$$\nabla \cdot \mathbf{D} = 4\pi\rho$$

$$\nabla \times \mathbf{H} = \frac{4\pi}{c}\mathbf{J} + \frac{1}{c}\frac{\partial \mathbf{D}}{\partial t}$$

$$\nabla \times \mathbf{E} + \frac{1}{c}\frac{\partial \mathbf{B}}{\partial t} = 0$$

$$\nabla \cdot \mathbf{B} = 0$$

Let **J**=0, ρ=0, **D**=ε**E**, **B**=**H**:

$$\nabla \cdot (\varepsilon \mathbf{E}) = 0\,,\ \nabla \cdot \mathbf{B} = 0$$

$$\nabla \times \mathbf{B} - \frac{1}{c}\frac{\partial(\varepsilon \mathbf{E})}{\partial t} = 0\,,\ \nabla \times \mathbf{E} + \frac{1}{c}\frac{\partial \mathbf{B}}{\partial t} = 0$$

Combining:

$$\nabla \times (\nabla \times \mathbf{E}) + \frac{1}{c^2}\frac{\partial^2(\varepsilon \mathbf{E})}{\partial t^2} = 0$$

Assume a solution of the form $\mathbf{E}(\vec{x},t) = \mathbf{E}(\vec{x})e^{i\omega t}$

$$\nabla \times (\nabla \times \mathbf{E}) - k^2 \varepsilon \mathbf{E} = 0$$

$$\nabla(\nabla \cdot \mathbf{E}) - \nabla^2 \mathbf{E} - k^2 \varepsilon \mathbf{E} = 0$$

Using $\nabla \cdot (\varepsilon \mathbf{E}) = 0$

$$\nabla^2 \mathbf{E} + k^2 \varepsilon \mathbf{E} + \frac{\nabla \varepsilon}{\varepsilon}\mathbf{E} = 0$$

Assume the wave amplitude is slowly varying compared with the phase $\mathbf{E}(\vec{x}) = \psi(\vec{x})e^{-ikS(\vec{x})}$

$$\left[(ik)^2 \psi(\nabla S)^2 - ik\left(2\nabla S \cdot \nabla \psi + \psi \nabla^2 S\right) + \nabla^2 \psi\right] e^{-ikS} + k^2 \varepsilon \psi e^{-ikS} + \frac{\nabla \varepsilon}{\varepsilon}\psi e^{-ikS} = 0$$

$$(ik)^2 \psi(\nabla S)^2 - ik\left(2\nabla S \cdot \nabla \psi + \psi \nabla^2 S\right) + \nabla^2 \psi + k^2 \varepsilon \psi + \frac{\nabla \varepsilon}{\varepsilon}\psi = 0$$

Making the geometrical approximation (k is large) we can collect the terms of order k2:

$$k^2\varepsilon\psi - k^2\psi(\nabla S)^2 = 0$$

$$(\nabla S)^2 = \varepsilon \qquad \text{(eikonal equation)}$$

Collecting terms of order k:

$$-ik\left(2\nabla S\cdot\nabla\psi + \psi\nabla^2 S\right) = 0$$

$$2\nabla S\cdot\nabla\psi + \psi\varepsilon = 0 \qquad \text{(transport equation)}$$

Define a ray that is normal to the wavefront:

$$n\frac{d\hat{\mathbf{r}}}{ds} = \nabla S$$

$$ds = \sqrt{dx^2 + dy^2 + dz^2}$$

Take the gradient of the eikonal equation:

$$\nabla(\nabla S)^2 = \nabla\varepsilon$$

$$2(\nabla S\cdot\nabla)\nabla S = 2n\nabla n$$

$$\left(n\frac{d\hat{\mathbf{r}}}{ds}\cdot\nabla\right)\nabla S = n\nabla n$$

Note: $\frac{d\mathbf{A}}{ds} = \left(\frac{d\hat{\mathbf{r}}}{ds}\cdot\nabla\right)\mathbf{A}$

$$\frac{d}{ds}(\nabla S) = \nabla n$$

Finally, we arrive at the ray equation:

$$\frac{d}{ds}\left(n\frac{d\vec{r}}{ds}\right) = \nabla n$$

CHAPTER VII) SOFT X-RAY LASER GAIN AND 3D RAY-TRACE:

The ability to calculate the amplification of light in a plasma is of great interest. The amplification results from stimulated emission in a transition in which an excited level has a larger population density than the lower level creating a population inversion. To understand this behavior, one needs to know how gain is created, how it saturates, and how the resulting output laser pulse propagates. Gain is created through a population inversion between the 4d $^1S_0$ and the 4P $^1P_1$ states in the Ni-like ion (see figure 7.). The laser upper level is populated through monopole electron impact excitation from the ground level. The laser lower level is de-populated through a large radiative dipole transition to the ground level. This inversion is created in the high temperature region of the plasma and requires a large Ni-like population. With knowledge of the gain and plasma properties, a 3D ray trace can be applied to simulate the soft x-ray laser. This process is described in the following sections. In section VII.A the properties of laser amplification are discussed, followed by gain saturation in section VII.B. Finally the ray propagation and traveling wave mismatch are discussed in sections VII.C and VII.D.

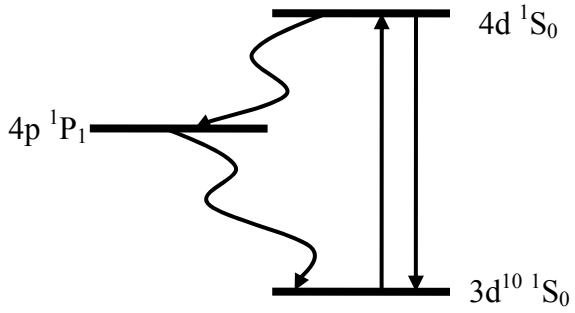

Figure 7.1: Simplified diagram of the Ni-like scheme. The laser upper level is the 4d $^1S_0$ state and is excited through electron impact excitation from the ground state. The laser lower level is the 4p $^1P_1$ state, and radiativly decays to the ground level.

VII.A) Laser Amplifcation

The soft x-ray lasers of interest for this work are either Amplified Spontaneous Emission (ASE) lasers or seeded soft x-ray lasers. For both types of lasers there is no laser cavity to affect the laser properties. For an ASE laser, spontaneous radiation emitted at the beginning of the gain medium is amplified as it propagates (see figure 7.). As a result, the characteristics of the output laser are entirely determined by the temporal and spatial characteristics of the gain medium. In the case of a seeded laser, the gain material will amplify the incident light, but if the gain is not uniform it will affect the characteristics of the resulting laser.

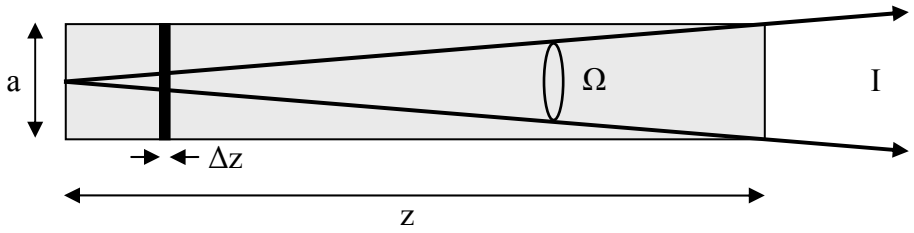

Figure 7.2: Simple diagram of amplified spontaneous emission

The behavior of light amplification and emission can be described by the radiative transfer equation

$$\frac{dI(\nu,\mathbf{r},t)}{d\mathbf{s}} = j(\nu,\mathbf{r},t) + g(\nu,\mathbf{r},t)I(\nu,\mathbf{r},t)$$

where $j(\nu)$ and $g(\nu)$ are the emissivity and small-signal gain coefficients respectively. This equation describes how the light is generated and amplifies as it propagates. When it is coupled with the ray equation (see section VII.C) and saturation effects (see section VII.D) a complete understanding of the soft x-ray laser can be obtained. If we integrate the

ASE laser over a constant gain without refraction the growth of the ASE laser intensity is given by[104]

$$I(\nu) = \frac{j(\nu)}{g(\nu)}\left[e^{g(\nu)z} - 1\right],$$

The emissivity is defined as the spontaneous emission into the solid angle Ω

$$j(\nu) = N_2 h\nu \frac{\Omega}{4\pi} A_{21}\Phi(\nu)$$

The small-signal gain coefficient is

$$g(\nu) = \left(N_2 - \frac{g_2}{g_1}N_1\right)\frac{c^2}{8\pi\nu^2}A_{21}\Phi(\nu)$$

In both formulas $\Phi(\nu)$ is the line profile.

VII.B) Gain Saturation

At sufficiently high intensities, the intensity no longer follows an exponential growth. At these intensities the stimulated emission rate causes changes in the populations. As a result, the population inversion decreases, reducing the gain and the growth rate of the laser beam. In the limiting case of a completely saturated beam the intensity increases linearly. In this limit, every ion in the laser upper and lower levels will undergo stimulated emission and absorption reducing the population inversion to zero. To accurately account for the effects of saturation, a self-consistent solution is needed. This requires including the stimulated rate coefficients in the atomic model (see chapter V). The stimulated rates for the laser transition are given by

---

[104] Joseph T. Verdeyen, *Laser Electronics*, second edition, Prentice Hall, New Jersey, 1981, p 210.

$$W_{ul}(\upsilon) = B_{ul}\rho(\upsilon)\Phi_{ul}(\upsilon) \qquad \text{(stimulated rate from the upper level to the lower level)}$$

$$W_{lu}(\upsilon) = B_{lu}\rho(\upsilon)\Phi_{ul}(\upsilon) \qquad \text{(stimulated rate from the lower level to the upper level)}$$

In these equations B_{ul} is Einstein's B coefficient from the laser upper level to the laser lower level, $\rho(\upsilon)$ is the photon density, and $\Phi(\nu)$ is the line profile. There are several relationships that can help simplify the stimulated rates:

$$g_2 B_{21} = g_1 B_{12}$$

$$B_{21} = \frac{c^3}{8\pi n^3 h \upsilon^3} A_{21}$$

$$\rho(\upsilon) = \frac{I(\upsilon)}{c/n}$$

With these equations we can rewrite the stimulated rate

$$W_{ul}(\upsilon) = A_{ul}\frac{\lambda^2}{8\pi}\frac{I}{h\upsilon}g(\upsilon) = \sigma(\upsilon)\frac{I(\upsilon)}{h\upsilon}$$

The total stimulated rate coefficient is the integral over the frequency range

$$W_{ul} = \int \sigma(\upsilon)\frac{I(\upsilon)}{h\upsilon}d\upsilon$$

$$W_{lu} = \frac{g_2}{g_1}W_{ul}$$

Now we can re-solve the rate equations with the stimulated rates included. This will allow us to include all saturation effects in a self-consistent manner.

As the laser propagates, it will change the excited state populations, reducing the gain. Solving the populations in a self-consistent manner requires solving for the atomic populations as a function of length along the line focus. This prevents the use of a 1D or 2D solution. To overcome these problems I created a post processor to simulate the soft x-ray laser. First, the model solves the hydrodynamic equations neglecting the effects of

stimulated emission. Then a 3D ray propagation code calculates the amplification of the line of interest coupled with a fully integrated atomic model. Note that the post-processor may take as long as the entire hydrodynamic model to finish.

VII.C) Ray Propagation:

As discussed in section VII.A, the path length through the gain medium is of fundamental importance. However, a simple analysis of a uniform gain medium and the geometry shown in figure 7. cannot be used within the plasma. The gain is not uniform, and more important there are strong electron density gradients. These electron density gradients cause a gradient in the index of refraction which will cause the laser beam to refract out of the gain region within a very short distance (< 1 cm). This puts a limiting condition on the maximum gain-length product in the plasma. To account for the refraction a propagation code is necessary.

The propagation code works by decomposing the output laser into a series of rays. Each ray is propagated through the plasma, experiencing gain and refraction. The output is then the sum of all of the rays. To propagate each ray, a 3D ray-tracing code is implemented. The code accounts for refraction as well as velocity mismatch between the pumping velocity and the soft x-ray laser velocity. Refraction is accounted for by solving the ray equation (see section VI.B.1).

$$\frac{d}{ds}\left(n\frac{d\vec{r}}{ds}\right)=\nabla n$$

$$ds=\sqrt{dx^2+dy^2+dz^2}$$

n = the index of refraction

To simplify the problem, we note that the refraction of the beam is typically several milliradians. As a result, we can invoke the paraxial approximation $ds \approx dx$:

$$\frac{d}{dx}\left(n\frac{d\vec{r}}{dx}\right)=\nabla n$$

If we are far from critical density, the index of refraction is (see section IV.F)

$$n=\sqrt{1-\frac{n_e}{n_c}}$$

$$\nabla n=-\frac{1}{2n}\frac{\nabla n_e}{n_c}$$

$$2nn_c\frac{d}{dx}n\left(\eta\frac{d\vec{r}}{dx}\right)=-\nabla n_e$$

Note that critical density is evaluated at the wavelength of interest. Usually, the index of refraction along the length of the target is nearly uniform $\left(\frac{dn}{dx}\approx 0\right)$ so

$$2n^2n_c\frac{d}{dx}\left(\frac{d\vec{r}}{dx}\right)=-\nabla n_e$$

Simplifying yields the final form of the ray equation

$$\frac{d^2\vec{r}}{dx^2}=\frac{-\nabla n_e}{2\left(n_c-n_e\right)}$$

We can also write this in terms of the individual coordinates:

$$\frac{d^2r_z}{dx^2}=\frac{-1}{2\left(n_c-n_e\right)}\frac{\partial n_e}{\partial z}$$

$$\frac{d^2r_y}{dx^2}=\frac{-1}{2\left(n_c-n_e\right)}\frac{\partial n_e}{\partial y}$$

This is the final form of the ray equation that we solve in the model. By solving the ray equation, we can calculate the path through the plasma, then multiply the differential path length by the local gain coefficient, and finally calculate the intensity growth for the ray. Note that to achieve a reasonable accuracy; typically 10^6 - 10^7 rays are solved per iteration for the lifetime of the gain.

Samples of the most intense rays from a simulation of a Ni-like Cd laser (section VIII.A) at 204 ps from the peak of the pre-pulse, (4 ps after the peak of the pump pulse) for the Ni-like Cd laser are shown in figure 7.a. The electron density profile used to calculate the path of the rays is shown in figure 7.b. Note that since the laser is saturating, the most intense rays do not follow a symmetric path about the center of the target length (located at 2mm). Instead they tend to originate in the high gain region further from the target surface, then follow a path that takes them closer to the target surface where the saturation intensity is larger. The larger saturation intensity in this region allows the rays to reach a higher intensity even if the gain coefficient is smaller. If the rays did not saturate the gain, the path of the most intense rays would be symmetric with respect to the center of the plasma.

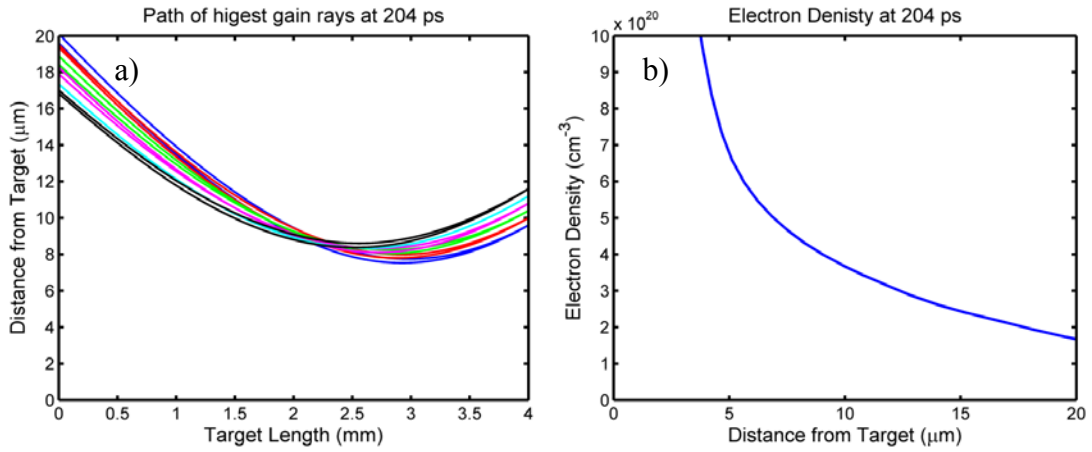

Figure 7.3: a) Plot showing the path of the maximum intensity rays for a Cd plasma at 204 ps after the peak of the pre-pulse (4 ps after the peak of the pump pulse). b) Cut of the electron density at 204 ps used for the ray propagation. The Cd plasma was excited by a 200 mJ, 120 ps pre-pulse, followed by a 1 J, 8 ps pump pulse with a delay of 200 ps.

VII.D) Traveling Wave / Velocity Mismatch:

A final issue to consider when calculating the soft x-ray laser amplification is the use of a traveling wave geometry and any resulting velocity mismatch that may occur. Using the traditional geometry of normal incidence pumping, the requirement for the consideration of a traveling wave geometry can be calculated by the time it takes the amplified light to travel from one end of the plasma to the other $t \approx L/c$. For a 4 mm long target, this time is 13 ps. Since the gain exists for at most ~10 picoseconds, the gain will change dramatically and often end before the amplified beam can reach the end of the target.

A traveling wave geometry is a geometry that shifts the pulse front so that it does not illuminate the entire line simultaneously. By delaying the pulse front the gain can "travel" with the amplified laser pulse, allowing for the use of much longer and more efficient targets. The geometry used in the experiments (grazing incidence pumping) is

inherently traveling wave. As is shown in figure 7., the grazing incidence causes a difference between the two path lengths of $\Delta L = L\cos\theta$. The difference between the speed of the amplified beam and the gain creates a velocity mismatch that between the creation of the gain and the arrival of the amplified beam.

$$\Delta t = \frac{L}{c}\left(1-\cos\theta\right)$$

For a 4mm target with a pumping angle of 23 degrees, the velocity mismatch is 1 ps (a 10X reduction).

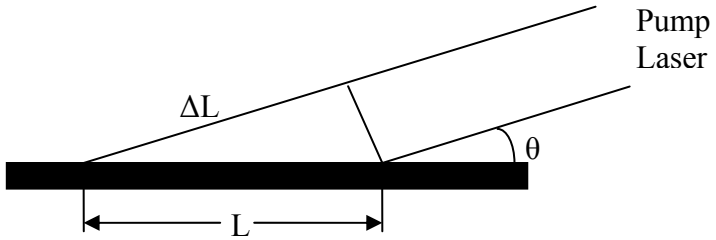

Figure 7.4: Grazing incidence pumping showing difference in path lengths

CHAPTER VIII) RESULTS:

The computer models developed as part of this dissertation can be used to model a wide variety of experiments. The 1.5D and 2D hydrodynamic models can be used to simulate many laser-created plasmas. However, the primary focus of this work is the study of laser-created plasmas used to generate soft x-ray lasers. The codes were used to study the physics of several soft x-ray laser experiments, and the model prediction were compared with the experimental results.

Simulation results of a 13.2 nm Ni-like Cd laser are presented in section VIII.A and compared with the experimental results. Section VIII.B includes simulation in which the code was used to predict the performance of a future experiment, in which a short wavelength 8.8 nm Ni-like La laser will be developed. Section VIII.C discusses the properties of an injection-seeded Ne-like Ti laser. Finally, in section VIII.D the near and far-field beam profiles of a seeded and unseeded Ni-like Ag laser are discussed and compared to experimental results.

In addition to simulating soft x-ray lasers, the models were used to understand the dynamics of plasmas created by a soft x-ray laser and simulate the spectra emitted by the plasma. In section VIII.E the results of an experiment in which a 46.9 nm soft x-ray laser was focused on Si and Cr targets to generate a plasma are presented. The plasmas were studied using the hydrodynamic model and synthetic spectra resulting from model simulations are compared to experimental measurements.

VIII.A) Ni-like Cd Soft X-ray Laser:

The 1.5D code was used to model the characteristic of a collisional soft x-ray operating at 13.2 in Ni-like Cd. This wavelength is of particular interest because it falls within the bandwidth of Mo/Si mirrors, and therefore it is of interest for the actinic inspection of lithographic masks. The experimental setup used in the development of the Ni-like Cd laser is described in Chapter I. It consists of a 120 ps, 200 mJ pre-pulse followed by a 1 J, 8 ps pump pulse focused at a 23° grazing incidence angle. Both beams are focused into a 4.1 mm FWHM x 30 μm FWHM line. The plasma was modeled using the 1.5D hydrodynamic model and the results are shown in figure 8.1. All of the plots show the plasma characteristics as a function of time and distance from the target surface. In the figures time t=0 refers to the peak of the 200 mJ pre-pulse.

The pre-pulse creates and heats the plasma to an electron temperature of about 100 eV (Fig. 8.1a). The mean degree of ionization reaches 20 corresponding to the Ni-like state of Cd (Fig. 8.1e). The ions are not directly heated by the laser pulse, but are heated through collisions with electrons. As a result, their temperature lags behind the electron temperature, and typically does not exceed 60 eV (Fig. 8.1b).

At the arrival of the short pump pulse, the plasma is quickly heated and the electron temperature rises above 600 eV (Fig. 8.1a). This heating occurs at an electron density of ~ 2×10^{20} cm^{-3} (Fig. 8.1c), determined by the grazing incidence pumping at 23º. This rapid heating causes a slight increase in the degree of ionization ensuring a large Ni-like population (Fig. 8.1e), as well as a large population inversion. The population inversion is transient in nature lasting approximately 15 ps, with a computed peak gain coefficient of 160 cm^{-1} (Fig. 8.1g). The ion temperature does not change significantly on this time scale,

remaining at 40-60 eV (Fig. 8.1b). This is important to limit the Doppler broadening, which along with collisional broadening, are the dominant broadening mechanisms. A large fraction of the heat is conducted to the cooler, higher density plasma region near the target surface. As a result of radiation and thermal conduction the plasma cools within 15-20 ps. Figure 8.2 shows a detailed view of the temporal evolution of the gain. From the cut of the computed gain, its duration is approximately 15 ps.

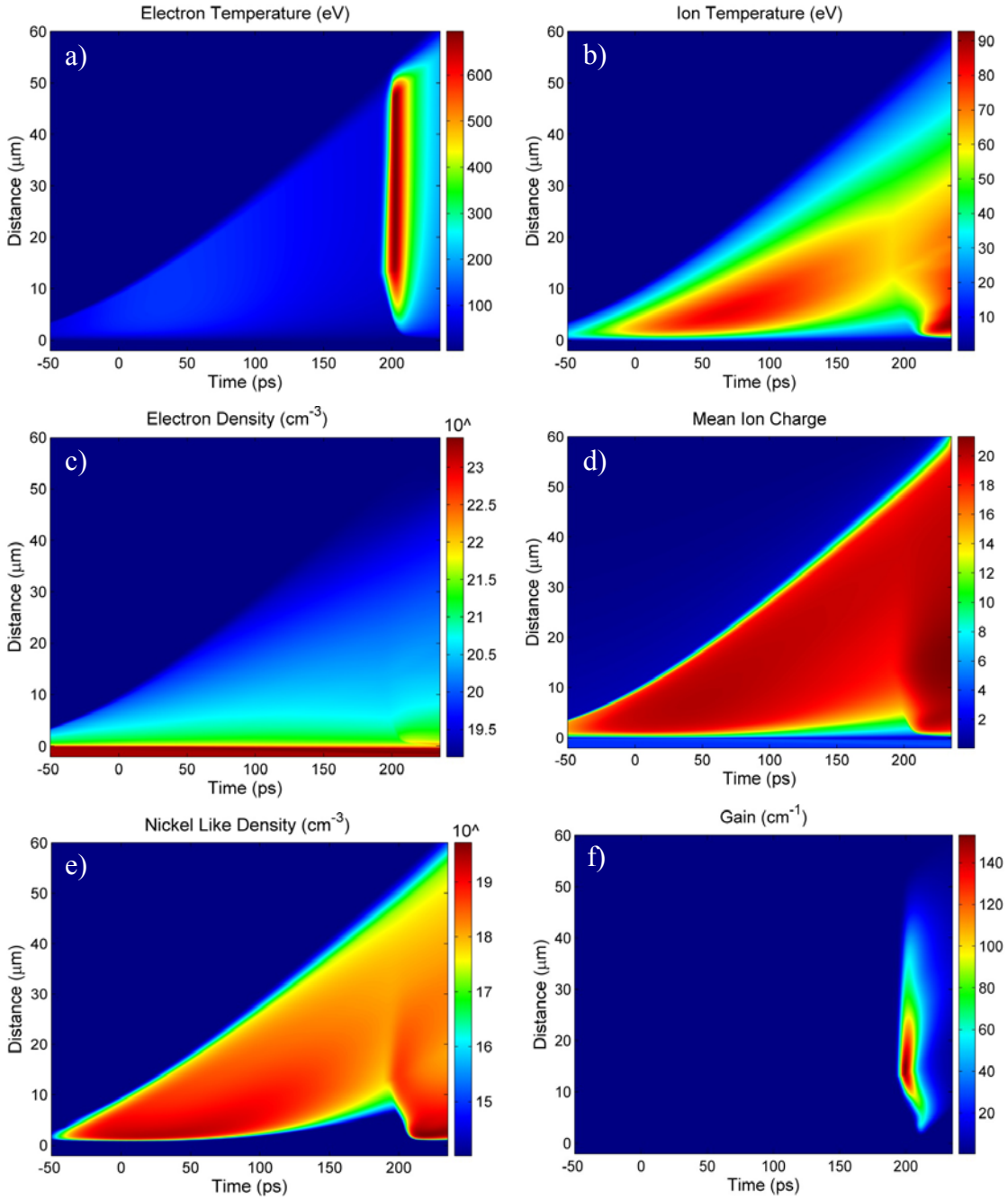

Figure 8.1: Plots of the plasma properties for a Cd plasma excited by a 200 mJ, 120 ps pre-pulse ($8x10^{11}$ W/cm^2), followed by a 1 J, 8 ps pump pulse ($6x10^{13}$ W/cm^2): a) electron temperature, b) ion temperature, c) electron density ($\log_{10}$), d) mean degree of ionization, e) Ni-like density ($\log_{10}$), and f) gain.

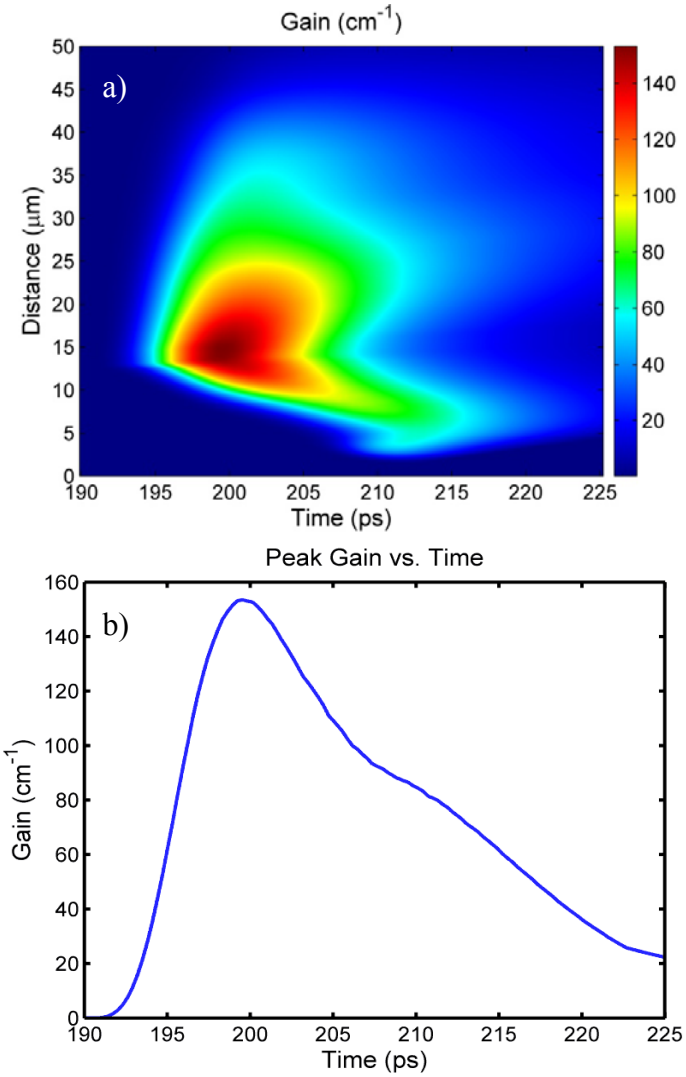

Figure 8.2: Plots of a) the temporal and spatial characteristics of the gain and b) the peak gain coefficient vs. time for 13.2 nm Ni-like Cd plasma excited by a 200 mJ, 120 ps pre-($8x10^{11}$ W/cm^2), followed by a 1 J, 8 ps pump pulse ($6x10^{13}$ W/cm^2).

The 13.2 nm soft x-ray laser was simulated using the ray-trace described in chapter VII. The simulated and measured energy vs. length are shown in figure 8.3. The simulated laser saturates at approximately 2.5 mm, while the experimental laser saturates at 2.5 - 3.0 mm. At 4mm, the output energy of the simulated laser is 2.5 μJ, which is larger than the

measured energy of 0.5 μJ, but this discrepancy is expected as the model is an ideal case in which the line focus and the target are assumed to be free of imperfections.

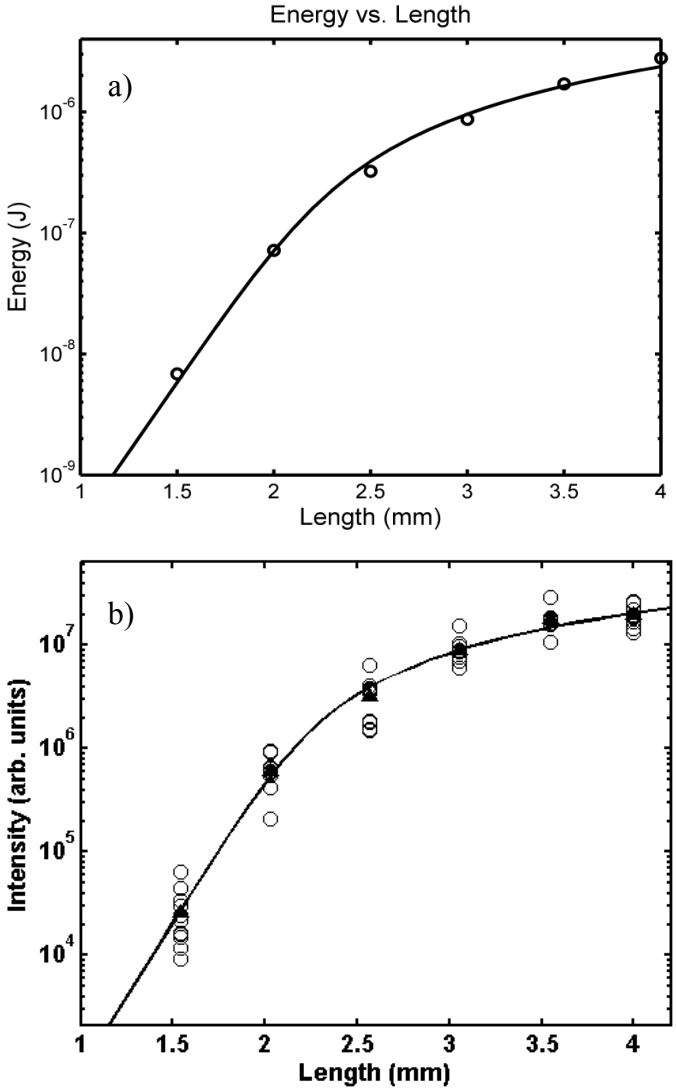

Figure 8.3: Plot of the simulated (a) and measured (b) energy vs. length for the 13.2 nm Ni-like Cd.

The ray trace simulation also calculates the near field and far field intensity distributions as shown in figure 8.4. From the simulation the beam size at the exit of the amplifier covers a region of about 20 μm x 20 μm. This corresponds to a fluence of 0.8 J/cm^2. The divergence of the laser is computed to be approximately 5 mrad x 10 mrad, in

acceptable agreement with the experimental divergence of 7 mrad x 14 mrad. The simulated deflection angle is 3 mrad. A more detailed discussion of the near-field and far-field profiles for a 13.9 nm Ni-like Ag amplifier are discussed in section VIII.D.

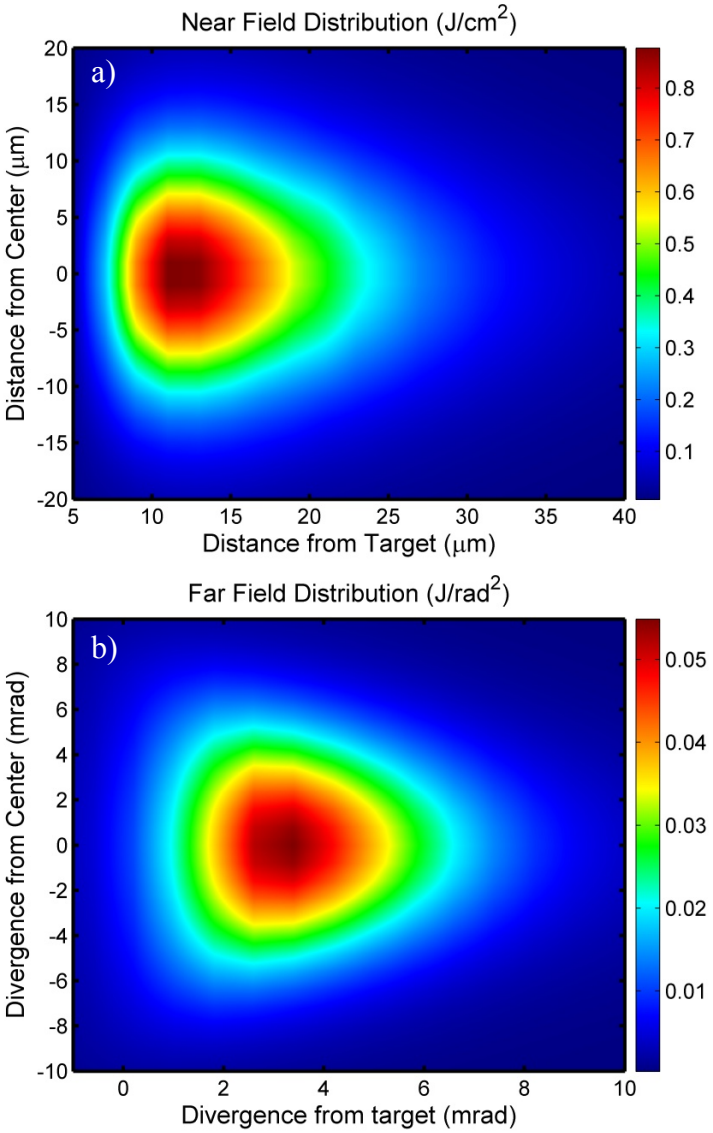

Figure 8.4: Plot of the simulated near field (a) and far field (b) images for the 13.2 nm Ni-like Cd. The near field beam is approximately 20 μm x 20 μm, while the far field image indicates that the divergence is 7 mrad x 14 mrad.

Finally, the ray trace calculation is capable of simulating the temporal and frequency profiles. These results are shown in figure 8.5. As the pulse travels through the amplifier its temporal profile narrows due to gain narrowing, and then broadens due to gain saturation. The predicted pulse width of 9 ps is larger than the measured 5 ps, but this is primarily due to the broadening caused by gain saturation, which does not occur in the experiment because the experimental laser intensity is lower and does not reach such a full degree of saturation as in the model. At 4 mm, the intensity of the laser pulse exceeds 8 x 10^{10} W/cm^2, which is more than 4 times the saturation intensity of 5 x 10^9 W/cm^2. The gain narrowed line width $\Delta\upsilon/\upsilon_0$ is computed to be 2.5 x 10^{-5}. At 2mm, saturation broadening has not occurred resulting in a pulse duration of 5 ps is good agreement with the measured pulse duration.

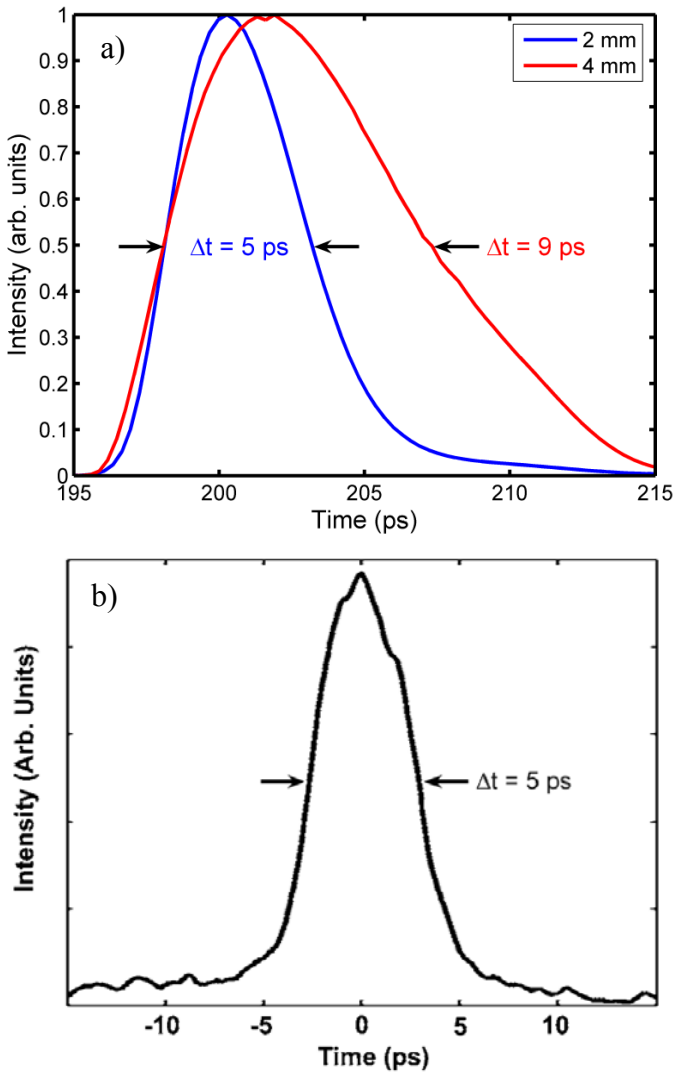

Figure 8.5: Plot of the simulated (a) and measured (b) temporal profile for the simulated 13.2 nm Ni-like Cd laser

VIII.B) Ni-like La Soft X-Ray Laser:

To illustrate soft x-ray laser amplification at shorter wavelength, the results of a simulation in Ni-like La are shown in figure 8.6. The basic setup and behavior is very similar to that of the Ni-like Cd plasma. However, in order to obtain amplification in the higher Z material, more energy must be used. The simulation was performed for a 2J, 300

ps pre-pulse focused into a 30 μm x 6 mm line, with a short pump pulse of 3 J, 6 ps focused into the same line at a grazing angle of 30°. As a result of the increased energy, the electron temperature is significantly hotter than in the case of the Ni-like Cd laser, reaching 800 eV (figure 8.6a) which is necessary to pump the laser transition. In addition, a steeper grazing angle of 30° was used so that the electron density at the peak gain could be increased from 2.6 x 10^{20} to 4.3 x 10^{20} (figure 8.6c). This higher density allows for an increased population inversion which helps to overcome the decrease in the stimulated emission cross section caused by the decreased laser wavelength. In spite of this increase in density, the gain is still significantly lower, reaching a peak gain coefficient of 70 cm^{-1} (figure 8.6 (e and f)).

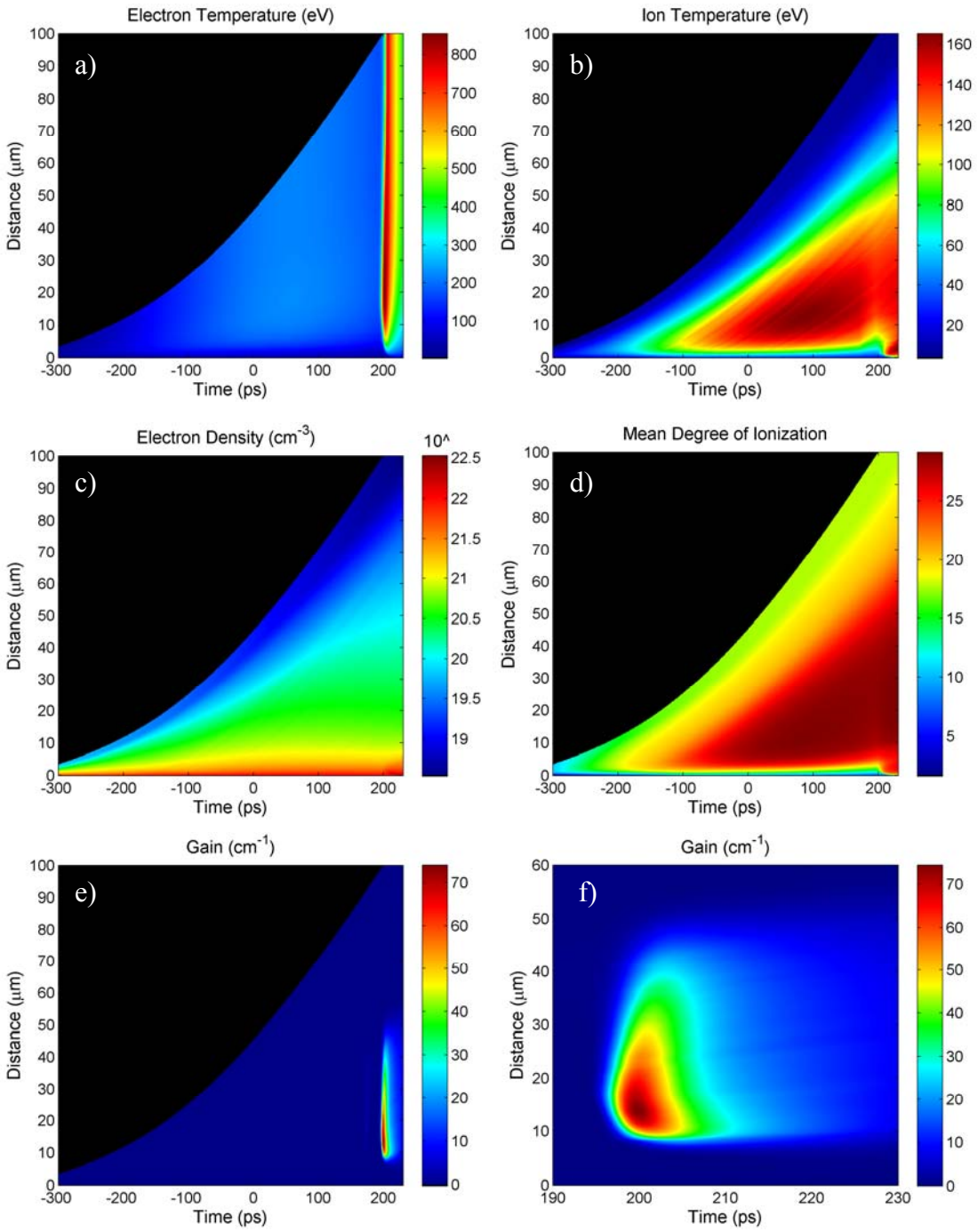

Figure 8.6: Plots of the plasma properties for a La plasma excited by a 2.5 J, 300 ps pre-pulse ($3x10^{12}$ W/cm^2), followed by a 3 J, 6 ps pump pulse ($2x10^{14}$ W/cm^2): a) electron temperature, b) ion temperature, c) electron density ($\log_{10}$), d) mean degree of ionization, and e,f) gain.

The soft x-ray laser characteristics of the shorter wavelength La laser is very similar to the behavior of the Ni-like Cd laser discussed previously. The primary difference is due to the lower cross section caused by the shorter wavelength. The resulting lower gain coefficient causes the ASE laser to saturate at longer length of ~4 mm (Fig. 8.7). However, the steeper angle used results in a larger population inversion, that causes a higher saturation intensity resulting in a higher saturated energy output of ~10 μJ for a 6mm long target..

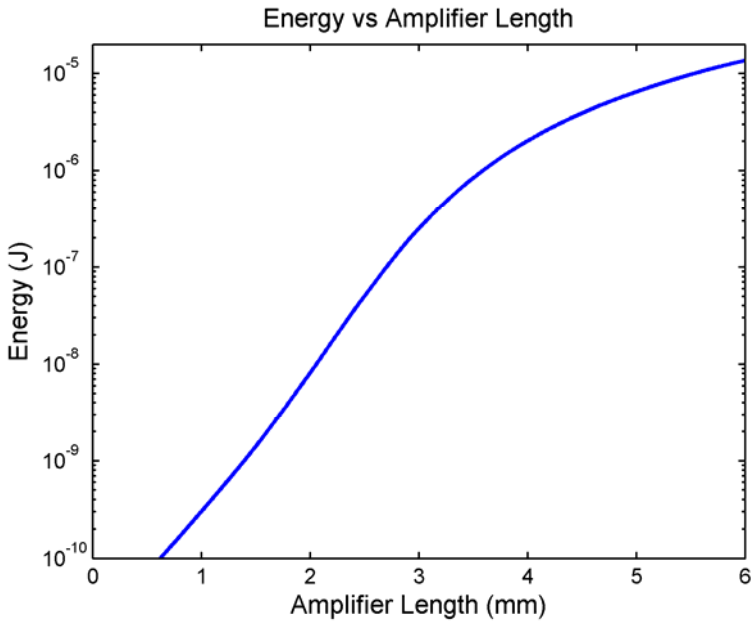

Figure 8.7: Simulated energy vs. length for a 8.8 nm Ni-like La soft x-ray laser.

VIII.C) Seeded 32.6 nm Ne-like Ti Soft X-Ray Laser Characteristics

In addition to simulating an ASE laser system, the computer models are capable of simulating the amplification of an externally injected seed pulse. In these experiments a seed beam is generated from a high harmonic pulse and in injected into the start of the plasma column[105]. Figure 8.8 shows the experimental and simulated seeded energy as a function of amplifier length. The amplification behavior can be divided into three distinct phases. The first phase, which takes place in the first ~1 mm of the amplifier, is dominated by the gain narrowing of the seed pulse whose initial 0.1 nm spectral bandwidth greatly exceeds that of the laser line. This leads to the amplification of only a fraction of its bandwidth (figure 8.9), resulting in the observed slow initial seed pulse energy increase. When the seed pulse bandwidth narrows sufficiently to approach the laser linewidth, a second amplification phase starts in which a quasi-exponential increase in the energy of the seed pulse takes place. This rapid increase ends after about 2.5 mm into the amplifier. At this length, the measured amplified seed pulse energy reaches a value consistent with the computed saturation intensity for the 32.6 nm line of Ne-like Ti at a plasma density of 2.6 x 10^{20} electrons/cm^3. The third amplification phase corresponds to the gain saturated regime in which efficient energy extraction occurs. The maximum measured amplified seed pulse energy 50–60 nJ is similar to that predicted by the model.

[105] Y. Wang, E. Granados, M. A. Larotonda, M. Berrill, B. M. Luther, D. Patel, C. S. Menoni, and J. J. Rocca, "*High-Brightness Injection-Seeded Soft-X-Ray-Laser Amplifier Using a Solid Target*", Physical Review Letters, **97**, 123901 (2006).

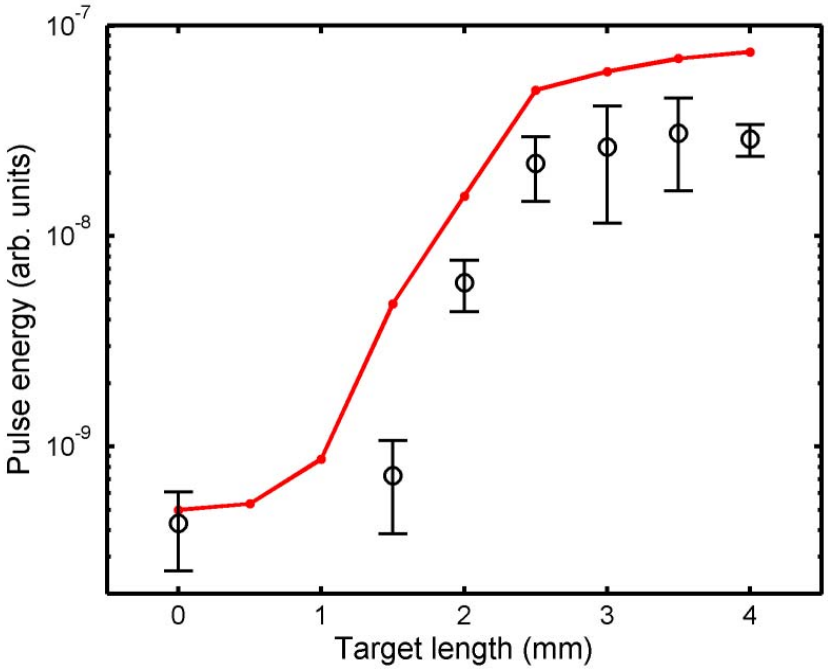

Figure 8.8: Simulated (red dots) and experimental energy (black points) vs. length for a seeded 32. 6 nm Ne-like Ti amplifier

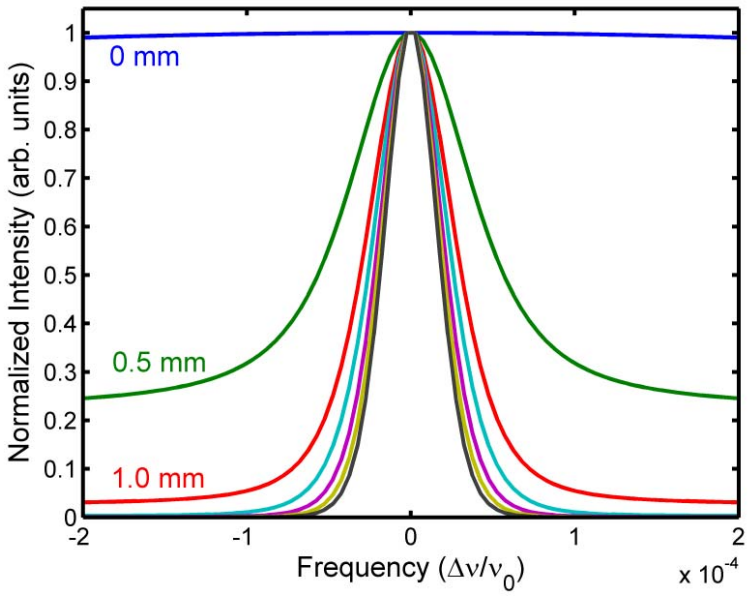

Figure 8.9: Simulated seeded laser profile as a function of frequency for each 0.5 mm cut through the amplifier.

Figure 8.10 shows the simulated variation of the amplified seed pulsewidth as a function of plasma amplifier length. Initially, the seed pulse broadens as its bandwidth narrows dramatically in the narrow bandwidth plasma amplifier. Subsequently, the simulations indicate that as the amplified seed pulse approaches the saturation fluence at about 2.5 mm within the amplifier the effect of gain saturation starts to contribute to additional pulse broadening. The pulsewidth is computed to increase from ~1.0 ps at 2 mm to 1.3 ps at 4 mm, an increase caused by additional line narrowing and saturation broadening. The simulated pulse duration of 1.2 ps at 3 mm is in good agreement with the measured pulsewidth of 1.1 ps[106]. The bandwidth of the amplified seed pulse at this point is computed to be 3.6×10^{11} Hz. As a result the computed time-bandwidth product is 0.43, close to the transform-limited value of 0.36 for our Voigt profile. Since the resulting pulse is close to transform limited, it is essentially fully temporally coherent.

[106] Y. Wang, M. Berrill, F. Pedaci, M. M. Shakya, S. Gilbertson, Zenghu Chang, E. Granados, B. M. Luther, M. A. Larotonda, and J. J. Rocca, "*Measurement of 1-ps soft-x-ray laser pulses from an injection-seeded plasma amplifier*", Physical Review A, **79,** 023810 (2009).

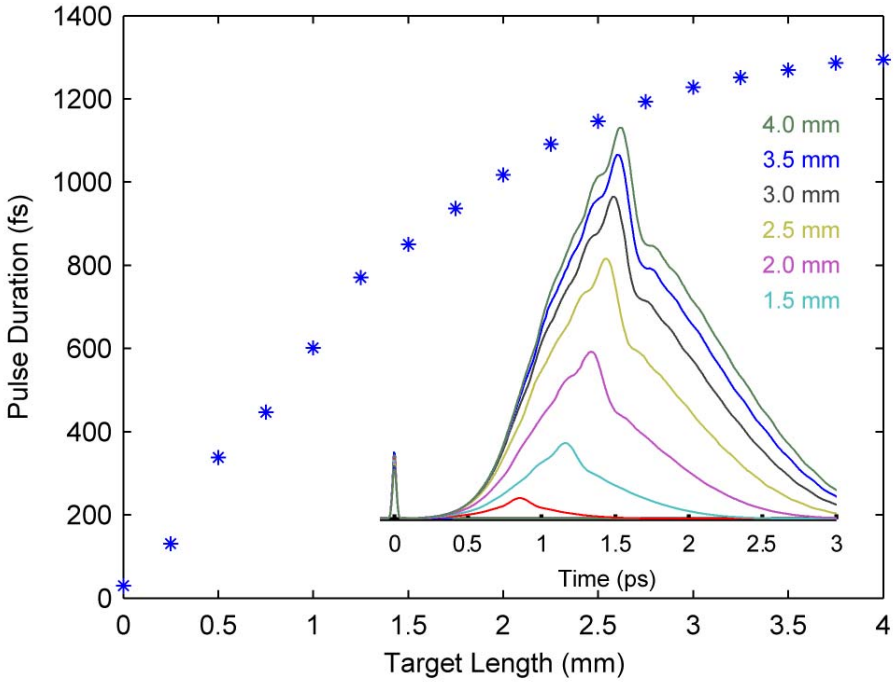

Figure 8.10: Simulated variation of the seeded Ne-like Ti laser pulsewidth as a function of amplifier length. In the first 2 mm of the amplifier rapid line narrowing of the amplified seed pulse results in a temporally broader pulse. In the last 2 mm the pulse broadens due to both additional line narrowing and gain saturation. The pulsewidth is defined as the time interval that contains 76% of the pulse energy, corresponding to the FWHM of a Gaussian distribution. The inset shows the computed temporal profiles of the amplified seed pulse as a function of amplifier length. The proceeding short pulse contains the non-amplified frequencies of the injected seed.

VIII.D) Near-Field and Far-Field Simulations of a 13.9 nm Ni-like Ag Amplifier

For many applications the beam quality is very important. Therefore for this reason as well as for fundamental reasons it is important to understand both the near and far field profiles of the seeded and ASE lasers. To understand all of the important effects the 2D plasma model must be used. Figure 8.11 shows the results of the 2D plasma model for the 13.9 nm Ni-like plasma amplifier created by a sequence of pump pulses consisting of a 10 mJ pre-pulse of 120 ps duration, followed after 5 ns by a second ~ 350 mJ pre-pulse impinging at normal incidence, which in turn was followed after 200 ps by a ~ 0.9 J pump

pulse of 6.7 ps duration impinging at a grazing incidence angle of 23 degrees. The pump pulses were focused onto the target to form a 30 μm x 4.1 mm FWHM long line. The length of the target was 3 mm. A small portion of the pump laser energy (~20 mJ) was split, compressed in a separate pulse compressor, and focused into a Ne gas jet with a f =1.2 m lens to produce the 59^{th} harmonic seed pulses.

Figure 8.11 shows the evolution of the electron density, electron temperature, and small signal gain . The left column shows the plasma properties as a function of time and distance from the target surface. Time t=0 represents the peak of the second (main) pre-pulse. The right column shows the 2D spatial distributions of the electron density, electron temperature, and small signal gain at the time delay of 202 ps after the peak of the main prepulse. The prepulse is computed to heat the plasma to ~ 90 eV (Fig. 8.11a), resulting in a degree of ionization of ~ 18 at the time of arrival of the short pulse. The short pulse rapidly heats the plasma to ~ 400 eV (Fig. 8.11(a,b)) in the region where the electron density is 2-3 x 10^{20} cm^{-3} (Fig. 8.11(c,d)), resulting in a small-signal gain coefficient of ~ 80 cm^{-1} (Fig. 8.11(e,f)) approximately 35 μm from the target surface.

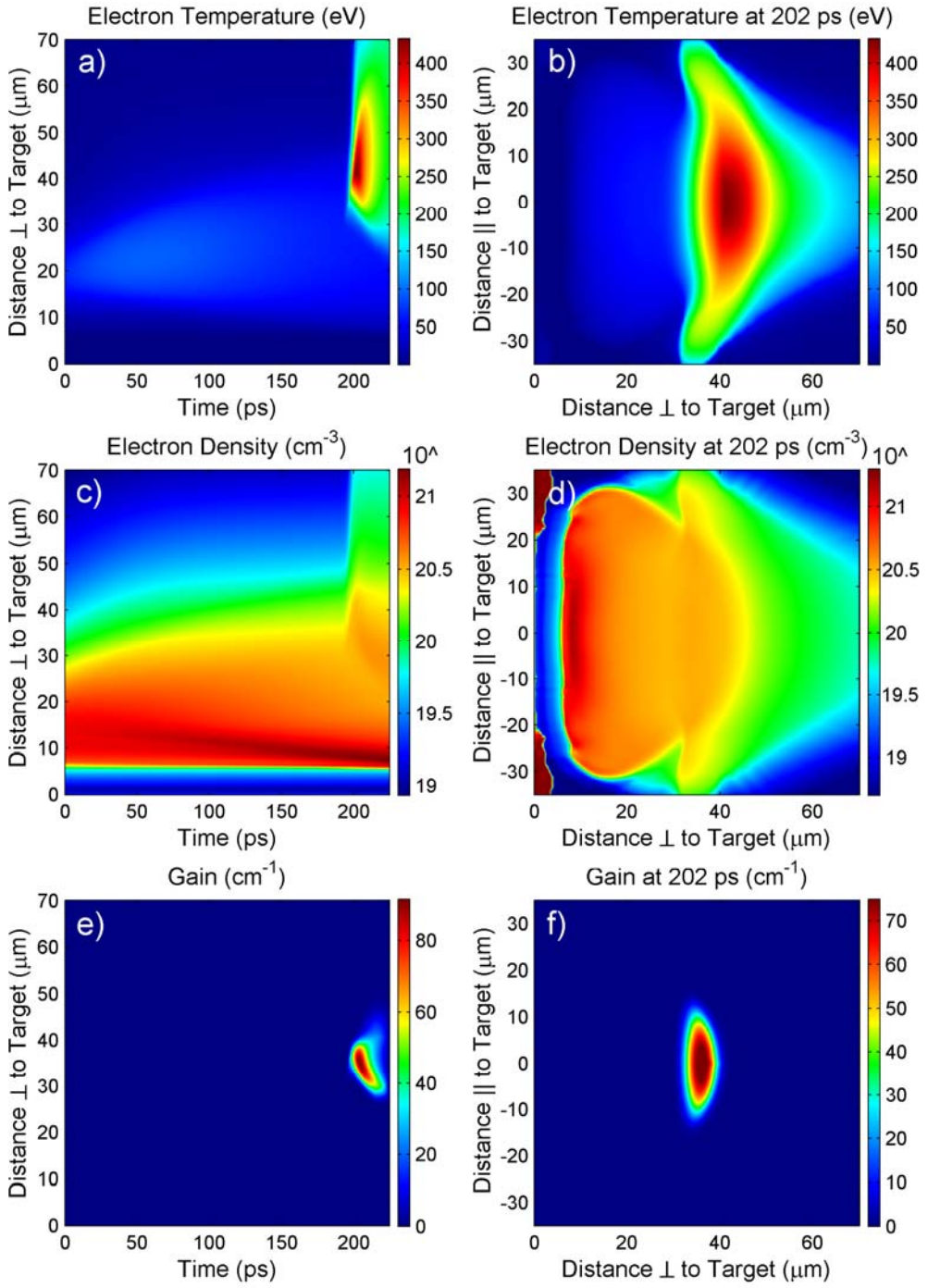

Figure 8.11: 2D plasma simulations of a 13.9 nm Ni-like plasma amplifier created by a 10 mJ, 120 ps pre-pulse ($2x10^{11}$ W/cm^2), followed after about 5 ns by a second ~ 350 mJ pre-pulse ($8x10^{11}$ W/cm^2), which in turn was followed after 200 ps by a ~ 0.9 J, 6.7 ps pump pulse ($4x10^{13}$ W/cm^2) at a grazing incidence angle of 23 degrees. The left column shows the electron temperature (a), electron density, (c) and gain (e) as a function of time and distance from the target surface. Time t=0 represents the peak of the second pre-pulse. The right column shows the 2D spatial profiles of the electron temperature (b), electron density, (d) and gain (f) at 202 ps corresponding to the time of the injection of the seed pulse.

The behavior of a seeded 13.9 nm Ni-like Ag laser is very similar to the 32.6 nm seed Ne-like Ti laser discussed previously. The energy vs. length, bandwidth vs. length, frequency profiles, and temporal profiles are shown in figure 8.12. As the seed amplifies, the amplifier bandwidth does not support the initial bandwidth of the harmonic seed. As a result, the initial amplification phase is governed by a slow growth in energy with substantial reduction in the bandwidth, and a corresponding increase in the pulse duration. Once the bandwidth of the amplified seed has narrowed to match the amplifier, quasi-exponential amplification occurs until saturation is reached. Finally, in saturation the maximum energy extraction occurs, and some additional temporal broadening occurs due to saturation broadening caused by re-pumping of the laser level. The left inset of figure 8.12 shows the dramatic narrowing of the line for the different amplifier lengths, while the right inset shows the temporal pulse shapes for the different amplifier lengths. The amplified pulse duration is approximately 1 ps in duration, very similar to the Ne-like Ti amplifier.

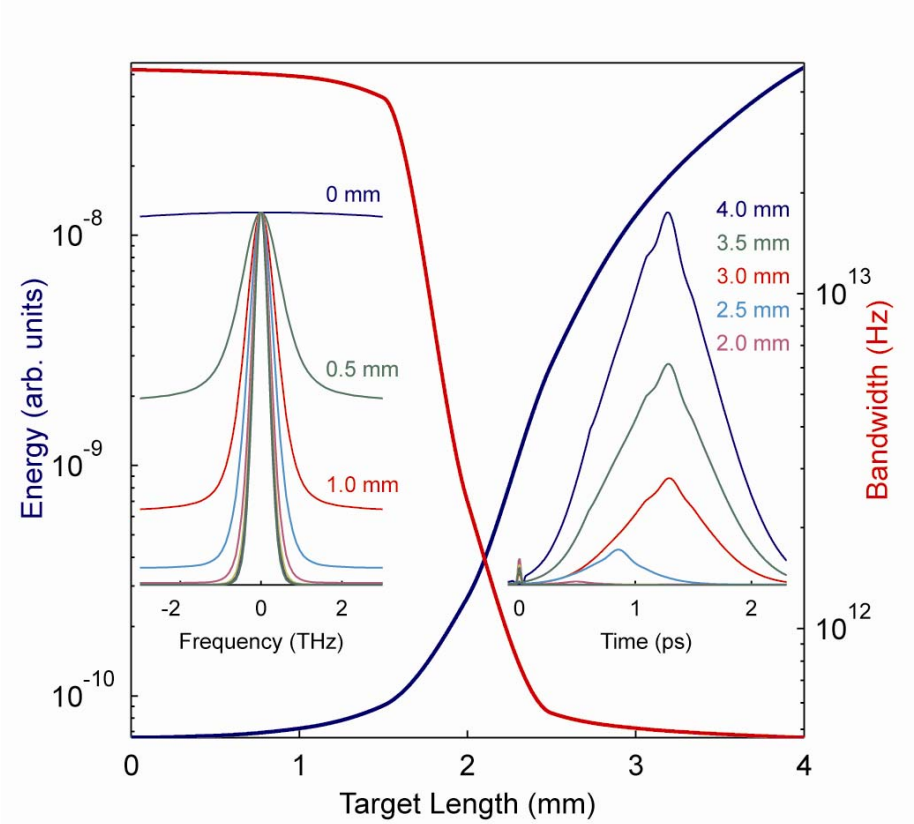

Figure 8.12: Computed variation of the energy, bandwidth, spectrum and pulse shape of the seeded 13.9-nm laser pulse as a function of the Ni-like Ag amplifier length. The left insert illustrates the rapid narrowing of the normalized spectrum as the seed pulse is amplified along the plasma column. In the main graph, the red curve describes the corresponding variation of the spectral bandwidth, defined for the purpose of this figure as the spectral width containing 76% of the pulse energy. This bandwidth decrease is accompanied by a slow initial increase of the pulse energy, which is followed by a quasi-exponential increase that tapers when the saturation fluence is reached (blue curve). The insert on the right illustrates the evolution of the laser pulse shape, which is characterized by rapid initial width increase due to the amplifier bandwidth limitations, and by slight asymmetries caused by gain saturation. The amplified pulse is preceded by a short pulse of nearly constant intensity composed of the broad spectrum of non-amplified frequencies.

In addition to studying the general behavior of the amplified seed, the near and far-field beam patterns were measured for the Ni-like Ag plasma amplifier[107]. A comparison between the measured and simulated far-field beam profiles for each of the two cases is illustrated in Fig. 8.13 along with the corresponding profile of the high harmonic seed.

[107] M. Berrill, D. Alessi, Y. Wang, S. R. Comingue, D. H. Martz, B. M. Luther, Y. Liu, and J. J. Rocca, "*Improved beam characteristics of solid-target soft x-ray laser amplifiers by injection seeding with high harmonics*", Optics Letters, In Press (2010).

When a harmonic seed pulse with a FWHM divergence of 0.5±0.03 x 0.7±0.04 mrad in the directions perpendicular and parallel to the target respectively was used to seed the plasma, an amplified pulse with a divergence of 1.4±0.14 x 0.7±0.07 mrad was measured to result (Fig. 8.13c). Simulations agree in showing that the divergence of the amplified beam in the direction parallel to the target surface closely resembles that of the seed beam, while the divergence perpendicular to the target surface is larger due to refraction**.** When the divergence of the harmonic seed was increased to 1.6±0.3 x 1.4±0.4 mrad, an amplified pulse with a divergence of 1.5±0.08 x 1.2±0.15 mrad was measured (Fig. 8.13d). The results show that when the divergence of the input harmonic seed is larger than ~1 mrad the far field of the amplified seed is almost completely dominated by the seed, while for smaller divergences it is controlled by both the input seed and refraction. These beam divergences are nearly an order of magnitude smaller than those corresponding to the unseeded amplifier (Fig. 1.8).

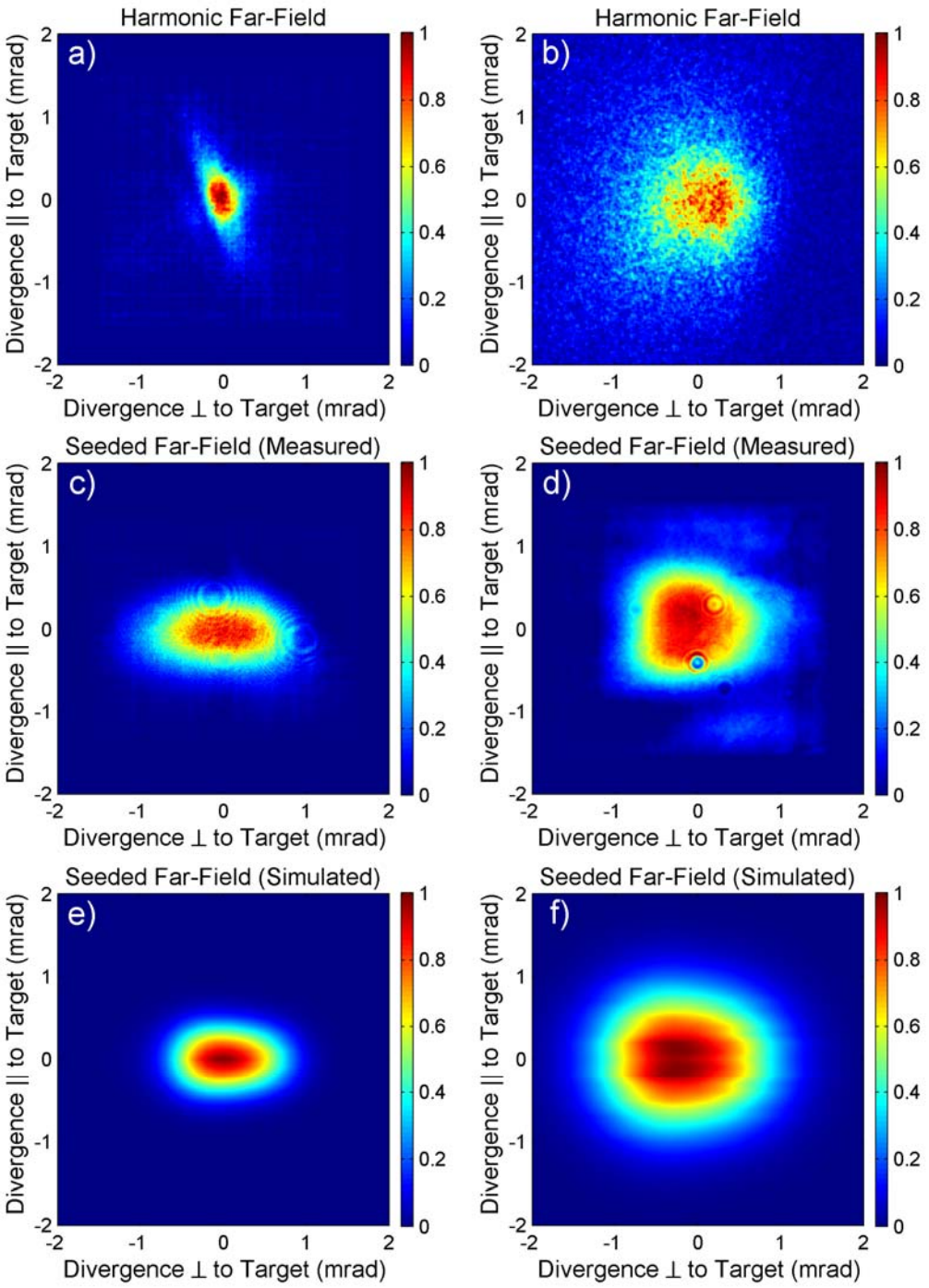

Figure 8.13: Comparison of far-field profiles of : a) and b) measured high harmonic seeds with two different divergences; c) and d) corresponding measured seeded laser beams ; and e) and f) simulated seeded laser beams.

Figure 8.14 compares the measured near-field profiles of the ASE and seeded beams. The location of the center of the near-field beam spot with respect to the target surface (Fig. 8.14a, 8.14c) is dominantly determined by the position of the peak of the gain (~ 35 μm from the target in Fig 8.11f), and was measured to be at a distance of 33±4 μm in good agreement with the simulated near field profile (Fig. 8.14b & 8.14d). Model simulations show that the location of the gain is in turn dependent on the early pre-pulse that is responsible for creating the initial plasma profile, and that the absence of this pre-pulse shifts the gain closer to the target surface (to a distance of ~ 15 μm). As the seed propagates through the plasma amplifier, its intensity quickly saturates, yielding a near field profile that is dominantly determined by the spatial distribution of the saturation fluence integrated over the amplifier length. The measured near-field size of the unseeded ASE laser (Fig 8.14a) is characterized by a full-width at half maximum of 11.3±4 x 13.3±3 μm in the directions perpendicular and parallel to the target surface respectively. The measured size of the seeded laser beam (Fig 8.14c) is smaller, 6.0±0.6 x 8.3±1.5 μm. The larger near-field spot size of the ASE laser in the direction parallel to the target surface is due to the larger divergence of the ASE laser, which allows rays with different trajectories to amplify across the entire gain region. By contrast the narrow divergence of the harmonic seed causes all the rays to effectively take similar paths, resulting in a narrower beam profile. This size difference is enhanced in the direction parallel to the target surface due to the larger gain size, and to the fact that the seeded beam is more sensitive to refraction caused by the electron density profile of the plasma amplifier (Fig. 8.11d) which acts as a weak negative lens. It should be noticed that the simulation results shown in Fig. 8.14 assume a perfect overlap between the laser pulses. Computations show that a 10 μm

misalignment causes the gain region and resulting near-field beam size to decrease by ~20% in the direction parallel to the target surface.

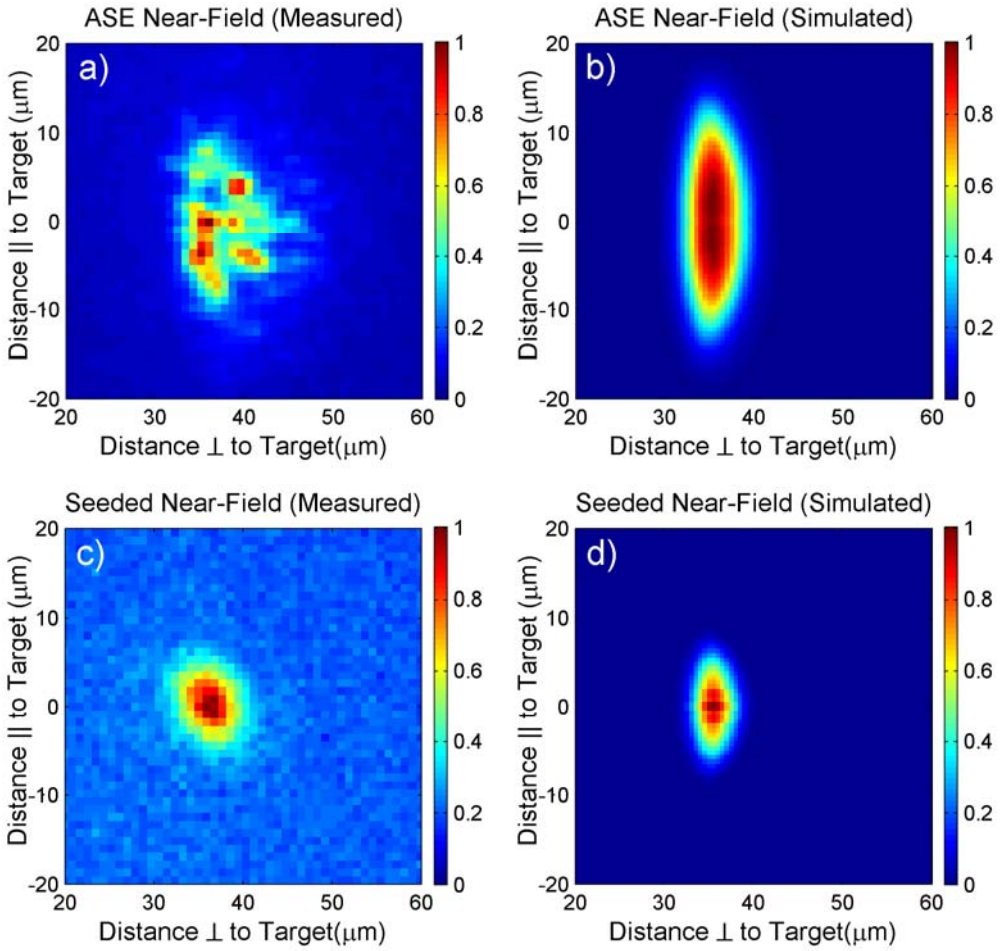

Figure 8.14: Measured and simulated near-field beam profiles for the un-seeded (ASE) and seeded lasers.

VIII.E) Photoionized Plasmas Created by Soft X-Ray Lasers

The development of high intensity soft x-ray lasers creates the opportunity to study the unique properties of plasmas created by intense monochromatic soft x-ray light. The table-top soft x-ray laser beams generated by collisional electron impact excitation of ions

in discharge-created and laser–created plasmas can be focused to generate plasmas with pulses ranging from the nanosecond[108] to the picosecond (section VIII.A and VIII.B) time scales. The advent of soft x-ray free electron lasers (FEL)[109] will allow the study of plasmas heated by extremely intense soft x-ray pulses in the complementary femtosecond time scale. In anticipation to experiments, theoretical studies have been conducted, that predict the characteristics of plasmas created with intense monochromatic soft x-ray light will depend strongly on the target material and differ significantly from those created with visible lasers[110]. However, no experimental results of the study of the characteristics of such plasmas have been reported.

We performed a spectroscopic study of plasmas created by focused soft x-ray laser pulses of ~1 ns duration on solid targets, and compared the results to hydrodynamic/atomic physics model simulations[111]. In this experiment, a 1.2 ns, 46.9 nm soft x-ray laser was focused onto a Si or Cr sample using a Sc/Si multilayer mirror, producing a focal spot of 10-15 μm diameter. Three pulse energies of 0.5 μJ, 3.1 μJ and 17 μJ; corresponding to peak intensities of $4x10^8$ W/cm^2, 2.5 $x10^9$ W/cm^2 and 1.4 $x10^{10}$ W/cm^2 respectively were used. The light emitted from the plasma was collected on a spectrometer. The computer models were used to simulate the plasma, which included photoionization as an additional absorption method. A post-processor was used to synthesize spectra based on multi-cell radiation transport and the computed populations and opacities. To improve the accuracy of

---

[108] B. R. Benware, A. Ozols, J. J. Rocca, I. A. Artioukov, V. V. Kondratenko, and A. V. Vinogradov, "*Focusing of a tabletop soft-x-ray laser beam and laser ablation*", Optics Letters, 24, Issue 23, pp. 1714-1716, 1999.

[109] Ackermann, W. et al. "*Operation of a free-electron laser from the extreme ultraviolet to the water window*" Nature Photonics 1, 336–342 (2007).

[110] M. Fajardo, P. Zeitoun, and J.-C. Gauthier, "*Hydrodynamic simulation of XUV laser-produced plasmas*", The European Physical Journal D, 29, 69-75, 2004.

[111] M. Berrill, F. Brizuela, B. Langdon, H. Bravo, C.S. Menoni, and J.J. Rocca, "*Warm Photoionized Plasmas Created by Soft X-Ray Laser Irradiation of Solid Targets*," Journal of the Optical Society of America B 25, B32, (2008).

the synthesized spectra the level energies and transition probabilities were calibrated using experimental data when available[112].

At the lowest irradiation energy investigated, 0.5 μJ, all three elements were found to be below the ablation threshold, in agreement with the simulations. At the intermediate energy of 3.1 μJ plasma radiation from neutral Cr atoms was observed (Fig. 8.17c). At this energy Si is very close to the ablation threshold, resulting in only very weak emission from two of strongest Si I lines in the ultraviolet spectra (Fig. 8.17a). These observations agree with model simulations (Fig. 8.15) that predict that the plasma reaches a peak temperature of 1.0 eV and a peak degree of ionization of 0.2 while Si, that is at the threshold of ablation, only reaches a peak temperature of 0.2 eV and a degree of ionization $Z<0.01$. The different behavior of these materials is to be expected, as the absorption length of the 46.9 nm laser light in Si (~300 nm) greatly exceeds that of Cr and Ag (~18 nm and ~7.5 nm respectively) Consequently, in Si the soft x-ray light interacts with a much larger volume of material which results in a higher ablation threshold, and in a colder plasma.

At the highest experiment irradiation energy (17 μJ) plasma radiation was observed for all three elements. Figure 8.17 shows the measured time integrated visible spectra corresponding to Si (Fig. 8.17(b) and Cr (Fig. 8.17 (d)) plasmas for this irradiation condition. The Si spectra of figure 8.17 (b) still only displays lines associated with neutral Si (Si I). Classified lines from singly charged silicon (Si II) that fall within the spectral window of the measurement (eg: 207.27 nm, 290.43 nm, 290.57 nm) are not observed, an indication that this is a very low temperature plasma, in agreement with model calculations. In contrast, spectra of plasmas created by irradiation of Cr targets with the same soft x-ray laser intensity show lines of Cr II (Fig. 8.17(d)). Figure 8.16 shows the computed plasma

[112] NIST Atomic Spectra Database Version 3, http://physics.nist.gov/PhysRefData/ASD/index.html

parameters for Si and Cr plasmas created under these irradiation conditions. The peak temperature for Si is 1.1 eV (Fig. 8.16(a)) while the Cr reaches a significantly higher temperature of 3.5 eV (Fig. 8.16(b)). This again reflects the difference in the photoionization cross sections at 46.9 nm: 6.1×10^{-19} cm^2 and 9.5×10^{-18} cm^2 for Si and Cr respectively. This difference in the cross section results in more energy being absorbed by fewer atoms for Cr than for Si. The larger Cr plasma temperature results in a computed peak degree of ionization of 1.6 for Cr as compared with a degree of ionization of only 0.2 for Si (Fig. 8.16(f) and 8.16(e) respectively). Due to the higher temperature the Cr plasma has an increased expansion velocity (Fig. 8.16(c,d)), that results in significantly denser plasma away from the target surface.

Figure 8.18 shows simulated spectra for Si and Cr for the irradiation conditions corresponding to the experimental spectra of Fig. 8.17(b) and 8.17(d). The computed Si spectra resembles well that observed in the experiments, showing only Si I lines. The synthesized Cr spectrum also reproduces most of the features of the experimental data, but shows a slightly larger ratio between Cr II and Cr I lines and the presence of weak Cr III lines. This is in part due to the fact that the synthetic spectra is calculated for the plasma conditions on axis of the irradiated spot, where the plasma has the highest temperature.

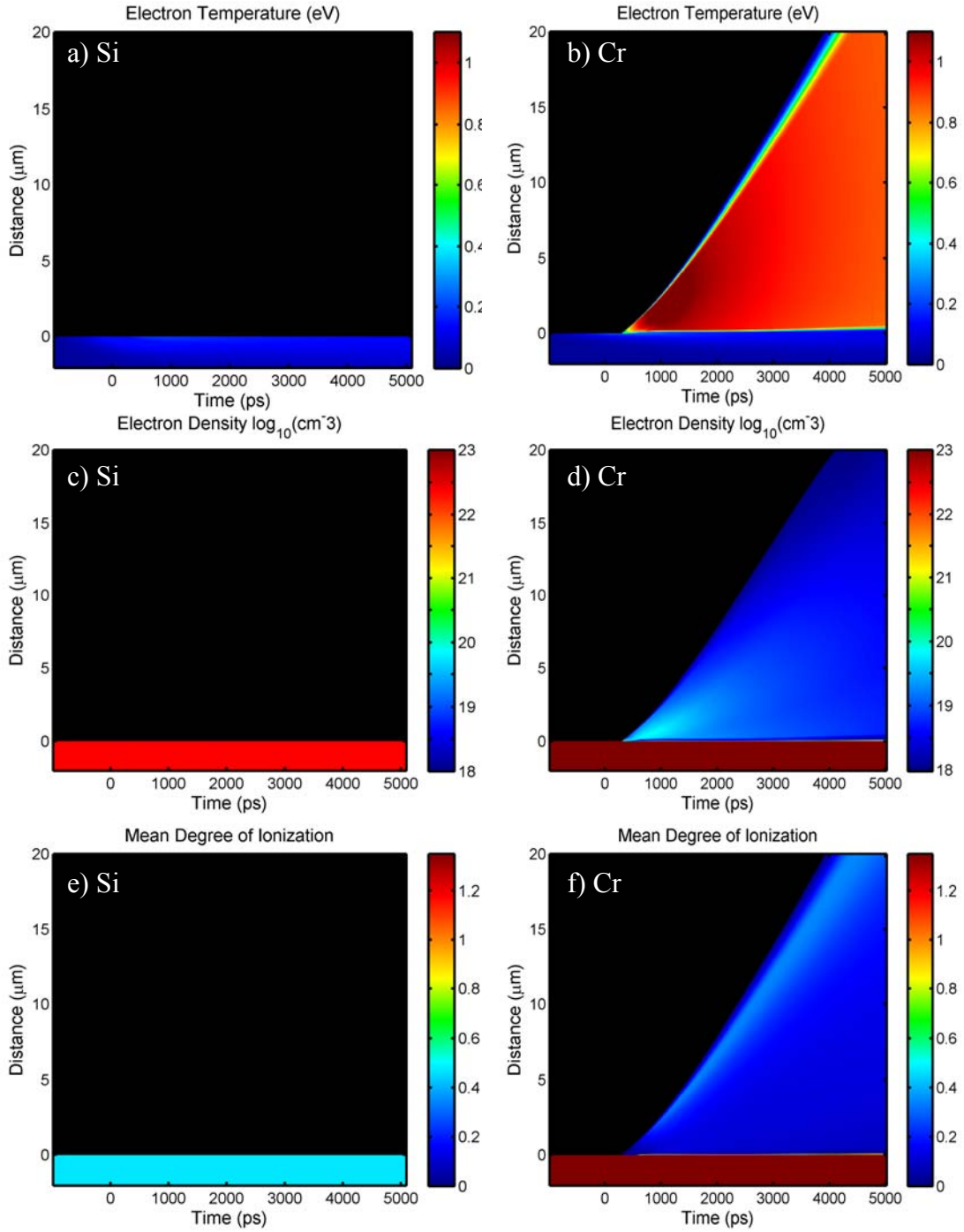

Figure 8.15: Simulated plasma parameters corresponding to Si and Cr plasmas generated by 3.1 μJ energy, 1.2 ns duration soft x-ray laser pulse irradiation (λ = 46.9 nm) of solid targets . Due to the smaller absorption cross section the Si (a) plasma is significantly colder that the Cr (b) plasma and does not reach the ablation threshold (c,d). Due to the lower temperature the Si plasma (e) has a much lower degree of ionization than the Cr plasma (f).

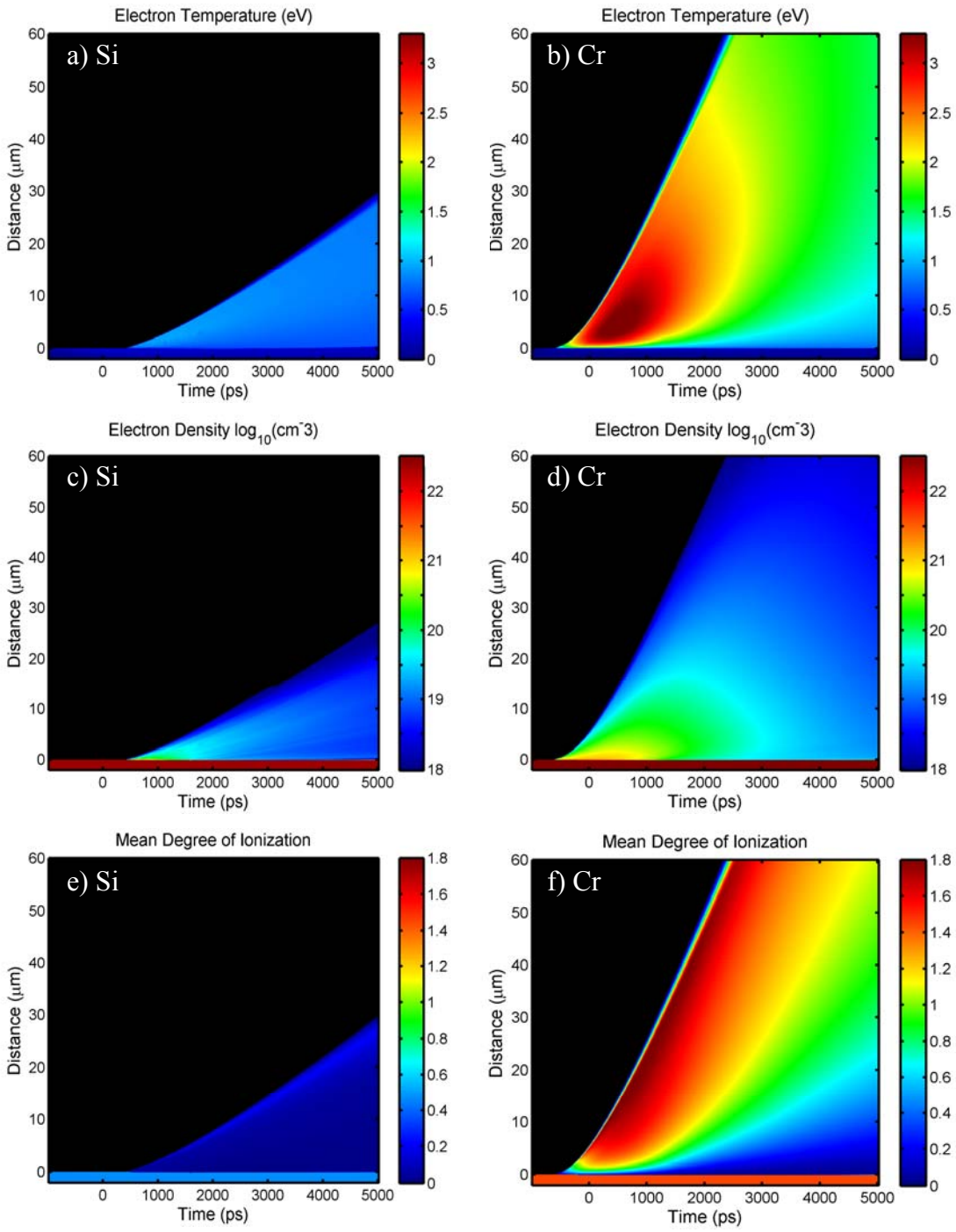

Figure 8.16: Simulated plasma parameters corresponding to Si and Cr plasmas generated by 17 μJ energy, 1.2 ns duration soft x-ray laser pulse irradiation (λ = 46.9 nm) of solid targets . Due to the smaller absorption cross section the Si (a) plasma is significantly colder that the Cr (b) plasma. The Cr plasma expands at a significantly higher rate (d). Due to the lower temperature the Si plasma (e) has a much lower degree of ionization than the Cr plasma (f).

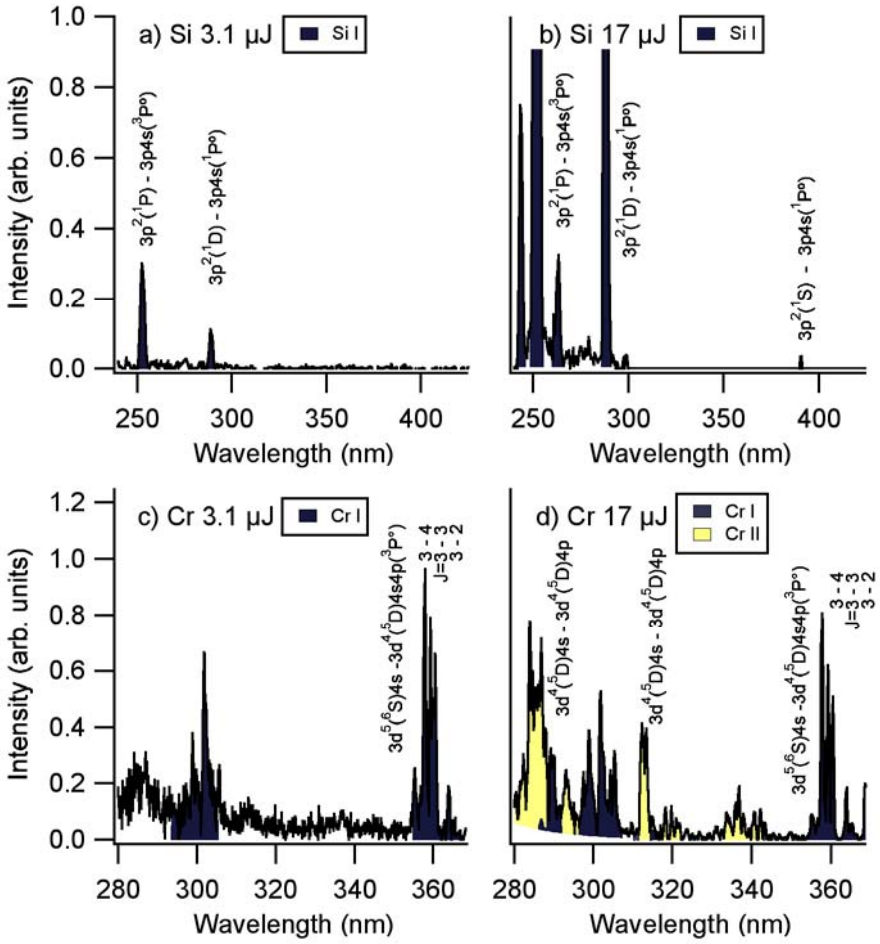

Figure 8.17: Measured spectra of Si and Cr plasmas created irradiating solid targets with 3.1 µJ and 17 µJ 46.9 nm soft x-ray laser pulses. At 3.1 µJ Si is only slightly above the ablation threshold (a), while for Cr (c) strong lines from the neutral atoms are present. At 17 µJ only neutral atom lines are present for Si (b), while the Cr (d) spectra show lines from both the neutral atoms and the singly charged ions.

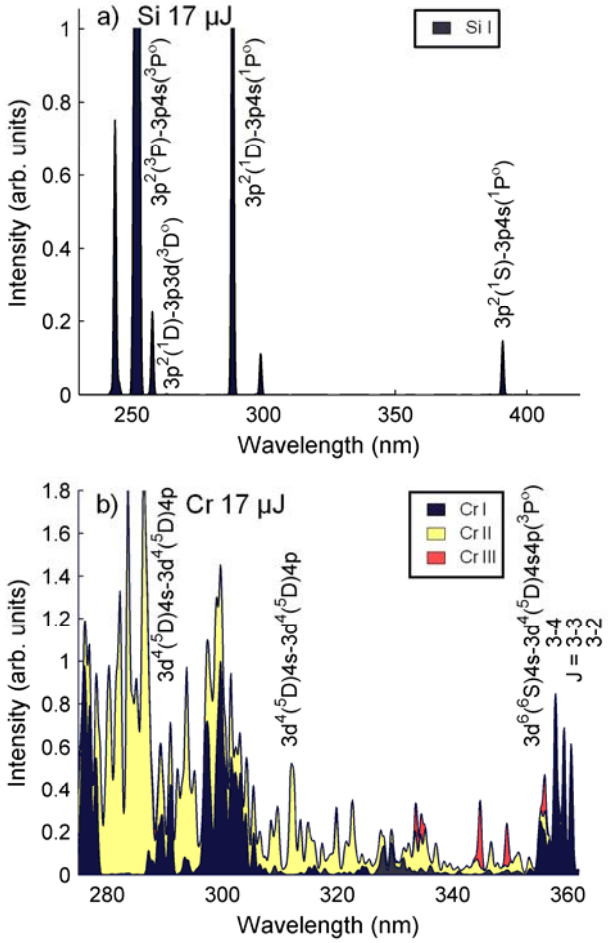

Figure 8.18: Simulated spectra for Si and Cr plasmas created by 17 µJ soft x-ray laser (λ = 46.9 nm) pulse irradiation. The Si spectra is completely dominated be neutral atom lines (Si I) (a), while the hotter Cr spectra contains large numbers of both Cr I and Cr II lines (b).

Simulations were also conducted for higher irradiation energies. The results show that as the intensity of the soft x-ray laser is increased, the behavior of the different elements tends to converge. When the laser energy is increased by a factor of 10, the temperature of the Si plasma is computed to increase slightly above 3.5 eV while the Cr plasma increases to 9.0 eV. Additionally, the mean degree of ionization increases to Z= 1.4 for Si and to 2.5 for Cr. If the laser energy is further increased by a factor of 60, to 1 mJ,

the electron temperature is computed to reach 7 eV for Si (Fig. 8.19(a)) and 16 eV for Cr (Fig. 8.19(b)), while the degree of ionization of the Si plasma, Z= 2.5 (Fig. 8.19(c)), is calculated to approach that for Cr, Z= 3.0 (Fig. 8.19(d)). The predicted convergence of the plasma parameters as the irradiation flux is increased is caused by the fact that the amount of mass ablated from the three materials tends to equalize at increased irradiation. This is caused by the more rapid increase in the degree of ionization for Cr and Ag that causes these plasmas to become more rapidly transparent than Si to the 25 eV laser photons (depleted of the absorbing neutral and singly charged ions). At high irradiation energies plasmas with a very uniform degree of ionization can be created. For example, the degree of ionization of a Cr plasma created under the high intensity condition (1 ns after the peak of a 1.7 mJ laser pulse) is computed to vary by less than 10% over 90% of the entire plasma volume. However, the plasma density within the volume changes significantly due to expansion. The degree of ionization at which the plasma becomes transparent increases with decreasing laser wavelength. Therefore shorter wavelength soft x-ray lasers will create hotter plasmas, and preserve the differences between elements until the plasma reaches a higher degree of ionization.

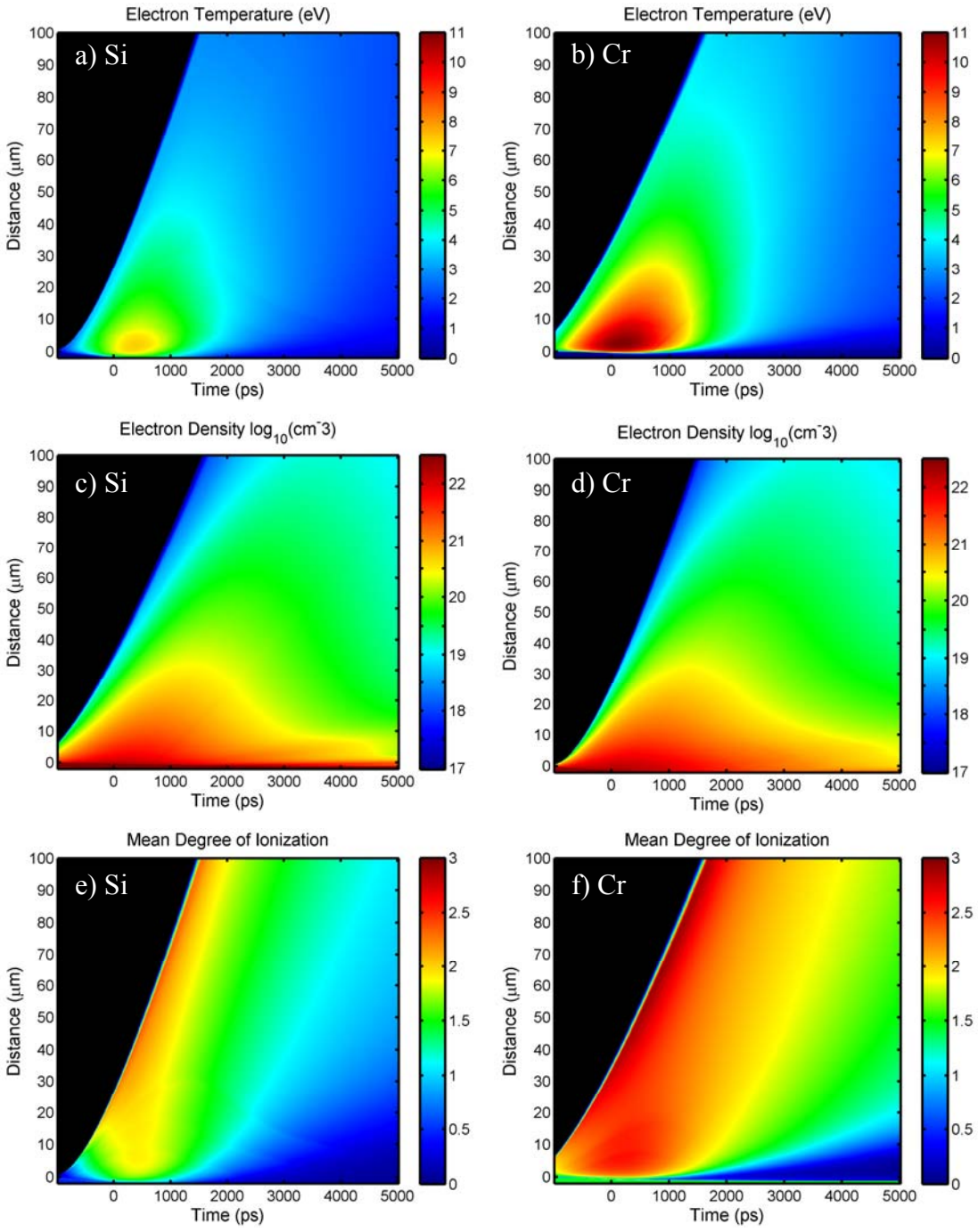

Figure 8.19: Simulated plasma parameters corresponding to Si and Cr plasmas generated by 1 mJ energy, 1.2 ns duration soft x-ray laser pulse irradiation (λ=46.9 nm) of solid targets . Due to the higher energy, the differences between the Si and Cr plasmas are significantly reduced. The Si (a) plasma is slightly colder that the Cr (b) plasma, while the electron densities are very close (c,d). The Si plasma (e) still has a significantly lower degree of ionization than the Cr plasma (f).

CHAPTER IX.) CONCLUSIONS:

The goal of this research was to create a computer model to better understand the physics involved in laser created plasmas and soft x-ray lasers. The soft x-ray lasers are pumped by electron impact excitation of highly charged ions in dense laser-created plasmas. To accomplish this, I created a 1.5D and a 2D hydrodynamic / atomic model capable of simulating laser created plasmas and used it to simulate the plasmas that give rise to the soft x-ray amplifiers. The models include all of the hydrodynamic equations, an equation of state, a complete thermodynamic model, and a comprehensive atomic model with multi-cell radiation transport. The atomic physic model includes all of the necessary ion species with atomic data for thousands of levels and is capable of computing the population inversion that gives rise to laser amplification. A 3D post processor ray trace was developed included to simulate the generated soft x-ray lasers. The simulations performed can fully characterize all of the important plasma properties as well as the resulting soft x-ray laser. Direct comparisons with experimental results allowed for a better understanding of the physics of laser created plasmas used for the generation of soft x-ray lasers, and provides a tool to advance their design.

The model was used to understand the physics and plasma dynamics involved in the generation of transient EUV lasers in Ni-like and Ne-like ions pumped by heating a laser created plasma with a picosecond laser pulse impinging at grazing incidence. For efficient laser amplification to occur, several conditions must be met. The density gradients must be

small to allow extended propagation of the amplified radiation in the gain media, the electron temperature and density must be sufficient to create a large population inversion in the Ni-like or Ne-like species, and the desired degree of ionization must be maintained. With the two pulse scheme described in the introduction, these conditions can be met.

The model was used to simulate a Ni-like Cd laser operating at 13.2 nm wavelength created by a 120 ps, 200 mJ pre-pulse focused at normal incidence, pumped by an 8 ps duration optical laser pulse of 1 J energy focused at a grazing incidence angle of 23 degrees. The first laser pulse allows the plasma to expand which will create small electron density gradients. The model simulated the plasma density profiles and predicted that they are approximately exponential and expand with time. The grazing incidence angle of the second pulse refracts in the plasma, coupling the pump energy into a localized region with electron density around 2×10^{20} cm^{-3}. The model shows that this allows the plasma to reach temperatures in excess of 600 eV, which results in the creation of a large population inversion in the Ni-like ions. This heating is significantly more efficient than the heating that would have occurred if the short pulse beam was directed at normal incidence. In the latter case most of the pulse energy would be absorbed closer to the target, where the density gradients are too steep for adequate propagation of the soft x-ray light along the gain region. In that case the more optimum gain region (at an electron density of 2×10^{20} cm^{-3}) heats up to only 400 eV, resulting in a significantly lower gain. As a result, the grazing incidence pumping geometry allows for a significantly increase in the pumping efficiency, that allows for implementation of saturated lasers with wavelengths in the 13 nm wavelength region using short pump pulse energies of only 1 J.

The simulation results confirm that the soft x-ray laser is the result of a transient population inversion that is much higher than those that can be created in steady state. This gives rise to large gain coefficients that allow soft x-ray laser to reach gain-saturation after only a few millimeters of amplification in the plasma. The transient gain coefficients can reach as much as an order of magnitude larger than the steady-state value, reaching a peak value of 150 cm^{-1}. Gain is computed to take place in a region of about 20 μm x 20 μm located at a distance of about 15 μm from the target surface. The large transient gain is possible because the laser upper level is directly pumped by strong monopole electron impact excitation from the ground level before the laser lower level has a chance to populate. The model also identified several mechanisms that terminate the gain. The first mechanism is cooling of the plasma by radiation and thermal conduction. The model predicted that significant cooling will occur within ~ 15 ps. A second mechanism is over ionization due to the increased temperatures. This ionization takes place in 10-20 ps. While both of these mechanisms will limit the duration of the EUV laser amplification, the model indicates that the gain is very transient in nature further limiting its duration. The transient nature of the gain puts an additional limitation on the lifetime of the gain that favors very short pulses.

Simulations of the 13.2 nm Ni-like Cd soft x-ray laser show good agreement between the computed laser output pulse characteristics and the observed experimental characteristics. The soft x-ray laser saturates at about 2 mm compared to the saturation in the experiment at 2.5-3.0 mm in the experiment due to the larger gain of the model. This difference in the gain can be attributed in part to the fact the model assumes an ideal plasma, while in reality the uniformity of the plasma, overlap between the pre-pulse and

pump pulse line focus, etc, are less than ideal. The higher gain, earlier saturation, and ideal nature of the modeled plasma produce pulses with an output energy of 2.5 μJ, compared to the experimental pulse energy of ~ 0.5 μJ. The simulated near field and far field images are in reasonable agreement with the experiment. The simulated beam shows a divergence of 5 mrad x 10 mrad while the experimental divergence is 7 mrad x 12-14 mrad. The simulated laser pulse duration is somewhat longer in duration (9 ps), than that measured in the experiment (5 ps) but this can be easily explained by the stronger saturation re-broadening in the simulation.

The model was used to better understand how the observed lasing in multiple elements along the Ni-like isoelectronic sequence from Mo to Sn was possible with practically the same pump pulse energy. Simulations at higher pulse energies were performed in Ni-like La in preparation for future experiments. The general behavior of the La laser was very similar to the behavior of the Ni-like Cd laser previously discussed. The primary difference is due to the smaller laser cross section caused by the shorter wavelength. To partially overcome this, a steeper angle was used to pump a higher density region. In spite of this, the gain was still lower resulting in saturation at a longer length of ~4 mm compared with ~2mm for the Ni-like Cd laser. However, due to the higher density and shorter wavelength, the saturation intensity is higher, allowing for approximately 10 μJ for a 6mm long amplifier.

In addition to the ASE lasers, simulations and experiments were performed in which the soft x-ray amplifier was seeded by a pulse generated through high harmonic generation. The seeding of the amplifier allows for a fully spatially coherent beam and better near and far-field beam profiles. The results of a seeded 32.9 nm Ne-like Ti seeded

laser and a 13.9 nm Ni-like Ag seeded laser were discussed. The behavior of the seed is governed by the bandwidth limitations of the amplifier and the initial seed pulse. When the pulse first starts to amplify, its bandwidth significantly narrows until it matches the bandwidth of the amplifier. As a result of the dramatic narrowing the pulse duration of the laser significantly broadens until it is essentially transform limited. Then the pulse experiences a quasi-exponential amplification until the saturation fluence is reached. In saturation, efficient extraction of the soft x-ray laser occurs along with a slight increase in the pulse duration due to saturation broadening. The final pulsewidth is ~1 ps in duration in good agreement with the experimental results. Simulations of the soft x-ray laser near-field and far-field profiles were conducted using results of the 2D hydrodynamic model. Comparisons with experimental results show very good agreement in both the beam size and the divergence. By seeding, a dramatic decrease in the divergence of ~10x was observed.

In addition to simulating the plasmas used for the generation of soft x-ray laser, we have studied warm plasmas generated by focusing 46.9 nm soft x-ray laser pulses of nanosecond duration onto Si and Cr solid targets. The critical density corresponding to this wavelength (5×10^{23} cm^{-3}) exceeds solid density, and the absorption is dominated by single photon photoionization. Spectra of the soft x-ray laser-created plasmas were compared with those of plasmas created with an optical (λ= 800 nm) laser. The results agree with hydrodynamic model demonstrating that the soft-x-ray laser plasmas differ from those created by visible lasers and are strongly element-dependent, with characteristics largely determined by the position of the laser wavelength relative to absorption edges and resonances. Measured spectra agree with model simulations in showing that soft x-ray

laser-created Si plasmas, a low absorption material at 46.9 eV, are significantly colder and less ionized than plasmas created from more highly absorbent materials such as Cr. This strong elemental dependence is computed to soften at higher nanosecond pulse irradiation intensities that deplete the low charge species, whose photoionization cross sections dominate the plasma absorption. High intensity soft x-ray lasers generating shorter pulses will be able to create highly uniform warm dense plasma over large volumes.

APPENDIX A) VARIABLE LIST

Constants

m_s - Mass of species s (g)

m_e - Electron mass (9.11×10^{-28} g)

m_p - Proton mass (1.67×10^{-24} g)

e - Electronic charge (4.8×10^{-10} esu)

c - Speed of light (3.0×10^{10} cm/s)

h - Plank's constant (6.626×10^{-27} ergs-s)

$\hbar$ - Modified Plank's constant, $\hbar = h/2\pi$

α - Fine structure constant (7.297×10^{-3})

Coordinates

z - Distance from target surface (cm)

y - Distance from line center (cm)

x - Distance along the line focus (cm)

Density variables

m_i - Ion mass (g)

ρ_s - Mass density of species s, $\rho_s = m_s n_s$ (g/cm^3)

ρ - Mass density of the plasma (g/cm^3)

M - Mass of zone (g/cm^2)

n_s - Density of species s (cm^{-3})

n_e - Electron density (cm^{-3})

n_i - Ion density (cm^{-3})

$\dot{n}_s$ - Net creation rate of species s (cm^{-3}s^{-1})

Velocity equation

$\vec{v}_s$ - Velocity of species s (cm/s)

$\vec{v}$ - Plasma Velocity (cm/s)

p - Total pressure (dynes/cm^2)

p_s - Partial pressure of species s, $p_s = n_s T_s$ (dynes/ cm^2)

$\vec{\tau}_{vis}$ - Viscosity tensor

η - Viscosity coefficient

Q - Artificial viscosity

f_{ext} - External Forces

Energy Conservation

T_s - Temperature of species s (ergs)

T_e - Electron Temperature(ergs)

T_i - Ion Temperature (ergs)

ε_s - Gas Dynamic Energy Density (ergs/cm^3)

$\dot{q}$ - Heat flux (ergs cm^{-3} s^{-1})

E_{abs} - Absorbed energy (ergs cm^{-3} s^{-1})

E_{atom} - Atomic energy losses (ergs cm^{-3} s^{-1})

1.5 D Properties

R - Half width of plasma density profile

L - Half width of plasma temperature profile

W - Full width of laser beam

v_x - Plasma velocity along the z axis

v_y - Plasma velocity along the y axis

Electro-Magnetic Variables

$\vec{E}$ - Electric Field (statvolt/cm)

$\vec{B}$ - Magnetic Induction (gauss)

$\vec{j}$ - Current Density (statamp/cm^2)

Conductivity properties

τ, τ_{ei} - Electron-ion collision time (s)

ν_{ei} - Electron-ion collision frequency (s^{-1})

σ_{ei} - Electron-ion collision cross section (cm^2)

$\ln \Lambda$ - Coulomb logarithm

μ - Chemical potential (ergs^{-1})

$\bar{v}_e$ - Thermal velocity (cm/s)

r_0 - Inter-atomic spacing (cm)

c_s - Adiabatic speed of sound (cm)

τ_{eq} - Electron-ion equilibration time (s)

κ_i - Ion thermal conduction coefficient (s^{-1}cm^{-1})

κ_e - Electron thermal conduction coefficient (s^{-1} cm^{-1})

ν_p - Plasma frequency (s^{-1})

ω_p - Plasma frequency (rad/s)

N_D - Debye number (rad/s)

λ_D - Debye length (cm)

Λ_B - DeBroglie wavelength (cm)

ω_e - Cyclotronic frequency (rad/s)

σ - Electrical conductivity (s^{-1})

n_c - Critical density (cm^{-3})

n - Index of refraction

v_g - Group velocity (cm/s)

ω - Laser frequency (rad/s)

λ - Laser wavelength (cm)

k - Wave number (cm^{-1})

α - Absorption coefficient (cm^{-1})

l_{abs} - Absorption length (cm)

Gain Variables

ω - Laser frequency (rad/s)

λ - Laser wavelength (cm)

I - Laser Intensity (ergs cm^{-2} s^{-1})

j - Emissivity (ergs cm^{-3} s^{-1})

g - Gain (cm^{-1})

$\Phi(\nu)$ - Line profile

$\Delta\nu$ - FWHM line width (s^{-1})

Atomic Model

Z - Mean degree of ionization, $Z = n_e / n_i$

E_{atom} - Atomic losses (ergs cm^{-3} s^{-1})

N_i^Z - Population of the i^{th} level in the Z^{th} ion (cm^{-3})

g_i - Multiplicity of the i^{th} level

$I_{i,j}^Z$ - Ionization rate coefficient from the i^{th} level of the Z^{th} ionn to the j^{th} level of the $Z+1^{th}$ ion (cm^3/s)

$\beta_{i,j}^Z$ - 3-Body recombination rate coefficient from the i^{th} level of the $Z+1^{st}$ ion to the j^{th} level of the Z^{th} ion (cm^6/s)

$\alpha_{i,j}^Z$ - Radiative recombination rate coefficient from the i^{th} level of the $Z+1^{st}$ ion to the j^{th} level of the Z^{th} ion (cm^3/s)

$D_{i,j}^Z$ - Dielectronic recombination rate coefficient from the i^{th} level of the $Z+1^{st}$ ion to the j^{th} level of the Z^{th} ion (cm^3/s)

$A^{\alpha Z}_{i,j}$ - Auto-ionization rate from the i^{th} level of the Z^{th} ion to the j^{th} level of the $Z+1^{st}$ ion (s^{-1})

$E_{i,j}^Z$ - Excitation rate coefficient from the i^{th} level to the j^{th} level in the Z^{th} ion (cm^3/s)

$d_{i,j}^Z$ - De-Excitation rate coefficient from the i^{th} level to the j^{th} level in the Z^{th} ion (cm^3/s)

$A_{i,j}^Z$ - Radiative De-Excitation rate from the i^{th} level to the j^{th} level in the Z^{th} ion (s^{-1})

$C_{i\to j}$ - Coupling coefficient from zone i to j.

$\Delta E_{i,j}^Z$ - Energy difference between the i^{th} level to the j^{th} level in the Z^{th} ion (ergs)

gf - Weighted oscillator strength

τ - Optical depth

$P_e(\tau)$ - Photon escape probability

APPENDIX B) Vector Identities

Gradient: $\vec{\nabla} f$

Cartesian: $\vec{\nabla} f = \hat{x}\frac{\partial f}{\partial x} + \hat{y}\frac{\partial f}{\partial y} + \hat{z}\frac{\partial f}{\partial z}$

Cylindrical: $\vec{\nabla} f = \hat{r}\frac{\partial f}{\partial r} + \hat{\phi}\frac{1}{r}\frac{\partial f}{\partial \phi} + \hat{z}\frac{\partial f}{\partial z}$

Spherical: $\vec{\nabla} f = \hat{r}\frac{\partial f}{\partial r} + \hat{\phi}\frac{1}{r}\frac{\partial f}{\partial \phi} + \hat{\theta}\frac{1}{r\sin\phi}\frac{\partial f}{\partial \theta}$

1. $\vec{\nabla}(f+g) = \vec{\nabla} f + \vec{\nabla} g$
2. $\vec{\nabla}(cf) = c\vec{\nabla} f$ for any constant c
3. $\vec{\nabla}(fg) = g\vec{\nabla} f + f\vec{\nabla} g$
4. $\vec{\nabla}(f/g) = \left(g\vec{\nabla} f - f\vec{\nabla} g\right)/g^2$ at $\vec{x}$, where $g(\vec{x}) \neq 0$
5. $\vec{\nabla}\left(\vec{F}\cdot\vec{G}\right) = \vec{F}\times\left(\vec{\nabla}\times\vec{G}\right) - \left(\vec{\nabla}\times\vec{F}\right)\times\vec{G} + \left(\vec{G}\cdot\vec{\nabla}\right)\vec{F} + \left(\vec{F}\cdot\vec{\nabla}\right)\vec{G}$

Divergence: $\vec{\nabla}\cdot\vec{F}$

Cartesian: $\vec{\nabla}\cdot\vec{F} = \frac{\partial F_x}{\partial x} + \frac{\partial F_y}{\partial y} + \frac{\partial F_z}{\partial z}$

Cylindrical: $\vec{\nabla}\cdot\vec{F} = \frac{1}{r}\frac{\partial(rF_r)}{\partial r} + \frac{1}{r}\frac{\partial F_\phi}{\partial \phi} + \frac{\partial F_z}{\partial z}$

Spherical: $\vec{\nabla}\cdot\vec{F} = \frac{1}{r^2}\frac{\partial}{\partial r}\left(r^2 F_r\right) + \frac{1}{r\sin\phi}\frac{\partial}{\partial \phi}\left(\sin\phi F_\phi\right) + \frac{1}{r\sin\phi}\frac{\partial F_\theta}{\partial \theta}$

1. $\vec{\nabla}\cdot\left(\vec{F}+\vec{G}\right) = \vec{\nabla}\cdot\vec{F} + \vec{\nabla}\cdot\vec{G}$
2. $\vec{\nabla}\cdot\left(c\vec{F}\right) = c\vec{\nabla}\cdot\vec{F}$ for any constant c
3. $\vec{\nabla}\cdot\left(g\vec{F}\right) = g\vec{\nabla}\cdot\vec{F} + \vec{F}\cdot\vec{\nabla} g$
4. $\vec{\nabla}\cdot\left(\vec{F}\times\vec{G}\right) = \vec{G}\cdot\left(\vec{\nabla}\times\vec{F}\right) - \vec{F}\cdot\left(\vec{\nabla}\times\vec{G}\right)$

Curl: $\vec{\nabla}\times\vec{F}$

Cartesian: $\begin{vmatrix} \hat{x} & \hat{y} & \hat{z} \\ \dfrac{\partial}{\partial x} & \dfrac{\partial}{\partial y} & \dfrac{\partial}{\partial z} \\ F_x & F_y & F_z \end{vmatrix}$

Cylindrical: $\begin{vmatrix} \dfrac{\hat{r}}{r} & \hat{\phi} & \dfrac{\hat{z}}{r} \\ \dfrac{\partial}{\partial r} & \dfrac{\partial}{\partial \phi} & \dfrac{\partial}{\partial z} \\ F_r & rF_\phi & F_z \end{vmatrix}$

Spherical: $\begin{vmatrix} \dfrac{\hat{r}}{r^2\sin\theta} & \dfrac{\hat{\theta}}{r\sin\theta} & \dfrac{\hat{\phi}}{r} \\ \dfrac{\partial}{\partial r} & \dfrac{\partial}{\partial \theta} & \dfrac{\partial}{\partial \phi} \\ F_r & rF_\theta & r\sin\theta F_\phi \end{vmatrix}$

1. $\vec{\nabla}\times\left(\vec{F}+\vec{G}\right)=\vec{\nabla}\times\vec{F}+\vec{\nabla}\times\vec{G}$
2. $\vec{\nabla}\times\left(c\vec{F}\right)=c\vec{\nabla}\times\vec{F}$ for any constant c
3. $\vec{\nabla}\times\left(f\vec{F}\right)=f\vec{\nabla}\times\vec{F}+\vec{\nabla}f\times\vec{F}$
4. $\vec{\nabla}\times\left(\vec{F}\times\vec{G}\right)=\vec{F}\left(\vec{\nabla}\cdot\vec{G}\right)-\left(\vec{\nabla}\cdot\vec{F}\right)\vec{G}+\vec{G}\left(\vec{\nabla}\cdot\vec{F}\right)-\left(\vec{F}\cdot\vec{\nabla}\right)\vec{G}$

Laplacian: $\vec{\nabla}^2 f$

Cartesian: $\vec{\nabla}^2 f=\dfrac{\partial^2 f}{\partial x^2}+\dfrac{\partial^2 f}{\partial y^2}+\dfrac{\partial^2 f}{\partial z^2}$

Cylindrical: $\vec{\nabla}^2 f=\dfrac{1}{r}\dfrac{\partial}{\partial r}\left(r\dfrac{\partial f}{\partial r}\right)+\dfrac{1}{r^2}\dfrac{\partial^2 f}{r\partial\phi^2}+\hat{a}_z\dfrac{\partial^2 f}{\partial z^2}$

Spherical: $\vec{\nabla}^2 f=\dfrac{1}{r^2}\dfrac{\partial}{\partial r}\left(r^2\dfrac{\partial f}{\partial r}\right)+\dfrac{1}{r^2\sin\theta}\dfrac{\partial}{\partial\theta}\left(\sin\theta\dfrac{\partial f}{\partial\theta}\right)+\dfrac{1}{r^2\sin^2\theta}\dfrac{\partial^2 f}{\partial\phi^2}$

1. $\vec{\nabla}^2\left(f+g\right)=\vec{\nabla}^2 f+\vec{\nabla}^2 g$
2. $\vec{\nabla}^2\left(cf\right)=c\vec{\nabla}^2 f$ for any constant c
3. $\vec{\nabla}^2\left(fg\right)=f\vec{\nabla}^2 g+2\vec{\nabla}f\cdot\vec{\nabla}g+g\vec{\nabla}^2 f$

APPENDIX C) NUMERICAL TECHNIQUES

APPENDIX C.1) The Crank-Nicholson Method

The first step in writing a computer simulation is producing the numerical form. While there are many possible techniques, one commonly used technique is the Crank-Nicholson method[113]. In this technique both the spatial and temporal derivatives are written in an implicit scheme. As a quick review, consider a grid with zones identified by *j*. The value of a variable *X* at the point x_j at time t_n is written as X_j^n. The value of a variable *X* at the midpoint of zone *j* in the Crank-Nicholson scheme is written as $X_{j+1/2}^n$.

In the Crank-Nicholson scheme this is $X\big|_{j+1/2}^{n} = \frac{X_{j+1}^n + X_j^n}{2}$

The derivative of quantity *X* with respect to *x* at the midpoint between the points x_j and x_{j+1} at time t_n may be written as

$$\left.\frac{dX}{dx}\right|_{j+1/2}^{n} = \frac{X_{j+1}^n - X_j^n}{\Delta x}$$

By using the Crank-Nicholson method with all derivatives written in an implicit form, the equations are unconditionally stable. This means that a perturbation in the input will be reduced and will not amplify. This is very important for insuring an accurate solution. Clearly, if an unstable solution is present the actual solution is impossible to determine. Note that the unconditional stability only applies if all derivates are written in the implicit

[113] J. Crank and P. Nicholson, "*A Practical Method for Numerical Evaluation of the Solutions of Partial Differential Equations of the Heat-Conduction Type*", Proceedings of the Cambridge Philosophical Society, vol. 50, 1947, p. 50-67.

scheme. Within an equation this is possible, however since the equations are coupled this is not possible for all variables simultaneously. For example the velocity equation depends on the pressure gradients which depend on the temperature profiles. However, the temperature equations depend on the expansion and compression, which depend on the velocity profile. As a result, the solution of one equation affects the solution of the other. This can give rise to instabilities even if the individual equations are stable.

APPENDIX C.2) Solution of Linear Equations

Many numerical equations are written as a set of coupled linear equations. In this method the systems of linear equations are written in a matrix form $Ax = b$. Here A is a matrix, x is a vector of unknowns, and b is the solution vector. A fast and accurate solution of the linear equations is important. Details on this topic can be found in any numerical analysis or linear equation textbook. The standard method for solving the set of equations is through Gaussian elimination with back substitution. Most computer packages are capable of performing this operation.

As was seen in section III.A.4 many equations can be written in a tridiagonal form. In this form, non-zero entries are only found along the primary diagonal, upper-diagonal, and lower-diagonal. As a result, it is possible to use a special algorithm to solve the system considerably faster than any other method. The algorithm employed is Crout Factorization for Tridiagonal Linear Systems. As a comparison, the number of multiplications/divisions needed to solve n linear equations using Gaussian Elimination is $\frac{1}{3}n^3 + \frac{1}{2}n^2 - \frac{5}{6}n$, while the tridiagonal solution requires only $5n - 4$ multiplications /

divisions. Because there is no n^3 or n^2 dependence, a tridiagonal system can usually be solved orders of magnitude faster for large systems of equations.

APPENDIX C.3) Interpolation

Frequently, when calculating the plasma properties the need for information between known points arises. This requires the use of interpolation to approximate the data. For a description of a number of interpolation methods see Burden and Faires[114].

Linear

One of the simplest interpolation methods is linear interpolation. This was used when we identified the midpoint in the Crank-Nicholson method. In general, linear interpolation between any two points is

$$y(x) = y_1 + \frac{y_1 - y_2}{x_1 - x_2}(x - x_1)$$

Often, interpolation is needed in multiple dimensions. Linear interpolation can be easily extrapolated to 3 or more dimensions. (See figure C.1)

[114] Richard L. Burden, J. Douglas Faires, *Numerical Analysis*, Sixth Edition, Brooks/Cole Publishing Company, 1997.

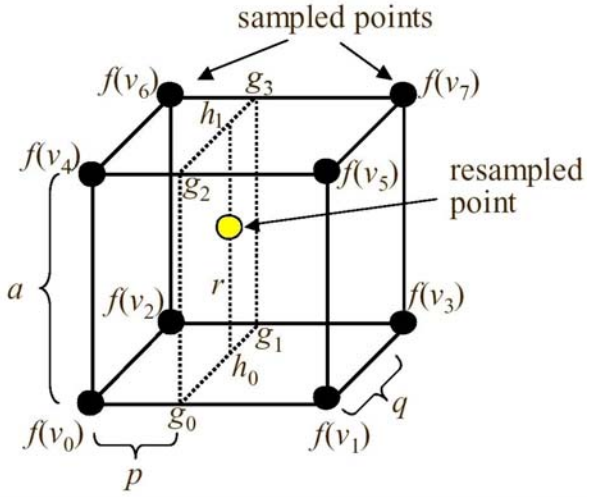

Figure C.1: Diagram illustrating points for trilinear interpolation

Linear interpolation:

$$g_0 = (1 - p/a) f(v_0) + (p/a) f(v_1)$$

$$g_1 = (1 - p/a) f(v_2) + (p/a) f(v_3)$$

$$g_2 = (1 - p/a) f(v_4) + (p/a) f(v_5)$$

$$g_3 = (1 - p/a) f(v_6) + (p/a) f(v_7)$$

Bilinear interpolation:

$$h_0 = (1 - q/a) g_0 + (q/a) g_1$$

$$h_1 = (1 - q/a) g_3 + (q/a) g_2$$

Trilinear interpolation:

$$f = (1 - r/a) h_0 + (r/a) h_1$$

Higher order linear interpolation can be easily extracted from the method for trilinear interpolation.

Upwind

Upwind interpolation is one of the simplest interpolation methods. The upwind schemes attempts to use differencing biased in the direction determined by the sign of the characteristic speeds. If we consider two points x_1 and x_2:

$$f = \begin{cases} y_1 & v < 0 \\ y_2 & v > 0 \end{cases}$$

When applied to a simple finite difference problem, it can introduce artificial diffusion. When applied to our hydrodynamic model, it offers the advantage of preserving the boundedness (monotonicity) of the solution.

QUICK

The Quadratic Upstream Interpolation for Convective Kinematics (QUICK) method[115] was developed to increase the order of the interpolation. It is based on quadratic interpolation favoring the points upwind. If we consider interpolation to the i-1/2 point:

$$f = \begin{cases} \frac{1}{8}\left(3y_i + 6y_{i-1} - y_{i-2}\right) & v > 0 \\ \frac{1}{8}\left(3y_{i-1} + 6y_i - y_{i+1}\right) & v < 0 \end{cases}$$

This interpolation has the advantage of being higher order, but can suffer from spurious oscillations.

[115] B. P. Leonard, "*A stable and accurate convective modeling procedure based on quadratic upstream interpolation*", Computer Methods in Applied Mechanics and Engineering, **19**, pp. 59-98 (1976).

SMART

The SMART method[116] was developed by Gaskell to provide a high order method for interpolation while still preserving the monotonicity of the solution. It can be shown that total variation diminishing (TVD) schemes preserve the monotonicity[117]. However, according to Gonunov's theorem[118] only first order linear schemes preserve monotonicity and are therefore TVD. To get around this, the SMART method is actually a combination of several interpolation method including QUICK and upwind interpolation. When possible, the QUICK method is used, but when this would violate the TVD properties the scheme reverts to an upwind scheme. To understand the scheme, consider figure C.2. Unless otherwise noted, the indices will be based of the figure below, and velocities will be assumed to be positive (flow to higher index cells)

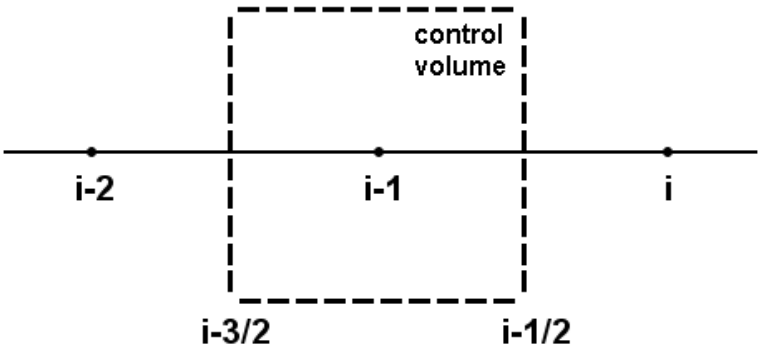

Figure C.2: Sample illustration showing the cell indecies for SMART interpolation

[116] P. H. Gaskell, A. H. C. Lau, "*Curvature-Compensated Convective Transport: SMART, A New Boundedness-Preserving Transport Algorithm*", International Journal for Numerical Methods in Fluids, **8**, 617-641 (1988)

[117] Godunov, Sergei K. (1959), "*A Difference Scheme for Numerical Solution of Discontinuous Solution of Hydrodynamic Equations*", Math. Sbornik, **47**, 271-306, translated US Joint Publ. Res. Service, JPRS 7226, 1969.

[118] P. H. Gaskell, A. H. C. Lau, "*Curvature-Compensated Convective Transport: SMART, A New Boundedness-Preserving Transport Algorithm*", International Journal for Numerical Methods in Fluids, Vol. 8, 617-641 (1988)

The variable is ϕ

$$\hat{\phi}_k = \frac{\phi_k - \phi_{i-2}}{\phi_i - \phi_{i-2}} \qquad \text{k = i-2, i-3/2, ..., i}$$

The interpolation is then

$$\phi_{i-1/2} = \begin{cases} \phi_{i-1} & if\ \hat{\phi}_{i-1} \notin [0,1] \\ 3\phi_{i-1} - 2\phi_{i-2} & if\ \hat{\phi}_{i-1} \in [0, \frac{1}{6}) \\ \phi_i & if\ \hat{\phi}_{i-1} \in (\frac{5}{6}, 1] \\ \frac{3}{8}\phi_i + \frac{6}{8}\phi_{i-1} + \frac{1}{8}\phi_{i-2} & if\ \hat{\phi}_{i-1} \in [\frac{1}{6}, \frac{5}{6}] \end{cases}$$

APPENDIX C.4) BLAS & LAPACK

For complicated models, efficient programming is required to reduce the computational requirements. I use a set of free packages programmed in Fortran to perform certain common operations as efficiently as possible. BLAS[119] (Basic Linear Algebra Subprograms) is a set of functions for performing basic linear algebra operations. LAPACK[120] (Linear Algebra PACKage) is a set of functions for solving common linear algebra problems. It includes algorithms such as Gaussian Elimination and matrix factorization. BLAS is available at http://www.netlib.org/blas/, and LAPACK is available at http://www.netlib.org/lapack/.

[119] C. L. Lawson, R. J. Hanson, D. Kincaid, and F. T. Krogh, "*Basic Linear Algebra Subprograms for FORTRAN usage*", ACM Trans. Math. Soft., 5 (1979), pp. 308--323.

[120] Anderson, et. al., *LAPACK Users' Guide*, Third Edition, Society for Industrial and Applied Mathematics, Philadelphia, PA , 1999, 0-89871-447-8.

APPENDIX D) Mathematical Derivations

This appendix contains some of the mathematical derivations used in the dissertation.

APPENDIX D.1) The divergence of the stress tensor:

$$\nabla \cdot \vec{\vec{T}} = -\nabla p + \nabla \cdot \vec{\vec{\sigma}}$$

$$\sigma_{ij} = \mu\left(\partial_i v_j + \partial_j v_i\right) + \lambda \partial_k v_k \delta_{ij}$$

$$\lambda = \tfrac{2}{3}\mu + \varsigma$$

$$\left(\nabla \cdot \vec{\vec{\sigma}}\right)_x = \partial_x \sigma_{xx} + \partial_y \sigma_{yx} + \partial_z \sigma_{zx}$$

$$\left(\nabla \cdot \vec{\vec{\sigma}}\right)_x = \left[\partial_x\left[\mu\left(\partial_x v_x + \partial_x v_x - \tfrac{2}{3}\nabla \cdot \vec{v}\right)\right] + \partial_y\left[\mu\left(\partial_y v_x + \partial_x v_y\right)\right] + \partial_z\left[\mu\left(\partial_z v_x + \partial_x v_z\right)\right]\right] + \partial_x\left[\varsigma\left(\nabla \cdot \vec{v}\right)\right]$$

$$\left(\nabla \cdot \vec{\vec{\sigma}}\right)_x = \nabla \cdot \left(\mu \nabla v_x\right) + \partial_x\left[\mu\left(\tfrac{1}{3}\nabla \cdot \vec{v}\right)\right] + \partial_x\left[\varsigma\left(\nabla \cdot \vec{v}\right)\right]$$

$$\nabla \cdot \vec{\vec{T}} = -\nabla p + \nabla \cdot \left(\mu \nabla \vec{v}\right) + \tfrac{1}{3}\nabla\left[\mu\left(\nabla \cdot \vec{v}\right)\right] + \nabla\left[\varsigma\left(\nabla \cdot \vec{v}\right)\right]$$

APPENDIX D.2) The dissipation function Φ:

$$\Phi = \nabla \cdot \left(\vec{\vec{\sigma}} \cdot \vec{v}\right) - \vec{v} \cdot \nabla \cdot \vec{\vec{\sigma}}$$

Note that $\vec{\vec{\sigma}} \cdot \vec{v} = v_i \sigma^{ij} n_j$

$$\sigma^{ij} = 2\mu E^{ij} + \left(\varsigma - \tfrac{2}{3}\mu\right) v^k_{,k} \delta^{ij}$$

Calculate $\vec{\vec{\sigma}} \cdot \vec{v}$

Look at the x component

$$\left(\vec{\vec{\sigma}} \cdot \vec{v}\right)_x = v_x \sigma^{xx} + v_y \sigma^{yx} + v_z \sigma^{zx}$$

$$\left(\ddot{\sigma}\cdot\vec{v}\right)_x = v_x\left[2\mu E^{xx} + \left(\varsigma - \tfrac{2}{3}\mu\right)v^k_{,k}\right] + v_y\left[2\mu E^{yx}\right] + v_z\left[2\mu E^{zx}\right]$$

$$E_{ij} = \tfrac{1}{2}\left(v_{i,j} + v_{j,i}\right)$$

$$\left(\ddot{\sigma}\cdot\vec{v}\right)_x = \mu\left[v_x\left(v^{x,x} + v^{x,x}\right) + v_y\left(v^{y,x} + v^{x,y}\right) + v_z\left(v^{z,x} + v^{x,z}\right)\right] + v_x\left(\varsigma - \tfrac{2}{3}\mu\right)v^k_{,k}$$

$$\left(\ddot{\sigma}\cdot\vec{v}\right)_x = \mu\left[\left(\vec{v}\cdot\nabla\right)v_x + \vec{v}\cdot\partial_x\vec{v}\right] + v_x\left(\varsigma - \tfrac{2}{3}\mu\right)\left(\nabla\cdot\vec{v}\right)$$

$$\ddot{\sigma}\cdot\vec{v} = \mu\left[\left(\vec{v}\cdot\nabla\right)\vec{v} + \tfrac{1}{2}\nabla\left(\vec{v}\cdot\vec{v}\right)\right] + \vec{v}\left(\varsigma - \tfrac{2}{3}\mu\right)\left(\nabla\cdot\vec{v}\right)$$

Calculate $\nabla\cdot\left(\ddot{\sigma}\cdot\vec{v}\right)$

$$\nabla\cdot\left(\ddot{\sigma}\cdot\vec{v}\right) = \nabla\cdot\mu\left[\left(\vec{v}\cdot\nabla\right)\vec{v} + \tfrac{1}{2}\nabla\left(\vec{v}\cdot\vec{v}\right)\right] + \nabla\cdot\vec{v}\left(\varsigma - \tfrac{2}{3}\mu\right)\left(\nabla\cdot\vec{v}\right)$$

$$\partial_x\left(\ddot{\sigma}\cdot\vec{v}\right)_x = \partial_x\mu\left[\left(\vec{v}\cdot\nabla\right)v_x + \tfrac{1}{2}\partial_x\left(\vec{v}\cdot\vec{v}\right)\right] + \partial_x v_x\left(\varsigma - \tfrac{2}{3}\mu\right)\left(\nabla\cdot\vec{v}\right)$$

Recall:

$$\nabla\cdot\ddot{\sigma} = \nabla\cdot\left(\mu\nabla\vec{v}\right) + \tfrac{1}{3}\nabla\left[\mu\left(\nabla\cdot\vec{v}\right)\right] + \nabla\left[\varsigma\left(\nabla\cdot\vec{v}\right)\right]$$

The dissipation function is[121]:

$$\Phi = \sigma'_{ij}\partial_j v_i$$

$$\lambda = \varsigma - \tfrac{2}{3}\mu$$

In Cartesian Coordinates (3D):

$$\Phi = 2\mu\left[\begin{array}{l}\left(\dfrac{\partial v_x}{\partial x}\right)^2 + \left(\dfrac{\partial v_y}{\partial y}\right)^2 + \left(\dfrac{\partial v_z}{\partial z}\right)^2 + \dfrac{1}{2}\left(\dfrac{\partial v_x}{\partial y} + \dfrac{\partial v_y}{\partial x}\right)^2 \\ + \dfrac{1}{2}\left(\dfrac{\partial v_y}{\partial z} + \dfrac{\partial v_z}{\partial y}\right)^2 + \dfrac{1}{2}\left(\dfrac{\partial v_z}{\partial x} + \dfrac{\partial v_x}{\partial z}\right)^2\end{array}\right] + \lambda\left[\frac{\partial v_x}{\partial x} + \frac{\partial v_y}{\partial y} + \frac{\partial v_z}{\partial z}\right]^2$$

In Cylindrical Coordinates (3D):

[121] Schaum's Outiline on Fluid Dynamics, Second Edition, pp.54, 326.

$$\Phi = \mu\left[\begin{array}{l} 2\left\{\left(\frac{\partial v_r}{\partial r}\right)^2+\left(\frac{1}{r}\frac{\partial v_\theta}{\partial \theta}+\frac{v_r}{r}\right)^2+\left(\frac{\partial v_z}{\partial z}\right)^2\right\}+\left(\frac{1}{r}\frac{\partial v_z}{\partial \theta}+\frac{\partial v_\theta}{\partial z}\right)^2 \\ +\left(\frac{\partial v_r}{\partial z}+\frac{\partial v_z}{\partial r}\right)^2+\left(\frac{1}{r}\frac{\partial v_r}{\partial \theta}+\frac{\partial v_\theta}{\partial r}-\frac{v_\theta}{r}\right)^2 \end{array}\right]+\lambda\left[\frac{\partial v_r}{\partial r}+\frac{1}{r}\frac{\partial v_\theta}{\partial \theta}+\frac{v_r}{r}+\frac{\partial v_z}{\partial z}\right]^2$$

In Spherical Coordinates (3D):

$$\Phi = \mu\left[\begin{array}{l} 2\left\{\left(\frac{\partial v_r}{\partial r}\right)^2+\left(\frac{1}{r}\frac{\partial v_\theta}{\partial \theta}+\frac{v_r}{r}\right)^2+\left(\frac{1}{r\sin\theta}\frac{\partial v_\phi}{\partial \phi}+\frac{v_r}{r}+\frac{v_\theta\cot\theta}{r}\right)^2\right\} \\ +\left\{\frac{1}{r\sin\theta}\frac{\partial v_\theta}{\partial \phi}+\frac{\sin\theta}{r}\frac{\partial}{\partial\theta}\left(\frac{v_\phi}{\sin\theta}\right)\right\}^2 \\ +\left\{\frac{1}{r\sin\theta}\frac{\partial v_r}{\partial \phi}+r\frac{\partial}{\partial r}\left(\frac{v_\phi}{r}\right)\right\}^2+\left\{r\frac{\partial}{\partial r}\left(\frac{v_\theta}{r}\right)+\frac{1}{r}\frac{\partial v_r}{\partial\theta}\right\}^2 \end{array}\right] + \lambda\left[\frac{\partial v_r}{\partial r}+\frac{1}{r}\frac{\partial v_\theta}{\partial\theta}+\frac{2v_r}{r}+\frac{1}{r\sin\theta}\frac{\partial v_\phi}{\partial\phi}+\frac{v_\theta\cot\theta}{r}\right]^2$$

If we substitute for λ, let ς = 0 we get:

In Cartesian Coordinates (1D):

$$\Phi = \mu\frac{4}{3}\left(\frac{\partial v_x}{\partial x}\right)^2$$

In Cartesian Coordinates (2D):

$$\Phi = \mu\left[2\left(\frac{\partial v_x}{\partial x}\right)^2+2\left(\frac{\partial v_y}{\partial y}\right)^2+\left(\frac{\partial v_x}{\partial y}+\frac{\partial v_y}{\partial x}\right)^2-\frac{2}{3}\left(\frac{\partial v_x}{\partial x}+\frac{\partial v_y}{\partial y}\right)^2\right]$$

In Cylindrical Coordinates (2D):

$$\Phi = \mu \left[\begin{array}{l} 2\left(\frac{\partial v_r}{\partial r}\right)^2 + 2\left(\frac{v_r}{r}\right)^2 + 2\left(\frac{\partial v_z}{\partial z}\right)^2 \\ +\left(\frac{\partial v_r}{\partial z} + \frac{\partial v_z}{\partial r}\right)^2 \\ -\frac{2}{3}\left(\frac{\partial v_r}{\partial r} + \frac{v_r}{r} + \frac{\partial v_z}{\partial z}\right)^2 \end{array} \right]$$

Numerical form for the dissipation function (2D):

We are using the indexing of SMARAI, where v is a face centered quantity, u is a cell centered quantity. If we assume a uniform grid spacing.

$$\Phi = \mu \left[2\left(\frac{\partial v_x}{\partial x}\right)^2 + 2\left(\frac{\partial v_y}{\partial y}\right)^2 + \left(\frac{\partial v_x}{\partial y} + \frac{\partial v_y}{\partial x}\right)^2 - \frac{2}{3}\left(\frac{\partial v_x}{\partial x} + \frac{\partial v_y}{\partial y}\right)^2 \right]$$

$$\Phi_{ij} = \mu_{ij} \left\{ \begin{array}{l} 2\left(\frac{v_{x,i+1,j} - v_{x,i,j}}{\Delta x}\right)^2 + 2\left(\frac{v_{y,j+1,i} - v_{y,j,i}}{\Delta y}\right)^2 \\ +\left(\frac{v_{x,i+1,j+1} + v_{x,i,j+1} - v_{x,i+1,j-1} - v_{x,i,j-1}}{2\Delta y} + \frac{v_{y,j+1,i+1} + v_{y,j,i+1} - v_{i,j+1,i-1} - v_{u,j,i-1}}{2\Delta x}\right)^2 \\ -\frac{2}{3}\left(\frac{v_{x,i+1,j} - v_{x,i,j}}{\Delta x} + \frac{v_{y,j+1,i} - v_{y,j,i}}{\Delta y}\right)^2 \end{array} \right\}$$

APPENDIX D.3) The Viscous Force

Recall the viscous force (with $\varsigma = 0$)

$$\nabla \cdot \vec{\tau}_{vis} = \nabla \cdot \left(\mu \nabla \vec{v}\right) + \tfrac{1}{3} \nabla \left[\mu \left(\nabla \cdot \vec{v}\right)\right]$$

In Cartesian Coordinates (1D):

$$\nabla \cdot \vec{\tau}_{vis} = \frac{4}{3} \frac{\partial}{\partial x} \left(\mu \frac{\partial v_x}{\partial x} \right) \hat{x}$$

In Cartesian Coordinates (2D):

$$\nabla \cdot \vec{\tau}_{vis} = \begin{array}{l} \left\{ \frac{4}{3} \frac{\partial}{\partial x} \left(\mu \frac{\partial v_x}{\partial x} \right) + \frac{\partial}{\partial y} \left(\mu \frac{\partial v_x}{\partial y} \right) + \frac{1}{3} \frac{\partial}{\partial x} \left(\mu \frac{\partial v_y}{\partial y} \right) \right\} \hat{x} \\ \left\{ \frac{\partial}{\partial x} \left(\mu \frac{\partial v_y}{\partial x} \right) + \frac{4}{3} \frac{\partial}{\partial y} \left(\mu \frac{\partial v_y}{\partial y} \right) + \frac{1}{3} \frac{\partial}{\partial y} \left(\mu \frac{\partial v_x}{\partial x} \right) \right\} \hat{y} \end{array}$$

In Cartesian Coordinates assuming μ is constant (2D):

$$\nabla \cdot \vec{\tau}_{vis} = \begin{array}{l} \mu \left(\frac{4}{3} \frac{\partial^2 v_x}{\partial x^2} + \frac{\partial^2 v_x}{\partial y^2} + \frac{1}{3} \frac{\partial}{\partial x} \frac{\partial v_y}{\partial y} \right) \hat{x} \\ \mu \left(\frac{\partial^2 v_y}{\partial x^2} + \frac{4}{3} \frac{\partial^2 v_y}{\partial y^2} + \frac{1}{3} \frac{\partial}{\partial y} \frac{\partial v_x}{\partial x} \right) \hat{y} \end{array}$$

In Cartesian Coordinates (3D):

$$\nabla \cdot \vec{\tau}_{vis} = \begin{array}{l} \left\{ \frac{\partial}{\partial x} \left(\mu \frac{\partial v_x}{\partial x} \right) + \frac{\partial}{\partial y} \left(\mu \frac{\partial v_x}{\partial y} \right) + \frac{\partial}{\partial z} \left(\mu \frac{\partial v_x}{\partial z} \right) + \frac{1}{3} \frac{\partial}{\partial x} \left[\mu \left(\frac{\partial v_x}{\partial x} + \frac{\partial v_y}{\partial z} + \frac{\partial v_z}{\partial z} \right) \right] \right\} \hat{x} \\ \left\{ \frac{\partial}{\partial x} \left(\mu \frac{\partial v_y}{\partial x} \right) + \frac{\partial}{\partial y} \left(\mu \frac{\partial v_y}{\partial y} \right) + \frac{\partial}{\partial z} \left(\mu \frac{\partial v_y}{\partial z} \right) + \frac{1}{3} \frac{\partial}{\partial y} \left[\mu \left(\frac{\partial v_x}{\partial x} + \frac{\partial v_y}{\partial y} + \frac{\partial v_z}{\partial z} \right) \right] \right\} \hat{y} \\ \left\{ \frac{\partial}{\partial x} \left(\mu \frac{\partial v_z}{\partial x} \right) + \frac{\partial}{\partial y} \left(\mu \frac{\partial v_z}{\partial y} \right) + \frac{\partial}{\partial z} \left(\mu \frac{\partial v_z}{\partial z} \right) + \frac{1}{3} \frac{\partial}{\partial z} \left[\mu \left(\frac{\partial v_x}{\partial x} + \frac{\partial v_y}{\partial y} + \frac{\partial v_z}{\partial z} \right) \right] \right\} \hat{z} \end{array}$$

Numerical form for viscous force (face-centered):

We are using the indexing of SMARAI, where v is a face centered quantity, u is a cell centered quantity.

$$\nabla\cdot\vec{\tau}_{vis} = \begin{matrix}\left\{\frac{4}{3}\frac{\partial}{\partial x}\left(\mu\frac{\partial v_x}{\partial x}\right)+\frac{\partial}{\partial y}\left(\mu\frac{\partial v_x}{\partial y}\right)+\frac{1}{3}\frac{\partial}{\partial x}\left(\mu\frac{\partial v_y}{\partial y}\right)\right\}\hat{x}\\ \left\{\frac{\partial}{\partial x}\left(\mu\frac{\partial v_y}{\partial x}\right)+\frac{4}{3}\frac{\partial}{\partial y}\left(\mu\frac{\partial v_y}{\partial y}\right)+\frac{1}{3}\frac{\partial}{\partial y}\left(\mu\frac{\partial v_x}{\partial x}\right)\right\}\hat{y}\end{matrix}$$

$$\left(\nabla\cdot\vec{\tau}_{vis}\right)_{x,i,j} = \begin{Bmatrix}\frac{4}{3}\frac{\mu_{i,j}\left(v_{x,i+1,j}-v_{x,i,j}\right)-\mu_{i-1,j}\left(v_{x,i,j}-v_{x,i-1,j}\right)}{\Delta x^2}\\ \frac{\mu_{i-1/2,j+1/2}\left(v_{x,i,j+1}-v_{x,i,j}\right)-\mu_{i-1/2,j-1/2}\left(v_{x,i,j}-v_{x,i,j-1}\right)}{\Delta y^2}\\ \frac{1}{3}\frac{\mu_{i,j}\left(v_{y,j+1,i}-v_{x,j,i}\right)-\mu_{i-1,j}\left(v_{y,j+1,i-1}-v_{x,j,i-1}\right)}{\Delta x\Delta y}\end{Bmatrix}$$

$$\left(\nabla\cdot\vec{\tau}_{vis}\right)_{y,j,i} = \begin{Bmatrix}\frac{\mu_{i+1/2,j-1/2}\left(v_{y,j,i+1}-v_{y,j,i}\right)-\mu_{i-1/2,j-1/2}\left(v_{y,j,i}-v_{y,j,i-1}\right)}{\Delta x^2}\\ \frac{4}{3}\frac{\mu_{i,j}\left(v_{y,j+1,i}-v_{y,j,i}\right)-\mu_{i,j-1}\left(v_{y,j,i}-v_{y,j-1,i}\right)}{\Delta y^2}\\ \frac{1}{3}\frac{\mu_{i,j}\left(v_{x,i+1,j}-v_{x,i,j}\right)-\mu_{i,j-1}\left(v_{x,i+1,j-1}-v_{x,i,j-1}\right)}{\Delta x\Delta y}\end{Bmatrix}$$

Note: $u_{i-1/2,j-1/2}$ is the value of μ at the node.

$$\mu_{i-1/2,j-1/2} = \tfrac{1}{4}\left(\mu_{i,j}+\mu_{i,j-1}+\mu_{i-1,j}+\mu_{i-1,j-1}\right)$$

Numerical form for viscous force (cell-centered):

We are using the indexing of SMARAI, where v and u are cell centered quantities.

$$\nabla\cdot\vec{\tau}_{vis}=\begin{matrix}\left\{\frac{4}{3}\frac{\partial}{\partial x}\left(\mu\frac{\partial v_x}{\partial x}\right)+\frac{\partial}{\partial y}\left(\mu\frac{\partial v_x}{\partial y}\right)+\frac{1}{3}\frac{\partial}{\partial x}\left(\mu\frac{\partial v_y}{\partial y}\right)\right\}\hat{x}\\ \left\{\frac{\partial}{\partial x}\left(\mu\frac{\partial v_y}{\partial x}\right)+\frac{4}{3}\frac{\partial}{\partial y}\left(\mu\frac{\partial v_y}{\partial y}\right)+\frac{1}{3}\frac{\partial}{\partial y}\left(\mu\frac{\partial v_x}{\partial x}\right)\right\}\hat{y}\end{matrix}$$

$$\left(\nabla\cdot\vec{\tau}_{vis}\right)_x=\frac{4}{3}\frac{\partial\mu}{\partial x}\frac{\partial v_x}{\partial x}+\frac{4}{3}\mu\frac{\partial^2 v_x}{\partial x^2}+\frac{\partial\mu}{\partial y}\frac{\partial v_x}{\partial y}+\mu\frac{\partial^2 v_x}{\partial y^2}+\frac{1}{3}\frac{\partial\mu}{\partial x}\frac{\partial v_y}{\partial y}+\frac{1}{3}\mu\frac{\partial^2 v_y}{\partial x\partial y}$$

$$\left(\nabla\cdot\vec{\tau}_{vis}\right)_{x,i,j}=\left\{\begin{matrix}\frac{4}{3}\frac{\mu_{i+1,j}-\mu_{i-1,j}}{2\Delta x}\frac{v_{x,i+1,j}-v_{x,i-1,j}}{2\Delta x}+\frac{4}{3}\mu_{i,j}\frac{v_{x,i+1,j}-2v_{x,i,j}+v_{x,i-1,j}}{\Delta x^2}\\ +\frac{\mu_{i,j+1}-\mu_{i,j-1}}{2\Delta y}\frac{v_{x,i,j+1}-v_{x,i,j-1}}{2\Delta y}+\mu_{i,j}\frac{v_{x,i,j+1}-2v_{x,i,j}+v_{x,i,j-1}}{\Delta y^2}\\ +\frac{1}{3}\frac{\mu_{i+1,j}-\mu_{i-1,j}}{2\Delta x}\frac{v_{y,i,j+1}-v_{y,i,j-1}}{2\Delta y}+\frac{1}{3}\mu_{i,j}\frac{v_{y,i+1,j+1}-v_{y,i+1,j-1}-v_{y,i-1,j+1}+v_{y,i-1,j-1}}{4\Delta x\Delta y}\end{matrix}\right\}$$

$$\left(\nabla\cdot\vec{\tau}_{vis}\right)_y=\frac{\partial\mu}{\partial x}\frac{\partial v_y}{\partial x}+\mu\frac{\partial^2 v_y}{\partial x^2}+\frac{4}{3}\frac{\partial\mu}{\partial y}\frac{\partial v_y}{\partial y}+\frac{4}{3}\mu\frac{\partial^2 v_y}{\partial y^2}+\frac{1}{3}\frac{\partial\mu}{\partial y}\frac{\partial v_x}{\partial x}+\frac{1}{3}\mu\frac{\partial^2 v_x}{\partial x\partial y}$$

$$\left(\nabla\cdot\vec{\tau}_{vis}\right)_{y,i,j}=\left\{\begin{matrix}\frac{\mu_{i+1,j}-\mu_{i-1,j}}{2\Delta x}\frac{v_{y,i+1,j}-v_{y,i-1,j}}{2\Delta x}+\mu_{i,j}\frac{v_{y,i+1,j}-2v_{y,i,j}+v_{y,i-1,j}}{\Delta x^2}\\ +\frac{4}{3}\frac{\mu_{i,j+1}-\mu_{i,j-1}}{2\Delta y}\frac{v_{y,i,j+1}-v_{y,i,j-1}}{2\Delta y}+\frac{4}{3}\mu_{i,j}\frac{v_{y,i,j+1}-2v_{y,i,j}+v_{y,i,j-1}}{\Delta y^2}\\ +\frac{1}{3}\frac{\mu_{i,j+1}-\mu_{i,j-1}}{2\Delta y}\frac{v_{x,i+1,j}-v_{x,i-1,j}}{2\Delta x}+\frac{1}{3}\mu_{i,j}\frac{v_{x,i+1,j+1}-v_{x,i+1,j-1}-v_{x,i-1,j+1}+v_{x,i-1,j-1}}{4\Delta x\Delta y}\end{matrix}\right\}$$

APPENDIX D.4) Thermal conduction:

For the thermal conduction in the hydrodynamic models we need to determine how to properly calculate the thermal flux between cell boundaries. The difficulty lies in the proper way to interpolate the thermal conductivity between the cell center (where the thermal conductivity is calculated and the cell face (where it is needed). While we could average the thermal conductivity, it is more accurate to match the thermal flux in each cell and let the midpoint temperature vary. Consider the equation for the thermal flux:

$$\vec{q} = -\kappa_s \nabla T_s$$

Consider two regions (1 & 2):

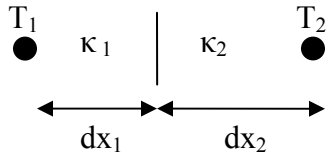

If the thermal conductivity is uniform, the energy conducted from 1 to 2:

$$\vec{q} = -\frac{\kappa(T_2 - T_1)}{\Delta x_1 + \Delta x_2}$$

If the thermal conductivity is not uniform:

$$\vec{q} = \frac{\kappa_1 \kappa_2 (T_1 - T_2)}{\kappa_2 \Delta x_1 + \kappa_1 \Delta x_2}$$

Note: $\Delta x_1, \Delta x_2$ are the distance from the zone midpoints to the wall

If the zones are equally spaced, but have different conductivities (Δx is the zone width):

$$\vec{q} = \frac{2\kappa_1 \kappa_2}{\kappa_1 + \kappa_2} \frac{T_1 - T_2}{\Delta x}$$